

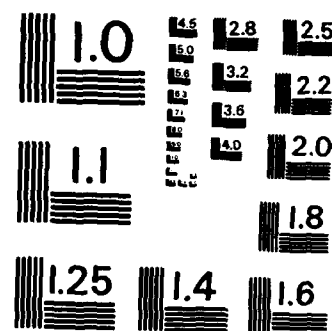
UNCLASSIFIED

CASE STUDIES OF THE STRUCTURE OF THE ATMOSPHERIC  
BOUNDARY LAYER ENTRAINMENT ZONE(U) AIR FORCE INST OF  
TECH WRIGHT-PATTERSON AFB OH T D CRUM 1985  
AFIT/CI/NR-85-129D F/B 4/2

1/3

F/G 4/2

NL



MICROCOPY RESOLUTION TEST CHART  
NATIONAL BUREAU OF STANDARDS-1963-A

UNCLASS

SECURITY CLASSIFICATION OF THIS PAGE (When Data Entered)

AD-A160 911

REPORT DOCUMENTATION PAGE		READ INSTRUCTIONS BEFORE COMPLETING FORM
1. REPORT NUMBER AFIT/CI/NR 85- 129D	2. GOVT ACCESSION NO. <b>AD-A160 911</b>	3. RECIPIENT'S CATALOG NUMBER
4. TITLE (and Subtitle) Case Studies Of The Structure Of The Atmospheric <b>BOUNDARY LAYER ENTRAINMENT ZONE</b>		5. TYPE OF REPORT & PERIOD COVERED <b>THESIS/DISSERTATION</b>
7. AUTHOR(s) Timothy D. Crum		6. PERFORMING ORG. REPORT NUMBER
9. PERFORMING ORGANIZATION NAME AND ADDRESS AFIT STUDENT AT: University of Wisconsin-Madison		8. CONTRACT OR GRANT NUMBER(s)
11. CONTROLLING OFFICE NAME AND ADDRESS AFIT/NR WPAFB OH 45433 - 6583		10. PROGRAM ELEMENT, PROJECT, TASK AREA & WORK UNIT NUMBERS
14. MONITORING AGENCY NAME & ADDRESS (if different from Controlling Office)		12. REPORT DATE 1985
		13. NUMBER OF PAGES 247
		15. SECURITY CLASS. (of this report)  UNCLASS
		16. DECLASSIFICATION/DOWNGRADING SCHEDULE
16. DISTRIBUTION STATEMENT (of this Report) APPROVED FOR PUBLIC RELEASE; DISTRIBUTION UNLIMITED		
17. DISTRIBUTION STATEMENT (of the abstract entered in Block 20, if different from Report) "Original contains color plates: All DTIC reproductions will be in black and white"		
18. SUPPLEMENTARY NOTES APPROVED FOR PUBLIC RELEASE: IAW AFR 190-1  25 Oct 85 LYNN E. WOLAVER Dean for Research and Professional Development AFIT, Wright-Patterson AFB		
19. KEY WORDS (Continue on reverse side if necessary and identify by block number)		
20. ABSTRACT (Continue on reverse side if necessary and identify by block number)  ATTACHED		

DTIC FILE COPY

DD FORM 1 JAN 73 1473

EDITION OF 1 NOV 65 IS OBSOLETE

UNCLASS

SECURITY CLASSIFICATION OF THIS PAGE (When Data Entered)

85 11 04 063

CASE STUDIES OF THE STRUCTURE OF THE ATMOSPHERIC

BOUNDARY LAYER ENTRAINMENT ZONE

Timothy D. Crum, Major, USAF

1985

247 pp

PHD Meteorology

University of Wisconsin-Madison

Abstract

The structure of the atmospheric entrainment zone, an interfacial layer between the convective boundary layer and the stable air aloft, is studied using data obtained during Boundary Layer Experiment 1983 in Oklahoma. Coincident high resolution aircraft and lidar observations provided a unique picture of the daytime continental entrainment zone. Fast-response Lyman alpha hygrometer output voltages from the aircraft are calibrated to

129

✓

PER CALL JC

A-1



## AFIT RESEARCH ASSESSMENT

The purpose of this questionnaire is to ascertain the value and/or contribution of research accomplished by students or faculty of the Air Force Institute of Technology (AU). It would be greatly appreciated if you would complete the following questionnaire and return it to:

AFIT/NR  
Wright-Patterson AFB OH 45433

RESEARCH TITLE: Case Studies of the Structure of the Atmosphere **BOUNDARY**  
**LAYER ENTRAINMENT ZONE**

AUTHOR: Timothy D. Crum

## RESEARCH ASSESSMENT QUESTIONS:

1. Did this research contribute to a current Air Force project?

☐ a. YES

☐ b. NO

2. Do you believe this research topic is significant enough that it would have been researched (or contracted) by your organization or another agency if AFIT had not?

☐ a. YES

☐ b. NO

3. The benefits of AFIT research can often be expressed by the equivalent value that your agency achieved/received by virtue of AFIT performing the research. Can you estimate what this research would have cost if it had been accomplished under contract or if it had been done in-house in terms of manpower and/or dollars?

☐ a. MAN-YEARS \_\_\_\_\_

☐ b. \$ \_\_\_\_\_

4. Often it is not possible to attach equivalent dollar values to research, although the results of the research may, in fact, be important. Whether or not you were able to establish an equivalent value for this research (3. above), what is your estimate of its significance?

☐ a. HIGHLY  
SIGNIFICANT

☐ b. SIGNIFICANT

☐ c. SLIGHTLY  
SIGNIFICANT

☐ d. OF NO  
SIGNIFICANCE

5. AFIT welcomes any further comments you may have on the above questions, or any additional details concerning the current application, future potential, or other value of this research. Please use the bottom part of this questionnaire for your statement(s).

NAME \_\_\_\_\_

GRADE \_\_\_\_\_

POSITION \_\_\_\_\_

ORGANIZATION \_\_\_\_\_

LOCATION \_\_\_\_\_

STATEMENT(s): \_\_\_\_\_

CASE STUDIES OF THE STRUCTURE OF THE ATMOSPHERIC  
BOUNDARY LAYER ENTRAINMENT ZONE

by

TIMOTHY DOYAL CRUM

A thesis submitted in partial fulfillment of the  
requirements for the degree of

Doctor of Philosophy  
(Meteorology)

at the

UNIVERSITY OF WISCONSIN-MADISON

1985

CASE STUDIES OF THE STRUCTURE OF THE ATMOSPHERIC  
BOUNDARY LAYER ENTRAINMENT ZONE

Timothy D. Crum

Under the supervision of Professor Roland B. Stull

Abstract

The structure of the atmospheric entrainment zone, an interfacial layer between the convective boundary layer and the stable air aloft, is studied using data obtained during Boundary Layer Experiment 1983 in Oklahoma. Coincident high resolution aircraft and lidar observations provided a unique picture of the daytime continental entrainment zone. Fast-response Lyman alpha hygrometer output voltages from the aircraft are calibrated to yield meteorological units of humidity. These humidity measurements compare well with those made by ground-based sensors. Humidity values indicative of surface layer air are observed at all levels within rising thermals, and the corresponding top-hat



humidity cross sections suggest little lateral entrainment.

Selection of specific humidity as a conditional sampling criteria for surface layer air in the entrainment zone results from a comparison of coincident aircraft data traces and ground-based lidar range height indicator scans.

Using this conditional sampling criteria, two approaches are taken to describe the humidity structure of the entrainment zone. The first uses the linear mixing character of specific humidity. This yields vertical profiles of the proportion of surface layer air that are described well by the cumulative distribution function of asymmetrical double exponential functions. The second approach models frequency distributions of three types of air in the entrainment zone: unmixed free atmosphere (dry); unmixed surface layer air (moist); and a mixture of these two. The resultant modeled frequency distributions of specific humidity capture the following observed features: Low in the convective boundary layer, surface layer air is frequently observed with little mixture air and no free atmosphere air. Higher in the convective boundary layer, near the middle of the entrainment zone, the proportion of free atmosphere and mixture air increase while unmixed surface layer air decreases. As one approaches the top of the entrainment zone, surface layer and mixture proportions

decrease to zero leaving only free atmosphere air. These results can be useful in cloud models and for future studies of the boundary layer.

APPROVED:

A handwritten signature in cursive script, appearing to read "Roland B. Stull".

Roland B. Stull

## Acknowledgements

My most sincere appreciation goes to the people who assisted, guided and supported me during my three years of graduate work at the University of Wisconsin. Professor Roland Stull has always made himself available to provide the assistance and moral support I needed to successfully complete this work. His efforts will never be forgotten and will be always gratefully appreciated. Dr Edwin Eloranta also unselfishly gave of his time and talents to assist this research effort--far above his obvious expertise in the UW lidar system. Ed, my thanks to you.

I also thank the members of my PhD committee: Professors David Houghton, Charles Stearns, Pao Wang, and Gregory Reinzel for their interest and useful critiques.

Much of the lidar graphics and other computer assistance that I received were provided by Dan Forrest and Bob Chojnacki.

The Atmospheric Physics Section of the Argonne National Laboratory graciously shared the data they collected during BLX83 with us. They also were very helpful during phone and face-to-face discussions concerning analysis of the data.

Most importantly, this research would not have been possible without the dedication, understanding, and support of my wife and

two sons, John and Mark. They carried the burden of not seeing me often during the past three years and when they did it was only to have me being preoccupied with my work.

During my graduate study at the University of Wisconsin I was supported by the Air Force Institute of Technology Civilian Institutions Program. The research was supported by Grants ATM-8414371 and ATM-8211842 from the National Science Foundation.

## Table of Contents

	Page
Abstract	i
Acknowledgements	iv
Table of Contents	vi
List of Figures	ix
List of Tables	xiv
1. Introduction	1
1.1 Definition and Goals	1
1.2 Significance and Literature Review	5
1.3 Outline of Methodology	9
2. Boundary Layer Experiment 1983 and Instrumentation	11
2.1 Introduction	11
2.2 NCAR Queen Air Aircraft	11
2.3 Queen Air Individual Sensor Description and Performance	17
2.3.1 Humidity	17
2.3.2 Temperature	22
2.3.3 Radiation	23
2.3.4 Winds	23
2.4 UW Lidar System	26
2.5 Argonne National Laboratory Instrumentation	29
2.6 NCAR Portable Automated Mesonetwork	30

2.7	Data Processing	31
3.	High speed moisture measurement, calibration, and flux calculation	40
3.1	Overview	40
3.2	Sensor Selection	41
3.3	Lyman alpha Calibration	46
3.4	Computed Surface Flux Values and Comparisons with Other Measures of Flux	51
3.5	Conclusion	71
4.	Development of conditional sampling criteria	72
4.1	Method of Analysis	74
4.2	Sounding Case Studies	80
4.2.1	1428 CDT 14 June 1983	80
4.2.2	1106 CDT 27 May 1983	83
4.3	Horizontal Flight Leg Case Studies	87
4.3.1	1358 CDT 7 June 1983	88
4.3.2	1325 CDT 7 June 1983	91
4.3.3	1450 CDT 7 June 1983	94
4.3.4	1129 CDT 27 May 1983	96
4.3.5	1214 CDT 16 June 1983	99
4.3.6	1529 CDT 28 May 1983	99
4.3.7	1325 CDT and 1450 CDT 7 June 1983	102
4.4	Further Discusssion	105
5.	Analysis and Synthesis of Entrainment Zone Characteristics	107

5.1	Overview	107
5.2	Observations of Mixing in the CBL	110
5.3	Linear Mixing Approach	121
5.3.1	Theory	121
5.3.2	Resultant Profiles of Entrainment Zone Structure	122
5.4	Mixture Approach	134
5.4.1	Theroy	134
5.4.2	Results	139
6.	Summary and Recommendations	157
Appendices		
A.	Maps and plots of data for case study days	163
B.	Unsuccessful attempts ot calibrate the Lyman alpha	198
C.	Lyman alpha calibration lines	202
D.	Alternate methods of flux determination	215
E.	Selection, Derivation and Illustration of Asymmetrical Double Exponential Functions	223
References		232

## List of Figures

Figure Number	Description	Page
1.1	Lidar RHI scan ending at 1213 CDT 16 Jun 83 showing position of entrainment zone	3
1.2	Lidar entrainment zone heights for 16 Jun 83	4
2.1	BLX83 sensor location	12
2.2	NCAR Queen Air aircraft	15
2.3	NCAR Queen Air flight pattern	16
2.4	Spectra plot for the Rosemount boom and reverse flow temperature sensors on a typical near-surface flight leg, 1653-1701 CDT 7 Jun 1983	24
2.5	Comparative time series plots of three temperature sensors carried on the Queen Air for a typical near-surface flight leg, 1653-1701 CDT 7 Jun 1983	25
2.6	Descriptive lidar RHI scan	28
3.1	Comparative time series plot of three Queen Air hygrometer sensors	43
3.2	Dewpointer, microwave refractometer and Lyman alpha spectra plot for a typical near-surface flight leg, 1653-1701 CDT 7 Jun 1983	44
3.3	Lyman alpha calibration line for Flight 2, 27 May 83	48
3.4	Flight 2 flux profiles	58
3.5	Flight 3 flux profiles	59
3.6	Flight 13 flux profiles	60
3.7	Flight 16 flux profiles	61
3.8	Plot of coincident Queen Air and PAM II pyranometer data	63



3.9	Plot of coincident Queen Air and ANL net radiation data	64
3.10	Plot of coincident Queen Air and ANL sensible heat fluxes	65
3.11	Plot of coincident Queen Air and ANL latent heat fluxes	66
3.12	Estimated ground storage term from Queen Air plotted as a function of time	68
3.13	Estimated ground storage term from ANL plotted as a function of time	69
4.1	Graphics used in display of coincident Queen Air and lidar data	75-77
4.2	Lidar RHI at 1427:56 CDT 14 Jun 1983 and Queen Air plots	81
4.3	Lidar RHI at 1427:56 CDT 14 Jun 1983 and Queen Air plots	82
4.4	Lidar RHI at 1105:34 CDT 27 May 1983 and Queen Air plots	84
4.5	Lidar RHI at 1105:34 CDT 27 May 1983 and Queen Air plots	85
4.6	Lidar RHI at 1358:08 CDT 7 June 1983 and Queen Air plots	89
4.7	Photo from Queen Air at 1358:36 CDT 7 June 1983	90
4.8	Lidar RHI at 1325:45 CDT 7 June 1983 and Queen Air plots	92
4.9	Plot of 20 HZ specific humidity and ambient temperature	93
4.10	Lidar RHI at 1450:06 CDT 7 June 1983 and Queen Air plots	95

4.11	Lidar RHI at 1129:16 CDT 27 May 1983 and Queen Air plots	97
4.12	Lidar RHI at 1213:32 CDT 16 June 1983 and Queen Air plots	100
4.13	Lidar RHI at 1528:55 CDT 28 May 1983 and Queen Air plots	101
4.14	Lidar RHI at 1325:45 CDT 7 Jun 1983 and Queen Air plots	103
4.15	Lidar RHI at 1450:06 CDT 7 June 1983 and Queen Air plots	104
5.1	Lidar RHI scan at 1052 CDT on 29 Apr 76 showing vectors of thermal motion in CBL	109
5.2	Histogram of specific humidity collected during a horizontal flight leg between 1145-1149 CDT 16 Jun 83	112
5.3	Histogram of specific humidity as a function of height on 28 May, Flight 3, Legs 2-11	114
5.4	Histogram of specific humidity as a function of height on 28 May, Flight 3, Legs 13-23	115
5.5	Histogram of specific humidity as a function of height on 14 Jun, Flight 13, Legs 1-10	116
5.6	Histogram of specific humidity as a function of height on 14 Jun, Flight 13, Legs 17-22	117
5.7	Histogram of specific humidity as a function of height on 16 Jun, Flight 16, Legs 5-11	118
5.8	Schematic of linear mixing approach indicator function	123
5.9	Plot of normalized height versus proportion of SL air on 28 May 83, Flight 3 Legs 3-11	126
5.10	Plot of normalized height versus proportion of SL air on 28 May 83, Flight 3 Legs 14-23	127

5.11	Plot of normalized height versus proportion of SL air on 14 Jun 83, Flight 14 Legs 1-11	128
5.12	Plot of normalized height versus proportion of SL air on 14 Jun 83, Flight 14 Legs 14-22	129
5.13	Plot of normalized height versus proportion of SL air on 16 Jun 83, Flight 16 Legs 1-12	130
5.14	Graphic example of the sum of three density functions	137
5.15	Vertical profile of parameter estimates from mixture approach, Flight 3, Leg 4-11	143
5.16	Vertical profile of parameter estimates from mixture approach, Flight 3, Leg 15-20	144
5.17	Vertical profile of parameter estimates from mixture approach, Flight 13, Leg 4-10	145
5.18	Vertical profile of parameter estimates from mixture approach, Flight 13, Leg 17-20	146
5.19	Vertical profile of parameter estimates from mixture approach, Flight 16, Leg 5-12	147
5.20	Comparison of observed and theoretical distribution (mixture approach) of specific humidity for Flight 3, Legs 4-9	149
5.21	Comparison of observed and theoretical distribution (mixture approach) of specific humidity for Flight 3, Legs 15-19	150
5.22	Comparison of observed and theoretical distribution (mixture approach) of specific humidity for Flight 13, Legs 5-10	151
5.23	Comparison of observed and theoretical distribution (mixture approach) of specific humidity for Flight 13, Legs 17-20	152
5.24	Comparison of observed and theoretical distribution (mixture approach) of specific humidity for Flight 16, Legs 6-11	153

5.25 Comparison of vertical profile of SL proportion 155  
estimates from original and modeled data for Flight 3,  
Legs 3-11.

## List of Tables

Table Number	Description	Page
2.1	Queen Air instrumentation	14
2.2	Portable Automated Mesonetwork II instrumentation	32
3.1	Computed versus observed cloud base for 7 Jun 83	50
3.2	Lyman alpha calibration coefficients for Queen Air flights during BLX83	52
3.3	Queen Air measurements of surface energy budget terms obtained on near-surface flight legs during BLX83	56
4.1	Queen Air flight level winds for horizontal flight legs when coincident lidar RHI scans were available	98
5.1	Estimated Proportions of SL air existing in EZ measured by Queen Air during EZ flights using linear mixing approach	124
5.2	Asymmetrical double exponential parameters of best fits to vertical profiles of proportion of SL air estimated from linear mixing approach	133
5.3	MLE estimates of parameters from mixture approach	142

## Chapter 1

### Introduction

#### 1.1 Definition and Goals

The boundary layer is the region of the atmosphere next to the earth's surface that varies in direct response to surface forcings (Stull, 1985a). During daylight hours in fair weather conditions over land, one of these forcings is the heating of the air by the earth's surface as the ground is warmed by the sun. The resulting convection is often initially confined to a shallow layer called the mixed layer (ML) or convective boundary layer (CBL), which then deepens during the day as solar heating continues. In the CBL buoyant parcels of heated air organize as thermals and rise until they reach a capping stable layer. Turbulence at the top of the CBL drives the entrainment of this stable layer air down into the CBL. This entrained mass not only results in the growth of the CBL during the day, but it mixes down air of different temperature, humidity, and pollutant concentration to modify the respective CBL properties. Driedonks (1982) and Tennekes and Driedonks (1981) give summaries of the past

theoretical and observational work done in understanding the growth of the CBL, and work in this area continues (e.g. Boers et al., 1984; Binkowski, 1983).

The turbulent interface between the stable capping layer aloft and the CBL below is called the entrainment zone (Deardorff et al., 1980), a region of finite depth that is roughly 10 to 40 % of the depth of the CBL. Figure 1.1 shows an example of how the daytime CBL and position of the entrainment zone appear on a lidar range height indicator (RHI) scan (X-Z plane). The heights indicated in Figure 1.1 are subjectively determined using the following definitions. The top of the highest thermal defines  $h_2$ , the top of the entrainment zone. The average mixed layer depth is at  $Z_1$  (where a 50-50 % mixture of ML air from below and free atmosphere air from above exists). The bottom of the entrainment zone is at  $h_0$  (where 90-95 % of the air is ML air). A sequence of RHI scans can be subjectively analyzed to follow the evolution of the daytime CBL and more specifically the depth of the entrainment zone. Figure 1.2 shows such an example of the daytime growth of the CBL and changes in the depth of the entrainment zone in response to solar heating of the earth's surface. The purpose of this study is to investigate the structure of the atmosphere's entrainment zone using field experiment data and parameterize its structure to allow for future development of theory and models leading to better forecasts of the CBL and fair weather cumulus

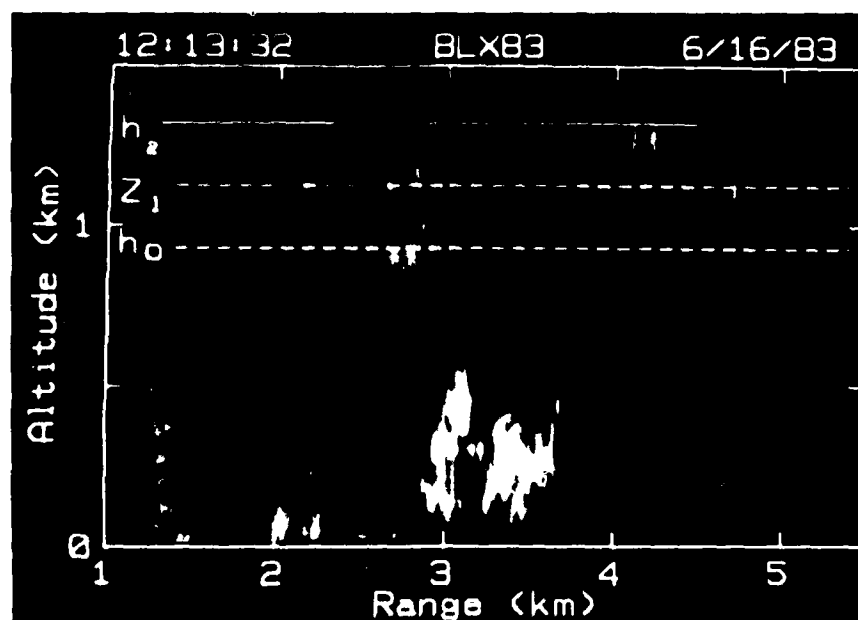


Figure 1.1 Lidar range height indicator scan at 1213 CDT on 16 Jun 1983. Thermals in the mixed layer appear white or gray, while capping stable layer air from the free atmosphere appears black in this computer enhancement. The average CBL height ( $Z_i$ ) is indicated on the image as well as the bottom ( $h_0$ ) and top ( $h_2$ ) of the entrainment zone. The depth of the entrainment zone is  $h_2 - h_0$ . The heights  $h_0$ ,  $Z_i$ , and  $h_2$  are subjectively determined.



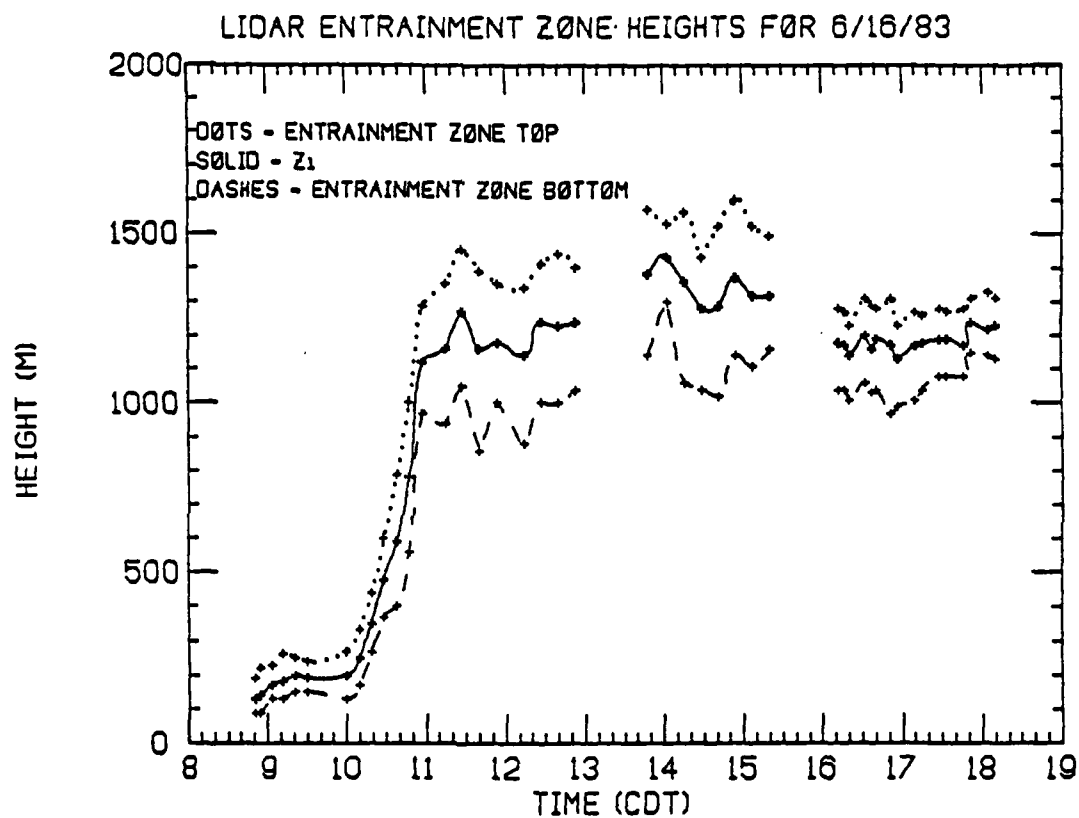


Figure 1.2 Daytime change of entrainment zone depth as subjectively determined from lidar RHI imagery for 16 Jun 83. Missing heights are due to lidar equipment outages. The lower heights after 1530 CDT are due to the effects of subsidence.

onset and coverage. Specific goals include:

(1) Development of conditional sampling criteria to measure the amount of surface layer air existing in the entrainment zone.

(2) Determine the amount of surface layer air existing at various levels in the entrainment zone.

(3) Parameterize in terms of analytical functions the distribution of surface layer quantities (i.e. specific humidity) as a function of height through the entrainment zone.

## 1.2 Significance and Literature Review

Understanding the evolution of the entrainment zone and the CBL is important for forecasts of temperature and pollutant levels near the surface, for cumulus cloud cover estimates, and for the boundary conditions used in large-scale numerical weather prediction models. Fair weather cumulus clouds may form at the top of the CBL if the rising parcels of air reach their lifting condensation level (LCL). As the CBL grows, the height of the LCL generally increases because the free atmosphere air entrained into the CBL is usually drier than the original CBL air, which causes a decrease of CBL humidity. Time series plots of the rise of the LCL and height of the CBL are shown by Wilde (1984). However, as Manton (1982) among other researchers has learned, forecasts of

cumulus onset and coverage are dependent on more than just the height of the CBL.

Despite the importance of the entrainment zone in understanding the growth of the CBL and the onset of cumulus clouds, little observational data exist on the entrainment zone characteristics (Caughey et al., 1979 and Palmer et al., 1979). Lidar measurements of entrainment zone thickness were obtained by Boers et al. (1984). The scarcity of observations is due in part to the relative inaccessibility of the entrainment zone to direct measurements. The entrainment zone's position varies from a few tens of meters above the ground in the morning to, in some cases, 2 km or more in the afternoon. This places the entrainment zone out of the reach of instrumented towers for much of the day and necessitates the use of instrumented balloons or aircraft for direct observations.

Deardorff et al. (1980) simulated the atmospheric CBL in a water-filled laboratory tank experiment to study the entrainment zone. Using milk as a tracer of the simulated CBL (versus clear water for the stable layer above) Deardorff et al. obtained estimates of the amount of CBL fluid reaching various levels in the tank by illuminating thin horizontal layers of the tank with a spread laser beam, and then photographing the tank from above. The resultant vertical profile of the amount of CBL air reaching given altitudes smoothly varies from 90 % at the entrainment zone

bottom to 0 % at the top, and has a shape resembling the cumulative distribution function of a double exponential function (Wilde et al., 1985). This profile contrasts with one approximated by a power law used by Manton (1982) in a fair-weather cumulus model. Manton estimated the exponent in his power law after looking at the results of earlier laboratory tank experiments by Deardorff et al. (1969), but states that the choice was somewhat arbitrary and needs to be explicitly tested.

Deardorff et al. (1980) define the entrainment zone to be the region between the top of the tallest thermal and the level where 90 - 95 % of the air is of CBL origin. Since the cumulus cloud cover fraction is dependent on the amount of CBL air that reaches and exceeds its LCL, precise measurement of the amount of CBL air as a function of height in the entrainment zone is important. Wilde et al. (1985) demonstrate that there is a natural variability in the LCL of thermals in a region and that the expected coverage of cumulus clouds is related to the probability that CBL air is likely to be at or above its local LCL. Unfortunately, Wilde et al. (1985) lacked accurate information on the frequency distribution of the CBL air in the entrainment zone (which is the result of this study), and were forced to use Deardorff's parameterization.

Most boundary layer studies using measurements from instrumented aircraft had their focus below the entrainment zone

and/or were not in continental regions (Khalsa and Greenhut, 1985; Grossman, 1984; Greenhut and Khalsa, 1982; Greenhut and Bean, 1981; Lenschow and Stephens, 1980; and Bean et al., 1976 among others). Coulman and Warner (1977) took extensive aircraft measurements just below cumulus cloud base in a continental situation but with relatively slow response sensors. Palmer et al. (1979), Caughey et al. (1979), Moores et al. (1979) and Rayment and Readings (1974) used instrumented balloons to collect data in the entrainment zone. However, no studies have been published in which an instrumented aircraft with fast-response sensors has flown repeated horizontal flight legs with great vertical resolution in the entrainment zone.

Improved sensor technology and data processing capability during the past 20 years have permitted an improved capability to perform in situ observations with instrumented aircraft in the boundary layer. Developments and improvements in remote sensing devices (sodar, radar and lidar) have also allowed their use in observing the CBL and the entrainment zone (Taconet and Weill, 1982 and 1983; Coulter, 1979; Russell and Uthe, 1978; Kunkel et al., 1977; Hall, 1975; Rowland, 1973; Uthe, 1972; and Konrad, 1970 are examples).

### 1.3 Outline of Methodology

The entrainment zone research presented here utilizes a unique data set obtained directly by an instrumented aircraft, the NCAR Queen Air, and remotely by the University of Wisconsin ground-based lidar. This and other supporting data were collected during the 1983 Boundary Layer Experiment (BLX83), a field experiment conducted southwest of Oklahoma City, OK in May and June 1983.

The large number of sensors employed in BLX83 and used in this study are discussed in Chapter 2. One of the airborne sensors, a Lyman-alpha hygrometer, is critical for study of the entrainment zone. A technique for converting voltages from this fast response Lyman alpha hygrometer to meteorological units is developed in Chapter 3. This calibration technique is also tested against two independent sets of measurements in that chapter.

In Chapter 4 the aircraft and lidar data are combined to aid the development of conditional sampling criteria for the aircraft data. Unique coincident lidar imagery of the CBL and time series of data collected by an in situ aircraft flying within the lidar's field of view have resulted in new thoughts on conditional sampling criteria, on evidence that not all thermals are created equal, and on the cross-section profiles of temperature and humidity within thermals.

The results of the calibration and conditional sampling work were applied to horizontal flight leg data to determine the humidity structure of the entrainment zone. Two approaches were used to analyze the resulting data. These approaches and their results are presented in Chapter 5.

## Chapter 2

### Boundary Layer Experiment-1983 and Instrumentation

#### 2.1 Introduction

The data for this study was collected during May and June 1983 southwest of Oklahoma City OK during the NSF-sponsored field experiment Boundary Layer Experiment-1983 (BLX83) (Stull and Eloranta, 1984). An instrumented aircraft, lidar, flux tower, rawinsondes, and portable automated mesonetwork reporting stations were the most heavily used sensors in this study. Figure 2.1 shows the geographical placement of the sensors.

One of the unique features of BLX83 was the concurrent measurement of the atmosphere by a wide variety of in situ and remote sensing instruments. Each system has its own characteristics and errors, but when the observations from many sensors are combined, some unmistakable conclusions emerge. This chapter covers the characteristics of the sensors that this study relied on most heavily.

#### 2.2 NCAR Queen Air Aircraft

During BLX83, the NCAR Research Aviation Facility Beechcraft



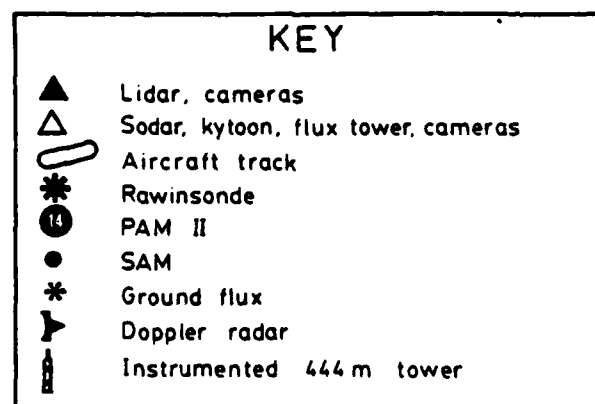
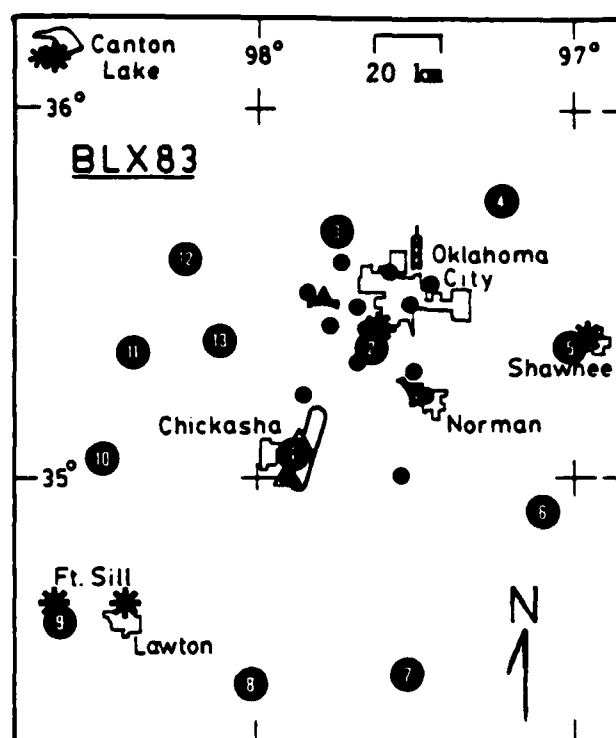


Figure 2.1 Physical layout of BLX83 data sources (Stull and Eloranta, 1984). The primary field site is located near the center at PAM station #1. This was also used as the initial point for the aircraft racetrack flight patterns.

Queen Air number N306D was used. The aircraft is equipped with an inertial navigation system (INS) which computes the aircraft's attitude, altitude, velocity, and latitude and longitude. This information along with measurements of air temperature, pressure, dew point, geometric altitude, and long- and short- wave radiation are collected at rates given in Table 2.1. The data sampled at 5 Hz, was averaged to 1 Hz with a Hermite interpolation algorithm. This and the 25 Hz data were filtered with 0.5 and 10 Hz respectively 4-pole low-pass Butterworth filters and written on the magnetic tapes made available for analysis. The Airborne Research Instrumentation System IV (ARIS IV) (Duncan and Brown, 1978) handles the data collection and writing data to magnetic tape.

The sensors used for measuring the three wind components, temperature, and fast-response hygrometer were located close to one another near the tip of the Queen Air's 1.83 m long nose boom (Figure 2.2).

The Queen Air flew a sequence of straight and level flight legs in a race track pattern with one side of the pattern aligned with the lidar's center beam. These legs were flown at various preplanned altitudes in order to collect data at various heights in the boundary layer (Figure 2.3). On days with no clouds,

Table 2.1 Queen Air Instrumentation

Parameter Measured	Combined Performance of Transducer, Signal Conditioning and Recorder			Sample Rate (Hz)
	Range	Accuracy	Resolution	
Aircraft Latitude	$\pm 90^\circ$	$\pm 0.066^\circ$	$0.001^\circ$	25
Aircraft Longitude	$\pm 180^\circ$	$\pm 0.066^\circ$	$0.001^\circ$	25
Aircraft Ground Speed	0 to 400 m/s	$\pm 1$ m/s	0.04 m/s	25
Aircraft Vertical Velocity	$\pm 50$ m/s	$\pm 0.1$ m/s	0.012 m/s	25
Aircraft True Heading	$0^\circ$ to $360^\circ$	$\pm 0.05^\circ$	$0.001^\circ$	25
Aircraft Pitch Angle	$45^\circ$	$\pm 0.008^\circ$	$0.005^\circ$	25
Aircraft Roll Angle	$45^\circ$	$\pm 0.008^\circ$	$0.005^\circ$	25
Static Pressure	400-1035 mb	$\pm 1$ mb	0.25 mb	5
Temperature (ATB)	-20 to 40 C	$\pm 0.5$ C	0.024 C	25
Temperature (ATRF)	-20 to 40 C	$\pm 0.5$ C	0.024 C	25
Dewpoint Temperature	-50 to 50 C	$\pm 0.5$ C	0.025 C	5
Lyman Alpha	$\pm 10$ V		0.0024 V	25
Refractometer	0 to 300 N		0.05 N	25
Radiometric Surface Temp	10 to 60 C	$\pm 1.0$ C	0.015 C	5
Infrared Radiation	0 to 500 w/m <sup>2</sup>		0.15 w/m <sup>2</sup>	5
Visible Radiation	0 to 1400 w/m <sup>2</sup>		0.40 w/m <sup>2</sup>	5



Figure 2.2 NCAR Queen Air N306D instrumented aircraft used during Boundary Layer Experiment 1983. The 20 Hz sensors are mounted on the instrumented boom. One of the strain gauges is near A. The three temperature sensors were: B, boom Rosemount; C, reverse flow; and D, fast response. The Lyman alpha hygrometer is near E.

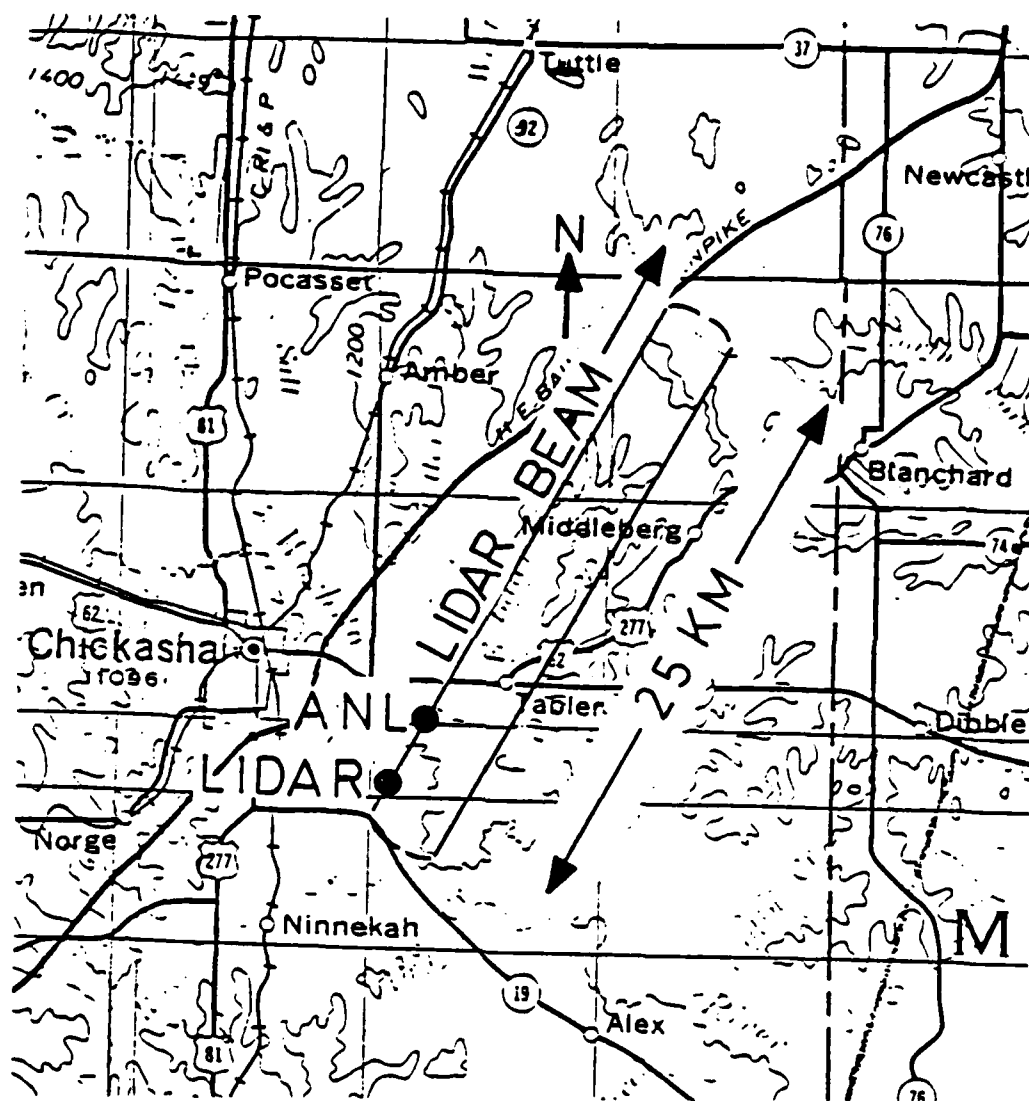


Figure 2.3 Location and orientation of principal ground-based equipment and Queen Air racetrack flight pattern during Boundary Layer Experiment 1983. Details of the lidar and Argonne National Laboratory (ANL) sites are discussed in sections 2.4 and 2.5.

flight legs were flown at approximately 0.3, 0.6, 0.8, 0.9, 1.0, 1.1, 1.2, 1.3  $Z/Z_i$  (where  $Z_i$  is the average depth of the CBL as in Deardorff et al., 1980). This sequence, which was preceeded and followed by an ascending or descending sounding leg, was known as an "entrainment zone flight." On days with fair weather cumulus, a "cloud-base flight" was flown with legs at 0.5  $Z/Z_i$ , cloud base - 100 m, and the middle of the clouds, also preceeded and followed by a sounding. There were four entrainment zone flights and seven cloud-base flights during BLX83. On all flights, the soundings were made from near the surface to above the top of the entrainment zone. Also, low altitude flight legs were flown immediately preceeding or following the soundings so that an estimate of the surface fluxes and  $w_*$  (the free convection scaling velocity) values could be made via the eddy correlation technique.

## 2.3 Queen Air Individual Sensor Description and Performance

### 2.3.1 Humidity

#### (1) Chilled mirror technique (dewpointer)

Two of these sensors (EG&G Model 137) were mounted on the main fuselage of the Queen Air (one on top and the other on the

bottom) approximately 8.8 m from the nose boom sensors. They use the principle of cooling/heating a reflective mirror until the mirror temperature reaches the dew point (or frost point) when condensate is in equilibrium on the mirror surface.

Light emitted by a lamp is reflected by the mirrors and detected by photo-resistors in the optical sensing bridge and converted to an electrical signal. The signal drives an amplifier whose output signal is fed back to the cooler and thus controls the mirror temperature.

At small depressions, the sensor mirror can typically cool or heat at a rate of 2 C/s. However, as will be discussed in section 3.2, the actual instrument response time is greater than one second.

## (2) Microwave Refractometer

This type of sensor was first developed in the mid 1950's. The particular sensor used on the Queen Air was supplied by NOAA Environmental Research Laboratory and mounted on the top of the fuselage near the entrance door approximately 9.6 m aft of the boom sensors.

The refractometer operates on the principle that at microwave frequencies the refractive index of air depends on air density and the density of water vapor and carbon dioxide. Using

the approximation that the mixing ratio of carbon dioxide is constant through the boundary layer, the atmospheric radio "refractivity" (N) has empirically been found for frequencies less than 30 GHz (Bean and Dutton, 1968) to be

$$N = 77.6 \frac{P_D}{T} + 72 \frac{e}{T} + 3.75 \times 10^5 \frac{e}{T^2} \quad (2-1)$$

The first term on the right hand side is the dry air component of the microwave refractive index while the last two terms are the water vapor component.  $P_D$ , T and e are dry air pressure (mb), absolute temperature (K) and water vapor pressure (mb) respectively.

Commonly, the above expression is simplified and solved for water vapor pressure by

$$e = \frac{T}{4810} \frac{TN}{77.6} - P \quad (2-2)$$

where N is the refractive index value provided by the refractometer.

The refractometer operates both on a sealed reference cavity and on a cavity exposed to the environment at 9.39 GHz. The differences in the resonant frequencies of the reference and environmental cavities are continuously measured, passed through an amplifier to magnify the small atmospheric refractivity changes of a few parts per million, and then collected by the



ARIS IV system.

The nature of the refractometer data will be discussed in section 3.2.

(3) Lyman alpha

The idea of using the absorption of Lyman alpha radiation (band center at 121.56 nm) by water vapor to provide high speed humidity measurements, first discussed in the late 1960's, led to NCAR's development of the Lyman-alpha hygrometer (Buck, 1976).

The Lyman-alpha hygrometer emits radiation in the Lyman-alpha spectrum using a uranium hydride,  $UH_3$ , discharge lamp. The radiation passes through a gap (typically of the order of 1 cm) exposed to the environment. The radiation intensity is sensed by a receiver at the other side of the gap where it is converted to a voltage that is processed by the ARIS IV system.

There are three significant absorbers of Lyman alpha radiation in the atmosphere: water vapor, oxygen and ozone. In the boundary layer, the ozone concentration yields an absorption approximately three orders of magnitude smaller than that of oxygen and four orders of magnitude smaller than that of water vapor. Hence, ozone can be neglected.

Considering only oxygen and water vapor, the difference between the emitted and sensed Lyman alpha radiation is described

by Beer's Law.

$$I = \int_{\lambda_1}^{\lambda_2} I_o(\lambda) \exp - \left[ \sum_{j=1}^2 K_j(\lambda) \rho_{oj} \right] d\lambda \quad (2-3)$$

where  $\lambda_1, \lambda_2$  = wavelength bounds of the Lyman alpha window (115 and 132 nm).

$K_j$  = absorption coefficient of the  $j$  th gas component.

$\rho_{oj}$  = density of the  $j$  th gas component.

Equation 2-3 is replaced (Buck and Post, 1980) by

$$\rho_v = \frac{f_v (V_{pp})}{X} \quad (2-4)$$

where

$$V_{pp} = \ln(V) - \ln(V_o) - f_{21} \left( \frac{PX}{T} \right) - f_c(X) \quad (2-5)$$

$V$  is the output voltage of the Lyman alpha log amplifier,  $V_o$  is the system gain,  $X$  is the path length across which the Lyman alpha radiation is attenuated by the environment, and

$$\begin{aligned} f_v = & 0.7 - 1.83V_{pp} - 0.091V_{pp}^2 - 0.102V_{pp}^3 \\ & - 0.297V_{pp}^4 - 0.00311V_{pp}^5 \end{aligned} \quad (2-6)$$

$f_v$  is the empirical calibration curve relationship between the output signal and reference hygrometer. The oxygen correction ( $f_{21}$ ) is determined by an empirical adjustment to the theoretical oxygen absorption expected at the Lyman-alpha line

$$f_{21} = -0.033 - 7.5 \times 10^{-6} \frac{P^2 X}{T} \quad (2-7)$$

In section 3.3 the calibration method employed in converting the Lyman alpha voltage output to meteorological units will be discussed.

#### 2.3.2 Temperature

Three temperature sensors were carried on the Queen Air: (1) Rosemount (ATB); (2) reverse flow (ATRF); and (3) fast response (ATKP). All three sensors used platinum resistance wire exposed to the environment, and a correction was made for dynamic heating.

NCAR suggested the use of the reverse flow sensor. The fast response sensor had a consistent but variable positive bias with respect to the other two temperature sensors, and was not recommended. Further tests showed that while the boom mounted Rosemount and reverse flow sensors yielded virtually the same sensible heat fluxes and had nearly identical spectral densities

(Figure 2.4), the time series plot of all three sensors (Figure 2.5) showed that the reverse flow had a slightly faster response. Having two temperature sensors which give nearly identical results adds confidence to the temperature data collected. Also, Figure 2.4 shows little spectral energy near the Nyquist frequency of the sensors which suggests that the response times of the sensors was rapid enough to capture nearly all of the temperature variation on our flights.

### 2.3.3 Radiation Measurements

(1) Short-wave radiation (0.285 to 2.8  $\mu\text{m}$ ) measurements, both downward and upward, were made with Eppley spectral pyranometers. The e-folding response time of these sensors is on the order of one second.

(2) Long-wave infrared radiation (3.5 to 50  $\mu\text{m}$ ) measurements, both downward and upward, were made with Eppley pyrgeometers. The e-folding response time of these sensors is on the order of two seconds.

### 2.3.4 Winds

All three components of the wind were measured by a combination of output from strain gauges mounted on the tip of

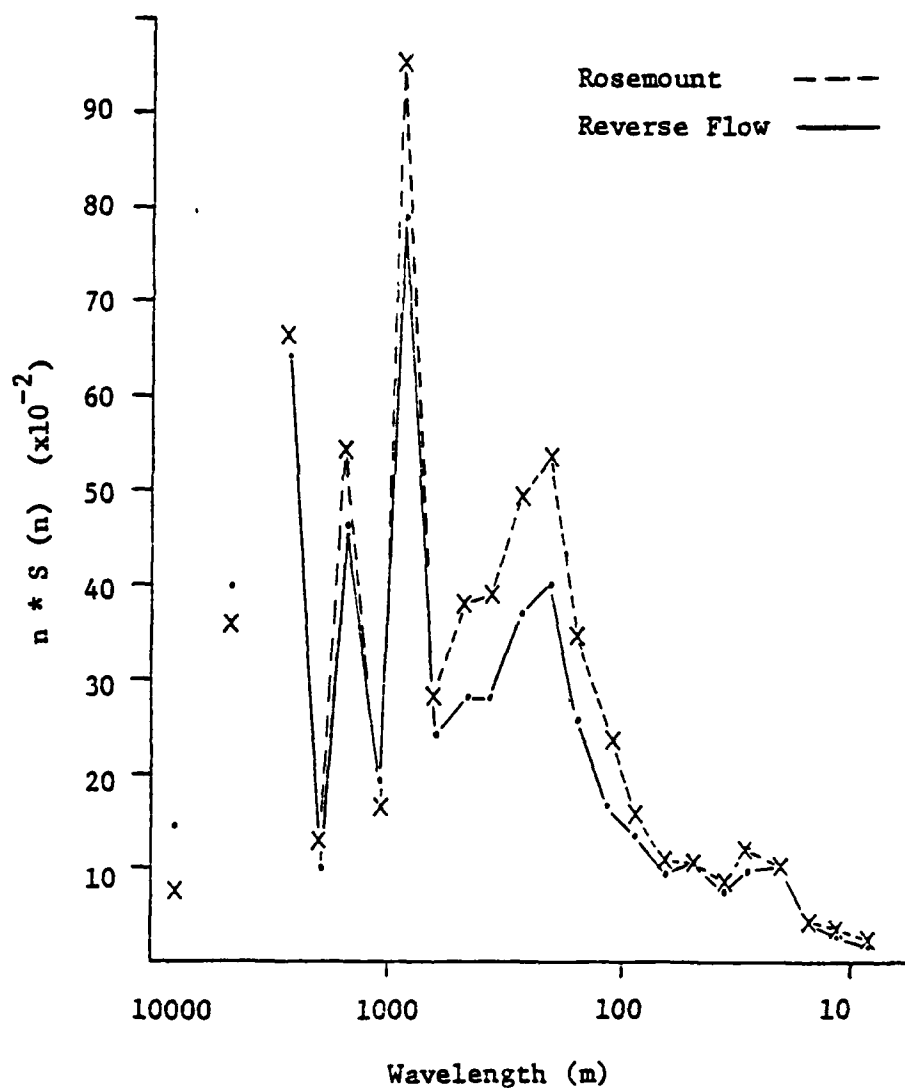


Figure 2.4 Typical plot of  $n * S(n)$  versus  $\log(n)$  (expressed as wavelength) plot of spectra of Rosemount and reverse flow temperature sensors from a near-surface flight leg (1653-1701 CDT 7 Jun 1983).  $S(n)$  is spectral density and  $n$  is the wavenumber. The area under the plot is proportional to the contribution of variance for that wavenumber interval. The total spectral energy and its distribution of the two sensors are nearly identical.

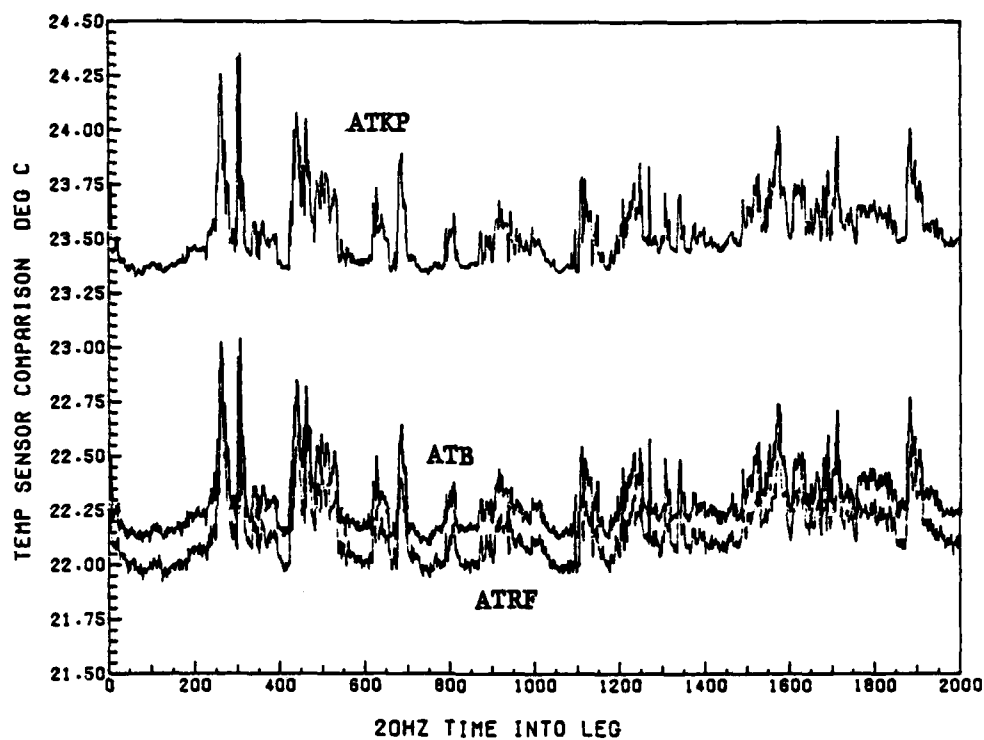


Figure 2.5 Sample time series comparison of the three temperature sensors carried on the Queen Air. The consistent positive bias of the fast response sensor (ATKP) and slightly faster response of reverse flow (ATRF) versus Rosemount (ATB) are evident. The data plotted is a portion of the near-surface flight leg flown at 1653-1701 CDT 7 Jun 1983.

the instrumented boom, from a sensitive pitot tube at the tip of the boom, and from information about the aircraft attitude angles (pitch, roll, and yaw) obtained from the Inertial Navigation System (INS). The strain gauges are attached to fixed vane sensors, which measure the component of force exerted perpendicular to the vane by the airstream (Lenschow et al., 1978).

The result is a three-dimensional wind vector with average horizontal velocity error of about 1 m/s and average vertical velocity error of about 10 cm/s (Kelley, 1973).

#### 2.4 University of Wisconsin Lidar System

The basic principles of the University of Wisconsin (UW) lidar (light detection and ranging) are documented by Sroga et al. (1980) and Kunkel et al. (1977). The ruby lidar fired monochromatic 694.3 nm laser beam shots with a pulse energy of about 0.7 J at a repetition frequency of 0.9 Hz, and scanned with 0.5 deg separating each shot. Individual shots are logarithmically amplified, digitized at 20 MHz and written to magnetic tape. The lidar's range resolution is 7.5 m and the normal usable data lies between 1.0 and 7.5 km downrange. Sequences of shots are combined to yield range height indicator and plan position indicator cross-sections through the boundary layer.

The amount of laser energy backscattered is dependent upon many factors which in turn help describe the structure of the atmosphere. These factors are expressed in the lidar equation

$$P(\theta, r, t_n) = E_n \frac{c}{2} \frac{A_R}{r^2} \beta_s(\theta, r, t_n) \frac{P'(\theta, r, t_n)}{4\pi} \exp \left[ -2 \int_0^r \beta_e(\theta, r', t_n) dr' \right] \quad (2-8)$$

where

$P(\theta, r, t_n)$	instantaneous received power from range $r$
$r$	radial distance along path of propagation
$\theta$	elevation angle of lidar profile
$t_n$	time of $n$ 'th lidar profile
$E_n$	energy transmitted with $n$ 'th laser pulse
$A_R$	area of receiver telescope
$c$	speed of light
$\beta_s(\theta, r, t_n)$	scattering cross section (per unit volume)
$\beta_e(\theta, r, t_n)$	extinction cross section (per unit volume)
$\beta_s(\theta, r, t_n)$	aerosol phase function for backscattering

In the daytime CBL, the aerosol content is usually greatest near the ground due to the proximity of natural and anthropogenic sources. This results in a greater reflectivity (A in Figure 2.6) than seen in the capping free atmosphere air



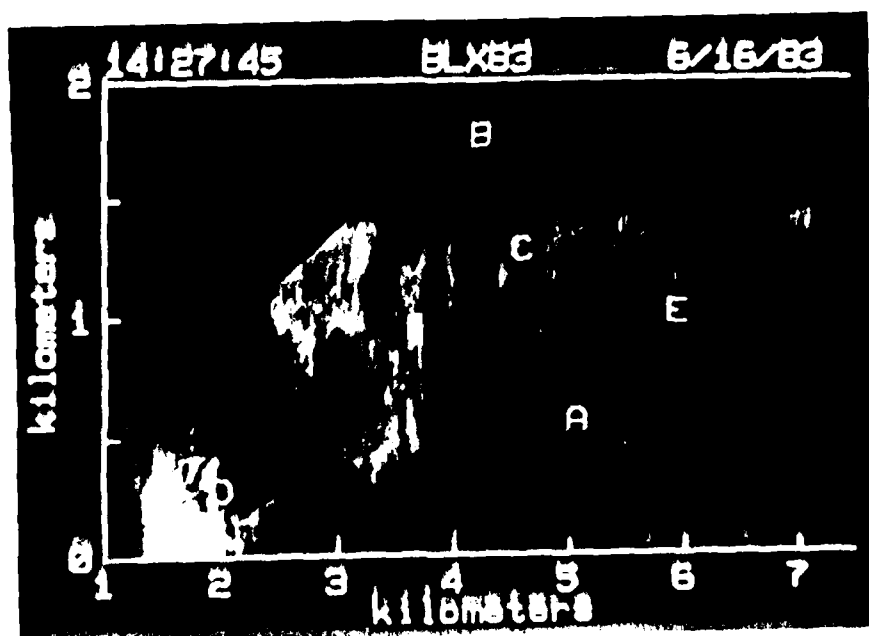


Figure 2.6 UW lidar range height indicator scan ending at 1427:45 CDT on 16 June 1983 showing how the reflectivity of laser energy is enhanced more in the convective boundary layer (A) than in the free atmosphere aloft (B). Aerosol swelling (C) and concentrated amounts of dust created by farming activity carried aloft in a thermal (left of D) can locally enhance the reflected energy. Near E, drier air from above is being entrained into the convective boundary layer which yields intermediate reflectivities.

aloft (B in Figure 2.6) which usually has a smaller aerosol density. The relative humidity of the air is important because at relative humidities greater than 65-75% the amount of backscattered energy increases due to aerosol swelling (C in Figure 2.6). As seen in Figure 2.6, the swelling takes place at the top of the tallest thermals which indicates that cloud formation may begin soon. Aerosol size and concentration combine to influence the amount of backscattered energy as seen by the bright return caused by dust created by farming activity being carried aloft in a thermal (D in Figure 2.6). The entrainment of drier free atmosphere air down into the CBL is taking place to the left of E in Figure 2.6.

In its configuration during BLX83, the UW lidar was operated from a fixed location pointing toward the northeast (Figure 2.3). Two lidar scan modes were used during this study: (1) The range height indicator (RHI) scans where shot elevation angles commonly varied between of 0.5 and 25 deg. (2) The wide angle plan position indicator (WPPI) scan where the shot angle in the vertical is held constant at a relatively small value, but the planar angle is varied between 22 or 40 deg on either side of the center line.

## 2.5 Argonne National Laboratory Instrumentation

The Atmospheric Physics Section of Argonne National

Laboratory operated a sodar, kytoon, and an instrumented tower approximately 3.2 km downrange of the center beam of the UW lidar. The fluxes of sensible and latent heat were the parameters measured on the instrumented tower that were most heavily used in this study.

Eddy correlation flux measurements of temperature, humidity and momentum were taken at a height of 5.17 m and averaged over a 25-minute period after a 200 sec running mean is removed from the data. The data is then passed through a 4-pole Butterworth filter with a 3 db point at 10 Hz. Instrumentation and methodology are described in detail by Hicks et al. (1980), Wesley et al. (1983) and Wesley (1983).

## 2.6 NCAR Portable Automated Mesonet (PAM II) Network

In order to obtain the spatial and temporal observation density required to calculate the vertical motion and advection of moisture and heat in the boundary layer, 13 Portable Automated Mesonet (PAM II) stations were positioned to collect near-surface observations of pressure, temperature, wet bulb temperature, wind direction and speed, peak wind speed, and rain accumulation. BLX83 was the first operational use of the PAM II system. The PAM II wind sensors were mounted at 10m and the temperature, pressure,

and moisture sensors were located at 2 m above ground level. The data was transmitted to NCAR at five-minute intervals by using the Geostationary Operational Environmental Satellite (GOES) as a data relay. Additional information concerning the PAM II system is contained in Brock and Saum (1983) and Pike et al. (1983). Table 2.2 contains the accuracy and reporting interval of the sensors.

## 2.7 Data Processing

### (1) Queen Air

Data from each "wings-level" flight leg was processed separately. The first step was to "despike" the data to remove any "bad" data points occurring more than a specified number of standard deviations from the mean. Presumably these "bad" data points could be caused by a sensor malfunction, an error in data recording, or an error in processing the data that led to a spurious value. Some researchers have used a selection criteria of three standard deviations ( $\sigma$ ), although a criterion of two  $\sigma$  was recently applied by Hanson (1984). These two and three  $\sigma$  criteria would discard 4.6% and 0.26% of the data respectively for an independent-normally distributed population. However, a time series of atmospheric data is not independent. Also, an examination of the frequency distributions of different

Table 2.2 PAM II Instrumentation

Parameter	Sensor	Accuracy	Recorded Resolution	Reporting Frequency
Wind	Propeller anemometer (U and V components)	1 m/s	0.1 m/s	1 / s
Wet- and dry- bulb temperature	NCAR psychrometer	0.25 C	0.05 C	20 / min
Pressure	NCAR barometer	1 mb	0.02 mb	25 / min

Criteria used as a gross check of archived PAM II data.  
Values outside of these bounds were flagged as bad/missing.

940 mb < Pressure > 990 mb

5 C < Temperature > 35 C

1 C < Wet Bulb Temperature < 31 C

0.0° < Wind Direction < 360.0°

0.0 m/s < Wind Velocity < 20 m/s

0.0 m/s < Peak Wind Velocity < 25 m/s

It was later learned that some of the PAM stations may have reported faulty values if wind speed were larger than 7.5 m/s (either U or V component). However, this study did not involve times when winds were that strong.

atmospheric variables at different altitudes revealed that few variables are normally distributed. At a given level there are various probability density function shapes among the measured variables and for a given variable, its frequency distribution varies with height.

An examination of the BLX83 aircraft data showed that there were few, if any "bad" data points. There were some points greater than three sigma from the mean, but they tended to be in consecutive strings with values near one another and not significantly greater than three sigma. This suggests that the "outliers" are the result of real atmospheric phenomena and not random noise or data recording errors. Approximately 1% of the temperature, wind velocity, and humidity values commonly exceed the three sigma level. By five sigma, this value drops by two or more orders of magnitude. Hence, in order to keep what are believed are real atmospheric phenomena, but to protect against the random sensor and/or data collection errors, a despike criteria of five sigma was used. Any value exceeding five standard deviations from the leg average (same criteria used by LeMone and Zipser, 1980) was replaced by the preceeding value.

A check of five flight legs showed that using five versus three sigma as a despike threshold resulted in the same sensible and latent heat fluxes and the same spectral density profile.

As is commonly done in boundary layer studies, the time

series of each variable was then detrended by a least squares best fit to the data. This then allows the assumption of a steady turbulent flow with time invariant average, required for the separation of a time series into mean and fluctuating parts (Desjardins and Lemon, 1974).

The computation of vertical fluxes of sensible heat, latent heat, and buoyancy in the boundary layer was then computed by the eddy correlation technique. Assuming a time invariant mean and a stationary time series a variable  $\xi$  can be split into mean,  $\bar{\xi}$ , and turbulent,  $\xi'$ , parts

$$\xi = \bar{\xi} + \xi' \quad (2-9)$$

enabling the vertical turbulent flux,  $F_{\xi}$ , of quantity,  $\xi$ , to be written as

$$F_{\xi} = \overline{\xi'w'} + \bar{\xi} \bar{w} \quad (2-10)$$

where  $\bar{w}$  is the mean vertical velocity for the flight leg, assumed to be zero, and  $w'$  is the turbulent departure of the vertical velocity from the mean.

With the usual assumption that the mean vertical motion for our flight legs (minimum flight leg length of about ten times the depth of the boundary layer) is zero, the total flux equals that

of the eddy component.

The sensible heat flux is computed by

$$S = \rho_{DA} C_p \overline{w'T'} \quad (2-11)$$

where  $\rho_{DA}$  is the density of dry air, and  $C_p$  is the specific heat at constant pressure.

The latent heat flux is computed by

$$LE = L_v \overline{w'\rho_v'} \quad (2-12)$$

where  $L_v$  is the latent heat of vaporization of water, and  $\rho_v$  is the absolute humidity ( $\text{g/m}^3$ ).

The buoyancy heat flux,  $B = \overline{w'\theta'_v}$ , is computed by

$$B = (1 + 0.61q) \overline{w'\theta'} + 0.61 \overline{\theta} \overline{q'w'} + 0.61 \overline{q'\theta'w'} \quad (2-13)$$

where  $q$  is the specific humidity ( $\text{g/kg}$ ).

In order to gain a greater understanding of the instrument characteristics and the structure of the boundary layer, plots of spectra were made. The time series records of individual variables and the product of some (i.e.  $\overline{q'w'}$ ,  $\overline{T'w'}$ ) were spectrum-analyzed by means of a Fast Fourier Transform and plotted on two different types of graphs: (1)  $n*S(n)$  versus  $\log(n)$ , where



the spectral energy is proportional to the area under the plot; and (2)  $\log(S(n))$  versus  $\log(n)$ , where power law relationships appear as straight lines.

The spectral density has a large variation among neighboring frequencies and smoothing techniques are commonly employed (Box and Jenkins, 1976). In order to plot the spectral plots on a regular line printer and to perform smoothing, the spectra were plotted in the frequency range of wave number one to the Nyquist Frequency. This range was usually divided into 40 frequency blocks. The resulting blocks of points were logarithmically averaged. The population of blocks ranged from one value per block at low frequencies and increased as higher frequencies were approached. The population of the highest frequency blocks often approached 1000. The averaged values were then plotted at the mid-point of each frequency band as in Bean et al. (1975). Figure 2.4, shown earlier, was calculated using this method.

Although mesoscale variations are of interest in their own right, a flight leg of length of 25 km such as typically flown during BLX83 is insufficiently long to accurately measure waves of these lengths. These insufficiently-resolved long waves can contaminate the data (Mahrt, personal communication).

In order to eliminate mesoscale variations and the influence of features with only a few cycles per flight leg, the time series were high pass filtered to eliminate wavenumbers three or smaller.

The minimum BLX83 flight leg length used for filtered flux calculations was 250 sec. With an average true airspeed of approximately 75 m/s, wavenumber three corresponds to a wavelength of 6.25 km. Thus, wavelengths greater than 6.25 km were eliminated. In marine boundary layer studies using an instrumented aircraft, Greenhut and Khalsa (1982) used a 4.2 km cutoff, Lenschow and Stephens (1980) used a 5 km cutoff, and Bean et al. (1975) used an 8.4 km cutoff.

An "ideal" high pass filtering was performed by calculating each time series' Fourier coefficients via a Fast Fourier Transform, setting equal to zero the coefficients of waves with lengths longer than 6.25 km, and then reconstructing the filtered time series by an inverse Fast Fourier Transform.

## (2) Portable Automated Mesonetwork (PAM II)

In order to compute advection of state and computed variables, via the PAM II data, the irregularly-spaced PAM II observations were interpolated to a regular grided domain by use of the Barnes analysis scheme (Barnes, 1964 and 1973). The Barnes technique was selected due to the reasons cited in Koch et al. (1981) -- computational simplicity, flexibility in setting the weighting factor, the well known low-pass filter response, only two passes through the data are required for convergence to

observed values and small scale "noise" filtering.

Horizontal waves with wavelength twice that of the grid spacing are the smallest that can be resolved. With this in mind, the grid interval size was selected such that the interval was no smaller than one half the average distance between each observation and its nearest observation neighbor (Koch et al., 1981). For the BLX83 region, this average distance was 0.45 degrees of latitude which resulted in a grid space interval of 0.25 degrees of latitude. In order to contain all observation sites within the grid, a 7x7 grid mesh was selected. Placement of this grid mesh over the observation sites made use of the fact that the grid point values are determined from the observations whose influence decrease exponentially by distance squared. The mesh location chosen maximized the sum of observation influence over the grid points.

In order to reduce the high frequency signal that an observation might generate due to measurement errors and the affects of individual thermals, the five-minute average data at each station was filtered temporally before being used by the Barnes analysis. Averaging over at least four thermals provides enough information to provide an estimate of the mean field at an observation site without averaging over a long period of time that would mask the small-scale signal. The limiting case of averaging period would be thermals with the longest period (deep CBL, weak

winds). Assuming that the horizontal and vertical dimensions of thermals are about the same (Kunkel et al., 1977), these limiting values are a CBL depth of 2 km and a mean wind speed of 5 m/s. This assumption says that the life cycle of an individual thermal would influence an observation site for 6.7 min. In order to average over at least four thermals would require averaging over at least 25 minutes or five observation reports. A binomial smoothing function (Panofsky and Brier, 1958) was chosen.

The estimated advection of quantities was the average advection over the interior 3x3 grid. The primary observation site was near the center of grid. The average advection  $A$  of variable  $q$  was found via

$$\bar{A}_q = \sum_{i=3}^5 \sum_{j=3}^5 \left[ \frac{q(i,j+1) - q(i,j-1)}{2\Delta n} u_{(i,j)} + \frac{q(i-1,j) - q(i+1,j)}{2\Delta n} v_{(i,j)} \right] \quad (2-14)$$

which avoided use of stations on the grid border.

## Chapter 3

### High Speed Moisture Measurement Calibration and Flux Calculation

#### 3.1 Overview

Moisture content has remained one of the most difficult atmospheric variables to measure. For studies of the entrainment zone with an instrumented aircraft, this problem is compounded by the need to obtain fast response moisture flux measurements. For this reason, a major portion of the research effort was spent calibrating and validating the mean humidity and moisture flux measurements. Of the three different types of moisture measuring devices carried on the Queen Air (chilled-mirror dewpointer, microwave refractometer, and Lyman-alpha hygrometer), close examination of the data and testing proved that the moisture values from the Lyman alpha could be the most accurate and reliable, given adequate calibration. The reasons and research supporting this conclusion are reviewed in this chapter.

The rapid-response Lyman alpha measurements provide a unique opportunity to study the vertical profile of moisture flux in the boundary layer and to allow conditional sampling of when the aircraft was in or out of surface layer air during entrainment

zone flights.

The major aspects of the Queen Air and the hygrometer systems were reviewed in Chapter 2. However, at the beginning of this research, there was not a clear choice about which sensor to use and a large amount of time was dedicated to the selection of an accurate and reliable fast response hygrometer. Simultaneous with this work, Friehe et al. (1985) and Buck (1985) have proposed alternate methods for Lyman alpha calibration. This chapter details the methods used in selecting, calibrating, and testing a fast response hygrometer.

### 3.2 Sensor Selection

Past research efforts have used "slow response" hygrometers similar to the chilled-mirror dewpointer (e.g., Hildebrand and Ackerman, 1984; Hanson, 1984; Coulman and Warner, 1977). Others used the faster response NOAA-supplied microwave refractometer, similar to the one mounted on the Queen Air (e.g. Greenhut et al., 1984; Greenhut and Khalsa, 1982; Bean et al., 1975) and Lyman alpha hygrometers (e.g. Lang et al., 1983; Schotanus et al., 1983; Milford et al., 1979).

For sensor selection, the desired qualities are:

- (1) Adequate measure of the humidity fluctuations over the

the frequencies of interest. Primarily, this required that the sensor respond fast enough to detect high frequency environmental changes (as seen by the moving sensor). The spectral density of such a sensor's measurements should show only a small amount of energy at the highest resolved frequencies.

(2) Reproduceability, namely consistent and reliable measurements when experiencing similar conditions.

(3) A time series plot which shows a rapid response of the sensor to environmental changes.

(4) Absolute accuracy of the measurements.

Even though the chilled-mirror dewpointer temperature can theoretically be changed 2C per second, Figure 3.1 shows that the dewpointer is clearly responding very slowly (lag of 4 to 6 sec) compared with the refractometer and Lyman alpha. Figure 3.2 shows virtually no energy at wavelengths shorter than 500 m. The refractometer and Lyman alpha show greater spectral energy at wavelengths much shorter than this. The drop off in dewpointer spectral energy at about 500 m is a reflection of the dewpointer's apparent response time of 6 sec on an aircraft traveling at 75 m/s. Because of this slow response, the dewpointer is used for mean humidity calculations only.

The microwave refractometer is reputed (Bean et al., 1975) to have a response time adequate to measure the humidity fluctuations

61

LA(solid), REF(short dash), DP  
FLT 7 LEG 2

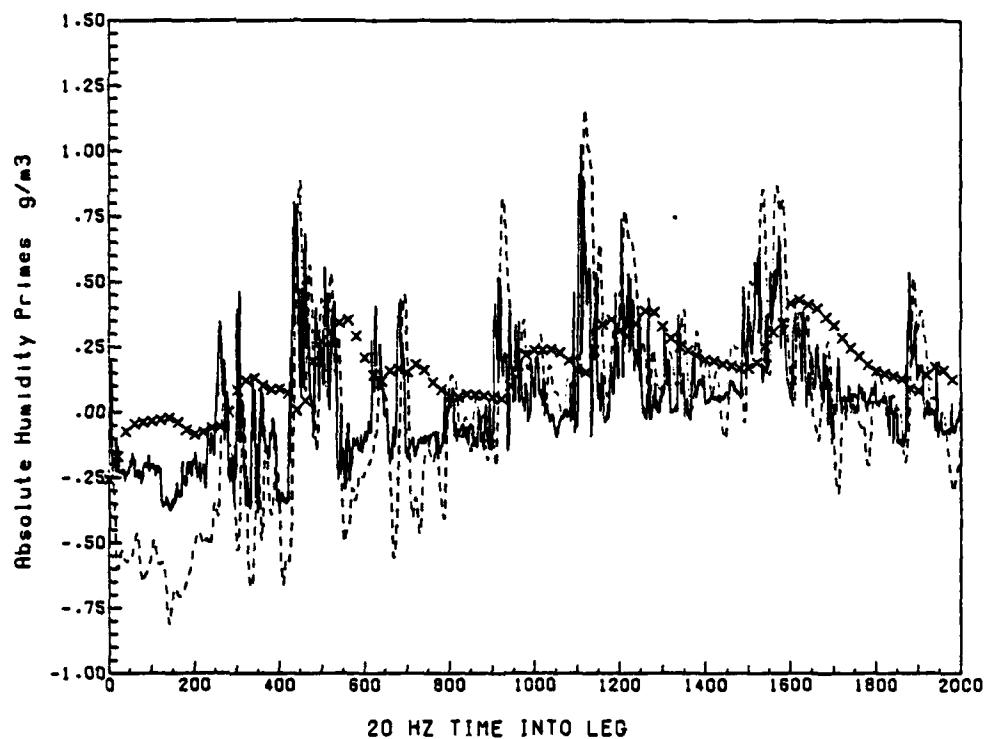


Figure 3.1 Sample time series of fluctuations of absolute humidity from the flight-leg average measured by the three hygrometers carried on the Queen Air. The sensors are: Lyman alpha (solid line); microwave refractometer (dashed line), and chilled-mirror dewpointer (X). The slow response time (on the order of 6 sec) of the dewpointer is readily apparent. The smoother trace of the refractometer shows the lack of response to high frequency fluctuations. The refractometer trace also appears to lag the Lyman alpha's by approximately 0.5 s. The Lyman alpha data has been processed by the calibration line presented in Appendix C. The data plotted is a portion of the near-surface flight leg flown at 1653-1701 CDT 7 Jun 1983.



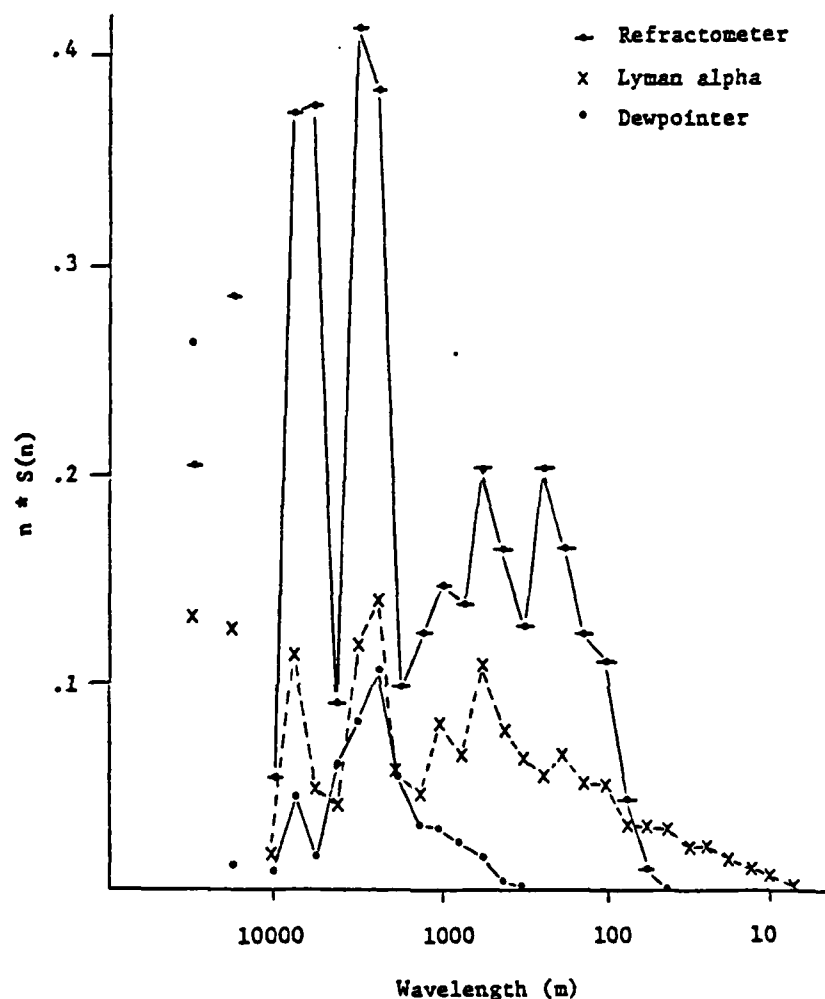


Figure 3.2 Typical plot of  $n \cdot S(n)$  versus  $\log(n)$  (expressed as wavelength) plot of spectra of chilled-mirror dewpointer ( $\cdot$ ), refractometer ( $\diamond$ ), and Lyman alpha ( $\times$ ) output.  $S(n)$  is spectral density and  $n$  is the wavenumber. The area under the plot is proportional to the contribution of variance for that wavenumber interval. The data is taken from a near-surface flight leg (1653-1701 CDT 7 Jun 1983) where more energy at smaller wavelengths is expected than at higher flight levels. Both the dewpointer and refractometer experience a drop off of spectral energy well below the Nyquist Frequency (a wavelength of 7.5 m for the 20 Hz sensor here).

encountered by an instrumented aircraft flying in the boundary layer. The refractometer has been used in many research studies measuring boundary layer ozone and energy fluxes (e.g. Greenhut et al., 1984; Greenhut, 1982; Bean et al., 1975). However, as seen in Figure 3.1, the refractometer's response during BLX83 does not appear as rapid as that of the Lyman alpha and tends to have approximately a 0.5 sec lag behind the Lyman alpha. The spectral density plot for the refractometer, Figure 3.2, shows a rapid drop off of energy well below its Nyquist frequency. This spectral signature suggests that air is not being flushed through the refractive cavity fast enough. Section 3.4 discusses the refractometer's failure to provide consistent and reliable measurements.

It must be pointed out that the microwave refractometer was mounted above the rear entrance door on top of the Queen Air fuselage and not on the instrument boom with the Lyman alpha hygrometer. This fuselage mount may have created the refractometer cavity flushing problem due to its being in the aircraft-skin boundary layer flow that occurs on top of the fuselage. Other refractometer users were able to mount the refractometer directly in the airstream on the nose boom and achieve satisfactory results. Also, the refractometer's primary operator and maintenance technician was not able to accompany the Queen Air to BLX83. This prevents a viable side-by-side

comparison of the Lyman alpha and microwave refractometer.

Even though the Lyman alpha's time trace (Figure 3.1) makes it appear to be the fastest response hygrometer and adequately measuring most of the variation in the moisture field (Figure 3.2), it remained to be seen whether the measurements obtained are reliable and accurate.

### 3.3. Lyman alpha Calibration

The Lyman alpha data supplied by NCAR to BLX83 researchers is in the form of voltages from the logarithmic amplifier output of the sensed Lyman alpha radiation. The task of converting these voltages to usable meteorological humidity units was not a well-documented or experienced one. The voltages to humidity transformation using equation 2-4 and 2-6 as in (Buck, 1976) resulted in unrealistically large latent heat flux (values nearly equal to the solar constant) for near-surface flight legs and leg-average specific humidities (nearly twice that of the chilled-mirror dewpointer values). Because of this inadequacy, seven calibration techniques were attempted in this study and are presented in Appendix B--all using the chilled-mirror dewpointer as the reference.

In equation 2-5,  $f_c$  is the collimation correction. From leg to leg during any one flight, system gain and collimations

correction should be constant. Hence, for a given flight only the oxygen correction needs to be made to the Lyman alpha output voltage

$$V_{pp} = \ln(V) - f_{21} \left( \frac{PX}{T} \right) \quad (3-1)$$

The leg-average dewpointer absolute humidity is plotted against the leg-average values of  $V_{pp}$  from equation 3-1. The main hypothesis in using the dewpointer as a reference is that for the level flight legs used (250-550 sec long) the average dewpointer value will equal the actual dewpoint of the atmosphere. During each flight, legs were flown from near the surface to above the top of the CBL thereby resulting in a wide range of mean humidities and mean voltages. The resultant calibration line for each flight is the best-fit regression line between the mean leg-average dewpointer humidities and leg-average voltages. These lines are assumed to apply to instantaneous values of  $q$ .

Figure 3.3 is an example of the data and resultant calibration line for Flight 2. Similar plots for the other flights are in Appendix C. Four attractive features of this approach are: (1) its directness and being based on the sensors used in our experiment; (2) the high degree of correlation between leg average  $V_{pp}$  (transformed Lyman alpha voltage) and dewpointer value of absolute humidity; (3) agreement with the findings of

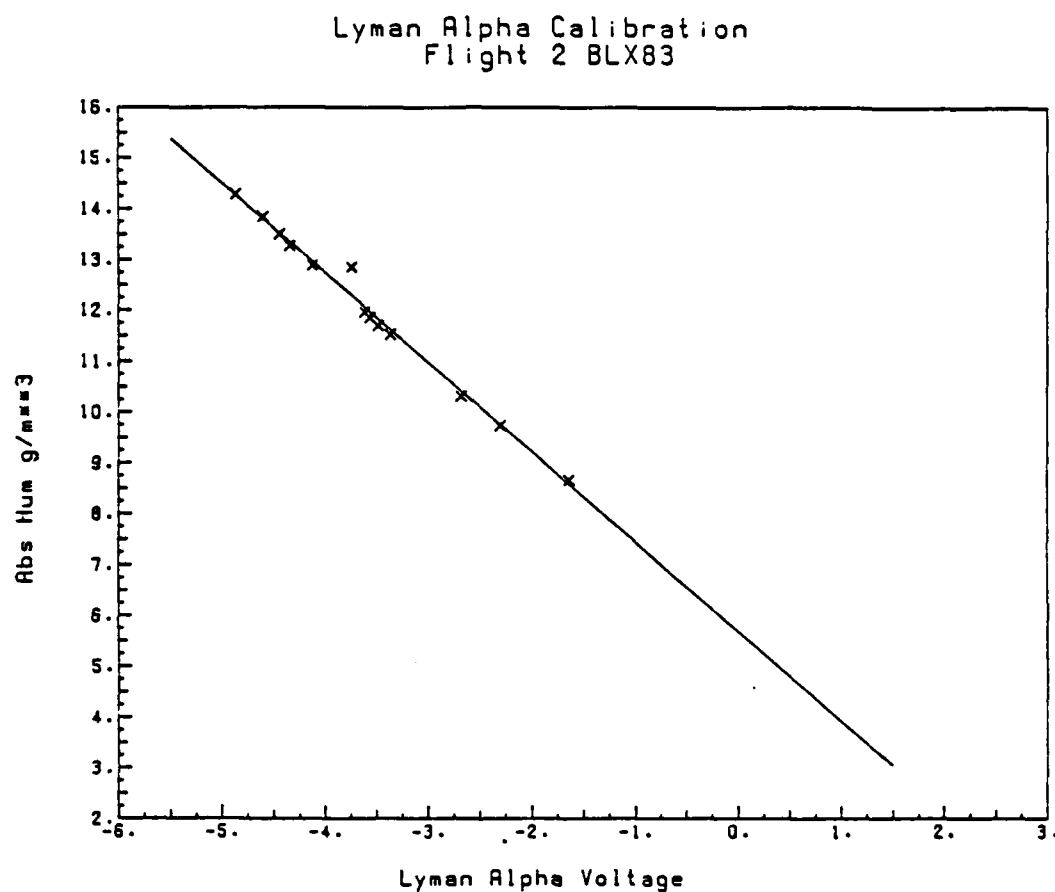


Figure 3.3 Plot of leg-average Lyman alpha voltages versus leg-average dewpointer ( $\text{g/m}^3$ ) for Flight 2, 27 May 83. The best-fit straight line is drawn.

Lang et al. (1983); and (4) the calibration lines allow direct use of the absolute values of humidity from the Lyman alpha output.

Each flight is calibrated separately because of flight-to-flight deterioration and change in the optical windows of the Lyman alpha sensors. Using the hypothesis that the slope ( $\beta_1$ ) and intercept ( $\beta_0$ ) of the regression through the calibration points is that of the population, a student-t test was used to determine whether the slope and intercept of the calibration curve for each entrainment zone flight were significantly different from the population (entrainment zone flights) value. Except for Flight 2, the slope and intercepts of all entrainment zone flights were significantly different (at the 5% confidence level) from the population values, which confirm that each flight should have its own calibration line.

As a check on the absolute values of humidity computed by these calibration lines, the computed pressure of lifting condensation level (PLCL) was compared against lidar-measured cloud bases. The coincident lidar and Queen Air data is described in greater detail in section 4.3. Using the lidar's height measurement expected error of plus or minus 25 m (Wilde, 1984), Table 3.1 shows the close agreement in cloud base estimation between the lidar and computed cloud base from the Lyman alpha, thereby providing strong evidence in support of the calibration method.

Table 3.1 Computed Versus Observed Cloud Base

Comparison of lidar-measured cloud base and Queen Air/Lyman alpha computed pressure of lifting condensation level/cloud base. Queen Air data from flight legs flown within 100 m of cloud base on 7 June 1983 with coincident lidar imagery. Individual thermals and cloud bases were compared.

Time (CDT)	Lidar Measured Cloud Base (m AGL)	Queen Air Computed Cloud Base (m AGL)
1316	1972	1959
1325	2020	2026
1450	2076	2055

Table 3.2 gives the calibration curve regression coefficients for each of the flights used. The correlation between leg-average voltage and leg-average humidity is very high, confirming that a linear regression (i.e., straight line) provides a good calibration.

#### 3.4 Computed Surface Flux Values and Comparisons with Other Measures of Flux

The latent heat fluxes calculated using raw dewpointer data yielded values that occasionally exceeded the solar constant (unrealistic) and yielded negative fluxes on near-surface legs where the flux was known to be positive. Also, consecutive flight legs at similar altitudes often gave latent fluxes of opposite sign (unrealistic). For these reasons the dewpointer data was not used to calculate fluxes.

The apparent inadequate response of the refractometer as discussed in section 3.2 eliminated the refractometer from contention as a reliable and consistent turbulent flux instrument or as a backup for the Lyman alpha. A further confirmation of the decision to not use the refractometer came from sequential near-surface legs where the latent heat fluxes would have presumably been relatively consistent, the refractometer-based fluxes often varied by a factor of two.



Table 3.2 Lyman alpha Calibration Coefficients

Let  $Y = \beta_0 + \beta_1 X$  where  $Y$  is the leg average of the top and bottom chilled-mirror hygrometers and  $X$  is the leg average  $V_{pp}$  from equation (3-4). This regression equation defines the humidity calibration lines for each flight, which were then used in the rest of this study.  $R$  is the correlation coefficient between  $X$  and  $Y$ , making  $R^2$  a measure of the variance explained by the regression.

Flight	Date Time	Residual Degrees of Freedom (DF)	$\beta_0$	$\beta_1$	R squared adjusted for D.F. (%)
2	27 May 1041-1239	11	5.6971	-1.76147	98.7
3	28 May 1438-1747	18	5.87042	-1.67627	99.9
6	7 Jun 1229-1517	18	5.24214	-1.58003	99.7
7	7 Jun 1642-1816	4	5.26613	-1.56662	100.0
8	8 Jun 1421-1725	8	5.00138	-1.64598	99.9
9	9 Jun 1456-1753	12	4.91912	-1.6838	99.9
11	12 Jun 1016-1228	13	4.95732	-1.96525	99.9
12	12 Jun 1428-1647	13	5.36073	-1.86673	99.8
13	14 Jun 1414-1702	13	6.19807	-1.56984	100.0
16	16 Jun 1111-1242	8	6.32494	-1.52133	99.9
17	17 Jun 1228-1425	11	4.1886	-2.09937	99.4

18	17 Jun 1552-1705	4	5.0861	-1.81224	99.7
20	18 Jun 1417-1614	13	4.4132	-2.0506	89.6

Near the surface, neglecting diabatic effects and advection--reasonable assumptions in the BLX83 cases, the surface energy balance can be written as

$$Q_{*} = SW \downarrow - SW \uparrow + LW \downarrow - LW \uparrow = LE + S + G \quad (3-2)$$

where  $Q_{*}$  is the net radiation,  $SW \downarrow$  is the downward short-wave radiation and  $SW \uparrow$  is the upward component,  $LW \downarrow$  is the downward longwave radiation and  $LW \uparrow$  is the upward component,  $S$  is the sensible heat flux positive upward into the air,  $LE$  is the latent heat flux positive upward into the air, and  $G$  is the flux of heat positive downward into the ground.

Bradley et al, (1981) were able to obtain a near balance of equation 3-2 with fixed, ground-based sensors. However, no work has been done to see whether the fluxes measured by an instrumented aircraft can balance surface energy budget. Such a balance would add confidence to the turbulent fluctuation data obtained by the Queen Air.

The Queen Air flew low enough during the near-surface legs to remain in what is commonly termed the surface layer or constant flux layer. As the name suggests, in this layer, approximately the lowest 10% of the convective boundary layer (CBL), fluxes are nearly constant with height. Hence, the fluxes measured by the Queen Air should closely approximate those at the surface. Table

3.3 contains a summary of the fluxes obtained during the these near-surface flight legs.

Other flight legs were flown at various altitudes relative to the average CBL top, allowing the vertical profiles of fluxes to be calculated. These sensible and latent heat fluxes measured by the Queen Air on four cloudless days are displayed in Figures 3.4 to 3.7, where the height has been normalized by  $Z_i$  (see Figures A.5, A.14, A.26 and A.33) and the fluxes are normalized by their surface values (see Table 3.3). The profiles of sensible heat and buoyancy flux have a nearly linear profile in the lower CBL due to the near constant value of potential temperature and a heating rate which is constant with height as is frequently reported in the literature (e.g. Wilczak and Businger, 1983; Nicholls and LeMone, 1980; Moores et al., 1979; and Wyngaard et al., 1978).

The predominance of negative buoyancy fluxes above approximately  $0.7 Z/Z_i$  is due to the downward turbulent transport of heat caused by entrainment of air from the capping stable layer aloft. This thermally indirect circulation consumes turbulent kinetic energy produced in the CBL (Wilczak and Businger, 1983).

The nearly constant value of latent heat flux below the entrainment zone implies the nearly non-changing value of moisture in the CBL. The fluxes are positive through most of the CBL due to evaporation from the surface and entrainment of dry air from the stable layer aloft. These two factors nearly balance each

Table 3.3 Queen Air Measurements of Surface Energy Budget Components

Summary of components of surface energy budget measured by the NCAR Queen Air during near-surface flight legs during BLX83. Consecutive flight legs are combined by a weighted average to give a more representative value of the fluxes when available. The latent and sensible heat fluxes were calculated by the eddy correlation technique from time series which had been linearly detrended. Except for the flight legs indicated by an asterisk, features with wavelengths greater than 6.25 km were removed from the series.

Date	Time (CDT)	Flt, Leg	Leg Length (s)	Net Radiation (w/m**2)	Sensible Heat Flux (w/m**2)	Latent Heat Flux (w/m**2)	Residual/ Ground Flux (w/m**2)
27May	1141	2,9	277	607.1	94.1	246.5	266.5
28May	1450	3,2	515	630.6	60.6	244.2	325.8
	1501	3,3	305	653.7	74.1	304.2	275.4
	1455	3,2&3		639.2	65.6	266.5	307.1
	1615	3,13	434	461.4	52.1	266.2	143.1
	1624	3,14	235*	491.9	61.3	257.7	172.9
	1741	3,23	280	250.4	9.1	206.7	34.6
7Jun	1229	6,2	410	695.4	93.7	243.1	358.6
	1240	6,3	202*	703.9	123.4	281.1	299.4
	1416	6,17	440	636.2	111.1	284.8	240.3
	1424	6,18	282	605.2	174.5	247.1	183.6
	1420	3,17&18		624.1	135.9	270.1	218.1
	1512	6,26	283	570.6	118.3	293.5	158.8
	1653	7,2	440	364.3	72.4	201.4	90.5
	1701	7,3	393	387.3	79.6	217.9	89.8
	1657	7,2&3		375.2	75.8	209.2	90.2
	1808	7,11	420	188.6	37.1	139.5	12.0
8Jun	1430	8,2	337	659.2	110.9	245.9	302.4
	1618	8,6	428	500.1	112.1	233.9	154.1
	1721	8,14	257	302.1	40.3	161.7	100.1
9Jun	1531	9,4	427	505.0	100.8	277.5	126.7
	1539	9,5	345	419.6	71.2	183.2	165.2
	1515	9,4&5		475.5	90.6	244.9	140.0
	1728	9,17	380	200.1	22.7	143.9	33.5
12Jun	1028	11,2	385	316.0	40.8	160.4	114.8
	1036	11,3	280	298.9	42.7	125.9	130.3
	1032	11,2&3		308.8	41.6	145.9	121.3
	1223	11,17	275	543.4	60.1	224.8	258.5
	1442	12,2	379	604.9	87.0	241.1	276.8
	1449	12,3	306	577.5	113.1	262.8	201.6

	1446	12,2&3		592.7	98.7	250.8	243.2
	1643	12,17	292	416.9	48.4	173.9	194.6
14Jun	1413	13,1	233*	702.4	77.9	393.8	230.7
	1527	13,11	275	609.4	80.9	300.6	227.9
	1639	13,21	250	452.4	55.2	326.3	70.9
	1645	13,22	313	441.1	62.1	301.4	77.6
	1642	13,21&22		446.1	59.0	312.5	74.6
16Jun	1111	16,1	263	586.2	59.5	234.1	292.6
	1224	16,12	275	579.2	81.6	241.1	256.5
17Jun	1242	17,2	320	610.1	101.5	312.9	195.7
	1248	17,3	266	400.2	51.2	223.9	125.1
	1245	17,2&3		514.8	78.7	272.5	163.6

Sensible(\*), Latent(Z), and Buoyancy(X) Fluxes  
1041-1239 CDT 27 May 83

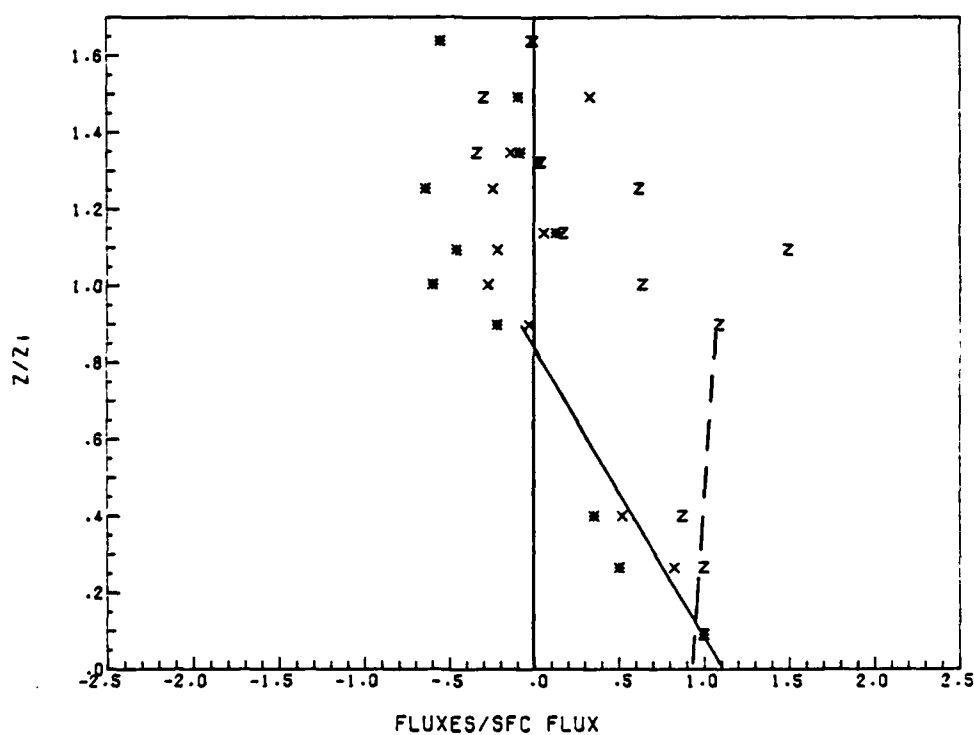


Figure 3.4 Plot of sensible heat flux (\*), latent heat flux (Z), and buoyancy flux (X) normalized by their surface values as a function of the flight leg's height above the ground normalized by  $Z_1$ . The flight legs were flown between 1041 CDT and 1239 CDT 27 May 1983. The best-fit regression line between the surface and  $0.9Z/Z_1$  is drawn for buoyancy flux (—) and latent heat flux (- -).

Sensible(\*), Latent(Z), and Buoyancy(X) Fluxes  
1450-1747 CDT 28 May 83

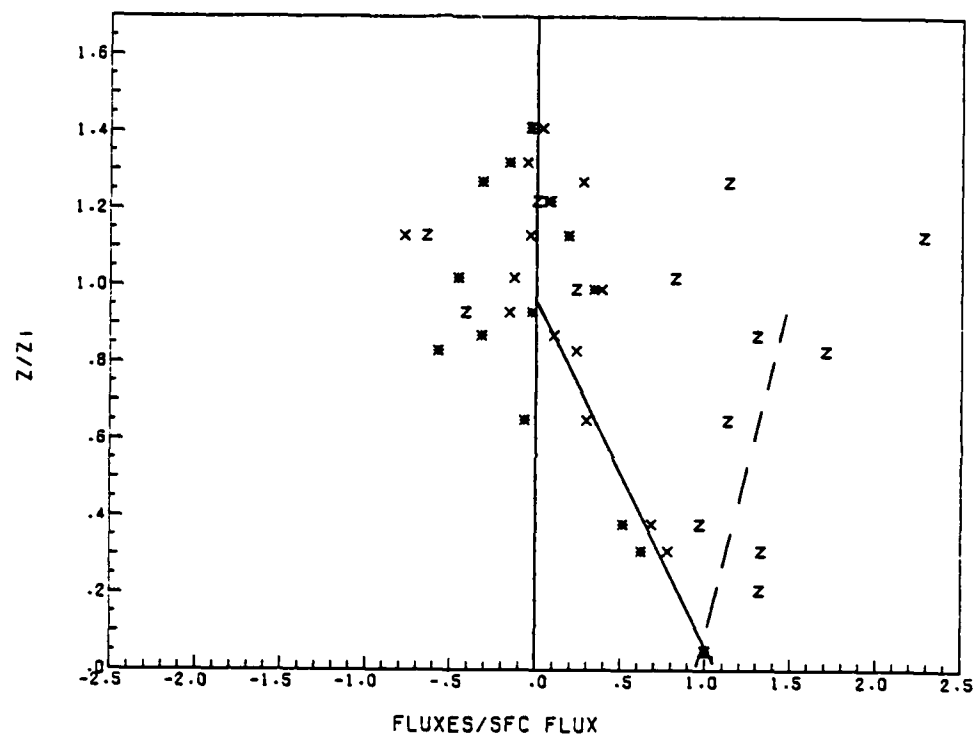


Figure 3.5 Same as Figure 3.4 except between 1450 CDT and 1747 CDT 28 May 1983.



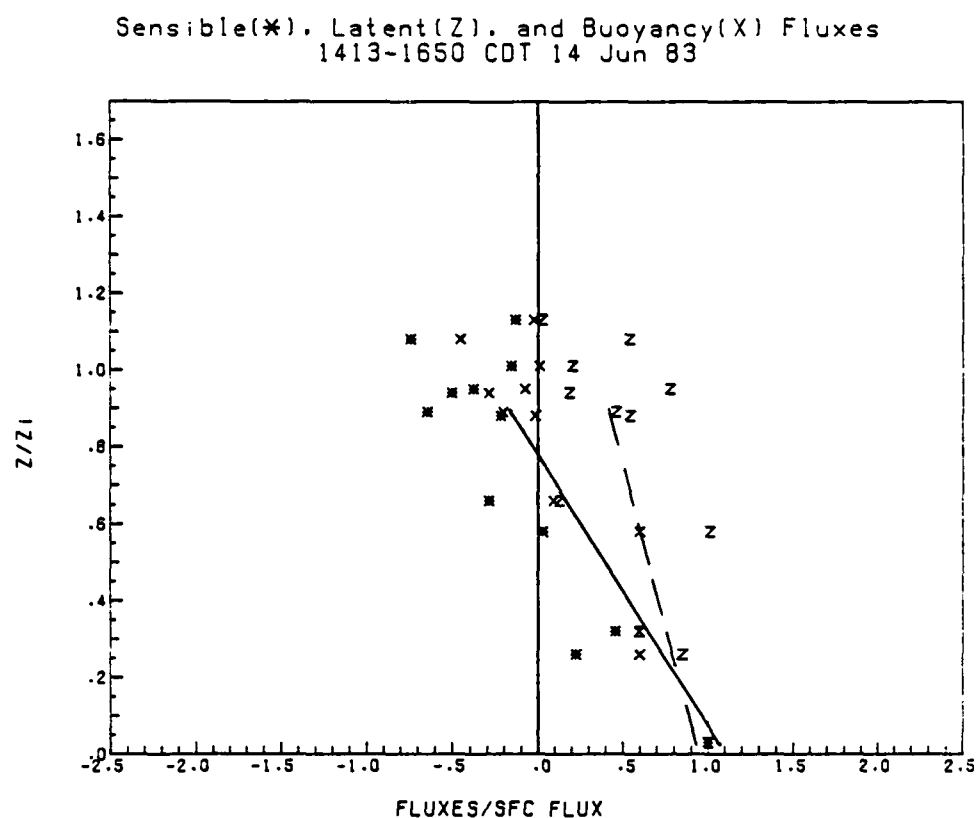


Figure 3.6 Same as Figure 3.4 except between 1413 CDT and 1650 CDT 14 Jun 1983.

Sensible(\*), Latent(Z), and Buoyancy(X) Fluxes  
1111-1229 CDT 16 Jun 83

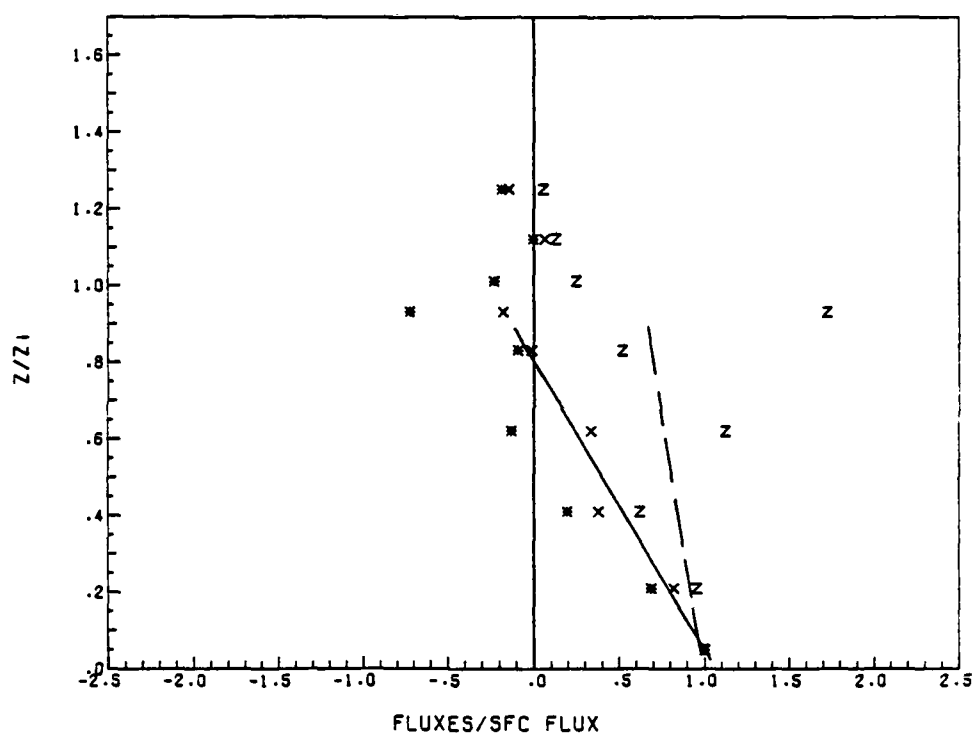


Figure 3.7 Same as Figure 3.4 except between 1111 CDT and 1229 CDT 16 Jun 1983.

other. However, due to the moistening of the air that is at the top of the CBL the slope of the flux becomes negative.

The flux profiles obtained during BLX83 (Figures 3.4 to 3.7) were similar to those seen by other investigators and are physically realistic. This helped add confidence in the validity of our data and data reduction techniques.

Some instrument redundancy was available at BLX83 which allows comparison of energy fluxes. The ANL instrumented tower and a PAM II station were colocated (Figure 2.3) and within 20 km of the near-surface leg paths flown by the Queen Air. Figure 3.8 shows the high level of agreement between coincident Queen Air and PAM II pyranometer data. The largest disagreements occurred when cumulus cloud cover was the greatest. Figure 3.9 shows the high level of agreement between coincident Queen Air and ANL net radiation ( $Q^*$ ) measurements. In both cases, slightly different averaging times and cloud coverages prevent perfect agreement. However, the agreement is great enough to reassure us that we are able to accurately measure radiation.

Due to the slightly different data reduction techniques and the fact that the ANL sensors were in a fixed location while the Queen Air moved over various locations, coincident ANL and Queen Air sensible and latent heat fluxes should not necessarily agree. Figures 3.10 and 3.11 show the comparison of the Queen Air and ANL fluxes. In the case of sensible heat flux, there does not appear

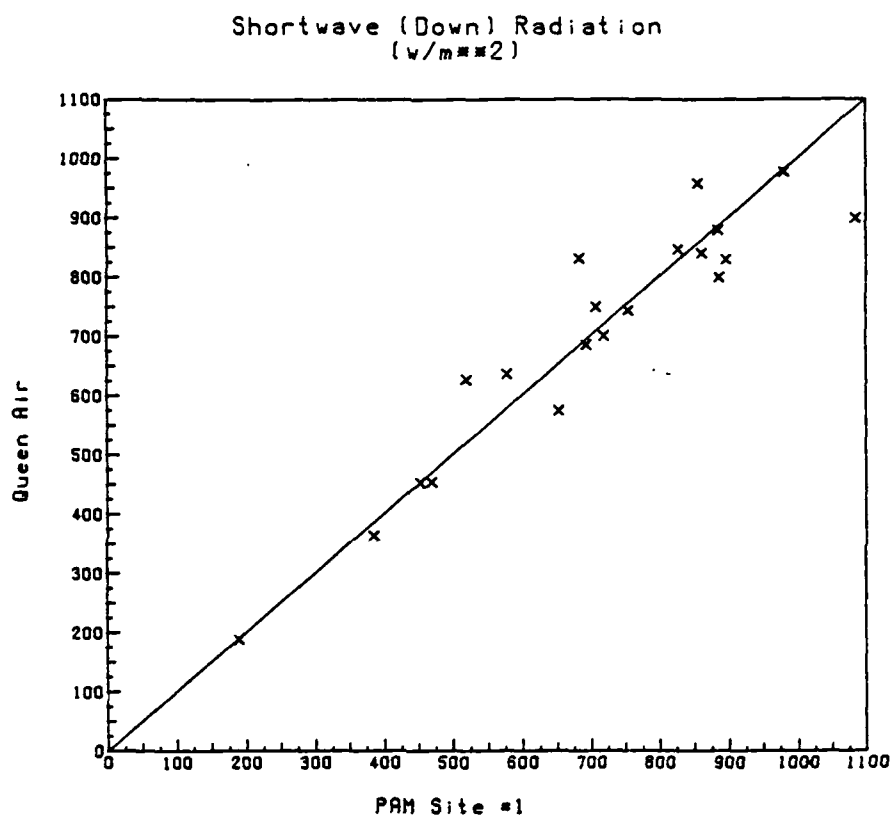


Figure 3.8 Plot of coincident Queen Air and PAM II measured downward-short wave radiation. Near perfect agreement (solid line) between the two sensors was obtained as the correlation between the two sensors was 0.96.

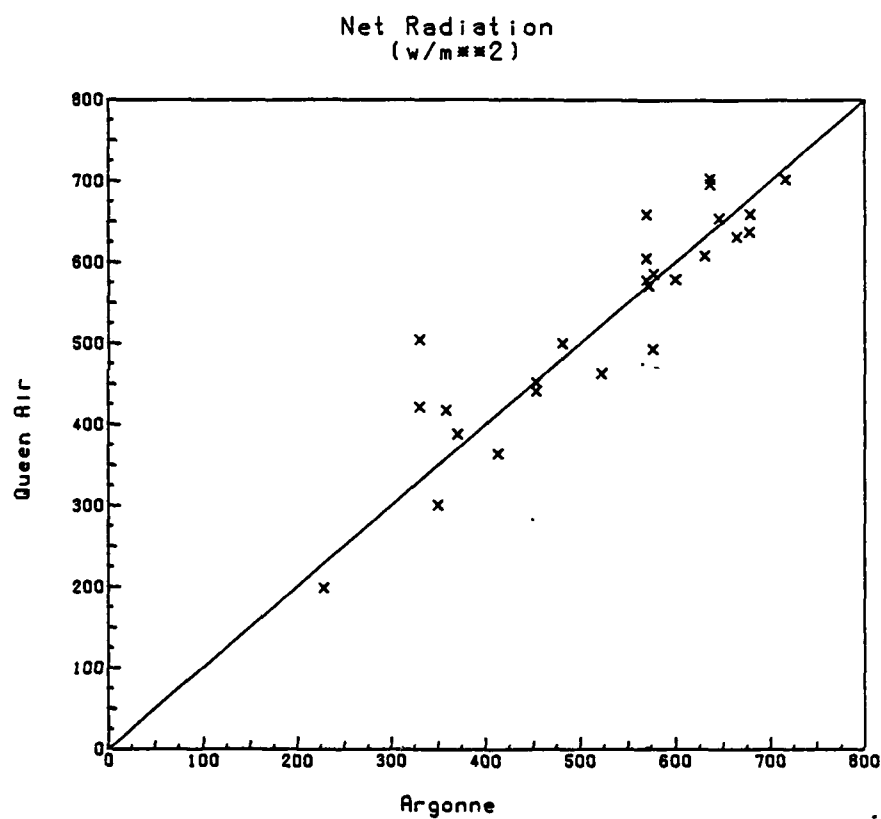


Figure 3.9 Plot of coincident Queen Air and Argonne National Laboratory measured net radiation. The solid line indicates perfect agreement between the two sensors. The correlation between the two sensors was 0.91.

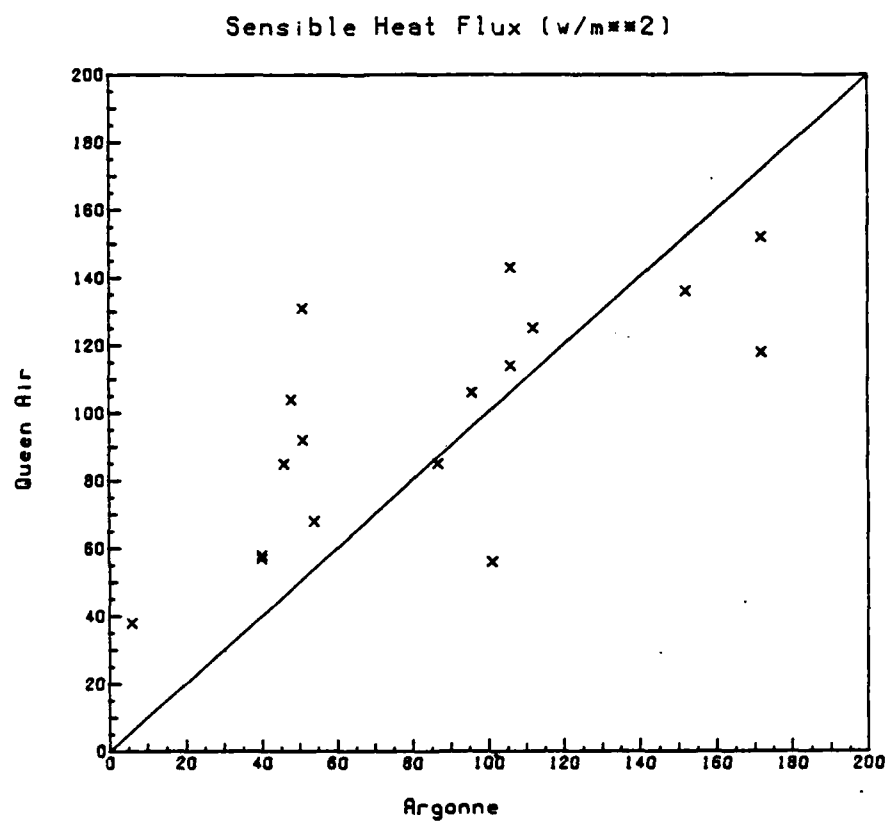


Figure 3.10 Plot of coincident Queen Air and Argonne National Laboratory sensible heat fluxes. Different data reduction techniques and locations of the sensors prevent perfect agreement (solid line) between the sensors.

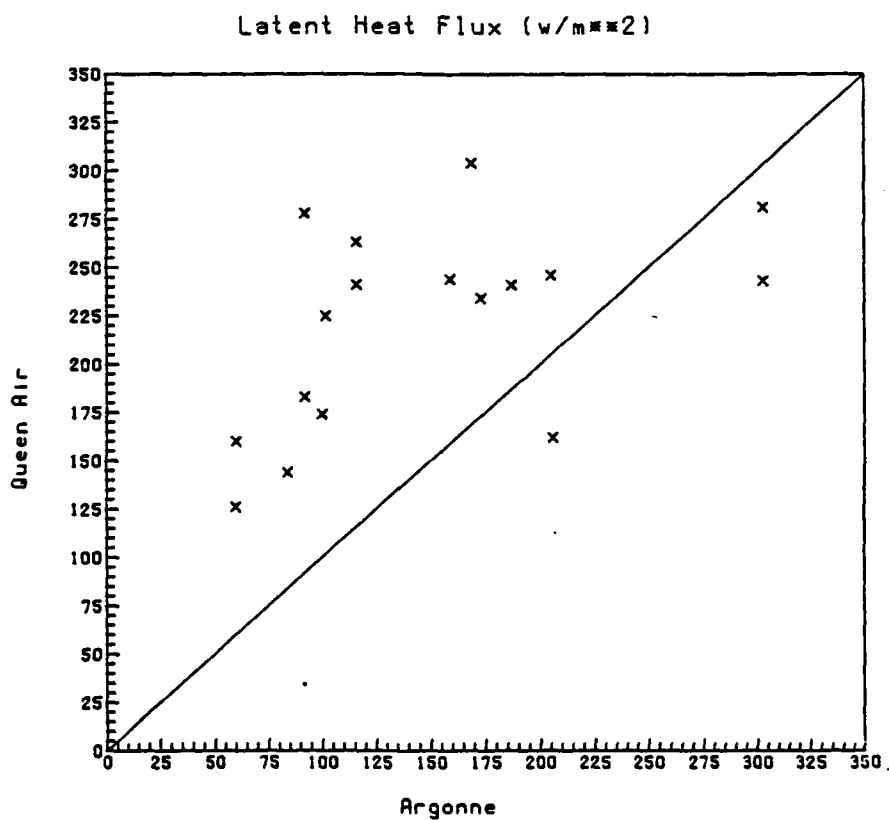


Figure 3.11 Same as Figure 3.10 except for latent heat flux. See text for details of the bias of the Queen Air to measure larger latent heat fluxes.

to be a strong bias between the two sensors. The bias of the Queen Air towards larger latent heat fluxes than ANL (Figure 3.11) is expected because the ANL sensors were in a field of short grass that would allow the rapid evaporation of soil moisture. Hence the soil around the ANL flux tower was drier during the afternoons when the majority of the Queen Air flights took place. Also, experience has shown ANL sensors to have a dry bias on the order of 10-20% (Wesley, personal communication, 1985) in latent heat flux measurements.

The apparent consistency in measured fluxes between the two sensor systems extends to the estimate of the unmeasured ground storage term ( $G$ ). This estimate comes from solving equation 3-2 for the residual/ground storage term  $G$ . These resultant ground storage values are plotted as a function of time in Figures 3.12 and 3.13. The Queen Air-derived fluxes have a sinusoidal pattern with a period and center time close to that of net radiation. The Queen Air implied values reach a maximum of nearly  $0.5 Q^*$  at solar noon.

Measurements and parameterizations of the magnitude of the ground storage term as reported in the literature are usually smaller than the values seen in Figures 3.12 and 3.13 for BLX83. Although measured at a fixed site in different locations with different vegetation cover and soil types, measurements of  $0.2 - 0.25 Q^*$  have been most recently reported (Kalanda et al., 1980;



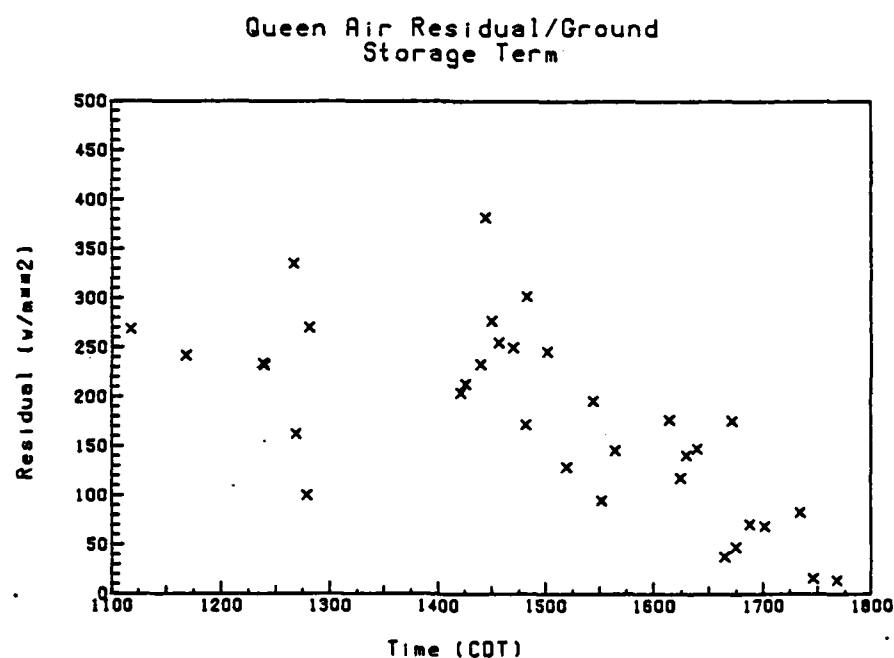


Figure 3.12 Plot of Queen Air surface energy budget residual/ground storage term as a function of time measured. The data was obtained from near-surface flight legs and waves with wavelengths longer than 6.25 km were filtered out. The data follows the diurnal pattern of solar insolation received at the surface.

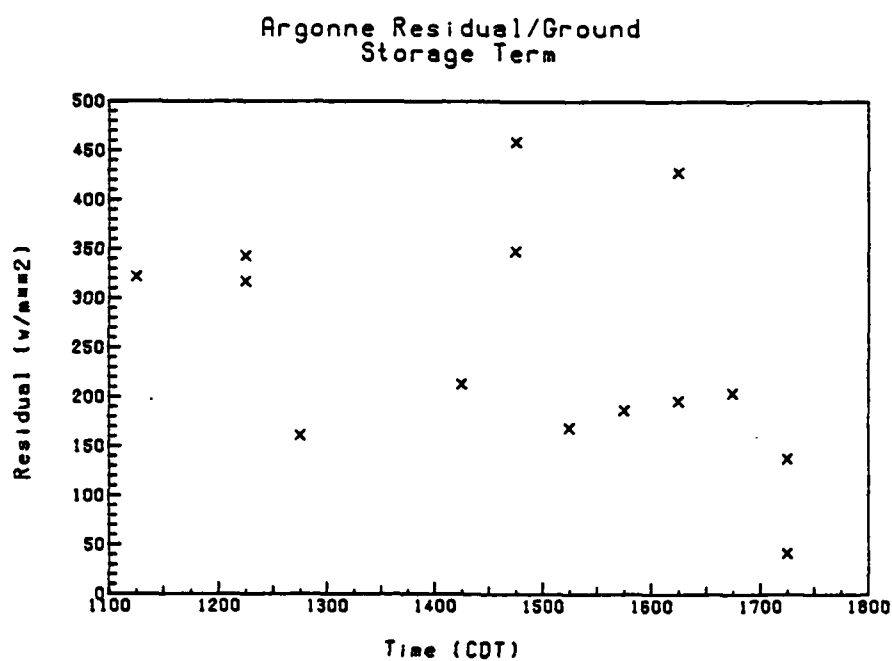


Figure 3.13 Same as Figure 3.12 except for Argonne National Laboratory at times of Queen Air flights.

Oke, 1979; and Landsberg and Maisel, 1972).

The spectra of Lyman alpha measurements shows an apparent lack of a spectral gap; namely, there is a greater amount of variation at long wavelengths (wavelengths near the length of the flight legs) for moisture than is observed for temperature. This result, similar to that of Milford et al. (1979), suggests that long wavelength contributions to fluxes may be more serious for latent than sensible heat fluxes. As a test, the sensible and latent heat fluxes were also computed without the high pass filter and with no detrending. This allows the contribution to the fluxes of waves between 6.25 km and the length of the flight leg to be retained. These revised fluxes did not differ significantly (less than 10% and some with a decrease of flux) from the filtered and detrended fluxes thereby leading us to believe that small-mesoscale flux contributions were not significant during the BLX83 days studied.

Appendix D has a summary of alternate methods of estimating the surface fluxes. These alternate methods were employed as a further check on the validity of the Lyman alpha based fluxes, but did not significantly impact the decision to accept the Lyman alpha values.

### 3.5 Conclusion

Although the residual/ground storage term resulting from the Queen Air fluxes appears large, the methodology for the Lyman alpha calibration is accepted.

The relative agreement between the Queen Air and ANL fluxes is significant in adding confidence to the Queen Air results. Also, the nearly instantaneous change of the Lyman alpha humidity value observed when entering a thermal (see section 4.3), spectra of the Lyman alpha output, and close agreement in computed and measured cloud base (Table 3.1) give confidence in not only the turbulent but also absolute value of the Lyman alpha data.

## Chapter 4

## Development of Conditional Sampling Criteria

In laboratory tank simulations of the atmosphere's boundary layer, an optical tracer can be used to identify whether fluid is from the capping stable layer or turbulent mixed layer below. Deardorff et al. (1980) used milk as an indicator of fluid originating in the mixed layer versus the clear water of the thermally stratified layer aloft. In the atmosphere, the process of deciding whether a sensor on an instrumented aircraft is in or out of mixed layer air or an active thermal is more difficult. Conditional sampling of the time series of various measured variables has been employed by other investigators to provide the discrimination.

Khalsa and Greenhut, 1985; Greenhut and Khalsa, 1982; Lenschow and Stephens, 1980; Coulman and Warner, 1980; and Manton, 1977 present recent examples of boundary layer research conditional sampling work. These approaches relied on correlating observations (i.e. increased specific humidity, temperature, or turbulent kinetic energy) to the desired event to be studied. From empirical determination, the experimenters then selected a threshold which, when crossed, would make a indicator function for

the event that they wished to sample (i.e. in- or out- of thermal conditions) assume one of its binary values (1=on, 0=off). For example, high humidity indicates a thermal, low humidity means the sensor is between thermals. However, this approach relies upon the assumptions made by the researcher(s) of what constitutes the "correct" conditions for the event. By utilizing coincident lidar and aircraft data such as taken in BLX83, one can avoid many of these problems.

A decade has passed since the first simultaneous in situ (instrumented aircraft) and remote sensor (high power pulse radar, FM-CW radar, and acoustic sounder) observations of the convective boundary layer were reported in the literature (Arnold et al., 1975; Readings et al., 1973). These observations helped to detail the temperature, moisture, and vertical velocity structure associated with the rising plumes and plunges of free atmosphere air from the top of the CBL.

Other investigators have related representative atmospheric structure to the output of remote sensors (Boers et al., 1984; Kaimal et al., 1982; Coulter, 1979; Russell and Uthe, 1978; Rowland, 1973; Uthe, 1972). Lidar-derived profiles of absolute humidity in the boundary layer have been compared with in situ measurements (Werner and Herrmann, 1981). Most recently, an airborne, downward-looking lidar and airborne atmospheric sensors were used to measure the structure of the planetary boundary layer

(Melfi et al, 1985).

However, researchers have never had coincident observations from a high frequency instrumented aircraft and the two-dimensional presentation of the CBL that a lidar range height indicator (RHI) scan offers.

In an effort to more objectively define conditional sampling thresholds and to study why large variations of heat fluxes sometimes exist in the entrainment zone, coincident lidar imagery and Queen Air time series plots were made and analyzed in this study. This chapter presents the coincident observations, an interpretation of the imagery and the resultant conditional sampling criteria used to identify surface layer air.

#### 4.1 Method of Analysis

The lidar RHI scans were combined with Queen Air sounding data and from selected horizontal flight legs that were along the lidar beam as the Queen Air flew toward the northeast in its racetrack pattern (Figure 2.3).

Figure 4.1 presents examples of three imagery displays such as will be superimposed in later figures. In (a) of Figure 4.1 is an example of lidar imagery displayed by itself. The azimuth angle of the lidar RHI scan is fixed. Both the horizontal and vertical length scales are displayed because this is a

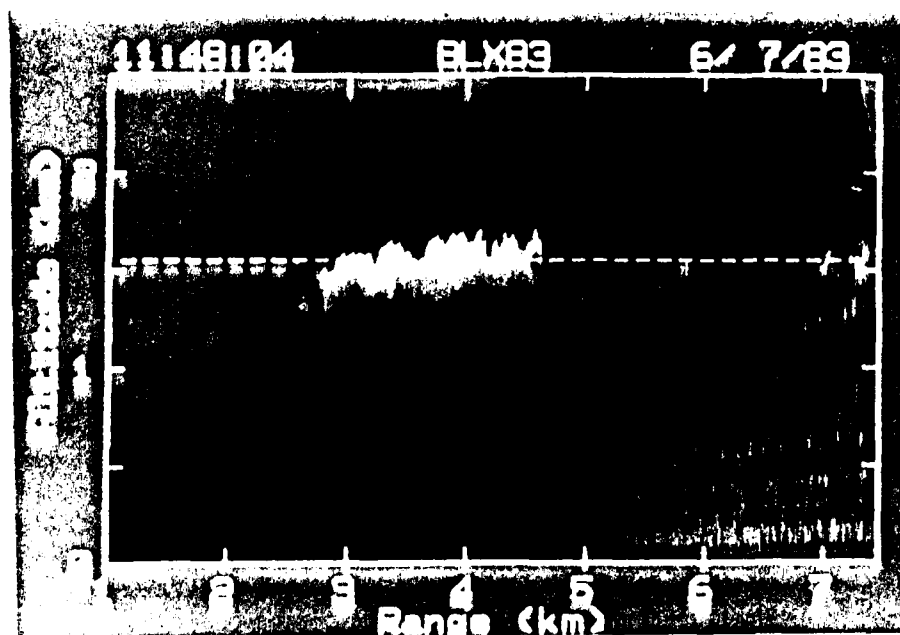


Figure 4.1a Display of lidar imagery and Queen Air sensor values in their most conventional presentation format and without superpositioning. This is an RHI scan of the atmosphere in the X-Z plane. The altitude of the Queen Air flight relative to the lidar image is indicated by the dashed line.



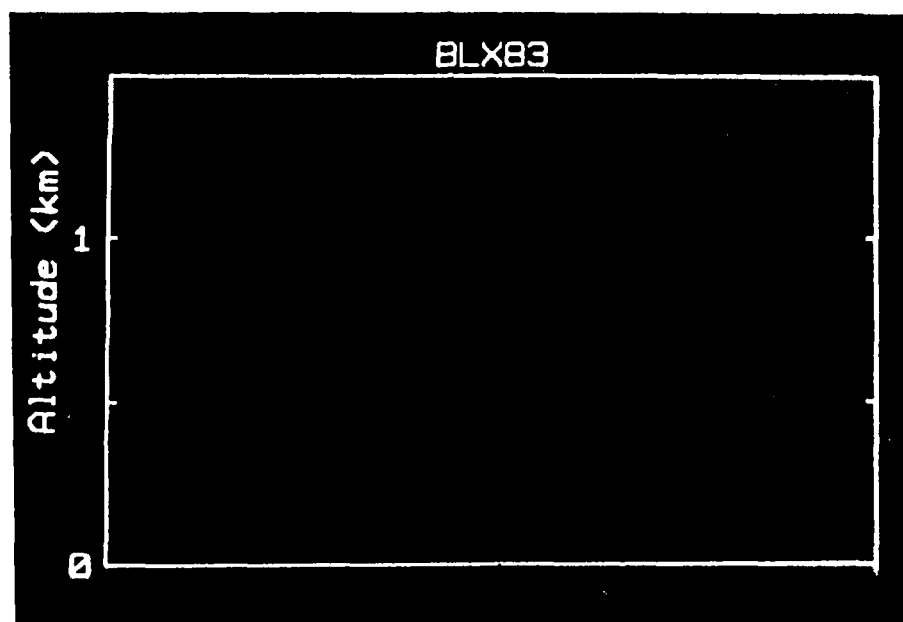


Figure 4.1b Display of lidar imagery and Queen Air sensor values in their most conventional presentation format and without superpositioning. In this type of figure, the data collected by the Queen Air during ascending or descending soundings is express as a function of altitude above the ground and the units of the variable measured.

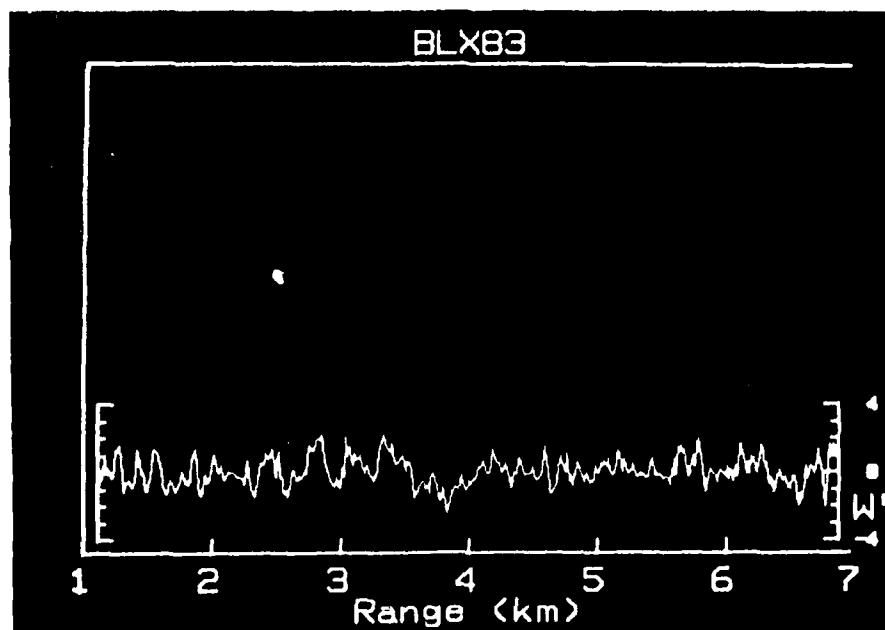


Figure 4.1c Display of lidar imagery and Queen Air sensor values in their most conventional presentation format and without superpositioning. This is a display of deviations from the leg-average of each of the three variables collected by the Queen Air during a horizontal flight leg as a function of distance downrange of the lidar and scaled by the units of the variable.

AD-A160 911

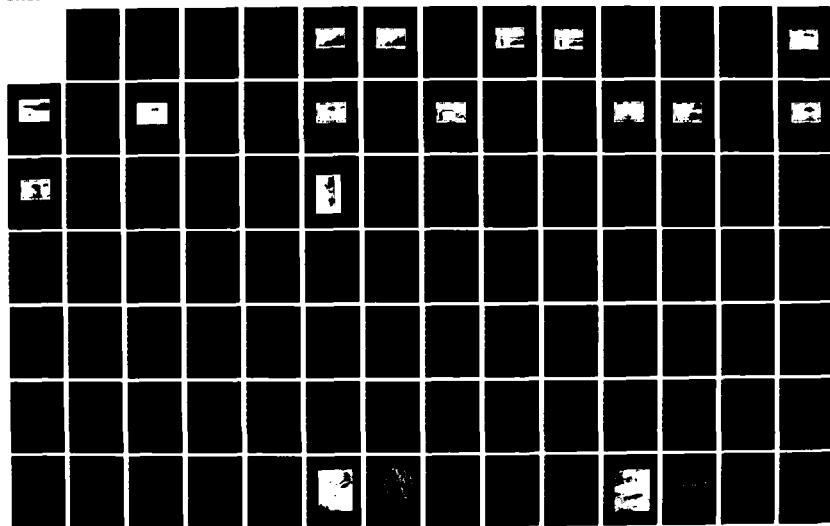
CASE STUDIES OF THE STRUCTURE OF THE ATMOSPHERIC  
BOUNDARY LAYER ENTRAINMENT ZONE(U) AIR FORCE INST OF  
TECH WRIGHT-PATTERSON AFB OH T D CRUM 1985  
AFIT/CI/NR-85-129D

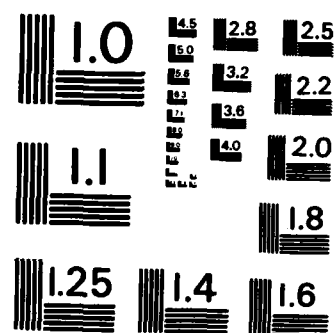
2/3

UNCLASSIFIED

F/G 4/2

NL





MICROCOPY RESOLUTION TEST CHART  
NATIONAL BUREAU OF STANDARDS-1963-A

two-dimensional remote sensing image of the atmosphere. The altitude of the horizontal Queen Air flight leg relative to the lidar image is indicated by the dashed horizontal line.

During ascent or descent soundings the aircraft typically traveled a horizontal distance of 50 km while changing 2 km in altitude. Part (b) of Figure 4.1 shows how the data collected by the Queen Air during its shallow-slope ascents or descents through the atmosphere is displayed. No horizontal length scale is used in this case because only the vertical profile of the variables is in interest here. For the representation of this Queen Air sounding data, 20 consecutive data points from the 20 Hz sensors were linearly averaged and their altitude determined via integration of the hypsometric equation. Due to the slow descent rate of the Queen Air, each averaged data point represents an average over approximately 3 m in the vertical. The lidar data selected (a in Figure 4.1) for presentation with the aircraft data (b in Figure 4.1) is an RHI scan near the time when the aircraft was penetrating the entrainment zone. The aircraft soundings were normally taken within 20 km of the lidar, but not directly in the lidar scan plane. This differs from the horizontal flight legs which were both simultaneous in time and coincident in space with the lidar scan.

The horizontal flight legs were selected after examining the Queen Air flight log (Stull, 1983) and lidar operations log for

flight legs with concurrent coplanar lidar RHI scans. Many of the flight legs under 0.6 Zi were not considered because the well-mixed nature of the CBL resulted in a nearly homogenous lidar image below this level. The mean CBL depth is defined here as in Deardorff et al. (1980), to be the height where lidar imagery depicts a 50%-50% mixture of mixed layer and free atmosphere air).

Part (c) of Figure 4.1 is a depiction of the Queen Air data of specific humidity, temperature, and vertical velocity collected during a horizontal flight leg. Here, the horizontal distance is important because it represents the horizontal location of the Queen Air (ground distance from the lidar) when the values displayed were obtained. Queen Air data (c in Figure 4.1) and lidar data were superimposed (a in Figure 4.1) on a video display and the time series plots of Queen Air data were aligned with the corresponding lidar RHI images based on the Queen Air INS position reports. In order to present the full range of the lidar data (1.0-7.5 km) and to have every pixel of lidar data coincide with each pixel of Queen Air data, the Queen Air data pixels shown here represent the linear average of three 20 Hz values. This results in a horizontal resolution of approximately 12 m. The lidar display enhancement used here depicts clouds and air parcels experiencing aerosol swelling as white, while moist aerosol-laden mixed layer air appears yellow-brown. The drier, less-polluted free-atmosphere air above the CBL often appears black in these

computer displays.

It became readily apparent from the superimposed imagery that the lidar and Queen Air data matched quite well. Also, for in-cloud and cloud base flight legs, 16mm photos taken every 8 sec from the Queen Air forward-looking automatic camera and 1 HZ upward-looking pyromometer and pygrometer data were used to confirm the match of lidar and Queen Air data.

#### 4.2 Sounding Case Studies

One advantage of using the UW lidar system to study the CBL is the ability to create rapid sequences of RHI scans. By sampling many thermals in space and time, this allows a representative measurement of the actual Ztop (the top of the tallest thermal) and of Zi (the mean depth of the CBL). Radiosonde or aircraft soundings sample only a column or sloping slice through the CBL; hence, on the average they will underestimate the maximum height (Ztop) to which thermals are rising to a greater extent than the lidar will.

##### 4.2.1 . 1428 CDT 14 Jun 83

In Figures 4.2 and 4.3 we see that the Queen Air began its ascent close enough to the ground to encounter the surface layer's

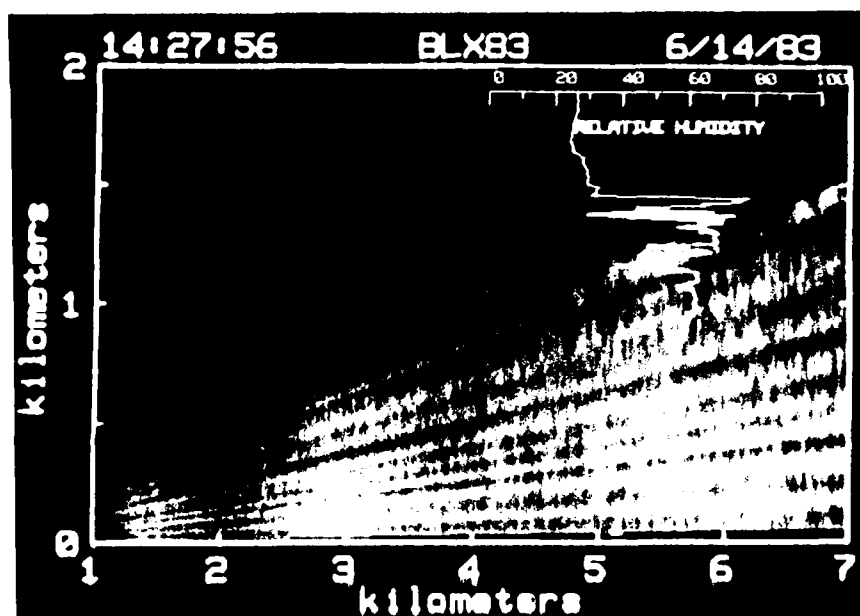


Figure 4.2. Lidar RHI scan ending at 1427:56 on 14 Jun 1983 with specific humidity and relative humidity traces for sounding flown by Queen Air from 1420-1432 CDT near the lidar site. The sounding and lidar data show approximately the same height for the top of the CBL.



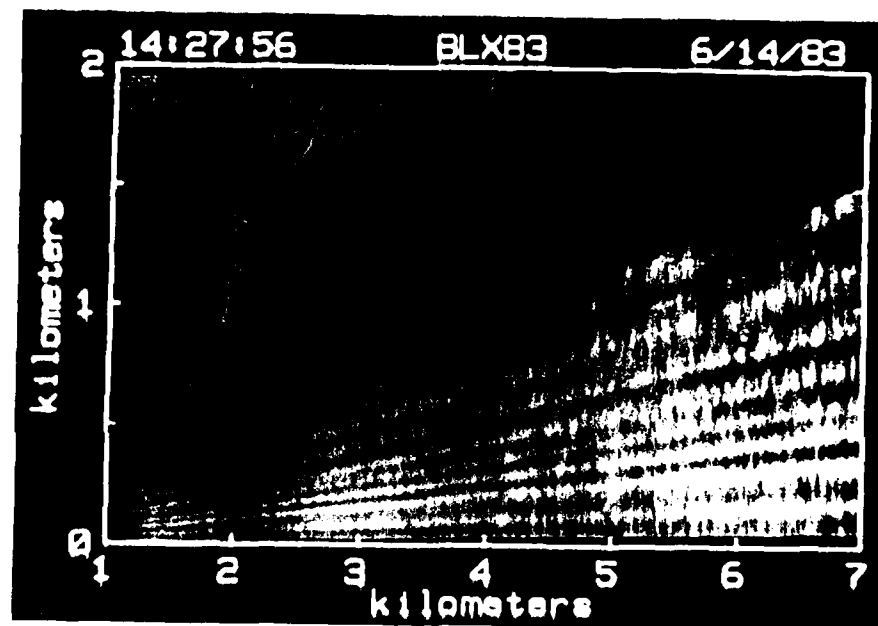


Figure 4.3. Same as Figure 4.2 except plots of potential temperature and height (above ground level) of the lifting condensation level.

superadiabatic lapse rate and the large lapse of moisture reported by Mahrt (1976). As the Queen Air continued its shallow ascent through the entrainment zone (998 - 1377 m) it encountered alternating columns of free atmosphere and surface layer (moist) air. Ztop is marked by the highest-altitude positive deviation from the relatively constant value of specific humidity and relative humidity in the stable layer aloft. This level also marks the base of the inversion aloft as seen by the rapid increase of potential temperature aloft. The Queen Air and lidar reported values of Ztop (1505 m) and Zi (1266 m) are in close agreement.

The CBL shown in these two figures is close to the classical idealized model of a moist polluted well-mixed layer capped by a cleaner, drier, warmer free atmosphere, with a well-defined inversion at the interface between these two layers.

#### 4.2.2 1106 CDT 27 May 83

Figures 4.4 and 4.5 show a more graphic case of where lidar imagery is essential to the understanding of the sounding. In this, as well as in many other soundings, the thermodynamic variables show the entrainment of dry air down to heights as low as  $0.3 Z_i$ , as Coulman (1978) reported. The drier air above the CBL (450 to 650 m) corresponds to the region of low backscattering of lidar energy (dark or black in the computer enhancement). In

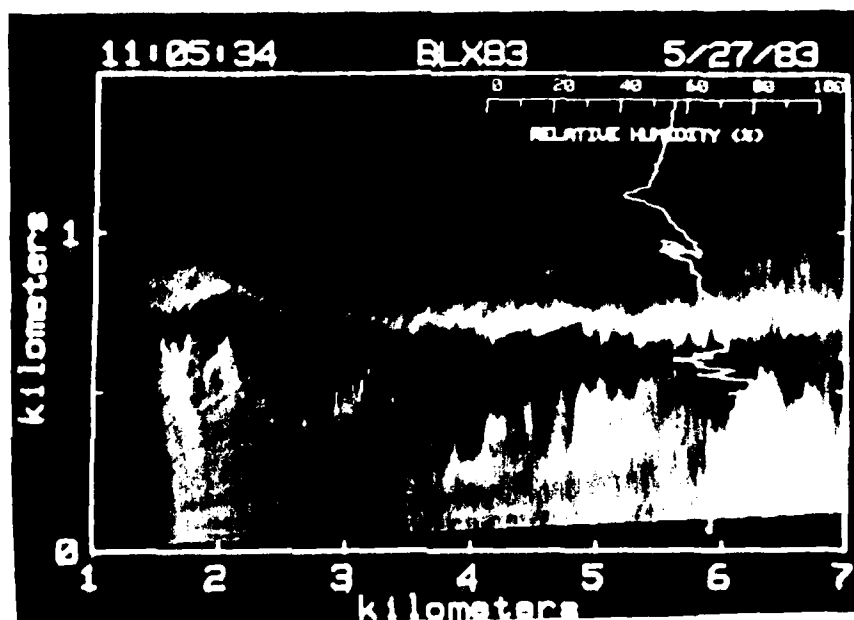


Figure 4.4. Lidar RHI scan ending at 1105:34 on 27 May 1983 with specific humidity and relative humidity traces for sounding flown by Queen Air from 1048-1057 CDT near the lidar site. The sounding and lidar data complement each other in this presentation of the layers aloft which have increased backscattering. The cluster of points near an elevation of 1 km was caused by the Queen Air leveling off for about two minutes and encountering various portions of the elevated layer.

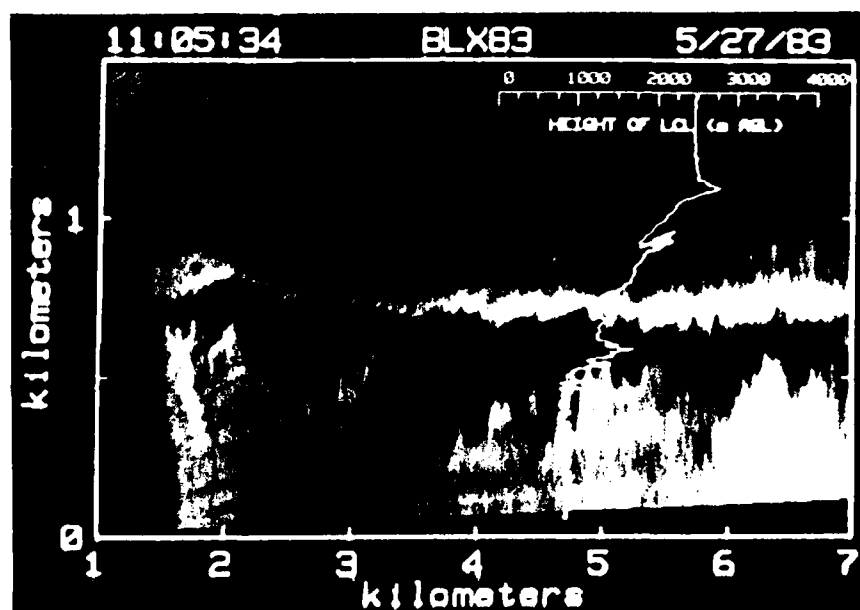


Figure 4.5. Same as Figure 4.4 except plots of potential temperature and height (above ground level) of the lifting condensation level.

the stable layer aloft is a dramatic example of how differential advection can bring in moister conditions and aerosols that reflect more lidar energy. Notice how the minimum of lidar reflectivity at 1200 m corresponds to the minimum in moisture, but the more moist layers above and below in the capping stable layer are more reflective. This case emphasizes how the lidar back scattering is closely related to the moisture content of the atmosphere and how structure in the thermodynamic variables above the CBL relate to real and observable (with a lidar) phenomena.

The lidar data collected before and after 1106 CDT revealed Kelvin-Helmholtz waves on the top of the first layer above the CBL (650 to 800 m). Periodically, as a tall-active thermal was advected along the lidar beam, the layer aloft above the thermal would rise. As the thermal entered the decay portion of its life cycle the layer aloft would return to its former level. This phenomena was similar to the observation of hummocks in the stable layer aloft being a reflection of the convective activity occurring below (Readings et al., 1973 and Browning et al., 1973). Later, as the CBL reached the base of the layer aloft of enhanced reflectivity, the two regions merged and lidar detection of the top of the thermals became difficult as there was little contrast in the reflectivity of the two layers.

These soundings revealed that near-surface values of specific humidity can be found near the top of the CBL, which suggests that

portions of the thermals experience little or no entrainment of drier air during their ascent. Also, point-by-point examination of the data suggests that the transition from near-surface specific humidity values to stable layer values can happen very rapidly in the horizontal.

#### 4.3 Horizontal Flight Leg Case Studies

For these legs, the actual horizontal flight altitude of the Queen Air in the lidar's field of view is indicated by the dashed horizontal line. Traces of  $q'$ ,  $T'$ ,  $w'$ ,  $u'w'$ ,  $v'w'$ , and turbulent kinetic energy (TKE) are deviations from the flight-leg average with the magnitude indicated on the scales (all units are MKS). The RHI scan shown in each case is the one closest to the time when the Queen Air would have been approximately 4 km downrange from the lidar (i.e. the scan when the Queen Air would be within the field of view of the lidar).

The Queen Air took approximately 80 sec to transit the entire range displayed on the RHI. Since the typical convective time scale for these cases was of the order of 800 sec and the strongest CBL mean wind speed was 8 m/s, we treat the RHI picture as a "frozen" representation of what the Queen Air encountered. However, in the strongest wind cases some nonalignment of the data was noted due to horizontal advection of the thermals with the

wind.

#### 4.3.1 1358 CDT 7 June 83

Figure 4.6 shows the traces of  $q'$ ,  $T'$ , and  $w'$  as the aircraft flew at an altitude of 2.066 km through a fair weather cumulus cloud at the top of a CBL thermal. A photo from the forward-looking automatic camera on the Queen Air, Figure 4.7, indicates that the aircraft penetrated the northern (left) edge of the cloud seen at 4.3 - 5.3 km downrange of the lidar. The lidar beam was slightly to the right of the aircraft track. Thus, the fact that the lidar and aircraft crossed through slightly different parts of the cloud explains why the Queen Air depicts cloud for the shorter interval of 4.3 - 4.8 km. The specific humidity and temperature profiles exhibit a nearly top hat shape with vertical velocity showing a turbulent motion with a length scale of about 200 m. At 4.8 km, a dry, warm subsiding area at cloud edge is encountered by the Queen Air before it moved into parts of the cloud (5.0 - 5.2 km) that have experienced entrainment of drier air. The rapid drop off of humidity and rise in temperature as the aircraft exited the cloud suggests that the sensors were not contaminated by cloud droplets. The cloud signature seen in the moisture and temperature traces at 4.3 - 5.3 km corresponds to a suppressed, negatively buoyant, forced cumulus

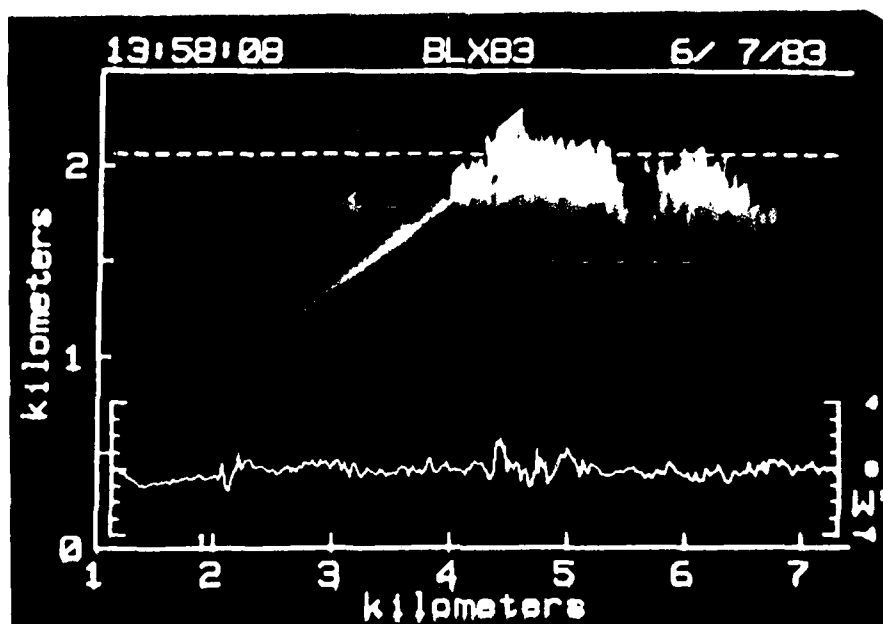


Figure 4.6. Lidar RHI scan ending at 1358:08 CDT on 7 June 1983 and concurrent Queen Air time series plots of deviations from the leg average of specific humidity (g/kg), temperature (K), and vertical velocity (m/s). The flight level of Queen Air during this mid-cloud leg and all horizontal flight leg cases that follow is indicated by the dashed line.



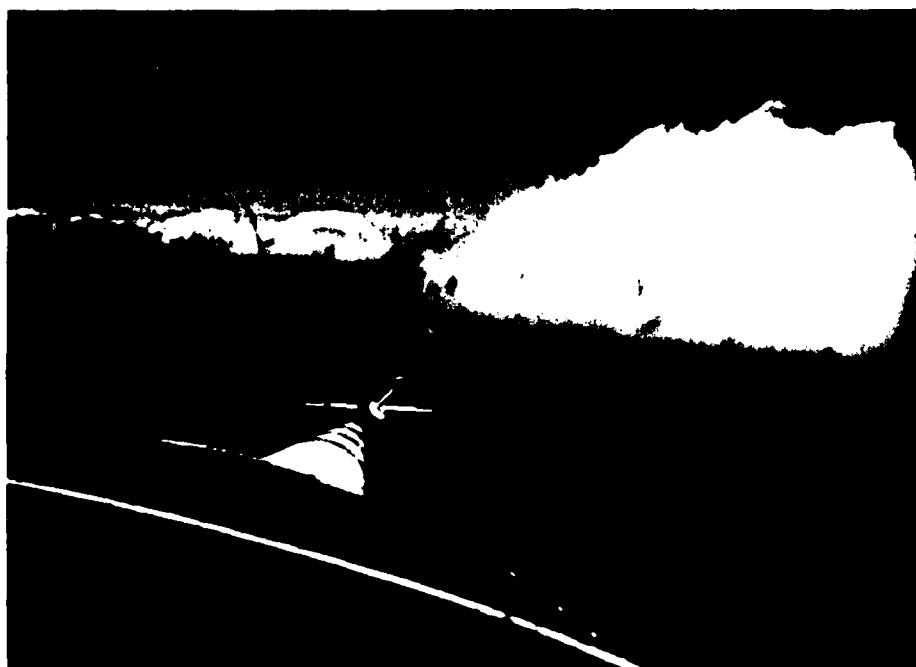


Figure 4.7. Photo taken at 1358:36 on 7 June 1983 during BLX83 by forward-looking camera in NCAR Queen Air aircraft. The cloud in the foreground is at a range of 1.26 km from the Queen air and at 4.3 km downrange from the lidar.

(Stull, 1985b).

#### 4.3.2 1325 CDT 7 June 83

The aircraft flew approximately 100 m below cloud base on the flight leg shown in Figure 4.8. Radiometric data and photos confirm that the thermal between 3.7 - 6.0 km (labeled as A on the figure) had just reached its lifting condensation level and was beginning to form a cloud. The thermal beginning at 7.2 km (B) does have a larger cumulus mediocris on top. Using the observation that thermals tend to have an aspect ratio of near one (Kunkel et al, 1977; Rowland and Arnold, 1975) the aircraft must have penetrated fairly close to the center of the thermal (A). The following observations are made as a result of this imagery.

(1) Moisture tends to maintain a "top hat" appearance in the thermal, while the "top hat" is not as evident in the temperature trace. See Figure 4.9 for a blowup view of the same specific humidity and temperature data superimposed on the lidar image in Figure 4.8. A similar observation of nearly constant humidity was made by Arnold et al. (1975). However, time series plots of data taken during near-surface flight legs show that this is not true there. In fact, we observed plumes in the surface layer which hadn't yet coalesced into thermals which had a greater variability

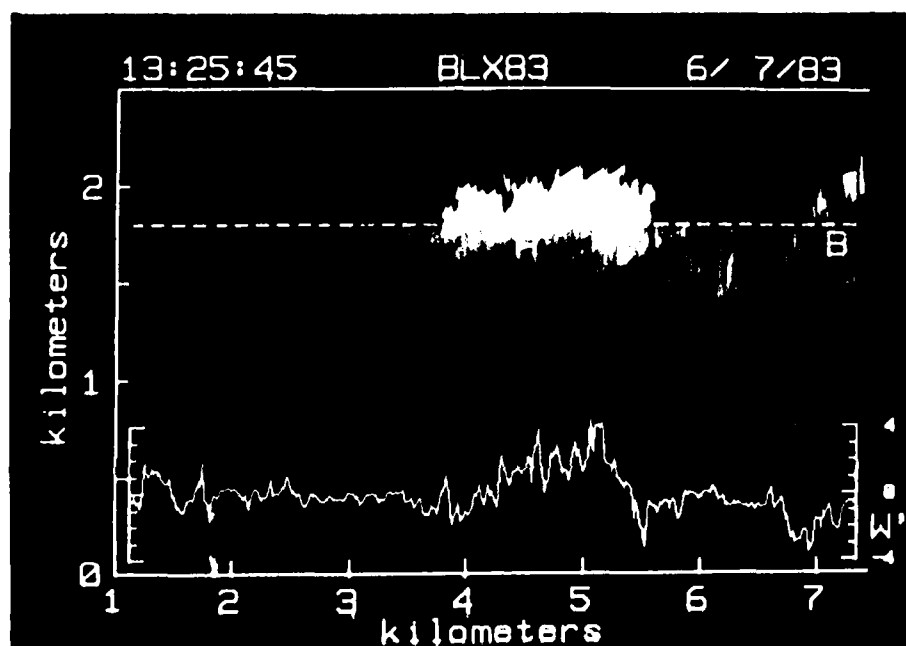


Figure 4.8. Same as Figure 4.6 except for scan ending at 1325:45 CDT on 7 June 1983. The lidar indicates thermals at A and B.

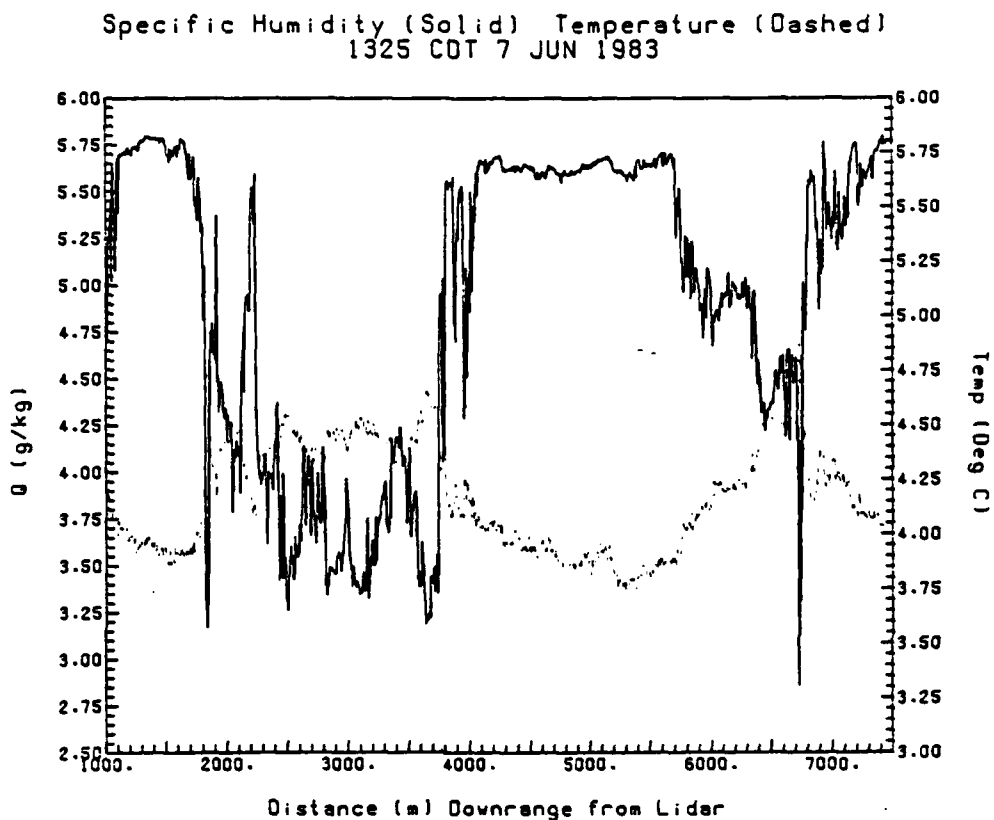


Figure 4.9. Plot of 20 HZ specific humidity (g/kg) and ambient temperature (C) showing the relative constancy of humidity in the thermal while temperature changes more within a thermal. This data is the same as that displayed in Figure 4.8.

of specific humidity over an interval of 200 m than thermals aloft over an interval of 1 km.

(2) The thermal between 3.7-6.0 km (A) has a specific humidity that is 0.15 g/kg less than that of the thermal beginning at 7.2 km (B). Hence, all thermals forming over a region of randomly distributed farm fields of different albedos and vegetation cover are not created equal. The implication is that some cloud-free thermals can be observed above the cloud-base level of other thermals.

(3) Moisture, better than temperature, marks the edges of thermals, as noted by Arnold et al. (1975).

(4) The regions of reduced (but nonzero) lidar backscattering (such as at the aircraft altitude at 5 km downrange from the lidar) have moisture values that lie between the surface layer and free atmosphere values. Hence, these less reflective regions consist of surface layer air that possibly has experienced entrainment of drier free atmosphere air.

#### 4.3.3 1450 CDT 7 June 83

Lidar and Queen Air photos confirm that the thermal in Figure 4.10 ending at 4.5 km (at A) has a cumulus mediocris on top. However, the thermal between 6.7 - 7.3 km (at B) is not cloud topped. Thus the lidar shows a cloud-free thermal higher than the

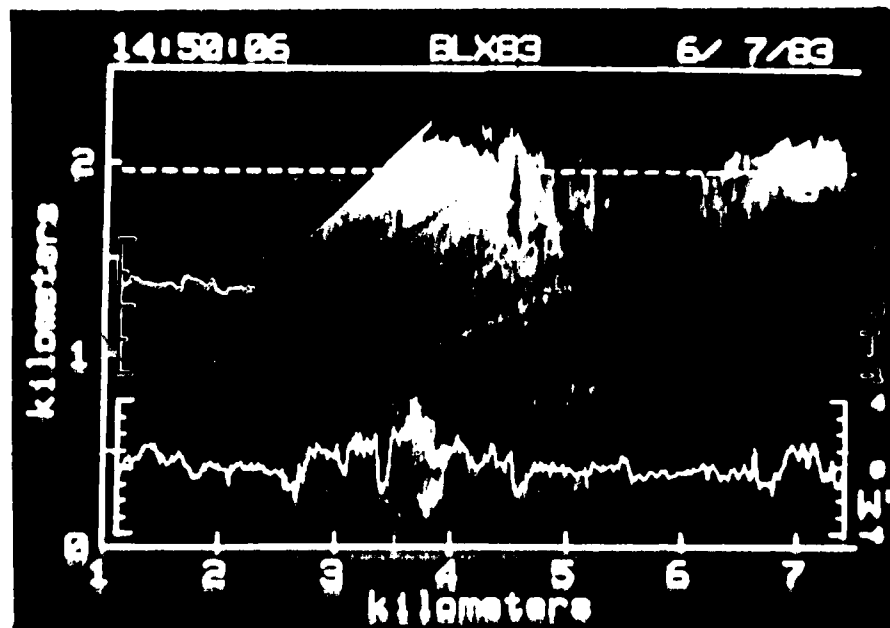


Figure 4.10. Same as Figure 4.6 except for scan ending at 1450:06 CDT on 7 June 1983. The thermals at A and B are discussed in the text.

cloud base of another cloud-topped thermal. The specific humidity of these two thermals differs by approximately 0.4 g/kg (the thermal at B being drier) while the temperatures of the two thermals are nearly the same. We believe that the specific humidity of the thermal at B is representative of its interior and the relatively constant value of humidity is indicative of little entrainment of drier air into the thermal.

The less reflective parcels of air in the entrainment zone (between 4.5 and 6.1 km range and 1500 to 2000 m altitude) correspond to air of lower humidity. Meanwhile, the enhanced region of reflectivity at 3.8 km between an altitude of 150 - 800 m is from dust created by farm activity being carried aloft by a thermal.

#### 4.3.4 1129 CDT 27 May 83

For this case, Figure 4.11 shows that the aircraft is flying much lower in the CBL. Contrasts of in- and out-of thermal conditions are less dramatic. However, moisture still appears to be the best indicator of in- and out-of thermal periods. The mean wind at the average flight level for this leg was from the SSW at 8.5 m/s (Table 4.1). There is a greater gradient of moisture and temperature on the upwind than on the downwind side of the thermals at 2.5 and 3.75 km. This is in agreement with the

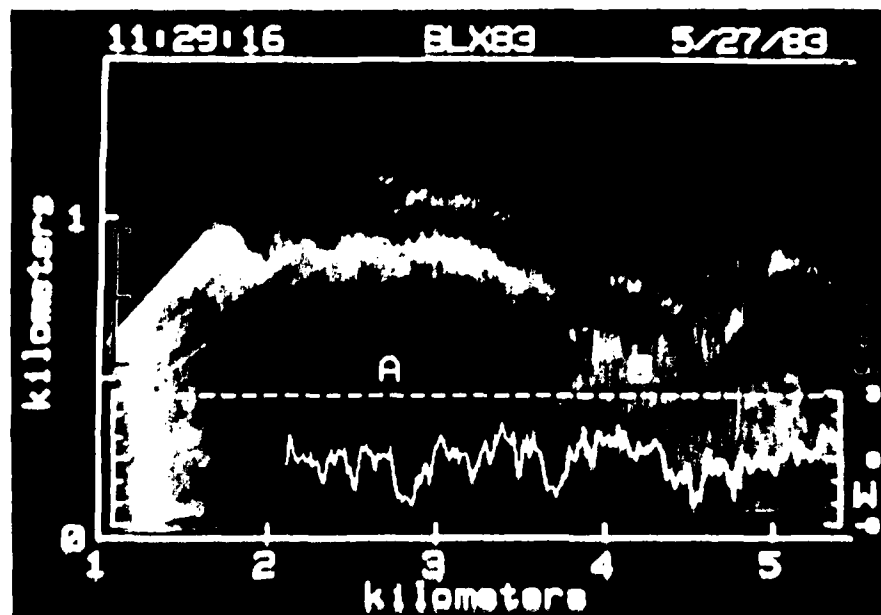


Figure 4.11. Same as Figure 4.6 except for scan ending at 1129:16 CDT on 27 May 1983. The thermals at A and B are discussed in the text.



Table 4.1

Details of Conditions for Queen Air Horizontal Flight Legs  
With Coincident Lidar Observations

The Queen Air and lidar had a heading of 021 (TRUE)

Figure	Date Time (CDT)	Queen Air Ground Speed (m/s)	Mean		Queen Air Altitude (m AGL)	Estimate of		Leg Type Zi/Alt
			Wind Dir/ Speed (m/s)	Wind Speed (m/s)		Zi	h	
						from lidar RHI		
4.6	7Jun 1357	79.5	133/1.55		2066	*	*	Mid cloud
4.8	7Jun 1326	79.8	134/2.38		1800	*	*	Cloud base -100m
4.10	7Jun 1450	80.8	160/2.21		1959	*	*	Cloud base -100m
4.11	27May 1129	83.0	202/8.5		447	525	700	0.85Zi
4.12	16Jun 1213	78.2	163/7.66		512	1235	1354	0.41Zi
4.13	28May 1529	77.3	272/2.7		643	733	812	0.88Zi

\* On these flight legs, the Queen Air was 100-200 m below cloud base. In cloud situations, Zi is often given the value of the cloud base and h is cloud top (not measured here) or the height of free convection, whichever is lower (Stull, 1985b).

findings of Kunkel et al. (1977).

#### 4.3.5 1214 CDT 16 June 83

Figure 4.12 shows another example of how dust created by farming activity (between 2.5 - 3.0 km and 3.5 - 4.5 km) is carried aloft by thermals. The Queen Air is flying at an altitude of roughly half the mean CBL depth, below the level of neutral buoyancy of most thermals. The lidar and aircraft data clearly show regions (near 3.7, 4.0 and 5.1 km) of drier and warmer free-atmosphere air making their way well down into the CBL. This highlights the large-scale (on the order of one km) eddies associated with entrainment into the CBL.

#### 4.3.6 1529 CDT 28 May 83

The flight leg shown in Figure 4.13 is flown in a cloudless entrainment zone, showing how aircraft data might be misinterpreted. There might be a temptation to call the drier and warmer slot of air at 2.5 km (at A) and 6.0 km (at B) small wisps or intrusions of free-atmosphere air into the corresponding plume that the aircraft encountered. We examined RHI scans immediately preceeding and following this scan. The sequence of scans revealed that the dry air slots at A and B are separations between

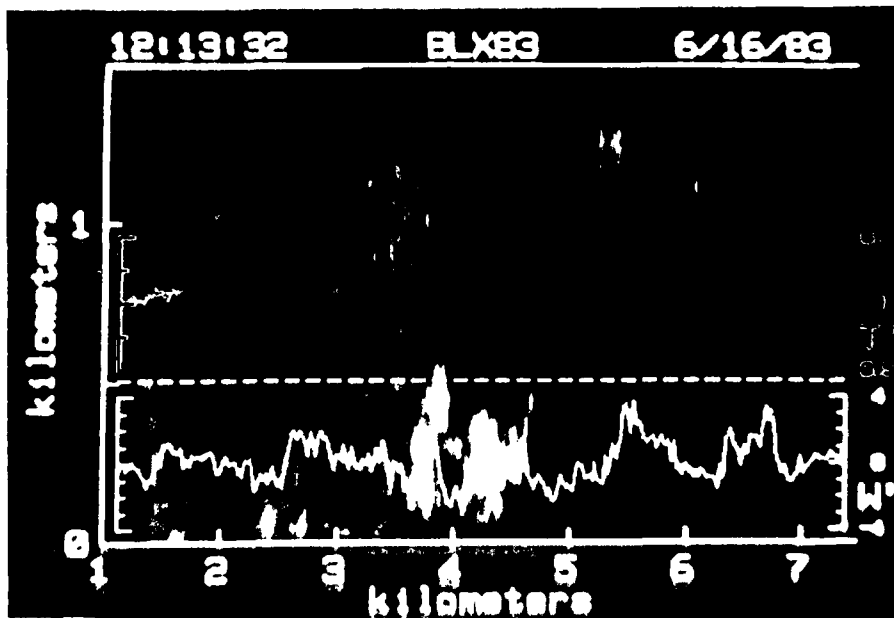


Figure 4.12. Same as Figure 4.6 except for scan ending at 1213:32 CDT on 16 June 1983.

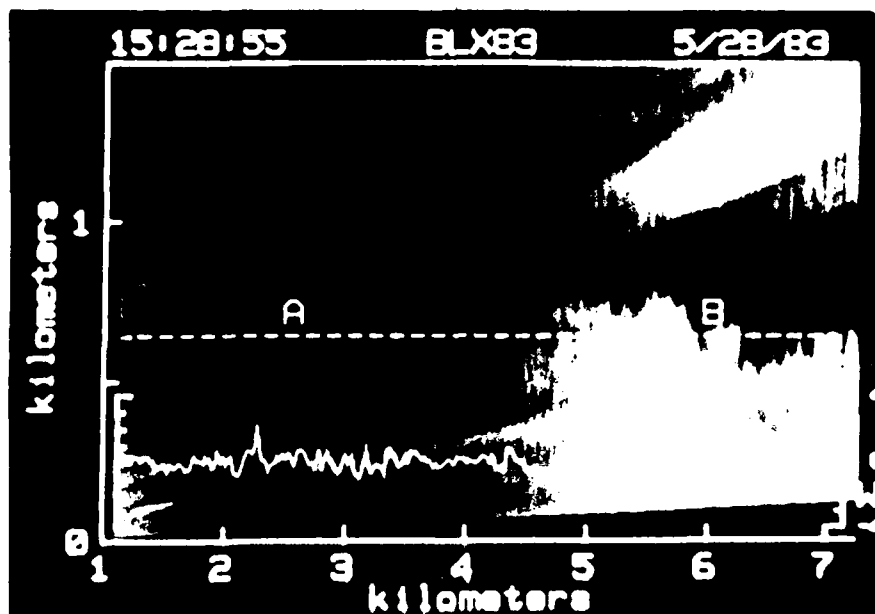


Figure 4.13. Same as Figure 4.6 except for scan ending at 1528:55 CDT on 28 May 1983. The stable layer at the Queen Air's flight level at points A and B are gaps between separate thermals.

different thermals in different stages of their life cycle. Lenschow and Stephens (1980) used a conditional sampling criteria for thermals that any segment of thermal or non-thermal conditions had to persist for at least 25 m. Their duration criteria would have correctly identified the thermal and non-thermal air here. However, the proximity of these distinct thermals show that care must be taken in conditional sampling work to adequately resolve separate thermals.

#### 4.3.7 1325 CDT 7 June 83 and 1450 CDT 7 June 83

Khalsa and Businger (1977) found that properly filtered high frequency turbulence is a possible indicator of thermals near the surface. The unfiltered plots of momentum flux ( $u'w'$  and  $v'w'$ ) and turbulent kinetic energy (TKE) are presented in Figures 4.14 and 4.15 to show the possible bias that could result with the use of TKE as an indicator function of thermals higher in the CBL.

As expected, the TKE in thermals A and B in Figure 4.14, is relatively large. However, the thermal at B in Figure 4.15 has about the same amount of TKE as the stable layer air encountered immediately before. Based on these observations, we recommend the use of moisture over temperature or turbulent kinetic energy as an indicator for being in or out of a thermal (above the surface layer).

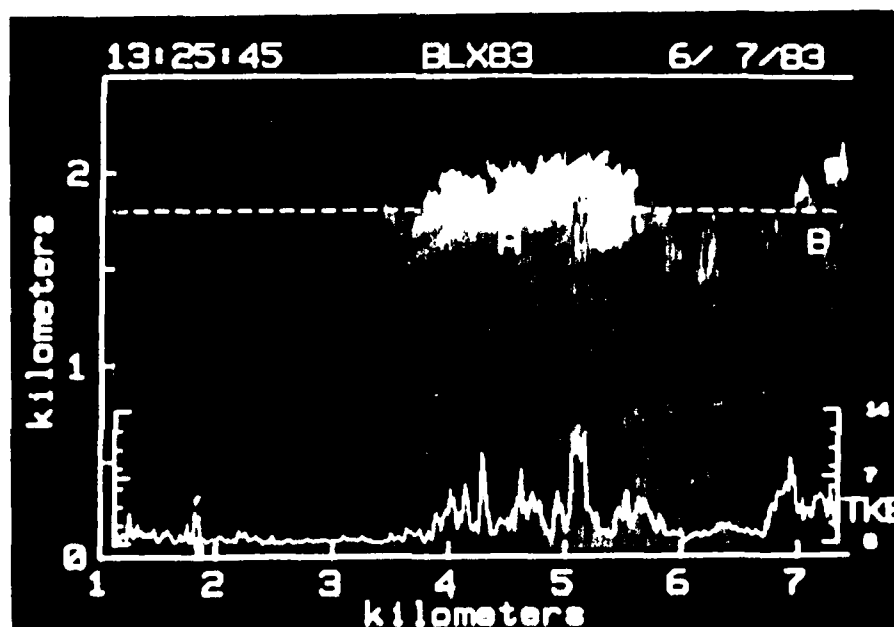


Figure 4.14. Lidar RHI scan ending at 1325:45 CDT 7 Jun 1983 and concurrent Queen Air time series plots of momentum fluxes  $u'w'$  and  $v'w'$  ( $(m/s)^2$ ) and turbulent kinetic energy ( $(m/s)^2$ ). The flight level of Queen Air is indicated by the dashed line. This figure and Figure 4.15 show that the thermals (at A and B) are in general more turbulent than their surroundings but not always.

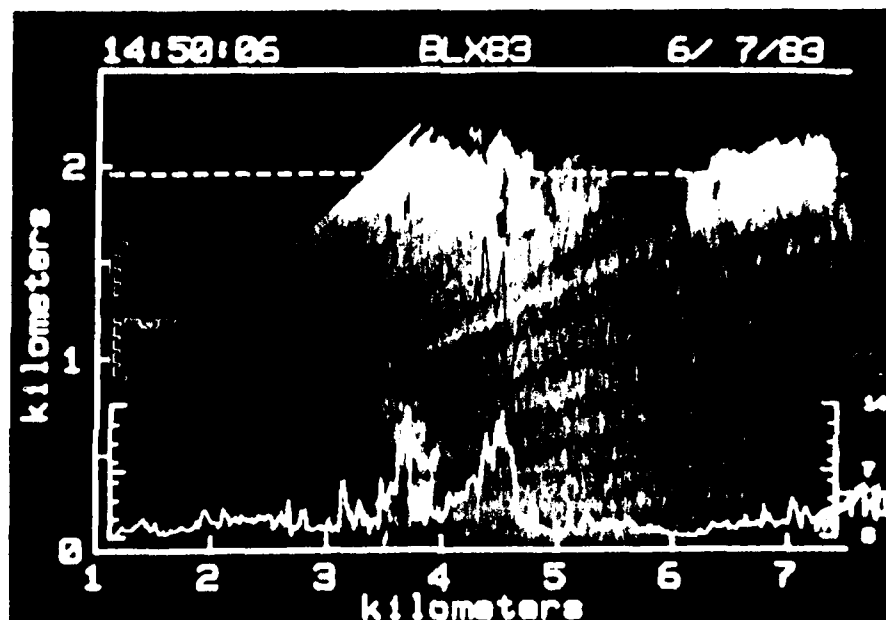


Figure 4.15. Same as Figure 4.14 except for scan ending at 1450:06 CDT on 7 June 1983. Note the relatively small increase in TKE in thermal B.

#### 4.4 Further Discussion

It becomes obvious when examining the vertical profile of humidity in Figure 4.4 how large and differing values of latent heat flux can be measured in the entrainment zone. Instead of the usual association of upward motion with moist eddies and sinking with dry eddies, the opposite is possible with the multiple layers of varying moisture content. Also, as the Queen Air intersects various portions of the undulating wave-like layers the eddy correlation technique could yield a false sign or magnitude of flux. This is a result of the eddy correlation assumption of horizontal homogeneity being violated.

Negative heat fluxes in the entrainment zone are possible without stratified moisture layers aloft. Negatively buoyant plumes returning to their level of neutral buoyancy or merely turbulent eddies of thermals can cause moist air to sink. This is analogous to the synoptic scale where warm advection can come from the north as an occluded cyclone passes to the south.

Making these photos and plots was essential to understanding what sampling criteria to use and to be able to visualize where the aircraft was with respect to thermals and mixed layer air when various traces of temperature, humidity, and momentum were



observed. This understanding and increased confidence in the sensor output was used in developing a theory on the structure of the entrainment zone presented in the following chapter.

## Chapter 5

### Analysis and Synthesis of Entrainment Zone Characteristics

This chapter contains the theory, methodology and discussion of results concerning the amount of surface layer (SL) air existing at various heights within the entrainment zone (EZ). Such information is critical for forecasting the onset time and fractional coverage of fair weather cumulus. Two approaches are taken to describe the amount of surface layer air existing at various heights in the entrainment zone. The first finds the average proportion of surface layer air in the air parcels encountered by the Queen Air during horizontal flight legs. The second approach estimates the fractional amount of the three types of air which exist in the entrainment zone--unmixed free atmosphere air, unmixed surface layer air, and a mixture of the first two.

#### 5.1 Overview

As air is heated near the surface, small buoyant plumes can form with sizes on the order of 100-300 m. Lidar observations of the daytime CBL support the notion that larger thermals form

higher in the CBL by the merging of these smaller plumes below  $0.1 Z_i$ , (Kaimal et al., 1976). These thermals tend to have diameters of  $0.8 - 1.5 Z_i$  (Kunkel et al., 1977). The thermals accelerate upward until reaching their level of neutral buoyancy, which is typically on the order of  $0.7 - 0.8 Z_i$ . Once above the level of neutral buoyancy these negatively buoyant thermals continue to rise but are decelerated by negative buoyancy, form drag, shear, and turbulence. These overshooting thermals often penetrate to  $1.1$  to  $1.3 Z_i$ , the amount of overshoot depending upon the strength of the capping stable layer(s), shear in the EZ, and the stability of the lower CBL. During all stages of the life cycle of thermals, the motion of the thermals, shear and turbulence act to create a very turbulent pattern of SL and free atmosphere (FA) air interaction. Figure 5.1 from Kunkel et al. (1977) shows the typical motion vectors of thermals observed in the CBL. The typical length of time it takes for these thermals to rise from the surface to the top of the CBL, convective scaling parameter  $t_*$ , is on the order of 800 sec for the case studies examined.

Time series plots of the mean CBL depth ( $Z_i$ ) and the thickness of the EZ (i.e., the depth between  $h_2$  and  $h_0$ ) for the times of these case studies are shown in Figures A.14, A.26 and A.33. These plots demonstrate that the EZ comprises a substantial portion of the CBL. Most of the interaction/mixing of FA and SL air takes place in the EZ and fair weather cumulus clouds are

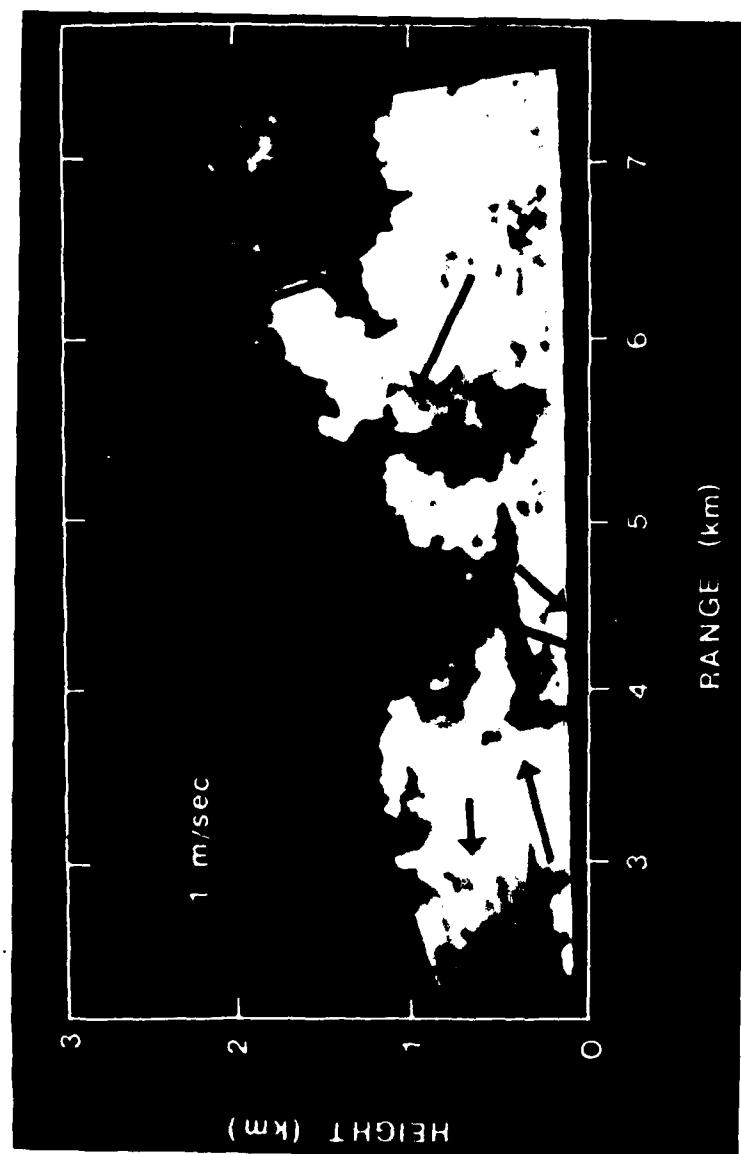


Figure 5.1 Wind vectors obtained from the displacement of plume structure between 1049:03 and 1051:47 on 29 Apr 76. These vectors show the very turbulent nature of the entrainment zone which in this case extends from 0.4 to 1.7 km. Taken from Figure 4a of Kunkel et al (1977).

based in the EZ.

The work discussed in Chapter 4 confirmed that specific humidity can be used as a discriminator between FA and SL air, and suggested that the specific humidity at each data point in a horizontal flight leg describes a realistic measure of the type of air at that point. Another result of the work in Chapter 4 and of viewing sequences of lidar RHI scans, was that one can see evidence of how FA air and SL air mix in the entrainment process.

The following work relies on the use of frequency distributions to make statements on entrainment zone structure and physics. In applying this concept, it is assumed that: (1) The recorded data is accurate; (2) The 18 - 30 km long flight legs yield representative samples of the entrainment zone and that the line samples yield similar results as an area sample (X-Y plane); (3) The flight legs were close enough in time to approximately measure vertical profiles in the entrainment zone at one instant. Convective scaling parameters were used where appropriate to remove some of the nonstationarity. Each sequence of entrainment zone legs took approximately one hour to fly; and (4) Representative observations of the free atmosphere and near-surface conditions have been obtained.

## 5.2 Observations of Mixing into the CBL

The data set used for these case studies was collected by the

Queen Air on three cloud-free days (28 May, 14 Jun, and 16 Jun 1983). As shown by the surface maps, satellite imagery, and soundings in Appendix A, the field site was experiencing anticyclonic conditions with relatively weak gradients and weak advection of temperature and humidity. The soundings in Appendix A, collected by the Queen Air, were used to help determine the source regions of air found in the EZ, and to better understand the structure of the EZ.

Horizontal flight leg data were analyzed to determine the frequency of occurrence of various specific humidities at each flight altitude. A major hypothesis in this chapter is that specific humidity can be used as a tracer of air parcels. Namely, parcels from the FA are relatively dry, while parcels originating near the surface are more moist. The histogram of specific humidities observed during a horizontal flight leg at 1.01 Z/Z<sub>1</sub> (Figure 5.2) shows a range of humidities with three modes, suggesting the presence of (1) unmixed surface layer air, (2) unmixed free atmosphere air, and (3) air resulting from a mixture from the first two source regions. The infrequent occurrence of humidities seen in Figure 5.2 near 4.3 g/kg and 7.75 g/kg is typical of histograms of specific humidity collected near Z<sub>1</sub>. These gaps are more pronounced at this level than elsewhere due to the large range of humidities involved. The tendency for the

/ 30

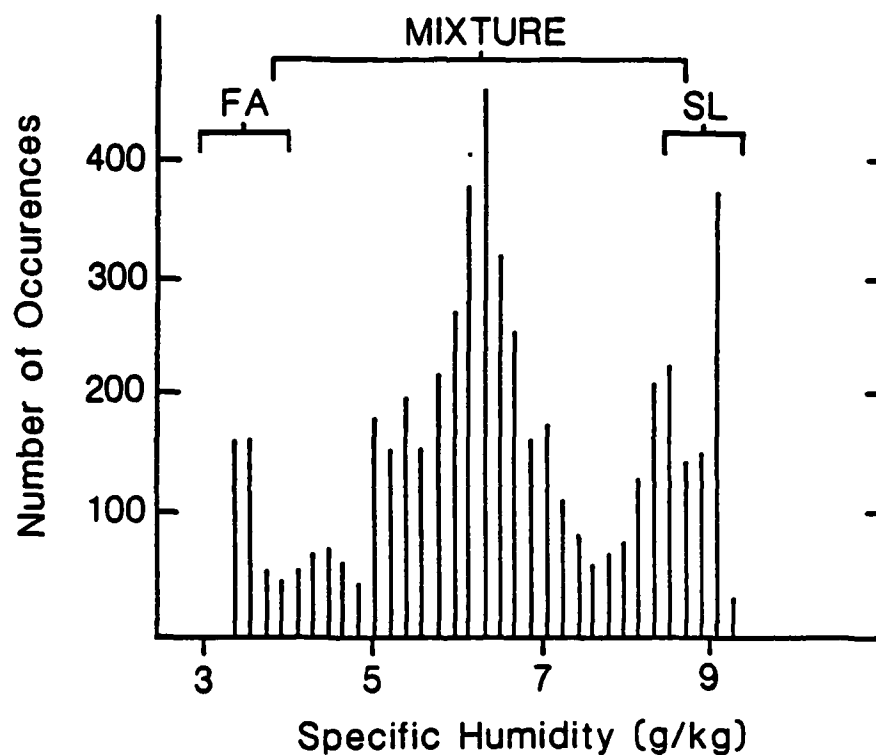


Figure 5.2 Histogram of relative frequency of occurrence of specific humidity measured by the Queen Air during a horizontal flight leg. The leg was flown at 1.01 Z/Zi between 1145 and 1149 CDT 16 Jun 83. The general character of the three types of air existing in the entrainment zone are evident here: (1) unmixed free atmosphere air centered at 3.36 g/kg; (2) unmixed surface layer air centered at 8.5 g/kg; and (3) mixture air centered at 6.3 g/kg;

mixtures to have an expected value/mode between that of the source regions will be discussed later.

Similar histograms were prepared for consecutive flight legs at other altitudes, thereby creating a more complete picture of mixing as a function of height. These histograms are presented in Figures 5.3-5.7 in an arrangement to show where, relative to the features at the specific humidity sounding, the histograms were obtained. The histogram corresponding to the highest flight leg shows the frequency distribution of specific humidity for nearby unmixed FA air. Similarly, the lowest flight leg histogram gives the distribution for unmixed surface layer air. By using these two histograms as "reference" measures of two distinct air masses, one can analyze the mid-level histograms in terms of these references. In particular, one can estimate the fraction of unmixed FA air, unmixed SL air, and mixture air at each height. Examples of the distribution of FA and SL specific humidities and how they can be fit by a probability density function are shown in greater detail in Appendix E. Different unmixed free atmosphere and surface layer air specific humidity frequency distributions are used as references for each case because the surface and free atmosphere environment changes from day to day.

Before getting into the details of this analysis, several statements and definitions can be made based on Figures 5.3-5.7.



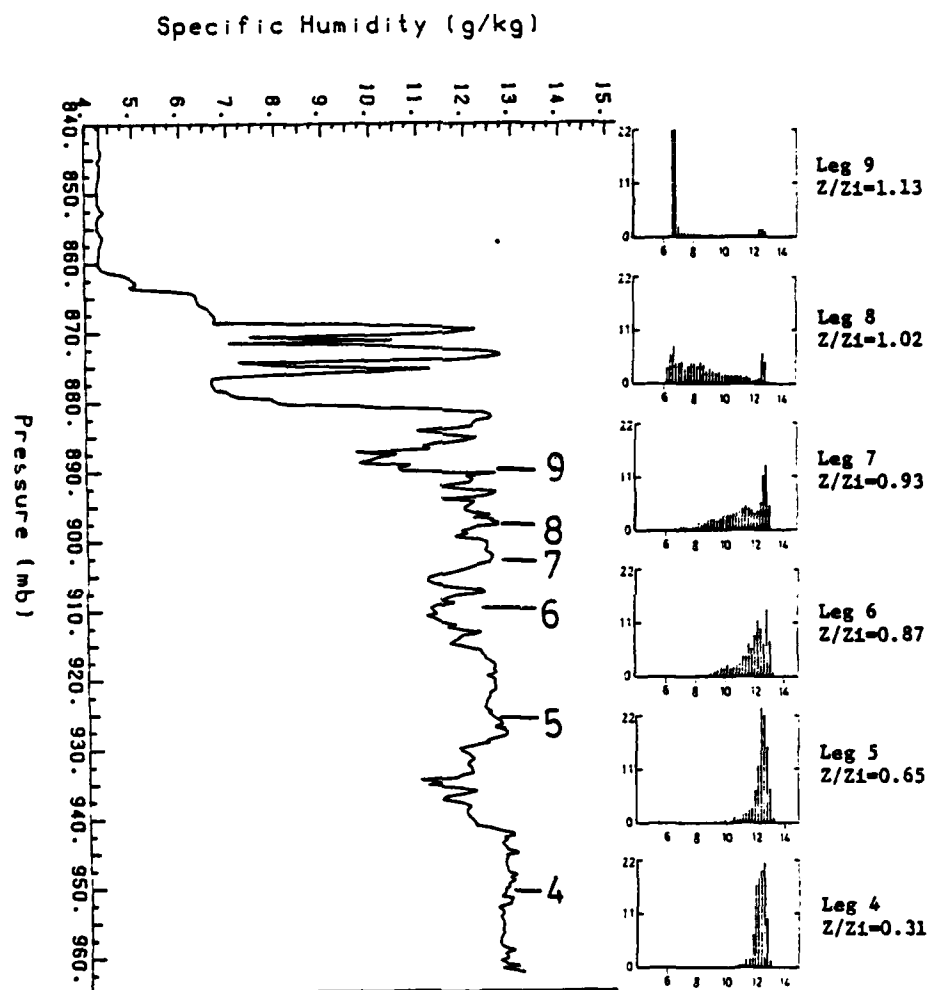


Figure 5.3 Vertical profile of specific humidity from Queen Air sounding and histograms (relative frequency of occurrence) of specific humidity values measured during horizontal flight legs 4-9 of Flight 3 between 1508 and 1547 CDT 28 May 83. The same scale of humidity is on each histogram.

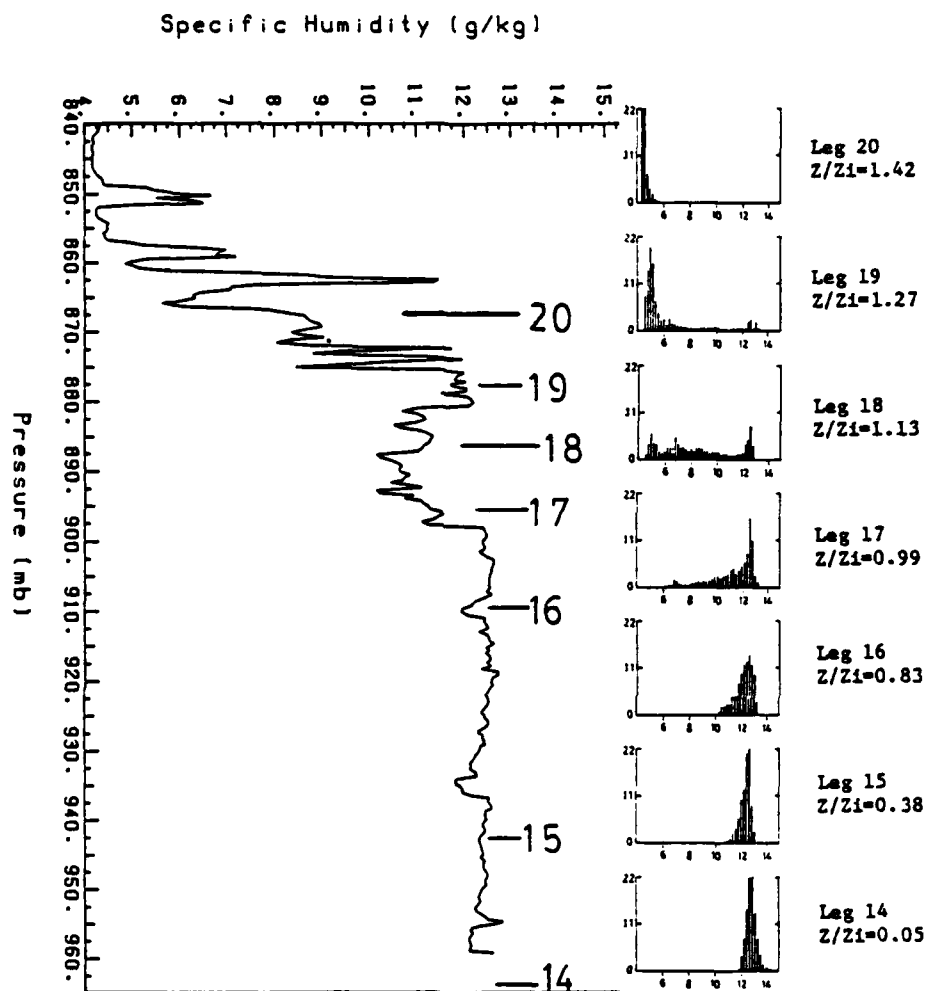


Figure 5.4 Same as Figure 5.3 except for Legs 14-20 (1625 and 1706 CDT) on Flight 3, 28 May 83. Leg 14 is the surface layer reference leg and Leg 20 is the free atmosphere reference leg.

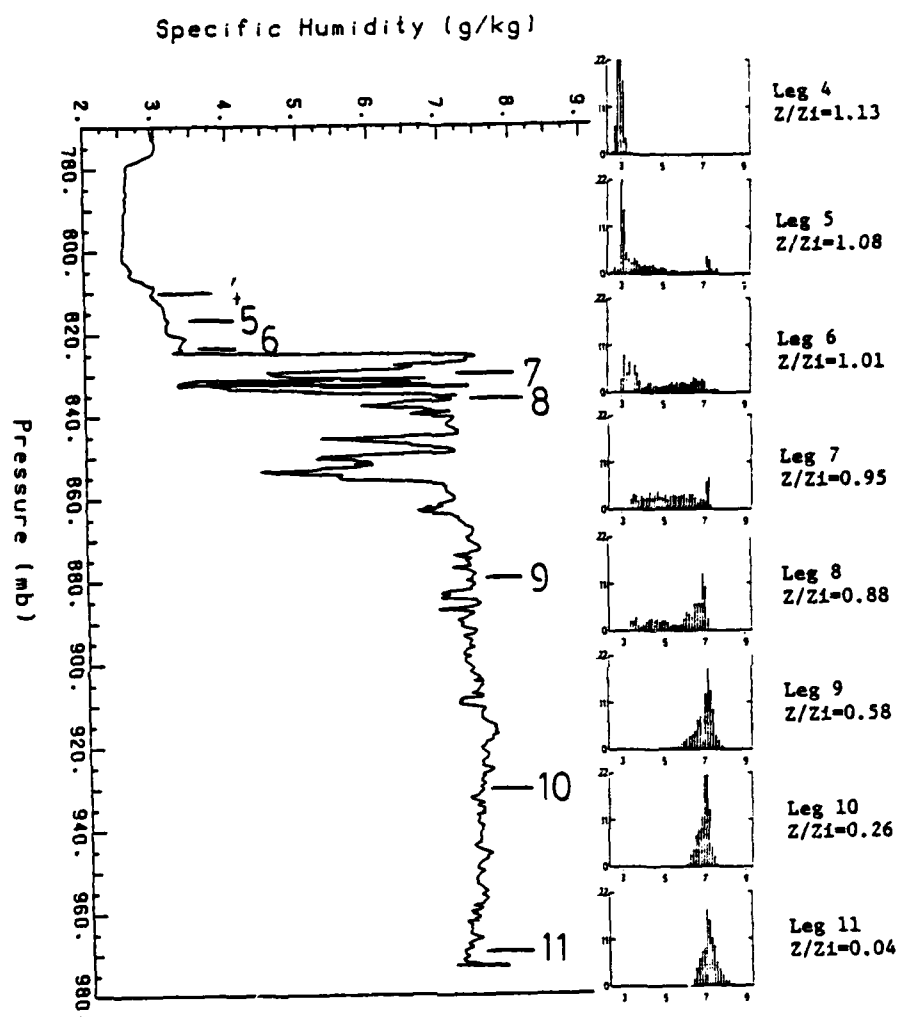


Figure 5.5 Same as Figure 5.3 except for Legs 4-11 (1437 and 1532 CDT) on Flight 13, 14 Jun 83. Leg 4 is the free atmosphere reference leg and Leg 11 is the surface layer reference leg.

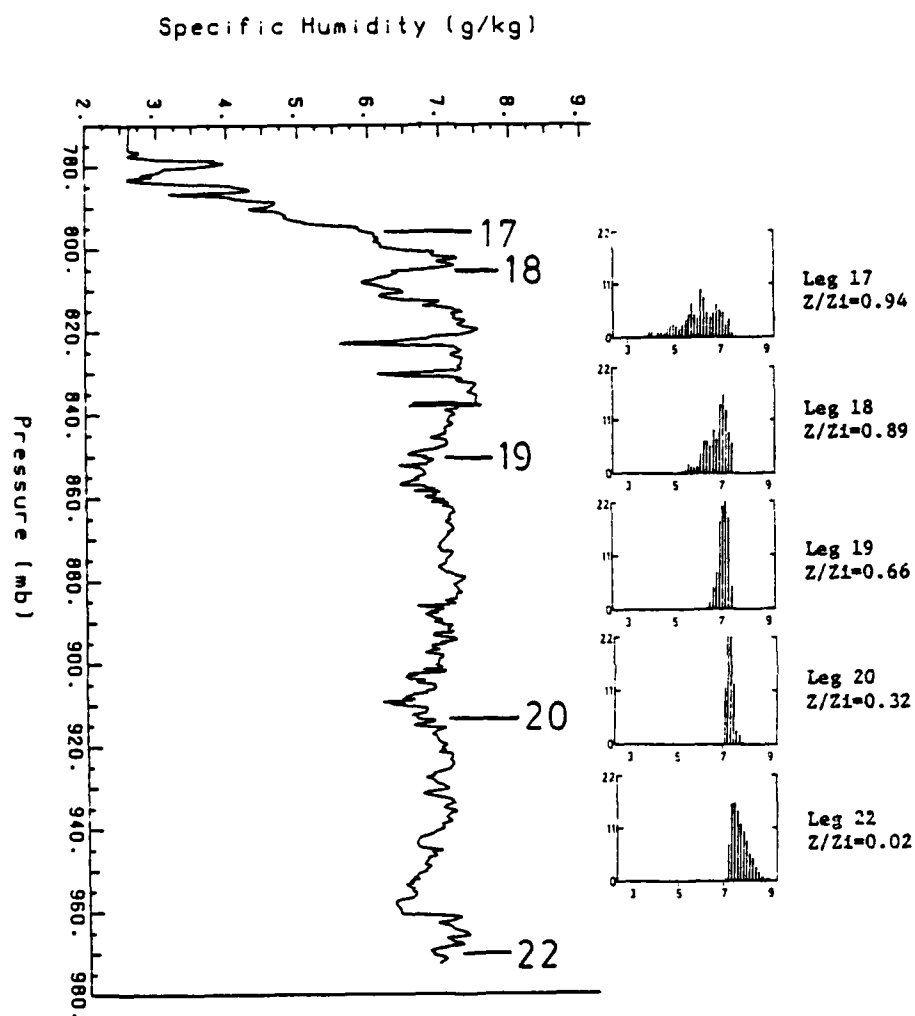


Figure 5.6 Same as Figure 5.3 except for Legs 17-22 (1611 and 1650 CDT) on Flight 13, 14 Jun 83. Leg 22 is the surface layer reference leg.

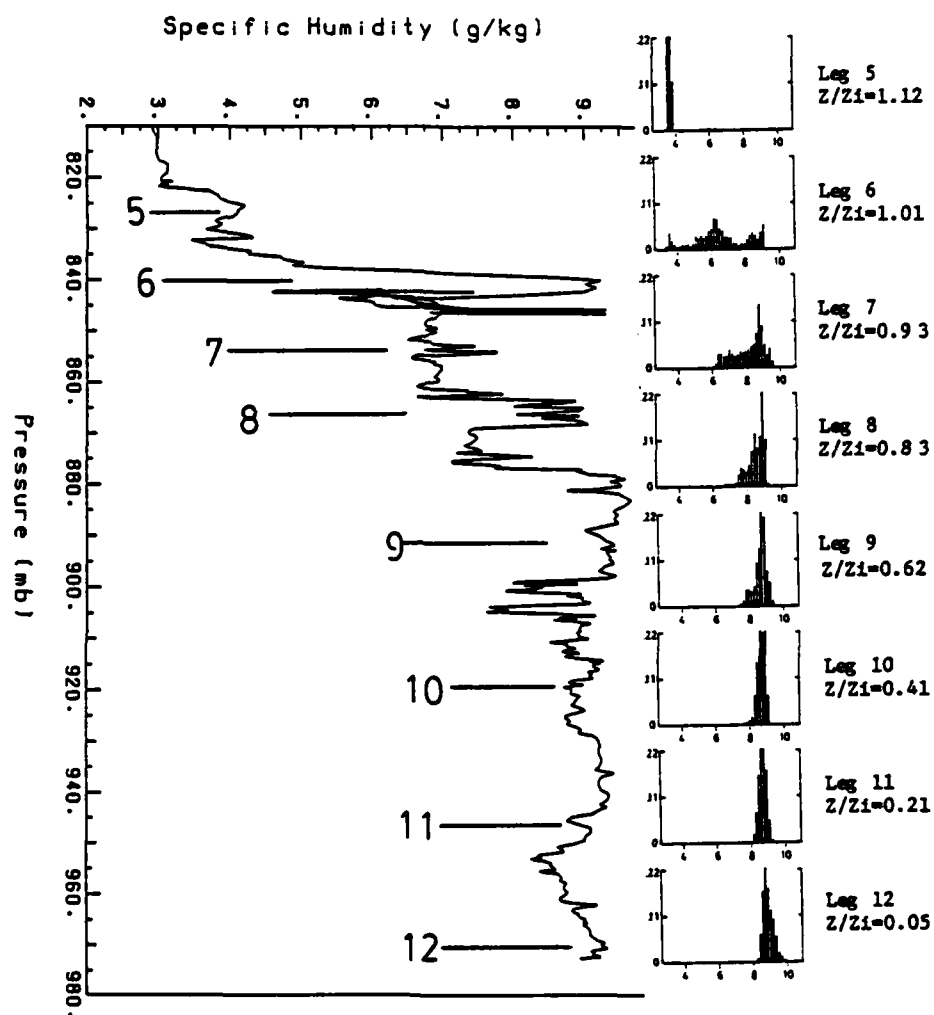


Figure 5.7 Same as Figure 5.3 except for Legs 5-12 (1138 and 1229 CDT) on Flight 16, 16 Jun 83. Leg 5 is the free atmosphere reference leg and Leg 12 is the surface layer reference leg.

(1) The shape and location of the FA and SL frequency distributions remain fairly constant as distance from the respective source region increases, although the amount of air with those respective frequency distributions do vary.

(2) Values of specific humidity like those found in the FA are found below  $1.0 Z_i$ , indicative of plunges of FA air down into the CBL. Unmixed FA air does not penetrate far into the EZ (in these cases taken after the greatest rate of growth of the CBL has taken place), although air containing a mixture of FA and SL air is found in the lower third of the CBL (as discussed in Chapter 4). The converse is not true because unmixed near-surface specific humidity values are seen at the tops of the tallest thermals due to the small amount of lateral entrainment that thermals experience.

(3) The frequency of occurrence of various specific humidity values in both the SL and the FA along a flight leg is variable. Nevertheless, these distributions can usually be approximated by an asymmetrical double exponential density function.

(4) Intermediate specific humidity values (between those of the SL and FA) also exist in the EZ. The frequency distribution of these humidities is associated with what will be called mixed air.

(5) The overall frequency distribution of specific humidity involves a general shifting of the observed humidities from free

atmosphere values near the top of the EZ toward surface layer values near the bottom of the EZ. At intermediate levels, more frequent occurrences of mixed air with larger humidities as one descends are encountered. At some levels, the frequency distribution of mixed air is nearly adjacent to that of the FA or SL and no "gaps" between the two sets of frequency distributions are apparent while near  $Z_i$  a gap is commonly observed.

The amount of mixed air at a level in the EZ is primarily a function of large-scale eddy mixing. Due to shear and the sinking of overshooting thermals, large volumes of FA air, mixed air, and SL air are mixed. Only a small amount of air is mixed along the side of thermals via lateral entrainment. One of the results of the work reported in Chapter 4 was the realization that lateral entrainment does not proceed far into thermals. Most of the lateral entrainment is limited to a narrow region next to the edges (typically less than 15% of the diameter of active thermals) termed the intromission zone (Crum et al., 1985). It is this evidence that mixing has taken place primarily along the edges of thermals that suggests that top-down entrainment is not playing a large role in these cases.

Deardorff et al. (1980) visually estimated the fraction of mixed layer (ML) fluid existing at a given height in the EZ in their laboratory tank simulation. They state that the accuracy of

their coverage was 10%. They classified mixtures with any ML fluid present as ML fluid. With our data set however, we can estimate the amount of SL air present in the EZ by two methods: (1) Linear Mixing Approach (section 5.3), and (2) Mixture Approach (section 5.4). These methodologies are used to formulate statistical models of mixing in the entrainment zone.

### 5.3 Linear Mixing Approach

#### 5.3.1 Theory

During his development of saturation point analysis, Betts (1982) states that the resultant specific humidity of all possible ratios of mixtures of two volumes of air (not just the mixture of equal volumes) lie along a mixing line. The location of the mixture on the mixing line is determined by the proportions of air mixed.

If we assume that we know the specific humidity of the two types of air involved in the mixing (FA and SL) we can find the fractional amount of surface layer air ( $F_{SL}$ ) in the resultant mixture by

$$F_{SL} = \frac{q_{OBS} - q_{FA}}{q_{SL} - q_{FA}} \quad (5-1)$$



where  $q_{OBS}$  is the specific humidity of the parcel sampled,  $q_{SL}$  is the specific humidity of the SL air and  $q_{FA}$  is the specific humidity of the FA air. So the intermediate specific humidity values seen on the histograms in Figures 5.3 through 5.7 correspond to differing proportions of SL and FA air being mixed together.

Using the linear mixing character of specific humidity, the amount of  $\alpha$  SL air in the EZ sampled during a flight leg is given by

$$\bar{\alpha} = \frac{1}{N} \sum_{i=1}^N F_{SLi}$$

where  $F_{SLi} = 0$  if  $q_i < F_{Amax}$   
 $F_{SLi} = 1$  if  $q_i > SL_{min}$  (5-2)  
 $0 < F_{SLi} < 1$  if  $F_{Amax} < q_i < SL_{min}$ ,  
 $F_{SLi}$  from eqn 5.1 otherwise

where  $N$  is the number of observations during the flight leg.

Figure 5.8 is an illustration of this indicator function.

### 5.3.2 Resultant Profiles of Entrainment Zone Structure

Table 5.1 contains the estimated proportion of surface layer air at various altitudes resulting when the indicator function in equation 5-2 was applied to each series of entrainment zone flight legs. Figures 5.9 - 5.13 are graphical representations of the

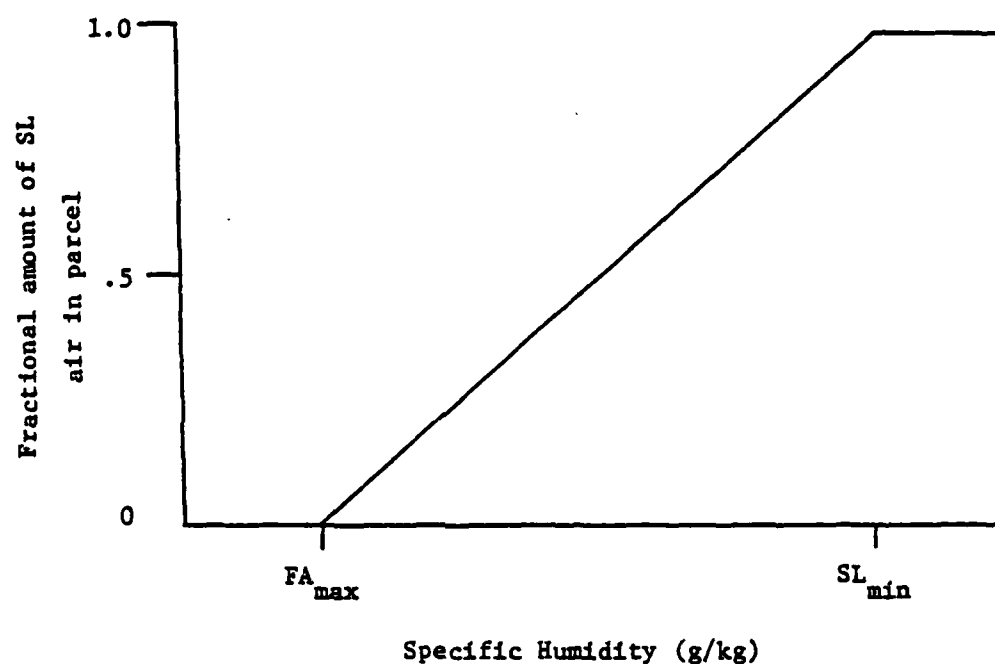


Figure 5.8 Schematic of indicator function for linear mixing approach for estimating the proportion of SL air. The inclined line is the mixing line due to the linear relationship of the mixing of various proportions of air with different specific humidity.

Table 5.1 Estimates of the proportion of surface layer air existing at various levels in the CBL as measured by the Queen Air and applying the linear mixing indicator function.

Flight, Leg	Start Time (CDT)	Altitude (m AGL)	Z/Zi	Proportion of SL air
Flight 3, 28 May 83				
3	1501	57	0.07	1.00
4	1508	232	0.31	0.9994
5	1515	467	0.65	0.9941
6	1520	619	0.87	0.9411
7	1527	663	0.93	0.8496
8	1533	722	1.02	0.41
9	1539	800	1.13	0.0939
10	1545	859	1.22	0.0164
11	1552	929	1.25	0.0
14	1625	57	0.07	1.0
15	1631	297	0.38	0.9956
16	1638	619	0.83	0.9789
17	1644	745	0.99	0.8358
18	1650	830	1.13	0.4031
19	1656	919	1.27	0.1371
20	1702	1018	1.36	0.0
23	1742	94	0.13	1.0
Flight 13, 14 Jun 83				
1	1414	65	0.03	1.0
4	1437	1621	1.13	0.0
5	1445	1549	1.08	0.2088
6	1452	1488	1.01	0.4521
7	1458	1427	0.95	0.6363
8	1505	1356	0.88	0.7559
9	1512	927	0.58	0.9911
10	1519	443	0.26	1.0
11	1527	84	0.04	1.0
14	1550	2047	1.15	0.0264
15	1557	1961	1.08	0.04
16	1604	1866	1.01	0.69
17	1611	1771	0.94	0.8481
18	1618	1678	0.89	0.9692
19	1624	1222	0.66	0.9985

20	1632	594	0.32	1.0
22	1645	66	0.02	1.0
Flight 16, 16 Jun 83				
1	1111	58	0.05	1.0
5	1138	1438	1.12	0.0
6	1145	1306	1.01	0.5893
7	1151	1176	0.93	0.905
8	1158	1078	0.83	0.9771
9	1204	795	0.62	0.9915
10	1212	533	0.41	0.9989
11	1218	272	0.21	1.0
12	1225	61	0.05	1.0

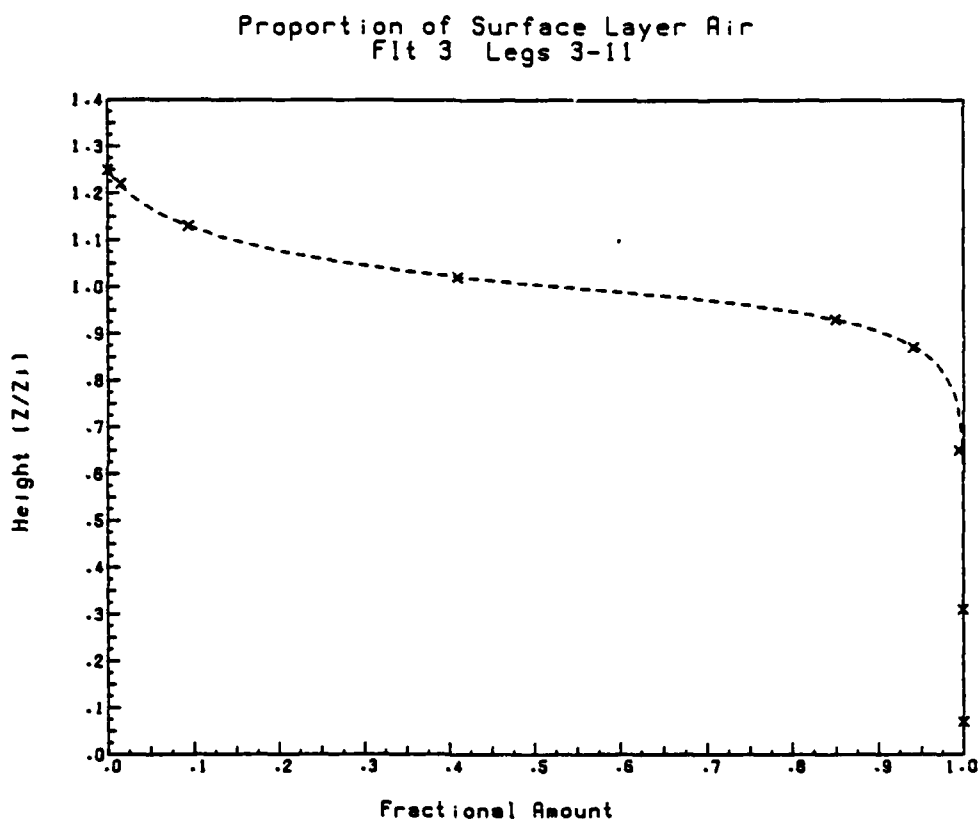


Figure 5.9 Plot of normalized height versus proportion of surface layer air present. The estimates are from the linear mixing approach. The best fit line of a cumulative distribution function of an asymmetrical double exponential function is drawn. The data was collected on Legs 3-11 of Flight 3, 28 May 83.

Proportion of Surface Layer Air  
Flt 3 Legs 14-23

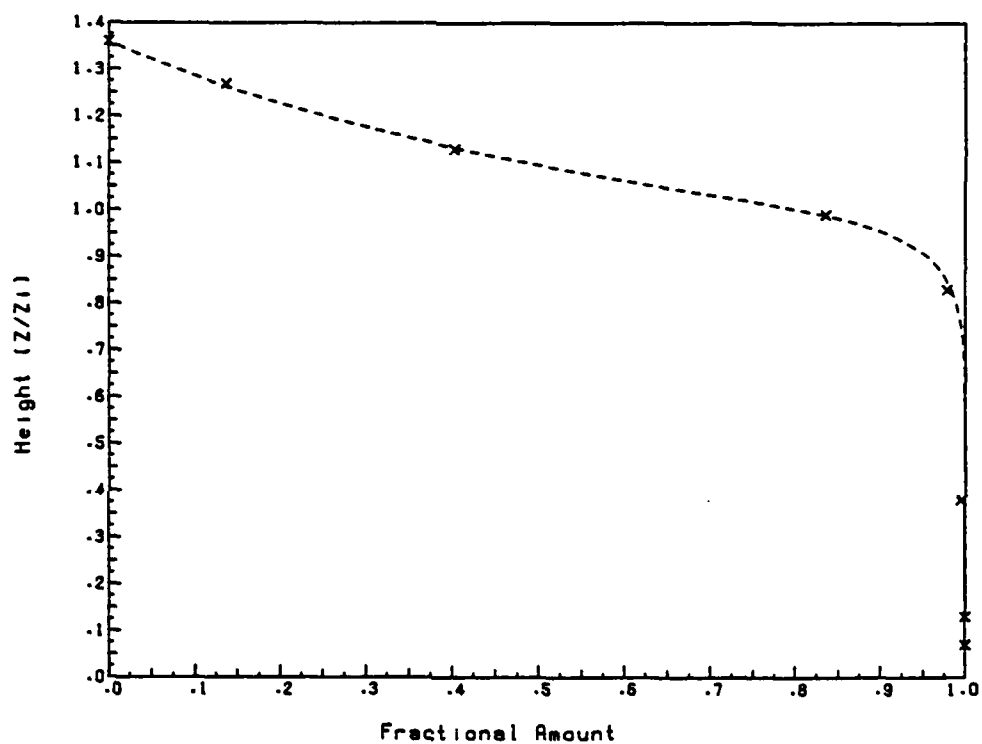


Figure 5.10 Same as Figure 5.9 except for Legs 14-23.

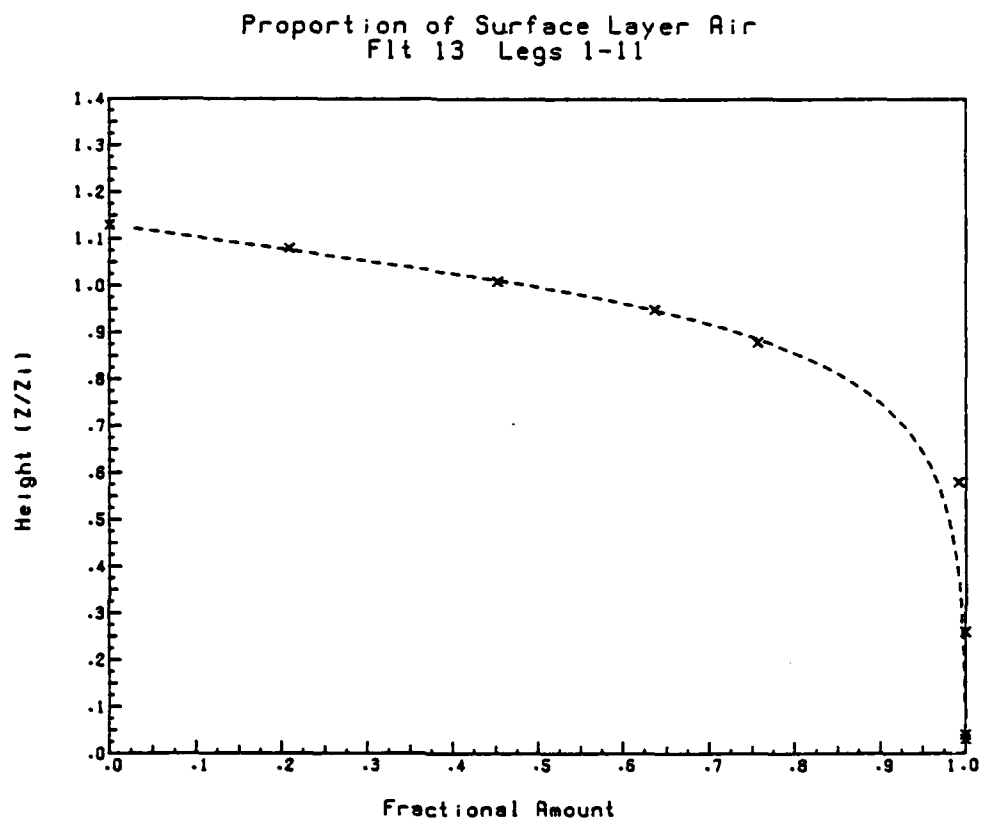


Figure 5.11 Same as Figure 5.9 except for Legs 1-11 of Flight 13, 14 Jun 83.

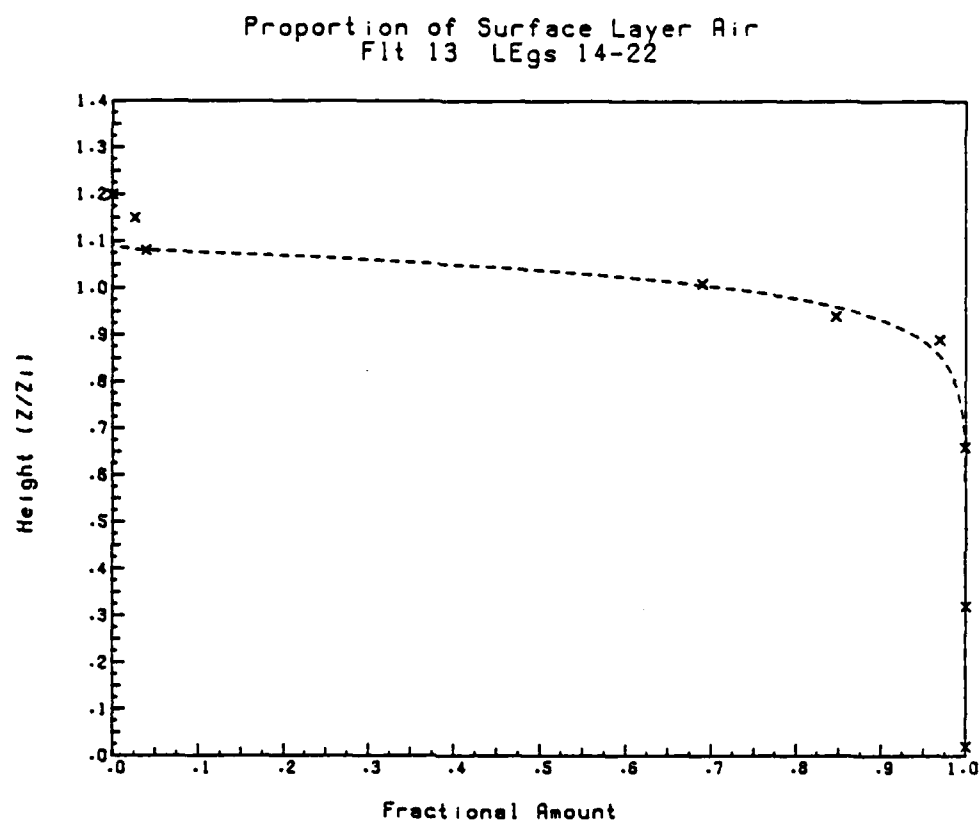


Figure 5.12 Same as Figure 5.9 except for Legs 14-22 of Flight 13, 14 Jun 83.



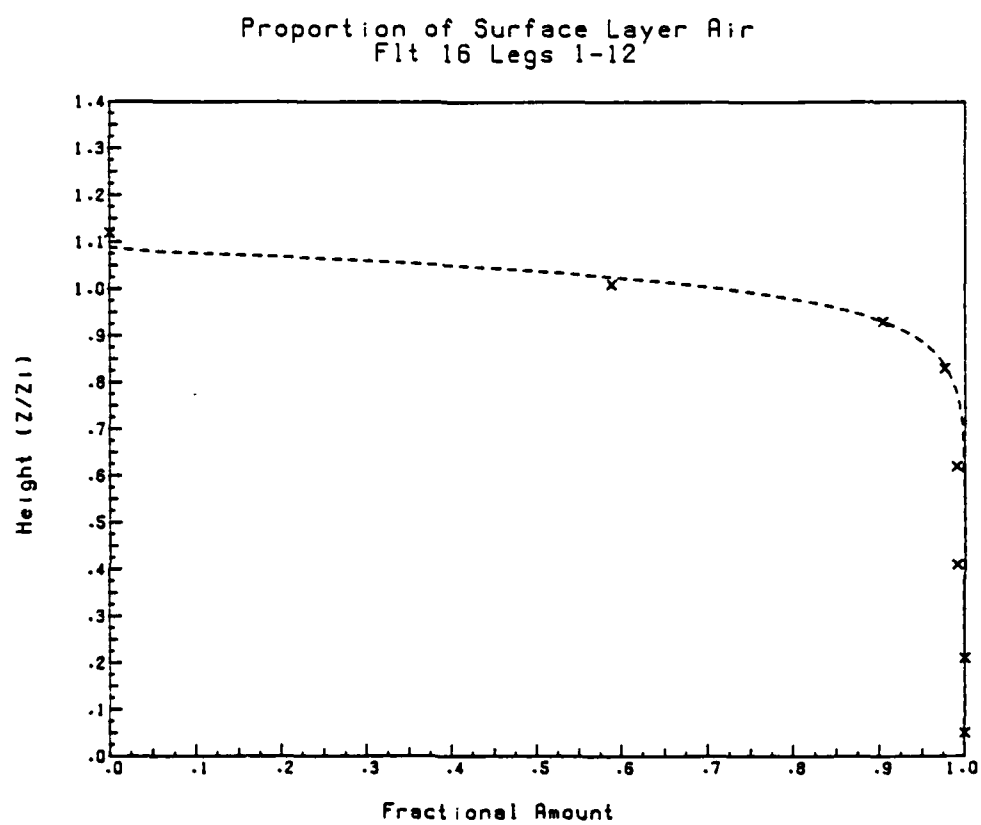


Figure 5.13 Same as Figure 5.9 except for Legs 1-12 of Flight 16, 16 Jun 83.

proportions as a function of normalized height. The shape of these proportion profiles is well explained by the cumulative distribution function (CDF) of an asymmetrical double exponential function, which is drawn in as the solid line. This is similar to the profile shape that Wilde et al. (1985) reported fit the Deardorff et al. (1980) tank data of the ML fluid in the simulated EZ.

The CDF of the asymmetrical double exponential function is used here merely as a method of fitting a curve to the data. This use of the asymmetrical double exponential function should not be confused with its use in fitting frequency distributions in the Mixture Approach. The CDF is the integral of the probability density function of the asymmetrical double exponential

$$f(Z) = \begin{cases} A \exp[-(Z-Z_m)/\alpha] & Z_m \leq Z < Z_T \\ A \exp[(Z-Z_m)/\beta] & Z_B \leq Z \leq Z_m \end{cases} \quad (5-3)$$

where  $Z_B$  is the height of the lowest flight leg,  $Z_T$  is the height of the highest flight leg,  $A$  is a normalization factor which allows the total area under the function to equal one, and  $Z_m$  is the point of asymmetry. The CDF at height  $H$  is

$$F(H) = \begin{cases} A\beta[\exp((H-Z_m)/\beta) - \exp((Z_B-Z_m)/\beta)] & H \leq Z_m \\ A\beta[1 - \exp((Z_B-Z_m)/\beta)] + A\alpha[1 - \exp(-(H-Z_m)/\alpha)] & H > Z_m \end{cases} \quad (5-4)$$

Equation 5-4 is then solved for the parameters ( $\alpha$ ,  $\beta$ ,  $Z_m$ ) which result in the smallest sum of squares difference between the function and the observations. The parameters of the best fit cumulative distribution functions that fit these entrainment zone flight profiles are listed in Table 5.2.

It is interesting to note that the inflection point of the fitted CDFs ( $Z_m$ ) is consistently near the subjectively determined (from lidar imagery) mean CBL depth ( $Z_i$ ). This suggests that the mean CBL height is the transition point of two different types of mixing because the inflection point in this cumulative distribution function occurs where the two exponential probability distribution functions join to form the double exponential distribution. Above  $Z_i$  the thermals are primarily interacting with the FA air for a short time and mostly in a SL-FA mixture. Below  $Z_i$  the time scale for interactions is larger, and mixing between a greater range of humidities takes place. So  $Z_i$  is more than just a convenient label to call the depth of the CBL.

The shape parameters  $\alpha$  and  $\beta$  for these fits do not appear to be related to the most appropriate CBL parameters. Earlier entrainment zone work has suggested that the depth and character

Table 5.2 Best fit estimates of parameters of asymmetrical double exponential cumulative distribution function based on proportion estimates listed in Table 5.1. The estimates are from the linear mixing approach. The resultant functions are plotted in Figures 5.9 - 5.13.

Flight	Legs	$\alpha$	$\beta$	$Z_m (Z/Z_1)$
3	1-11	0.088	0.061	0.99
3	13-23	0.316	0.068	1.02
13	1-11	9.424	0.155	1.03
13	13-23	0.0029	0.065	1.08
16	1-12	1.725	0.054	0.99

of the entrainment zone is related to: (1) the change of buoyancy across the capping stable layer  $\Delta\theta$ ; (2) the buoyancy flux at the surface; (3) the convective scaling velocity  $w_*$ ; (4) the interfacial Richardson number; or (5) the depth of the EZ ( $\Delta h$ ). Attempts to correlate the shape parameters with these five CBL parameters individually and in combinations were not successful (i.e. the shape parameters do not appear to be functions of the five CBL parameters examined).

A large step toward successful modeling of the entrainment zone is the confirmation that the cumulative distribution function of asymmetrical double exponentials describes the SL proportion as a function of height. The consistent good fit of the five series of flight legs (though the data was collected after the time of the most rapid growth of the CBL) and the laboratory tank results of Deardorff et al. (1980) further our confidence that this is the profile that the SL proportion assumes in daytime CBLs.

## 5.4 Mixture Approach

### 5.4.1 Theory

This approach was a result of observations made while working with the aircraft and lidar data and provides information on the entrainment zone structure that goes beyond that provided by the

Linear Mixing Approach. Lidar imagery and the histograms of specific humidity as a function of height (Figures 5.3-5.7) suggested three basic population sources of air parcels existing in the EZ. These sources were: (1) unmixed free atmosphere layer air; (2) a mixture of SL and FA air; and (3) unmixed surface layer air. Each source region has its own characteristic frequency distribution shape. It is hypothesized that the frequency distributions of sources (1) and (3) can be approximated by asymmetrical double exponential probability density functions, and the mixture (2) can be approximated with Gaussian distributions. See Appendix E for the analytical forms and example fits of these probability density functions.

The hypothesis that the mixed air will assume a Gaussian distribution is based on the following reasoning. The parcels of mixed air at a level will have reached their observed condition after from one to an indeterminate number of mixing interactions with other parcels of air containing 0 to 100% SL characteristics. This interaction results in a distribution formed by the convolution of the SL and FA air distributions. However, the limit of many interactions/convolutions of various distributions of random variables is a Gaussian distribution.

The shape parameters of the asymmetrical double exponential densities for the FA and SL air ( $\alpha$  and  $\beta$ ) can be analytically found via the method of maximum likelihood estimation (MLE). The

method of MLE estimators was selected rather than a graphical technique or method of moments because MLE parameter estimates of density functions often are the minimum variance unbiased and most consistent estimators available. Appendix E shows the derivation of the MLE estimators for the unknown parameters to be determined for the SL and FA air density functions. An example of the resultant fit for both a SL and FA leg is also presented in Appendix E.

Figure 5.14 shows an example of how the hypothesized three density functions in the EZ sum to yield an overall density. Examination of the distributions in Figures 5.3-5.7 suggest that this type of interaction is taking place between the FA and SL air.

The overall frequency distribution of specific humidity ( $q$ ) at a level in the CBL can be described by a sum of the individual distributions (Everitt and Hand, 1981)

$$f(q; P_1, \mu, \sigma) = \sum_{i=1}^3 P_i g_i(q; \mu, \delta) \quad (5-5)$$

where  $g_1$  is the functional form of the unmixed FA air frequency distribution, assumed to be double exponential and known;  $g_2$  is the form of the mixture air frequency distribution, assumed to be Gaussian with unknown  $\mu$  and  $\sigma$ ; and  $g_3$  is the form of the unmixed SL air frequency distribution, assumed to be double

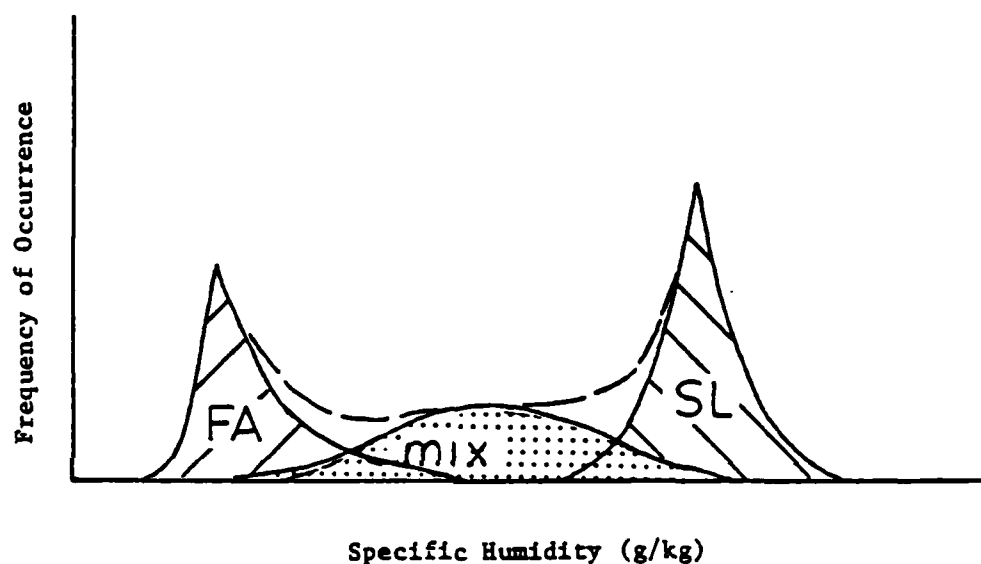


Figure 5.14 Graphic example of how three density functions: (1) FA, free atmosphere air (//); (2) MIX, mixed air which is a mixture of various proportions of FA and SL air (.....); and (3) SL, surface layer air (\\) sum to produce the observed density function (dashed line).



exponential and known. The mean of each function is  $\mu$  and its standard deviation is  $\sigma$ . The sum of the proportions  $P_1 + P_2 + P_3$  is unity.

In solving for the mixture parameters ( $\mu, \sigma$ ) and proportions ( $P_1, P_3$ ) by the method of maximum likelihood, we allowed the location parameters  $q_{m1}$  and  $q_{m3}$  for the double exponential distributions to shift to account for horizontal non-homogeneity and temporal changes of the specific humidity in the surface layer. Analysis showed that with consecutive (in time) flight legs at the same altitude, the frequency distributions of specific humidity would generally look similar but that their absolute location might shift some. For the FA case, this allowed for the slight vertical gradient of specific humidity that was sometimes observed above the CBL.

The logarithm of the likelihood function of equation 5-5 is

$$L = \sum_{i=1}^N \left[ \ln \sum_{j=1}^3 P_j g_j(q; \mu_j, \sigma_j) \right]$$

$$L = \sum_{i=1}^N \ln \left[ P_1 g_1(q; q_{m1}, \alpha_1, \beta_1) + P_2 g_2(q; \mu_2, \sigma_2) \right. \\ \left. + P_3 g_3(q; q_{m3}, \alpha_3, \beta_3) \right] \quad (5-6)$$

The desired values of the unknown parameters ( $q_{m1}, q_{m3}, \sigma_2, P_1, P_3$ , and  $\mu_2$ ) are the ones which maximize this function.

Thus the result of this effort will be estimates of the proportion of unmixed air and parameters of the assumed Gaussian

shape of the mixed air existing at various flight levels. In addition to being able to discover what these values are, these parameters provide the information needed to describe the theoretical distribution of specific humidities at various levels.

#### 5.4.2 Results

The modeled frequency distributions of specific humidity to be found are essentially the result of fitting the hypothesized frequency distributions to the observed frequency distributions. The estimates of the parameters in equation 5-5 selected were the ones which numerically maximized the likelihood function for the mixtures of the three distributions (equation 5-6). Two additional constraints were added: (1) the SL distribution was truncated for values greater than  $q_{m3} + 1.5$ ; and (2) the mean of the mixture distribution was restricted to be less than  $q_{m3} - 2\sigma_3$ .

The first of these constraints was imposed because the histograms of specific humidity show that the distribution of SL values aloft is not as skewed to the right as much as those measured near the surface. This is attributed to what is termed the natural filtering of plumes in the surface layer rather than mixing which would tend to allow a steady decrease of the frequency of occurrence of more humid values rather than the

observed sharp cutoff. That is, air which is the most humid has origins over surfaces where a larger proportion of the solar insolation has gone to latent heat rather than sensible heat. The result is that the most humid parcels tend to be less buoyant than the relatively drier ones and hence never rise out of the surface layer. The correction factor was found by examining the amount of right hand tails "cut off" in the frequency distributions for flight legs above the surface layer. This constraint was not parameterized as a function of height due to the irregularity of the amount cut off--although the amount cut off appeared to increase with height.

The constraint dealing with the maximum allowed value of the mean of the Gaussian distribution is more of a result of the statistical approach than one of the atmosphere. Conceptually, lower in the CBL as SL air mixes with mixture air of larger humidities, a point would be reached where the mean of the mixture air will be the same as that for the SL air, albeit in decreasing quantities. However, the MLE approach lets the Gaussian distribution explain a disproportionate proportion of the total observed distribution when there is difference between the specific humidities of the mixture air and SL air. Without this constraint, an unrealistic secondary maximum of the proportion of mixed air was observed at low altitudes. Lidar observations also suggest that this is not the case. The  $-2\beta_1$  factor was selected

because this was where the impact of this effect leveled off. For this reason the parameter estimates in the lower half of the CBL have the largest suspected error and the estimates of  $\mu$  and  $\sigma$  for the mixture air are most severely constrained.

Table 5.3 lists the maximum likelihood estimates of the proportions of the three types of air present in the CBL at any given level and the parameters of the estimated mixed air distribution (assumed to be Gaussian) for our entrainment zone flight legs. Figures 5.15 - 5.19 are graphical presentations of the vertical profiles of these MLE parameter estimates.

Quantitatively the estimates of the mixed parameters and follow the patterns expected. As one goes higher in the entrainment zone, the expected value of mixed air specific humidity decreases. Lidar imagery suggests this too. Mixed air parcels near the bottom of the EZ have probably experienced more interaction with mixed parcels and SL parcels (due to the closeness of the source region) than aloft.

At the bottom of the entrainment zone, many mixings have tended to reduce the contrast of humidities of mixed air. Near the top of the EZ fewer scales of turbulent mixing are in action and the parcels of SL air/thermals at this level are there for a very short period of time. Hence, a narrower range of mixing proportions result. Near the center of the entrainment zone,

116

Table 5.3 MLE estimates of the parameters in equation 5-6 for the mixture approach. These parameter estimates were obtained by numerically evaluating equation 5-6 for the maximum value obtained.

Leg	Z/Z <sub>1</sub>	Proportions		SL	$\mu_2$	$\sigma_2$
		FA	MIX			
FLIGHT 3						
4	0.31	0.0	0.0	1.0	11.70	0.77
5	0.65	0.0	0.05	0.95	10.92	0.59
6	0.87	0.0	0.39	0.60	10.92	1.11
7	0.93	0.0	0.6	0.4	10.4	1.31
8	1.02	0.09	0.77	0.14	8.39	1.48
9	1.13	0.8	0.14	0.06	8.01	1.34
15	0.38	0.0	0.0	1.0	10.03	1.92
16	0.83	0.0	0.43	0.57	11.75	0.7
17	0.99	0.02	0.5	0.47	10.31	1.53
19	1.27	0.3	0.64	0.06	5.79	1.51
FLIGHT 13						
5	1.08	0.55	0.33	0.12	4.26	0.76
6	1.01	0.2	0.66	0.15	4.9	1.21
7	0.95	0.08	0.7	0.21	5.21	0.87
8	0.88	0.07	0.36	0.57	4.93	0.75
9	0.58	0.0	0.26	0.74	6.5	0.66
10	0.26	0.0	0.0	1.0	6.5	0.76
17	0.94	0.0	0.78	0.22	5.87	0.75
18	0.89	0.0	0.5	0.5	6.55	0.44
19	0.66	0.0	0.11	0.89	6.77	0.11
20	0.32	0.0	0.0	1.0	7.05	0.17
FLIGHT 16						
6	1.01	0.07	0.71	0.21	6.20	0.96
7	0.93	0.0	0.66	0.34	7.79	0.93
8	0.83	0.0	0.53	0.47	8.21	0.49
9	0.62	0.0	0.3	0.7	8.27	0.41
10	0.41	0.0	0.11	0.89	8.33	0.24
11	0.21	0.0	0.0	1.0	8.24	0.64

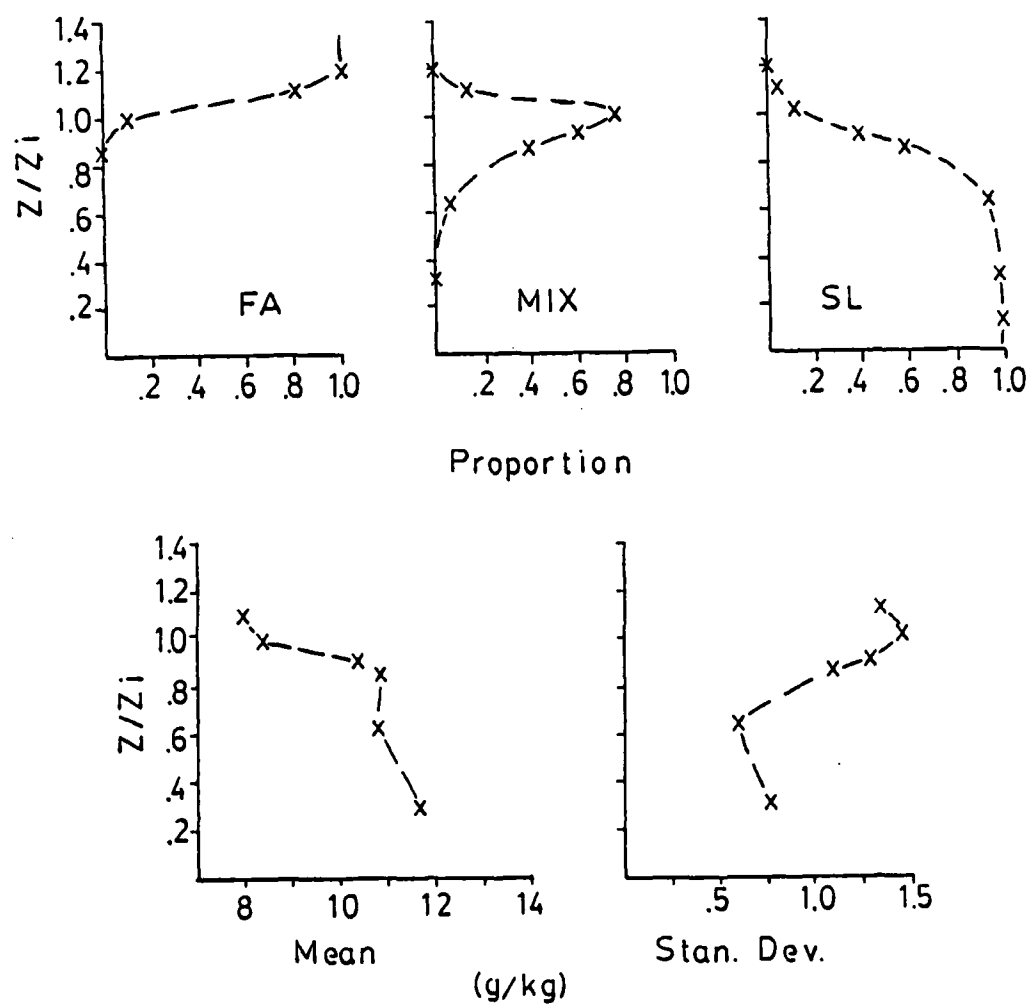


Figure 5.15 Vertical profiles of parameter estimates from the mixture approach, see text for details. The heights have been normalized by the mean CBL height ( $Z_i$ ). For Flight 3 Legs 4-11, 28 May 83.

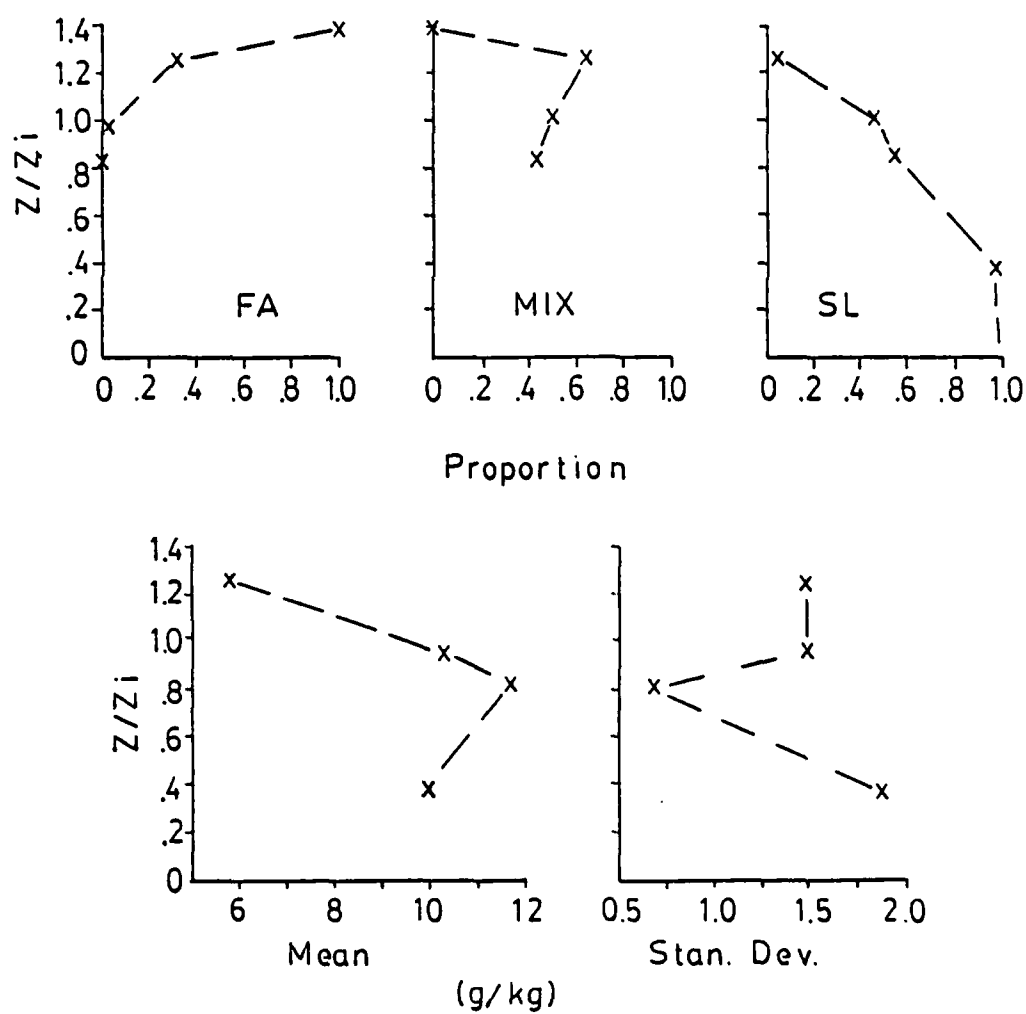


Figure 5.16 Same as Figure 5.15 except for legs 15-20.

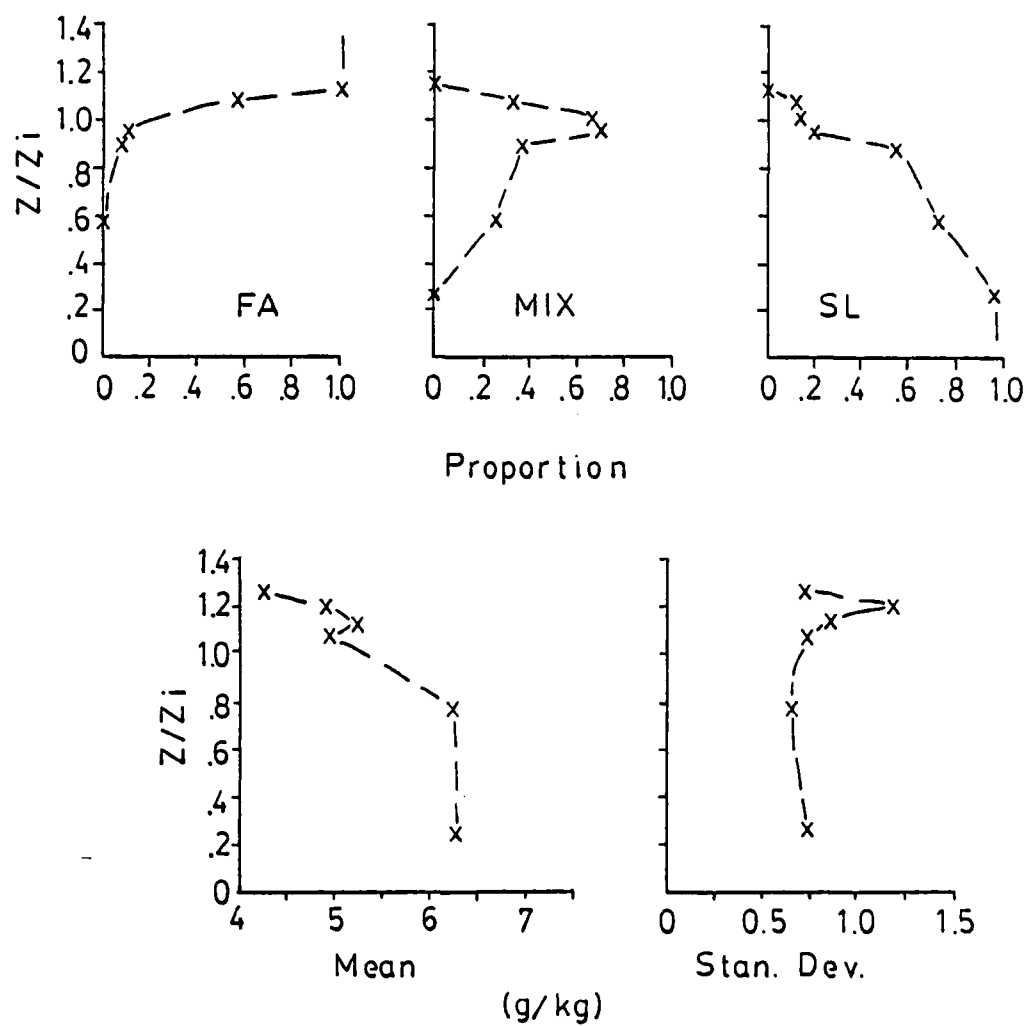


Figure 5.17 Same as Figure 5.15 except for Flight 13 Legs 4-10, 14 Jun 83.



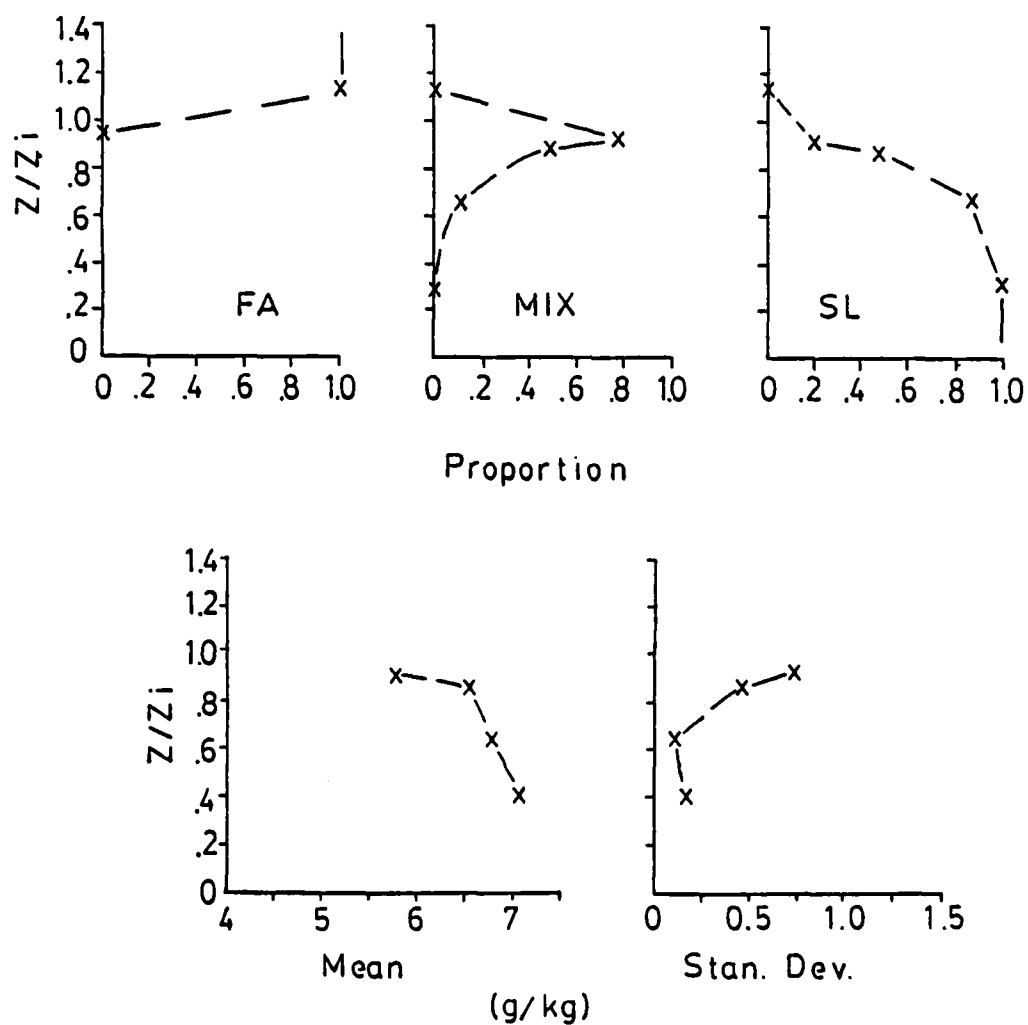


Figure 5.18 Same as Figure 5.15 except for Flight 13 Legs 17-20, 14 Jun 83.

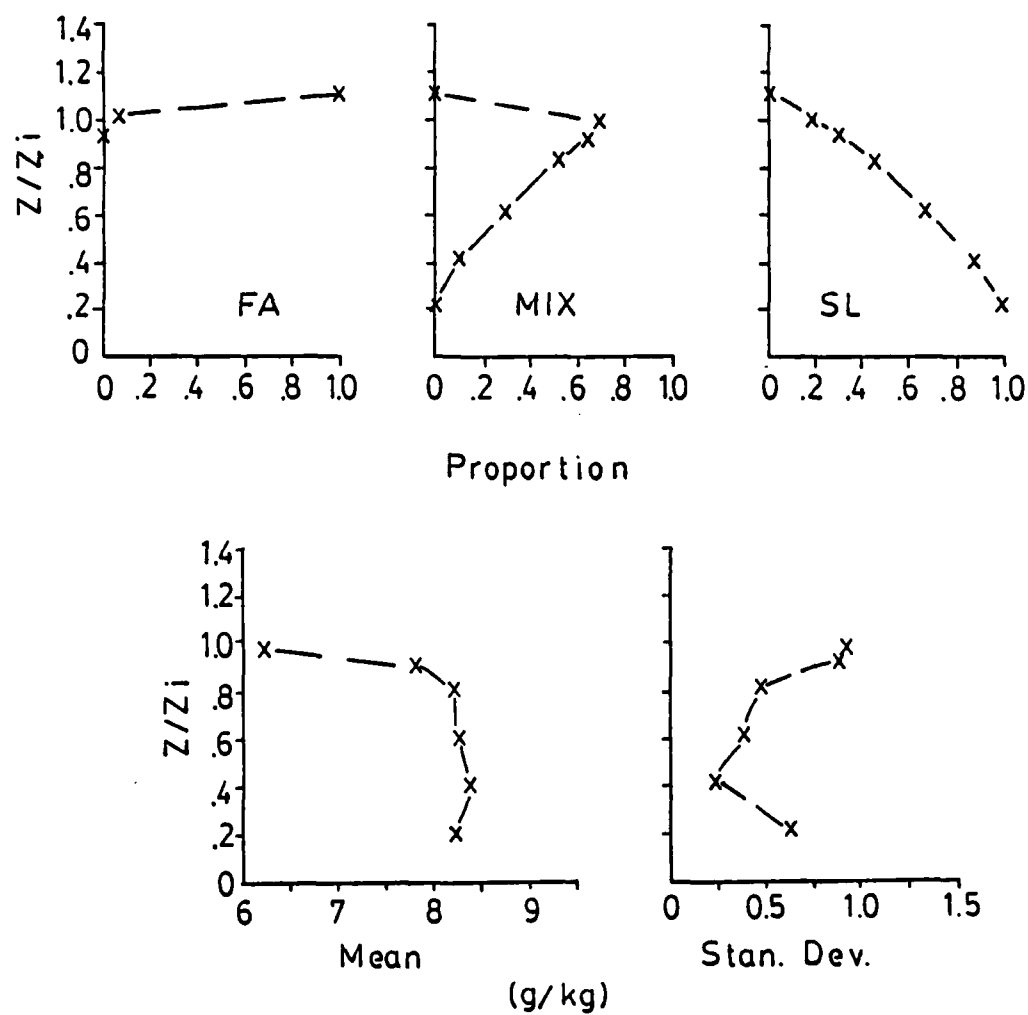


Figure 5.19 Same as Figure 5.15 except for Flight 16 Legs 5-12, 16 Jun 83.

there are plunges of FA air just beginning to mix, SL air in active thermals and in neutrally buoyant thermals, and mixture air from earlier mixings which all have a long period of time to interact. This sets up a large range of mixed air humidities and largest standard deviation (  $\sigma$  ) near Zi.

A check on the goodness of the hypothesis that the entrainment zone air consists of three populations with the specified frequency distributions is to compare the observed and modeled/fitted frequency distributions of specific humidity. Figures 5.20-5.24 show this comparison. In virtually all cases, the modeled distribution captures the major features seen in the observed distribution. The largest departures tend to occur near the top of the entrainment zone where the peak of the FA air frequency is not always captured. Specifically, this method failed for Flight 3, Leg 19. In this instance (Figure 5.21) the Queen Air encountered mostly FA air as evidenced by the large spike near 4.9 g/kg and some unmixed SL air near 12.6 g/kg. But in this case there were also about an equal number of specific humidities encountered between these two extremes. The mixture air tends to look lognormal with a long tail to the right in this case.

A further check on the goodness of the modeled fit to the frequency distributions was made. If the Mixture Approach modeled frequency distributions are representative, then using these

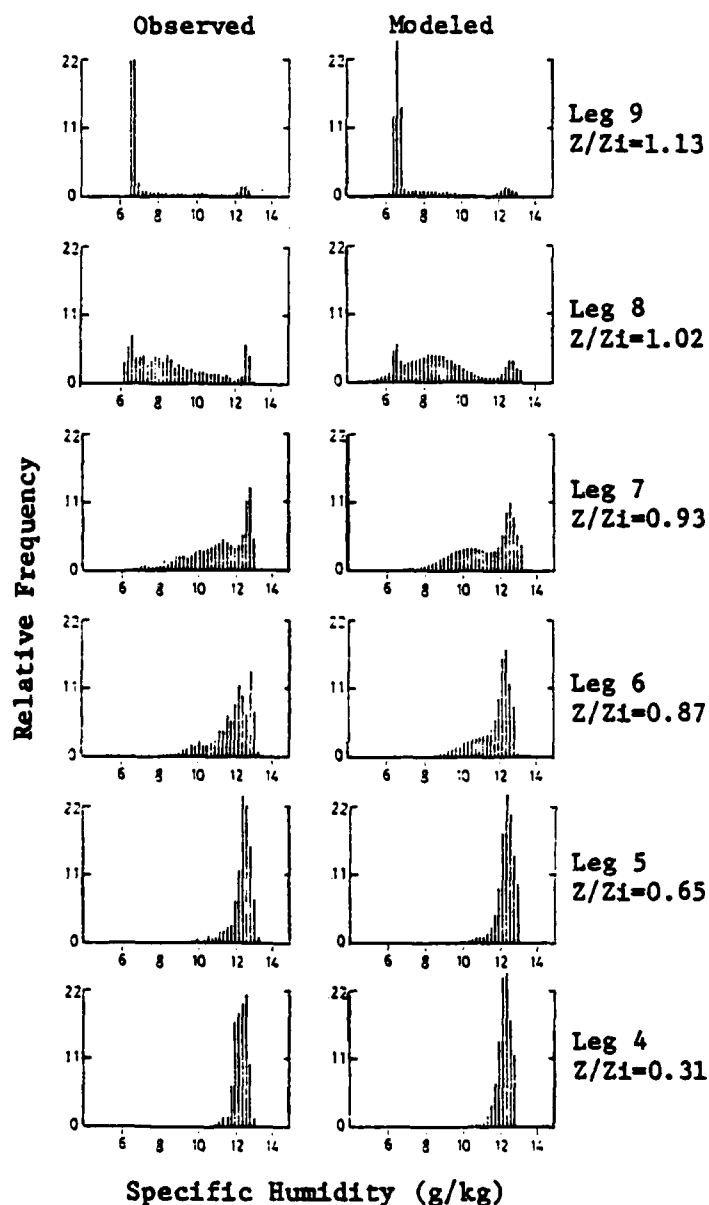


Figure 5.20 Side-by-side comparison of observed (left column) versus modeled (right column) frequency distributions of specific humidity for legs 4-9 of Flight 3, 28 May 83. The Y axis is relative frequency of occurrence and the X axis is specific humidity (both held constant on this figure). The theoretical distribution is composed of the sum of asymmetrical double exponential functions for FA and SL air while the assumed distribution of the mixed air is Gaussian. See text for details on parameter estimation.

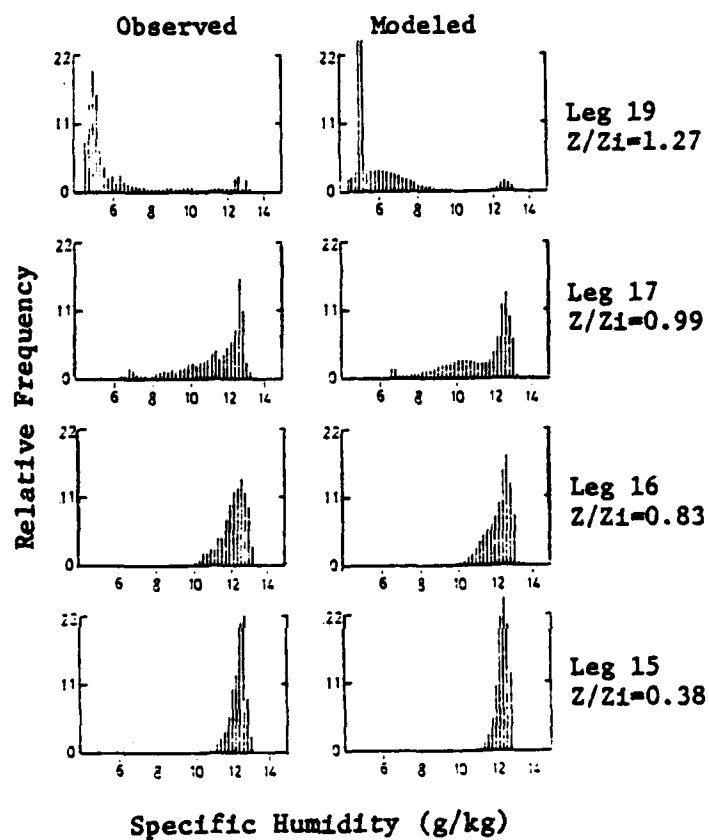


Figure 5.21 Same as Figure 5.20 except for Flight 3 Legs 15-19, 28 May 83.

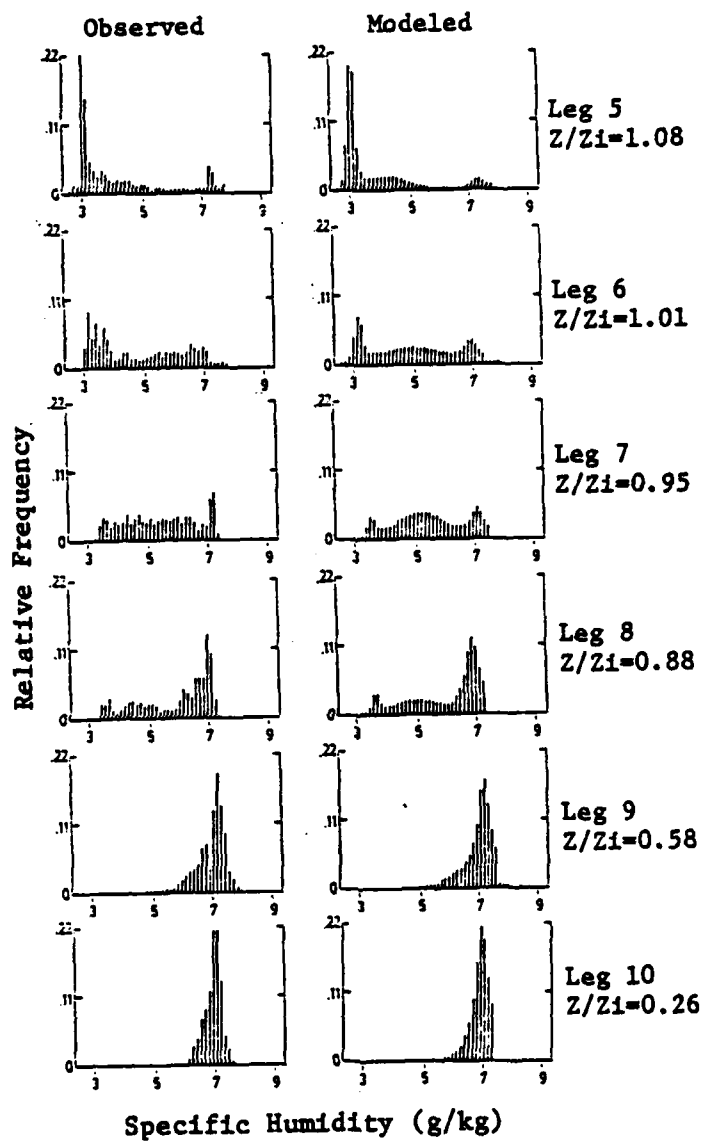


Figure 5.22 Same as Figure 5.20 except for Flight 13 Legs 5-10, 14 Jun 83.

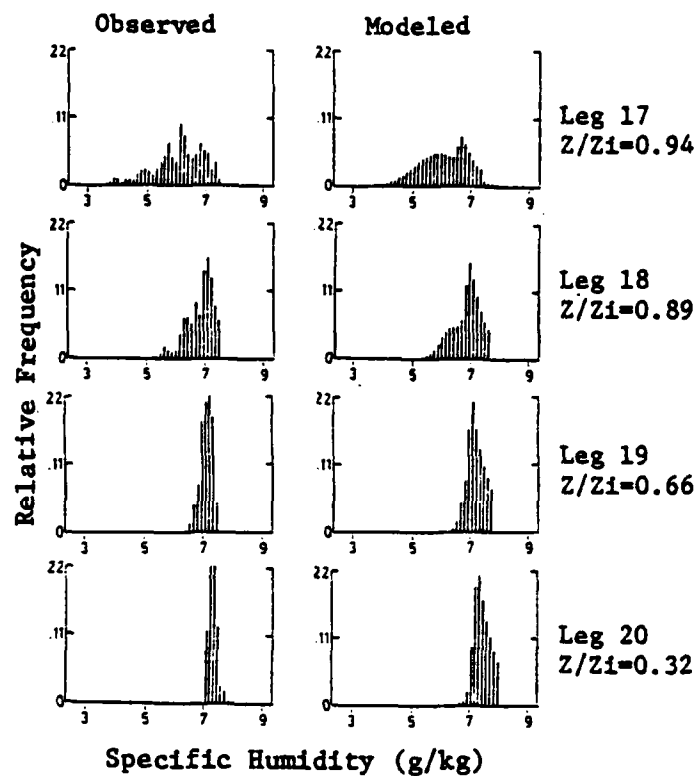


Figure 5.23 Same as Figure 5.20 except for Flight 13 Legs 17-20, 14 Jun 83.

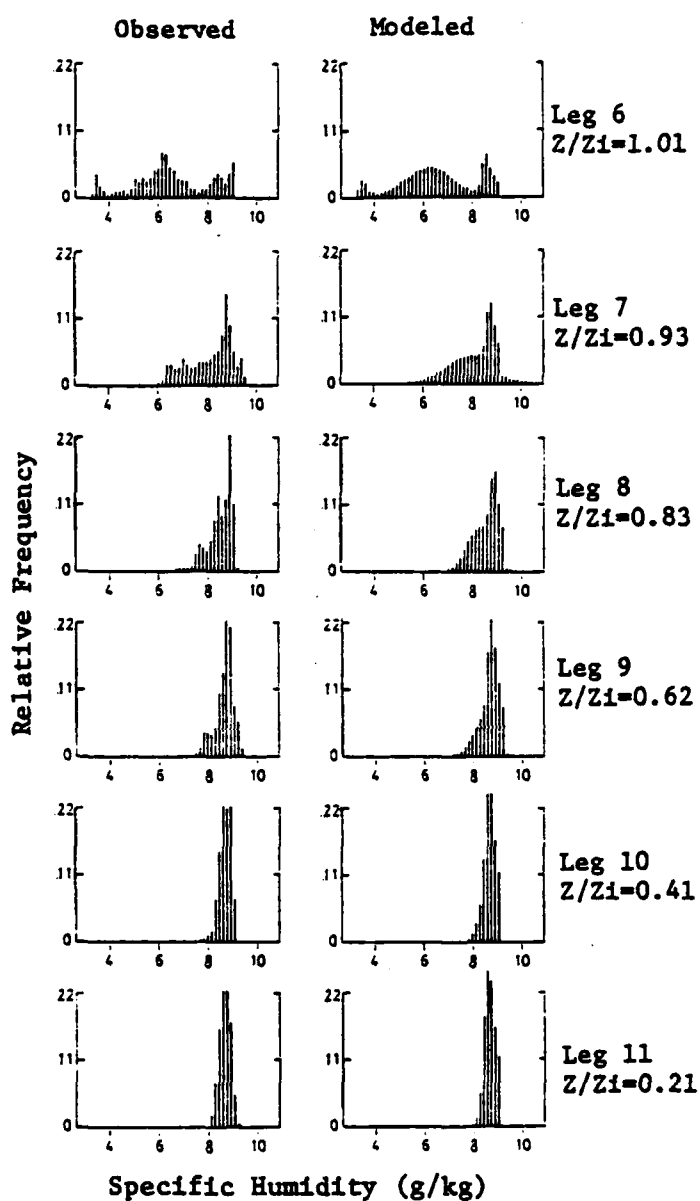


Figure 5.24 Same as Figure 5.20 except for Flight 16 Legs 6-11, 16 Jun 83.



distributions as input to the Linear Mixing Approach should yield vertical profiles of the proportion of SL air similar to those obtained with the original data. Using the approximation that all observations in a frequency interval have the specific humidity of the midpoint, the resultant proportions for all legs (except Flight 3 Leg 19) were within 2% of the value obtained with the original data--excellent agreement. Figure 5.25 shows an example comparison of the profile of SL proportions based on the original data and based on the modeled data. This check also shows how the Mixture Approach provides more information than the Linear Mixing Approach-- the results of the Linear Mixing Approach can be obtained from the Mixture Approach but not vice versa.

The Mixture Approach provides the vertical profile of the proportions of the three types of air and parameters of the Gaussian distribution. Knowledge of these values allow construction of the hypothesized specific humidity frequency distribution for any height--not just the levels where observations were made. An analytical expression was sought to describe the curves of Figures 5.15-5.19 as a function of CBL scaling parameters; but, unfortunately the limited sample size precluded any smooth fits. Future field experiments can hopefully overcome this shortfall.

Knowledge of the frequency distribution of specific

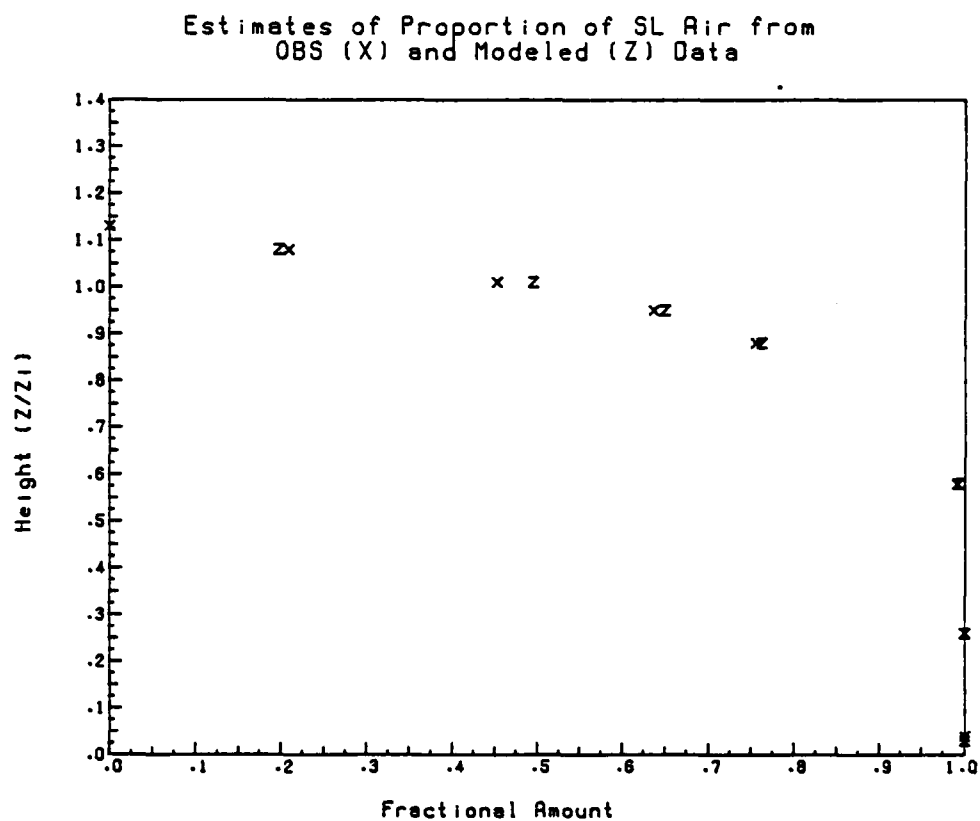


Figure 5.25 Comparison of estimated proportion of surface layer air from observed data (X) and from modeled distributions (Z). This data is from Flight 13 Legs 1-11. The observed data results are the same as those plotted in Figure 5.12.

humidity/pressure of the lifting condensation level as provided by the Mixture Approach coupled with forecasts of  $Z_i$  can lead to more accurate cumulus forecasts. Cumulus can form when air is lifted above its lifting condensation level. As we have seen in the lidar imagery of Figure 4.10 and the above frequency distributions of specific humidity, there is variability in the humidity content of thermals and individual parcels of air. Hence, estimates of the frequency distribution of specific humidity/pressure of lifting condensation level coupled with forecasts of the depth of the CBL reduces the cumulus onset and coverage forecast problem to determining the frequency of occurrence of specific humidity/pressure of the lifting condensation level from the frequency distribution.

## Chapter 6

### Summary and Recommendations

This study addressed three specific goals: (1) Develop conditional sampling criteria to measure the amount of surface layer air existing in the entrainment zone; (2) Determine the amount of surface layer air existing at various levels in the entrainment zone; and (3) Parameterize the distribution of surface layer quantities (i.e. specific humidity) as a function of height through the entire depth of the CBL. Accomplishment of these goals required the synthesis of BLX83 data from two primary observational systems: the NCAR Queen Air and the UW lidar system. Each was used separately and jointly to carry out this observational study of the atmosphere's entrainment zone.

In this study a method was developed to post-calibrate a Lyman alpha hygrometer carried on an instrumented aircraft after the data has been collected. A linear relationship was found between the horizontal leg-averages of chilled-mirror dewpoint humidities and the leg-average Lyman alpha voltages. The resultant conversion of Lyman alpha voltages to humidity was tested against two references. First, the turbulent measurements were confirmed by comparison of Lyman alpha derived humidities based fluxes with concurrent instrumented tower flux values and spectra

analysis of the Lyman alpha time series. Second, comparison of computed lifting condensation levels based on the Lyman alpha with concurrent lidar imagery of individual thermals' cloud base verified the absolute measure of humidity.

The combining of concurrent lidar and instrumented aircraft data provided a unique opportunity to study conditional sampling criteria and the structure of thermals in the CBL. These studies confirmed the need for fast-response turbulence sensors to conduct studies in the entrainment zone. Specific humidity was found to be the best indicator of in-thermal conditions above the surface layer, and each sample point was shown to represent real atmospheric conditions. With the confidence that the humidities measured were accurate, and having had the opportunity to see the corresponding data on lidar imagery, a statistical approach to diagnosing the entrainment zone structure was taken.

Time series plots and histograms of specific humidity collected during horizontal flight legs showed near-surface values of specific humidity in thermals extending to the top of the CBL. Using the linear mixing character of specific humidity as one approach, the profile of the proportion of surface layer air existing in the entrainment zone was found. This profile was well fit by the cumulative distribution function of asymmetrical double exponential functions though the parameters of the functions do not appear to be functions of the CBL parameters. A similar profile

was reported for earlier laboratory tank experiments. To account for the thermal-to-thermal variability of humidity as seen in the concurrent lidar and aircraft data and to provide more detail of the structure of the entrainment zone, a second statistical approach was taken.

The second approach was the result of examining the vertical profiles of histograms of specific humidity collected during horizontal flight legs flown after the greatest rate of growth of the CBL. This examination led to the conclusion that air in the entrainment zone is composed of three types: unmodified free atmosphere air, unmodified surface layer air, and a combination of these two (mixed air). It was hypothesized that the specific humidity frequency distribution of the mixed air would have a Gaussian distribution and that the frequency distribution of the unmixed FA and SL air could be fit by asymmetrical double exponential functions. The application of maximum likelihood estimators to the frequency distribution of specific humidity led to vertical profiles of the amount of each of the three types of air present. These profiles, which expand on the ones found via the Linear Mixing approach, show that for these cases unmixed free atmosphere air rarely penetrates far below the mean CBL depth and that the proportion of mixed air has a maximum near the mean CBL depth. The mean humidity of the mixed air increases with decreasing height.

Recommendations resulting from this study address three major areas: (1) future field experiments; (2) additional analysis; and (3) implementation of the observations resulting from this study.

Additional entrainment zone field experiments utilizing the same basic instrumentation and operations plan used in BLX83 should be carried out. These experiments would expand our knowledge of the entrainment zone structure by sampling under different stabilities and conditions which could lead to a better parameterization in terms of analytical functions of the amount of surface layer air existing in the entrainment zone as a function of height. Studies in both forced and free convection cases are suggested in order to be able to improve knowledge of the entrainment zone structure in both regimes. Also, further efforts should be made to parameterize the vertical profiles of the proportion of SL air and the three types of air present in the entrainment zone as a function of typical CBL parameters. Such a parameterization would allow a more useful application of the results found in this study.

Future experiments should incorporate a pre- and post-flight calibration of the fast response hygrometer carried on the instrumented aircraft. It is recommended that the hygrometer be encapsuled in a controlled calibration chamber with known humidities, allowing the resulting hygrometer values to be recorded for later calibration work. This will enable the

development of calibration curves/lines that do not involve any assumptions on the response characteristics of the reference hygrometer during in-flight conditions. This calibration should be performed in conjunction with each flight in order to account for any changes in the optical windows or electronics of the hygrometer.

Further study of the ability of an instrumented aircraft to estimate the surface fluxes should be carried out. Coincident instrumented-tower fluxes (sensible, latent, and ground storage) under the flight path of the aircraft should be collected for comparison of the fluxes and measurement of the surface energy budget (although point and line flux estimates will not necessarily agree).

The lidar data collected during BLX83 could be a large source of information for additional entrainment zone studies. One of the conclusions of the comparison of concurrent lidar and instrumented aircraft data was the apparent relation between lidar backscattering and humidity in the CBL. If the amount of backscattering can accurately be related to the amount of surface layer air in the entrainment zone, a larger number of cases and daytime evolution of the structure of the entrainment zone can be studied.

Lastly, comparative cumulus model forecasts using previously-used assumptions of the distribution of humidity in the



entrainment zone and the distributions described in this study should be undertaken. These tests would verify the expected improvement in forecasts of onset and coverage of fair weather cumulus. The sensitivity of the models to the shape parameters of the double exponential cumulative distribution function should also be examined.

The purpose of this study was to study the structure of the atmosphere's entrainment zone. The results presented here are one step toward a better understanding of the entrainment zone. The observational results can be used in a numerical model to test the improved forecasts of the onset and coverage of fair weather cumulus that should result from the increased understanding of the distribution of moisture in the entrainment zone.

## Appendix A

## Data Plots for Case Study Days

This appendix contains a data summary for the five days of BLX83 used directly in this study. It is intended to provide the primary data displays used in making the assumptions and directions taken in this study. These days are: 27 May, 28 May, 7 Jun, 14 Jun, and 16 Jun 1983.

For each case-study day, data is presented in the following order:

- 1) GOES visible satellite imagery
- 2) NWS surface analysis
- 3) Plot of soundings from Queen Air 20 Hz sensors--although a linear average of two consecutive data points is what is plotted.
- 4) Plot of entrainment zone heights during the time the Queen Air was airborne

The two soundings displayed in Chapter 4 are not replotted in this appendix. They are: (1) Figure 4.2 and 4.3, the sounding flown between 1420 and 1433 CDT 14 Jun 83; and (2) Figures 4.4

and 4.5, the sounding flown between 1048 and 1057 CDT 27 May 83.

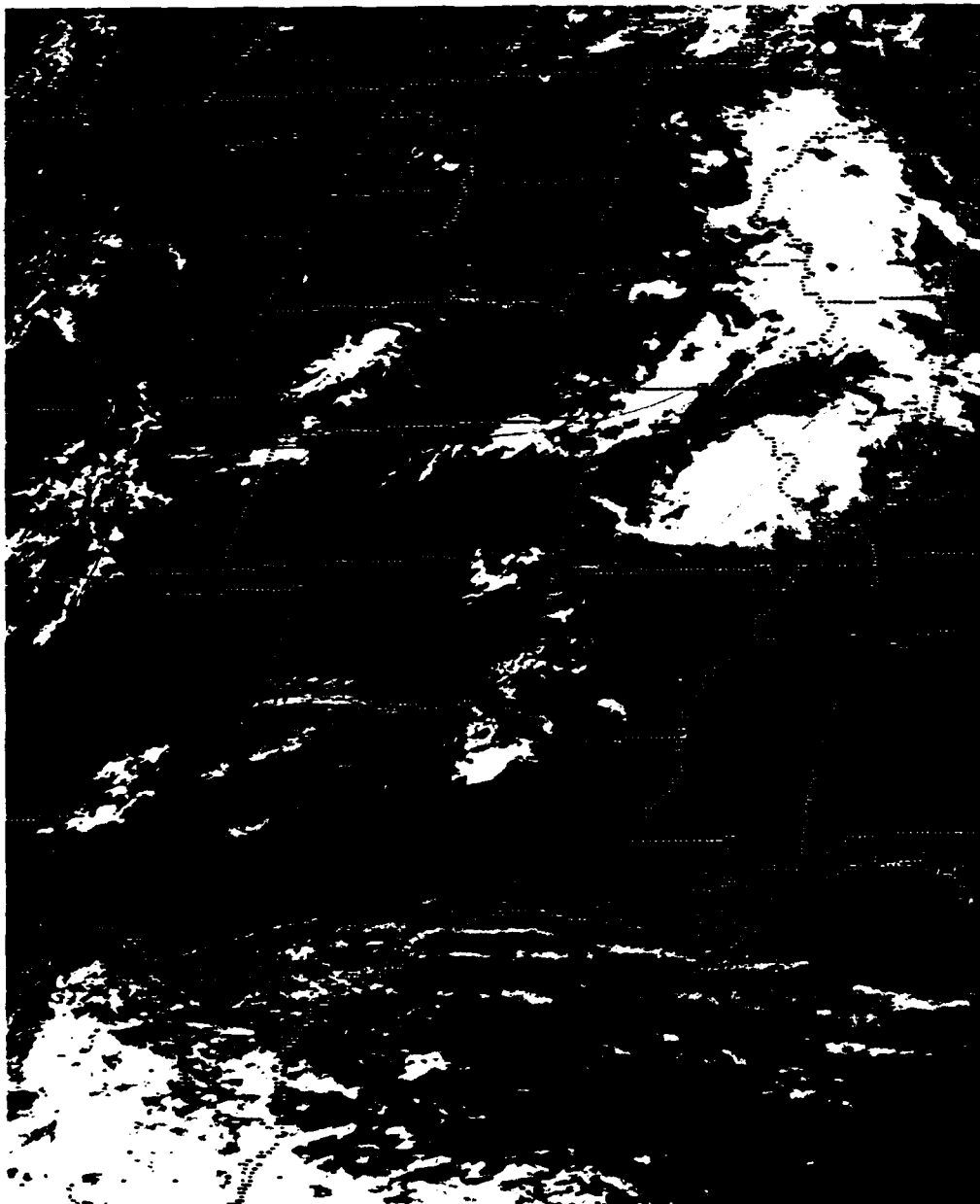


Figure A.1 GOES imagery at 1130 CDT on 27 May 83

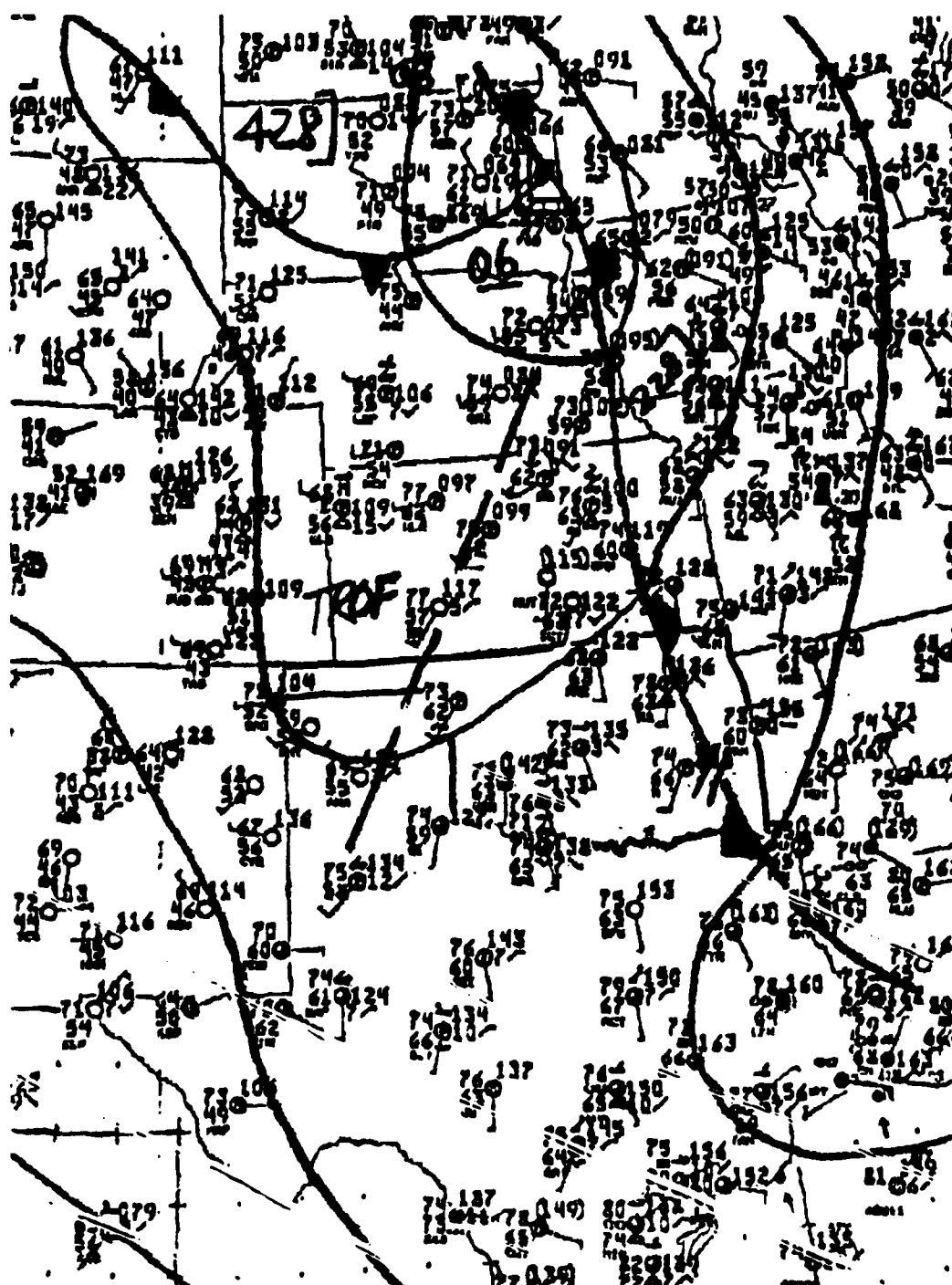


Figure A.2 NWS surface analysis for 1000 CDT on 27 May 83

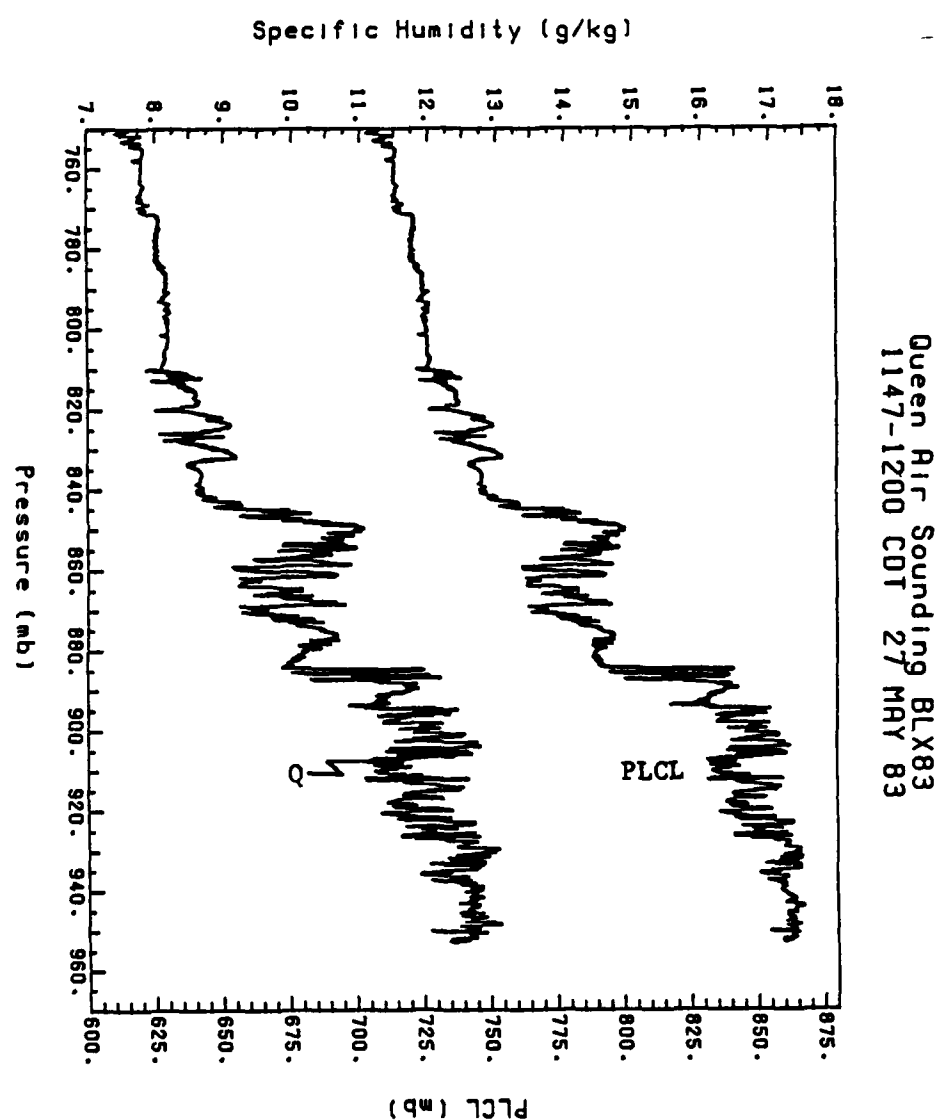


Figure A.3 Plot of specific humidity (Q) and pressure of lifting condensation level (PLCL) obtained by the Queen Air 20 Hz sensors during a sounding between 1147-1200 CDT 27 May 83, Flight 2.

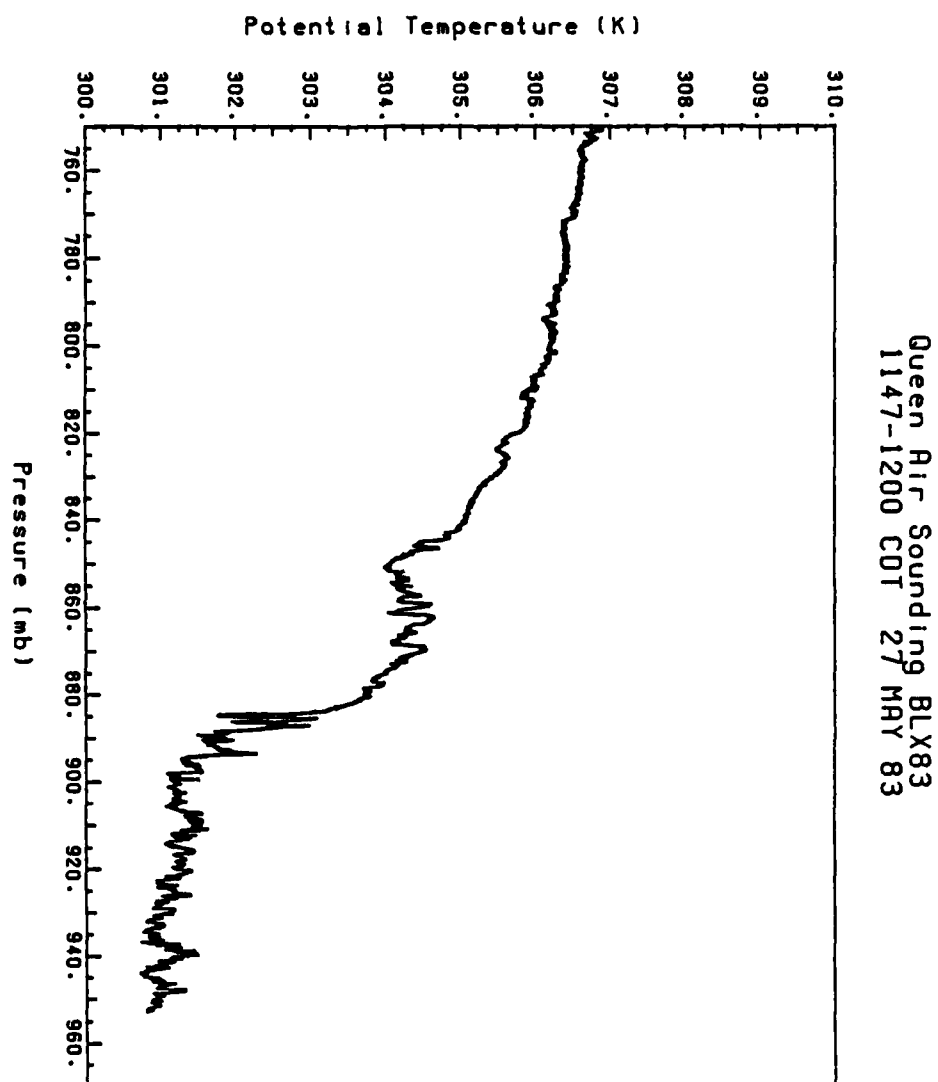


Figure A.4 Plot of potential temperature obtained by the Queen Air 20 Hz sensor during a sounding between 1147-1200 CDT 27 May 83, Flight 2.

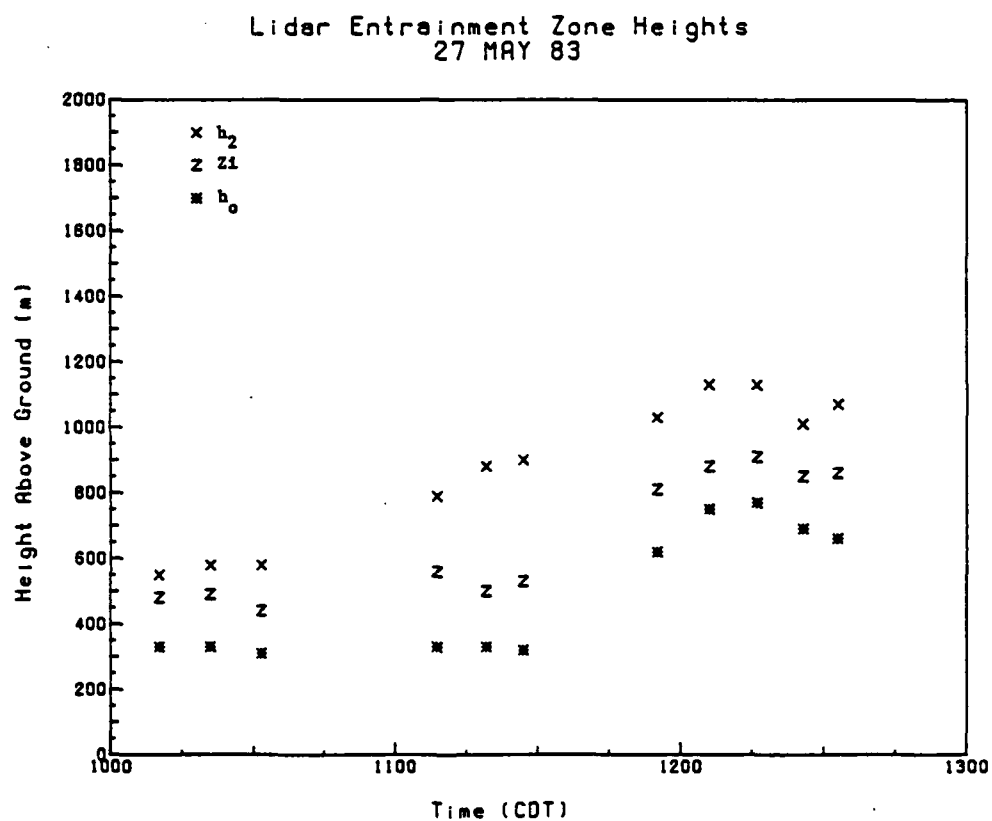


Figure A.5 Time series plot of subjectively-determined estimates, from lidar imagery, of top of CBL ( $h_2$ ), mean depth of CBL ( $Z_i$ ), and bottom of entrainment zone ( $h_0$ ) for times during Flight 2 of the Queen Air, 27 May 83.



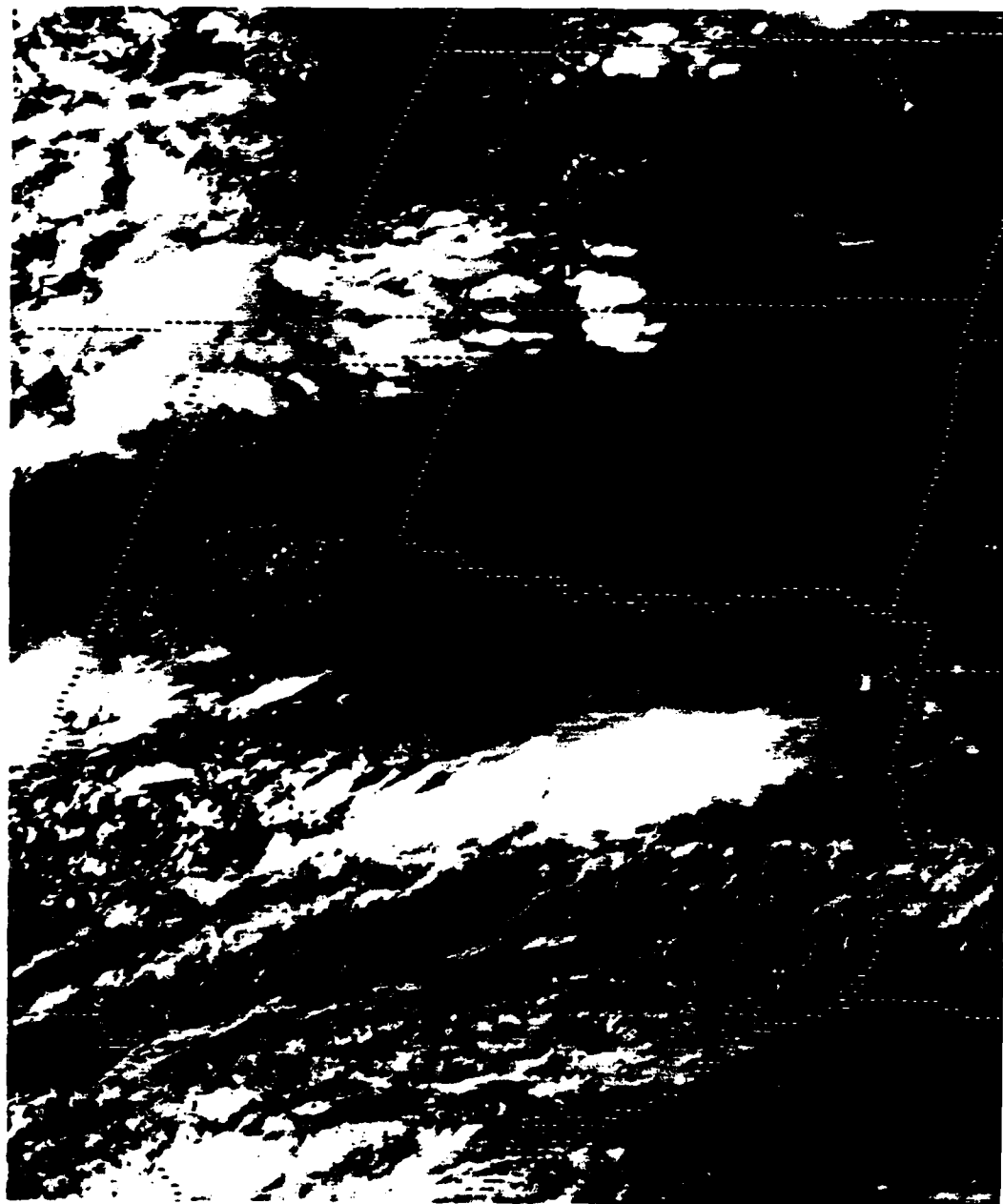


Figure A.6 GOES imagery at 1700 CDT on 28 May 83

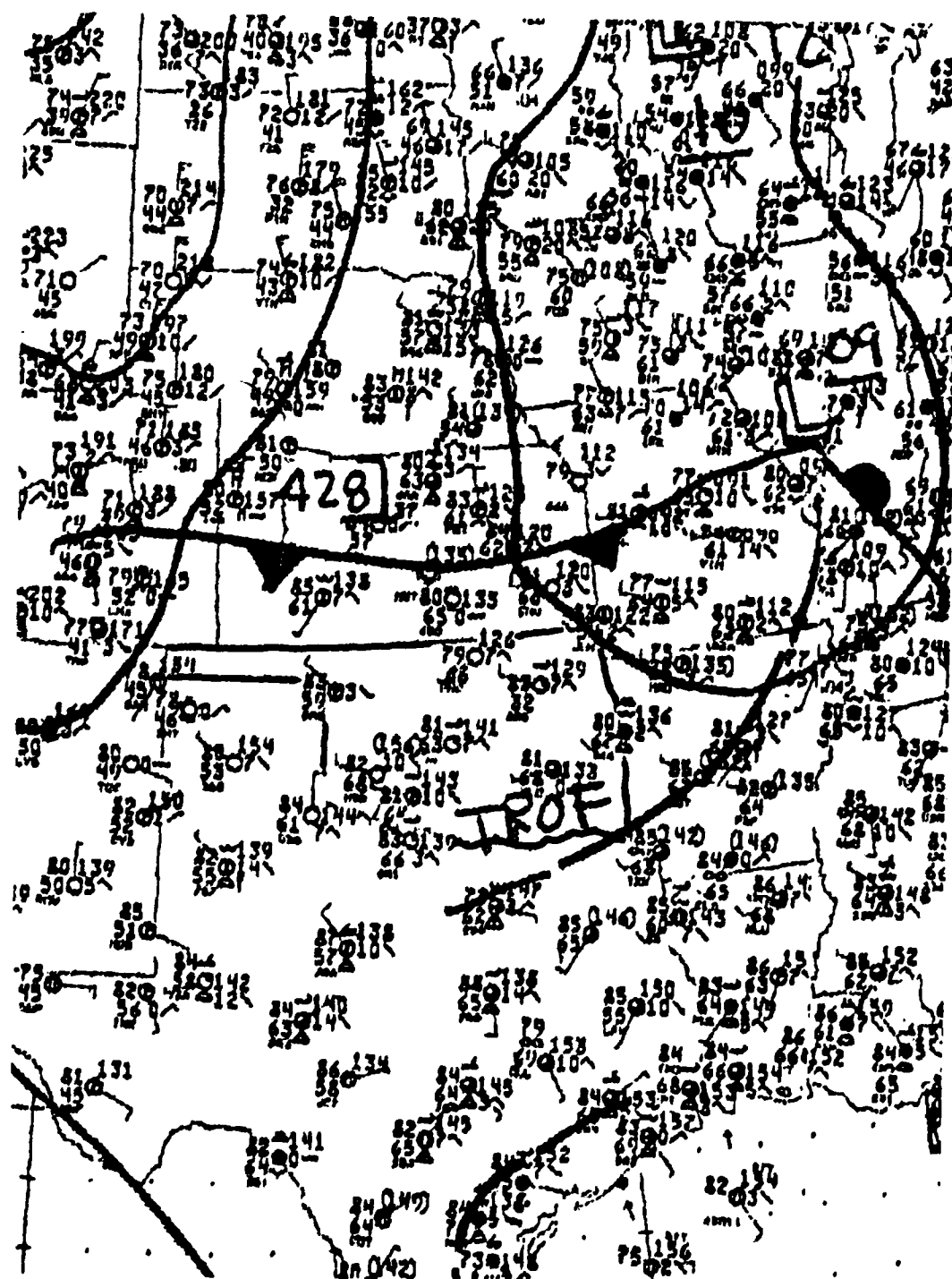
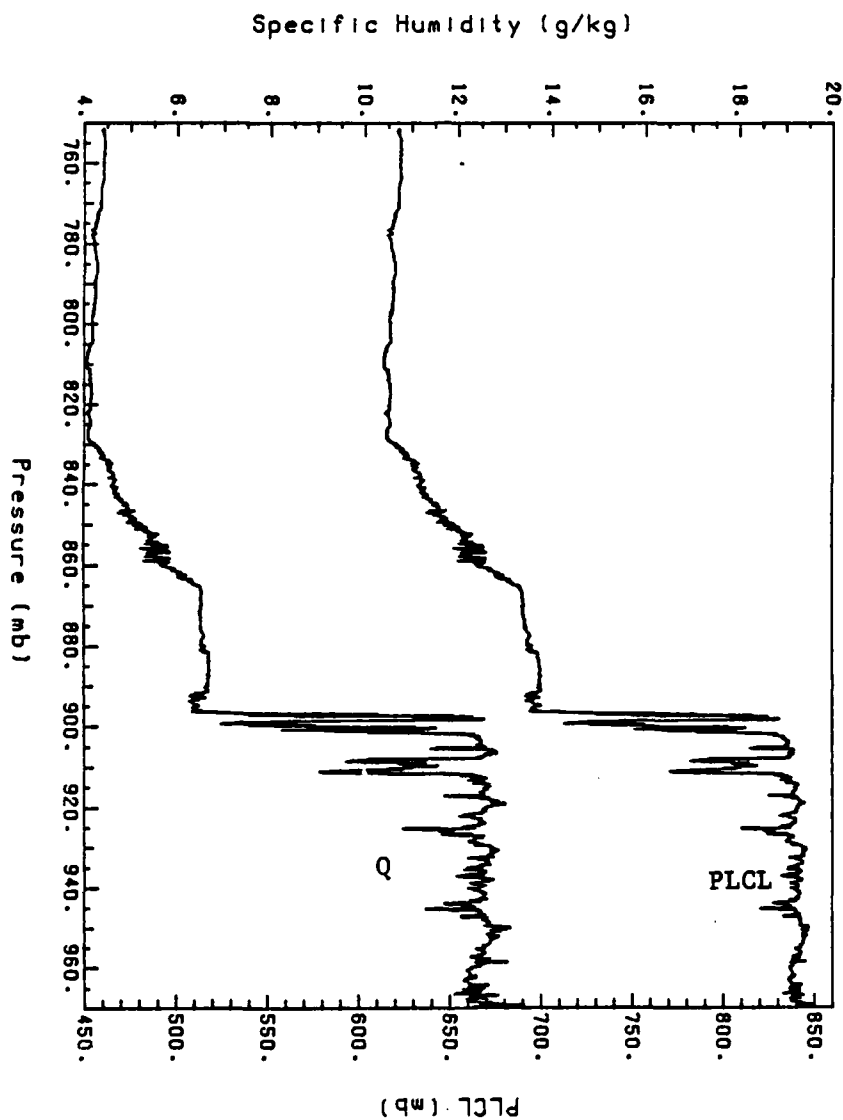


Figure A.7 NWS surface analysis for 1600 CDT on 28 May 83



Queen Air Sounding BLX83  
1438-1450 CDT 28 MAY 83

Figure A.8 Plot of specific humidity (Q) and pressure of lifting condensation level (PLCL) obtained by the Queen Air 20 Hz sensors during a sounding between 1438-1450 CDT 28 May 83, Flight 3.

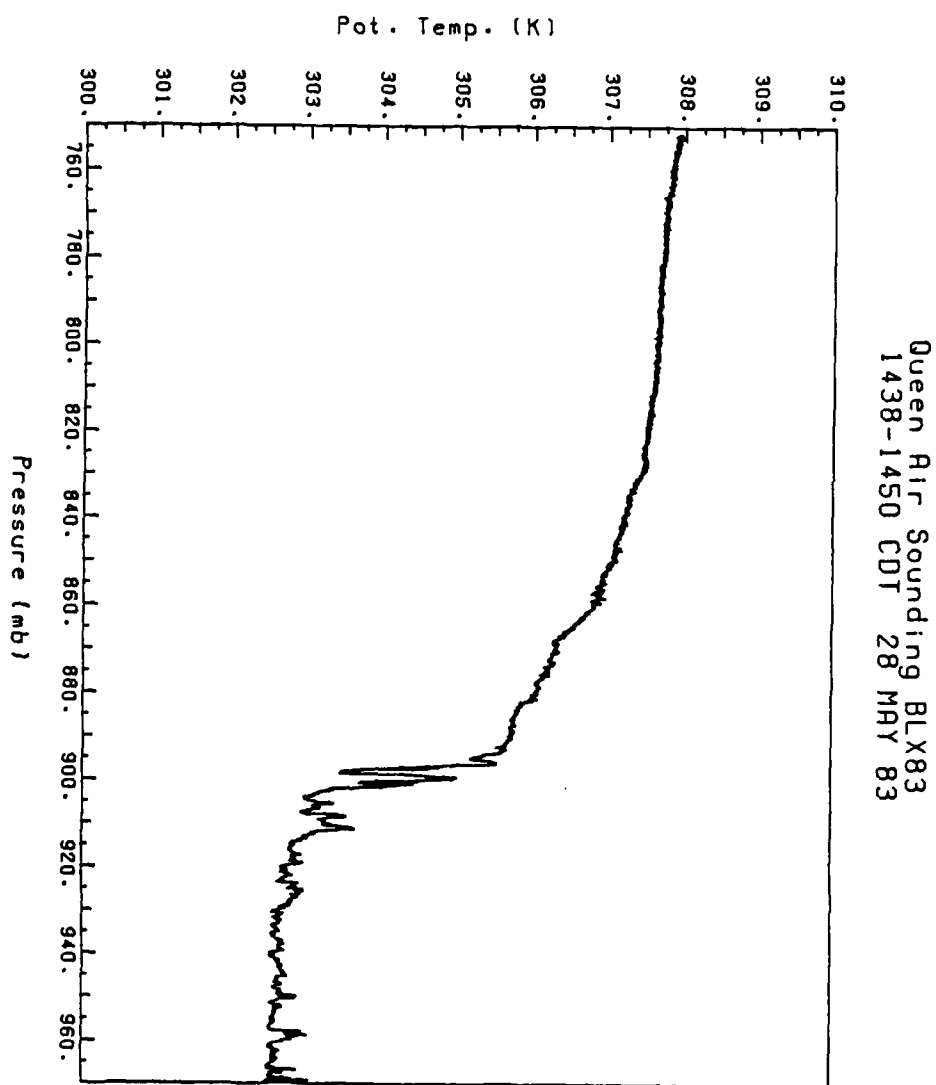


Figure A.9 Plot of potential temperature obtained by the Queen Air 20 Hz sensor during a sounding between 1438-1450 CDT 28 May 83, Flight 3.

AD-A160 911

CASE STUDIES OF THE STRUCTURE OF THE ATMOSPHERIC  
BOUNDARY LAYER ENTRAINMENT ZONE(U) AIR FORCE INST OF  
TECH WRIGHT-PATTERSON AFB OH T D CRUM 1985  
AFIT/CI/NR-85-129D F/G 4/2

3/3

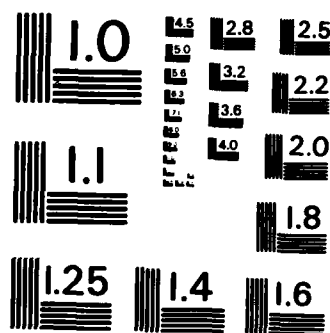
**UNCLASSIFIED**

F/G 4/2

NL

END

FILMED



MICROCOPY RESOLUTION TEST CHART  
NATIONAL BUREAU OF STANDARDS-1963-A

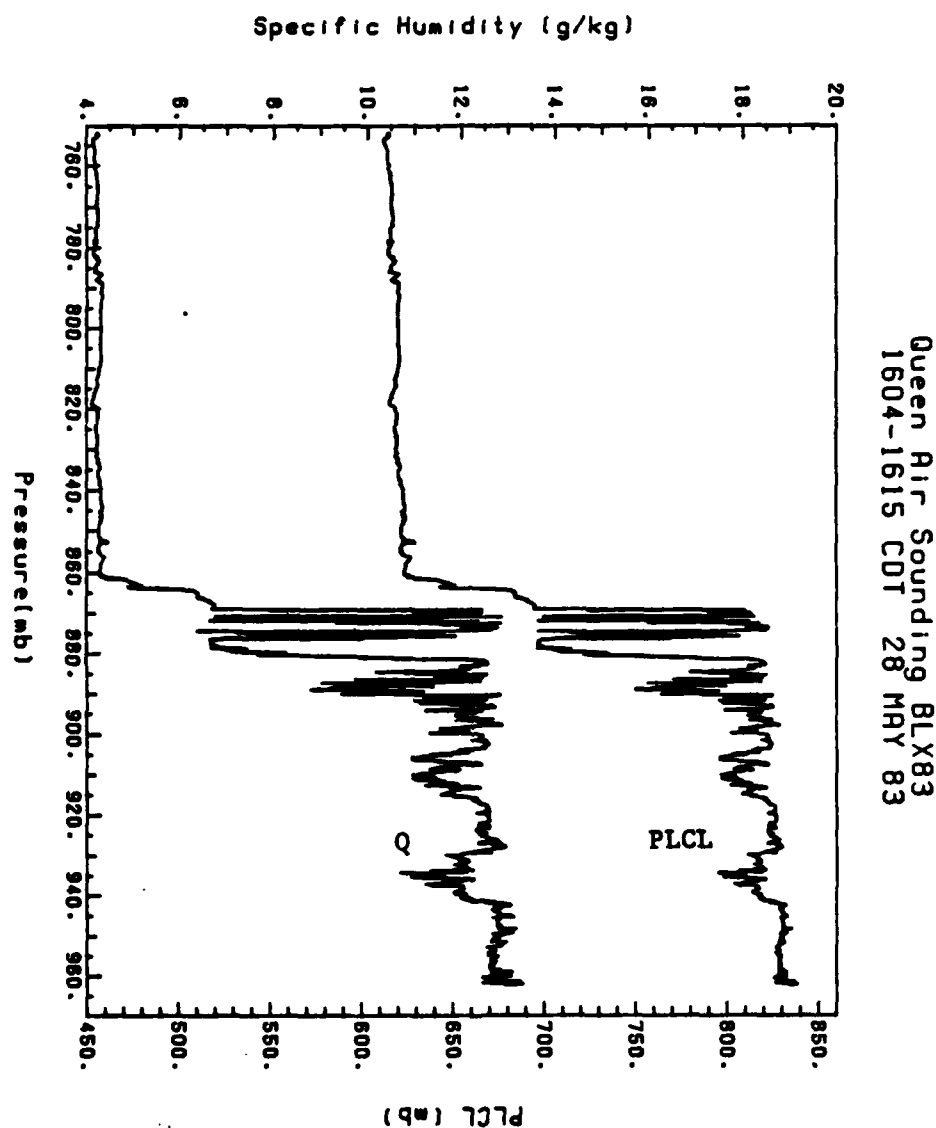


Figure A.10 Plot of specific humidity (Q) and pressure of lifting condensation level (PLCL) obtained by the Queen Air 20 Hz sensors during a sounding between 1604-1615 CDT 28 May 83, Flight 3.

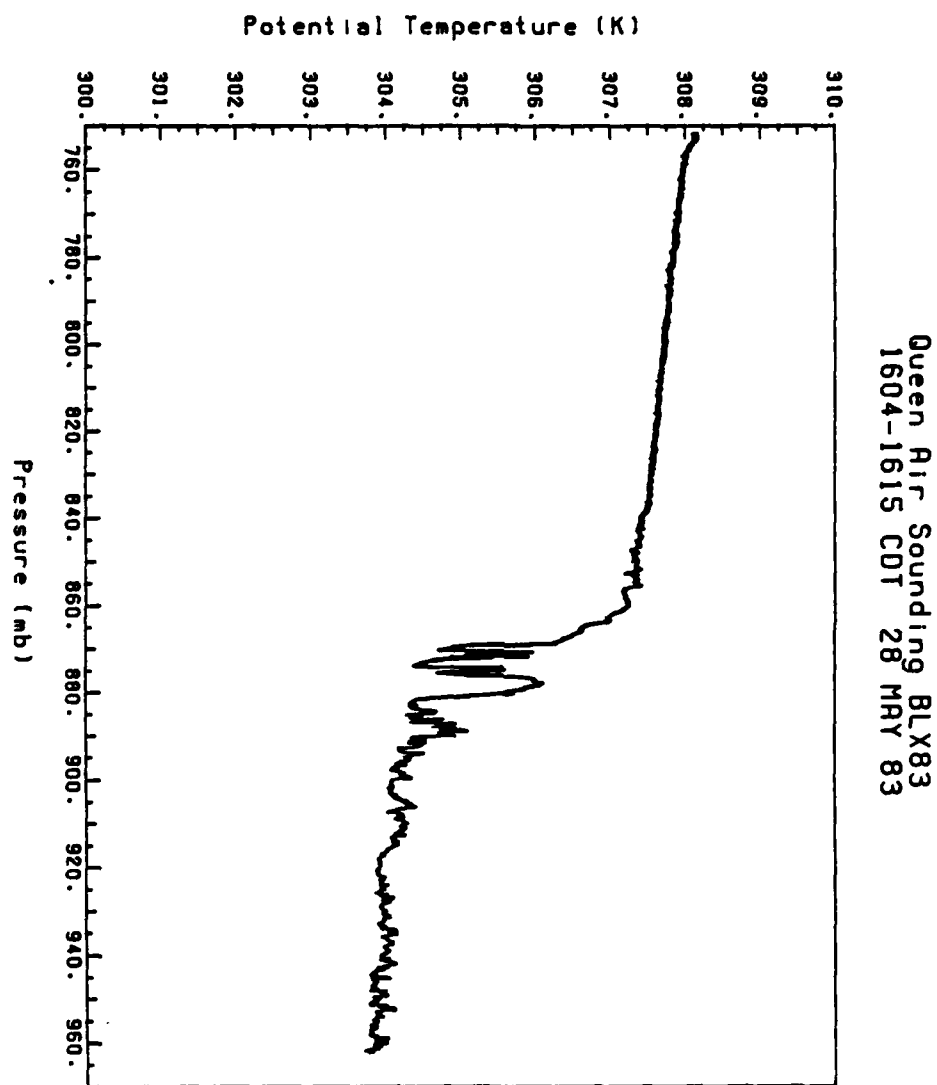


Figure A.11 Plot of potential temperature obtained by the Queen Air 20 Hz sensor during a sounding between 1604-1615 CDT 28 May 83, Flight 3.



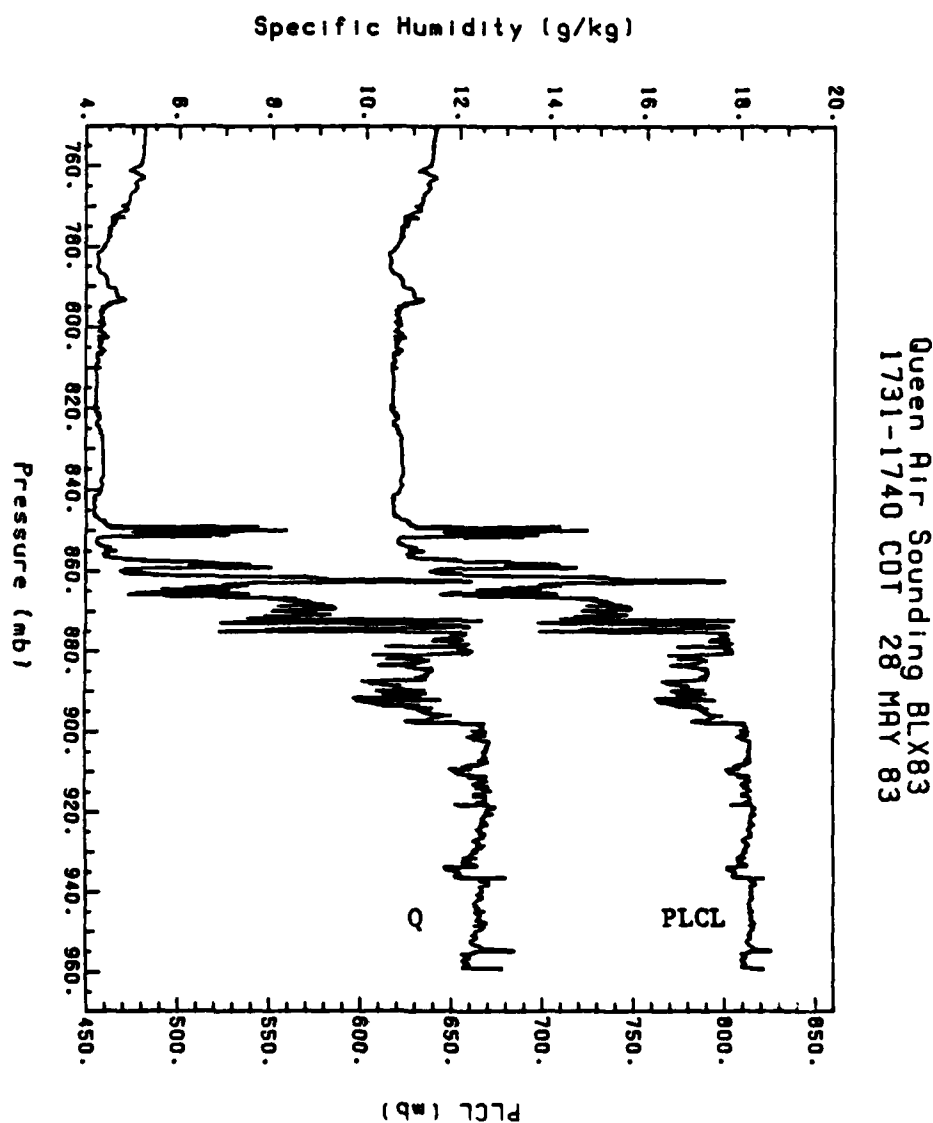


Figure A.12 Plot of specific humidity (Q) and pressure of lifting condensation level (PLCL) obtained by the Queen Air 20 Hz sensors during a sounding between 1731-1740 CDT 28 May 83, Flight 3.

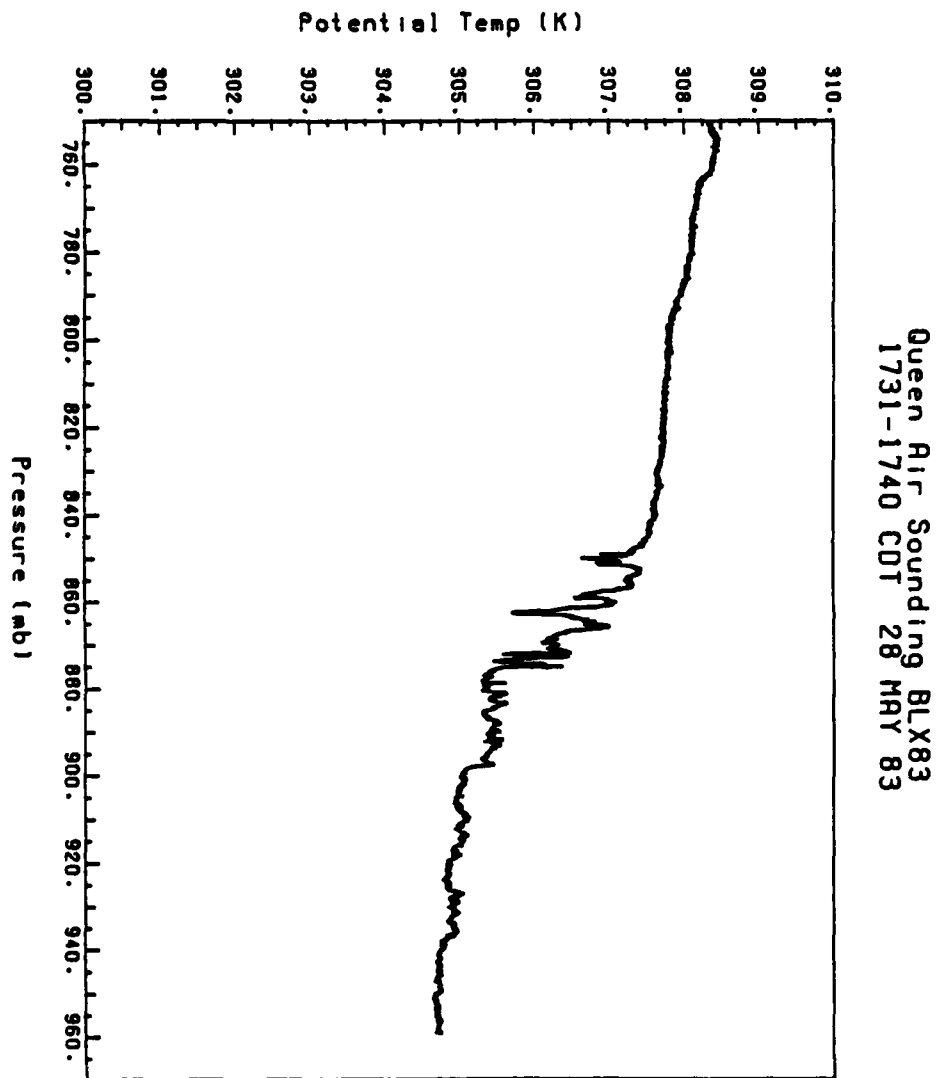


Figure A.13 Plot of potential temperature obtained by the Queen Air 20 Hz sensor during a sounding between 1731-1730 CDT 28 May 83, Flight 3.

Lidar Entrainment Zone Heights  
28 MAY 83

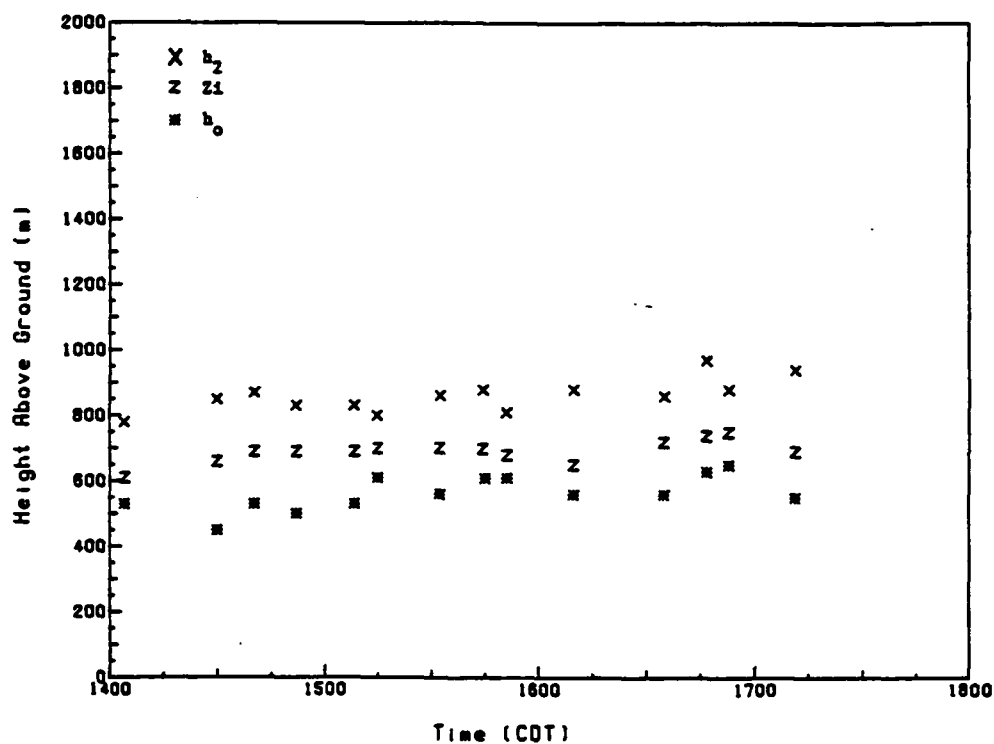


Figure A.14 Time series plot of subjectively-determined estimates, from lidar imagery, of top of CBL ( $h_2$ ), mean depth of CBL ( $Z_i$ ), and bottom of entrainment zone ( $h_0$ ) for times during Flight 3 of the Queen Air, 28 May 83.

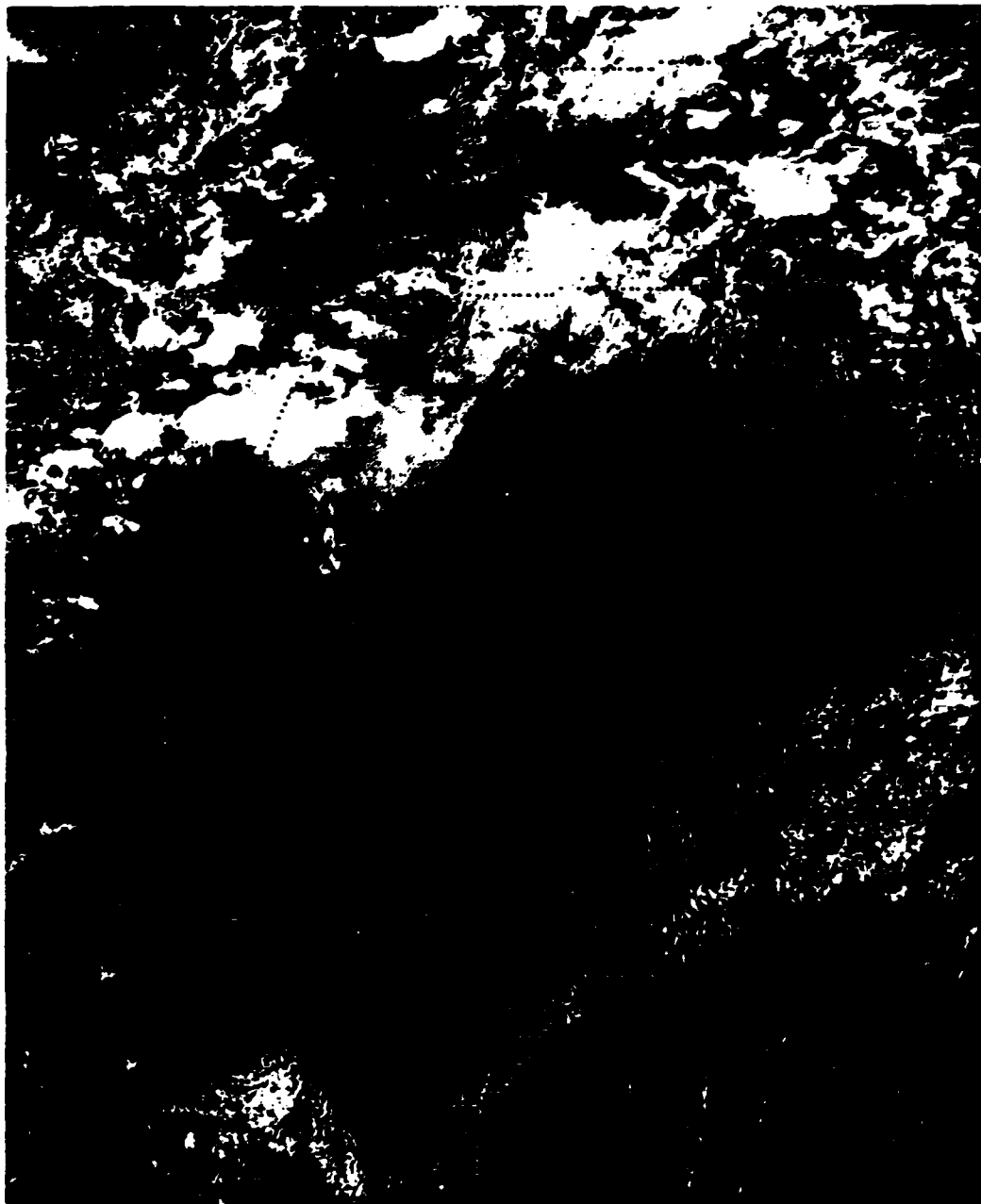


Figure A.15 GOES imagery at 1700 CDT on 7 Jun 83

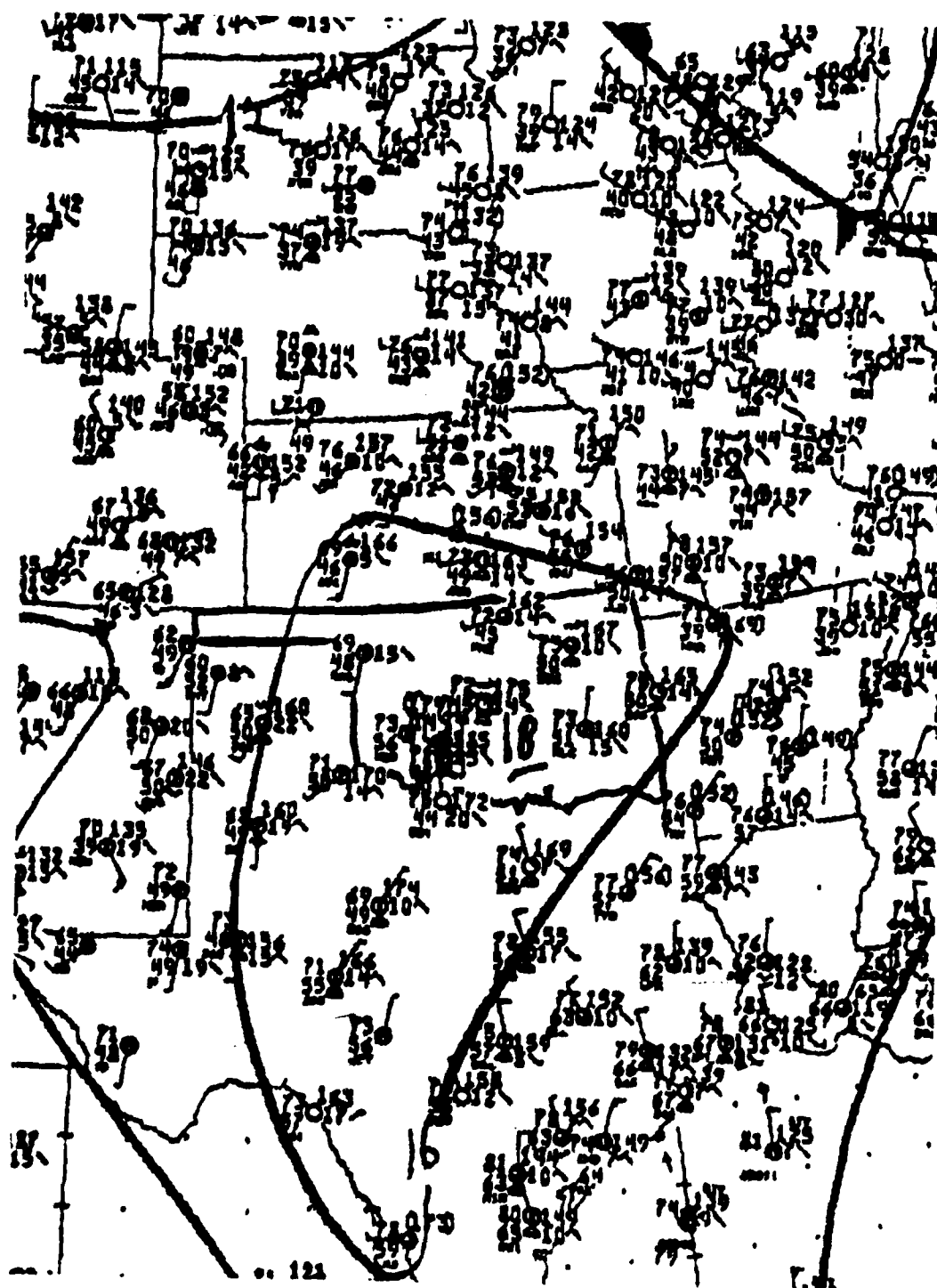


Figure A.16 NWS surface analysis for 1000 CDT on 7 Jun 83

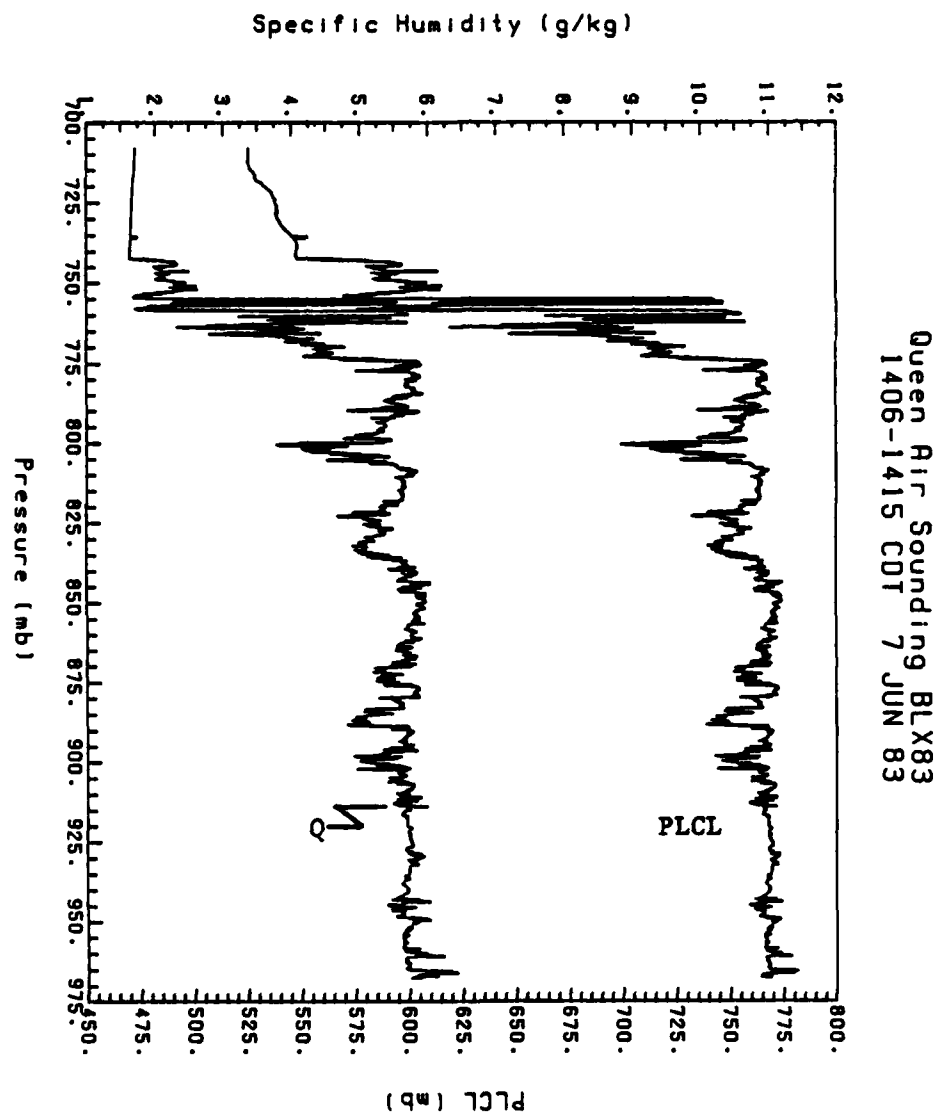


Figure A.17 Plot of specific humidity (Q) and pressure of lifting condensation level (PLCL) obtained by the Queen Air 20 Hz sensors during a sounding between 1406-1415 CDT 7 Jun 83, Flight 6.

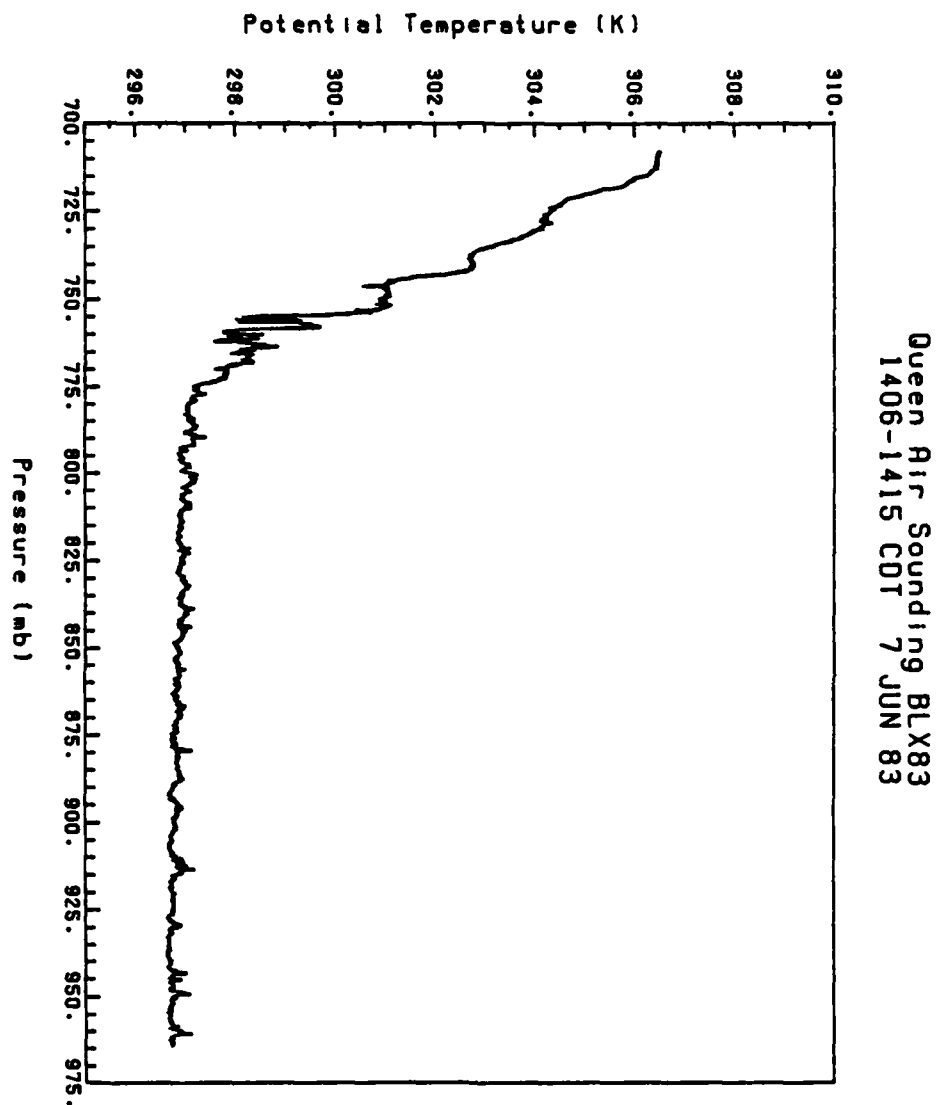


Figure A.18 Plot of potential temperature obtained by the Queen Air 20 Hz sensor during a sounding between 1406-1415 CDT 7 Jun 83, Flight 6.

Lidar Entrainment Zone Heights  
7 JUNE 83

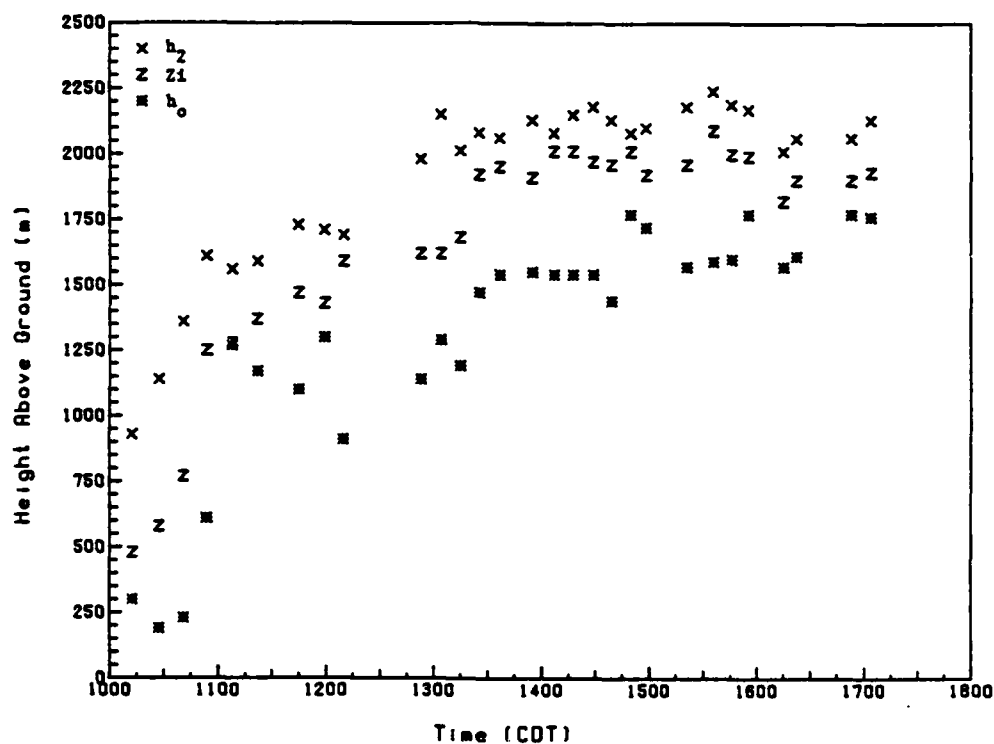


Figure A.19 Time series plot of subjectively-determined estimates, from lidar imagery, of top of CBL ( $h_2$ ), mean depth of CBL ( $Z_i$ ), and bottom of entrainment zone ( $h_0$ ) for times during Flight 6 of the Queen Air, 7 Jun 83.





Figure A.20 GOES imagery at 1630 CDT on 14 Jun 83

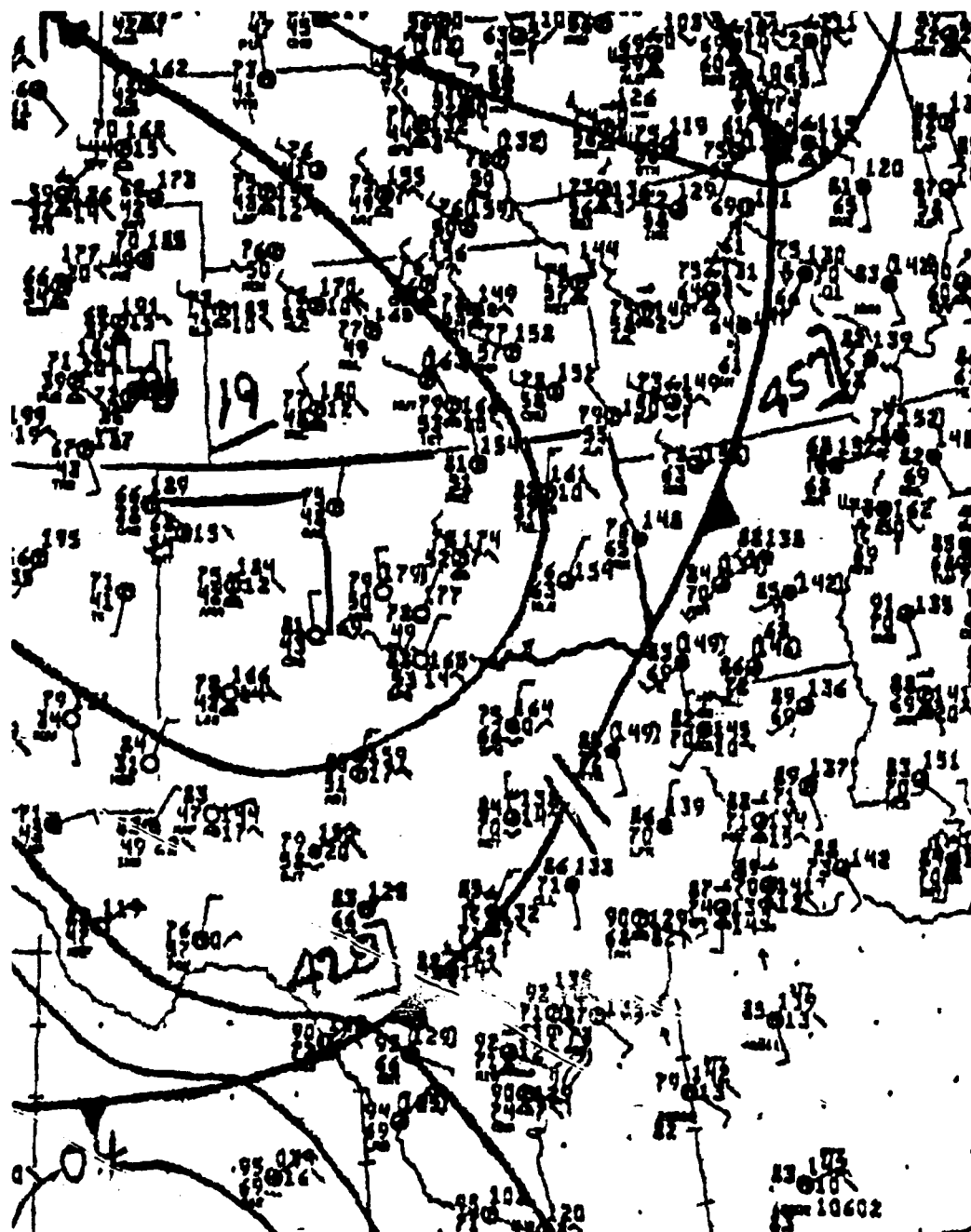


Figure A.21 NWS surface analysis for 1600 CDT on 14 Jun 83

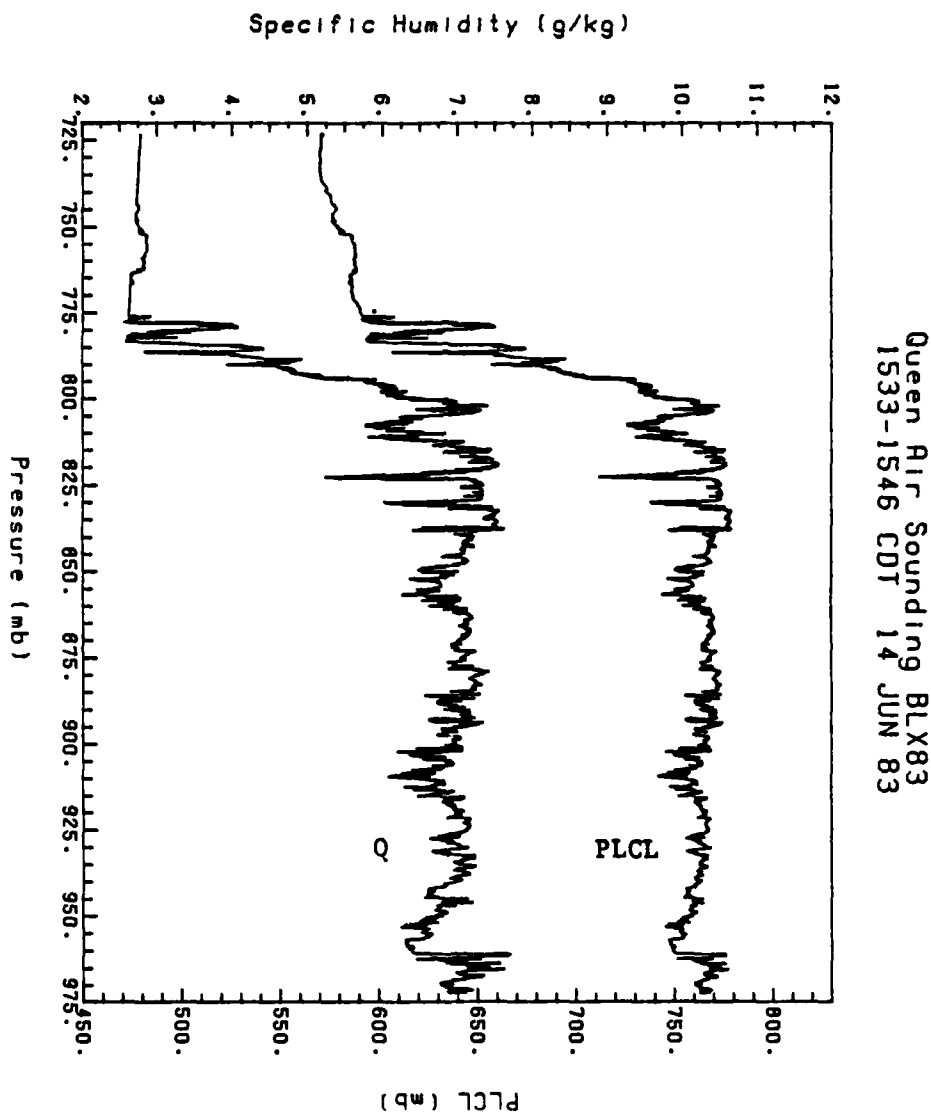


Figure A.22 Plot of specific humidity (Q) and pressure of lifting condensation level (PLCL) obtained by the Queen Air 20 Hz sensors during a sounding between 1533-1546 CDT 14 Jun 83, Flight 13. The constant value of specific humidity above 775 mb is due to saturation of the Lyman alpha logarithmic amplifier.

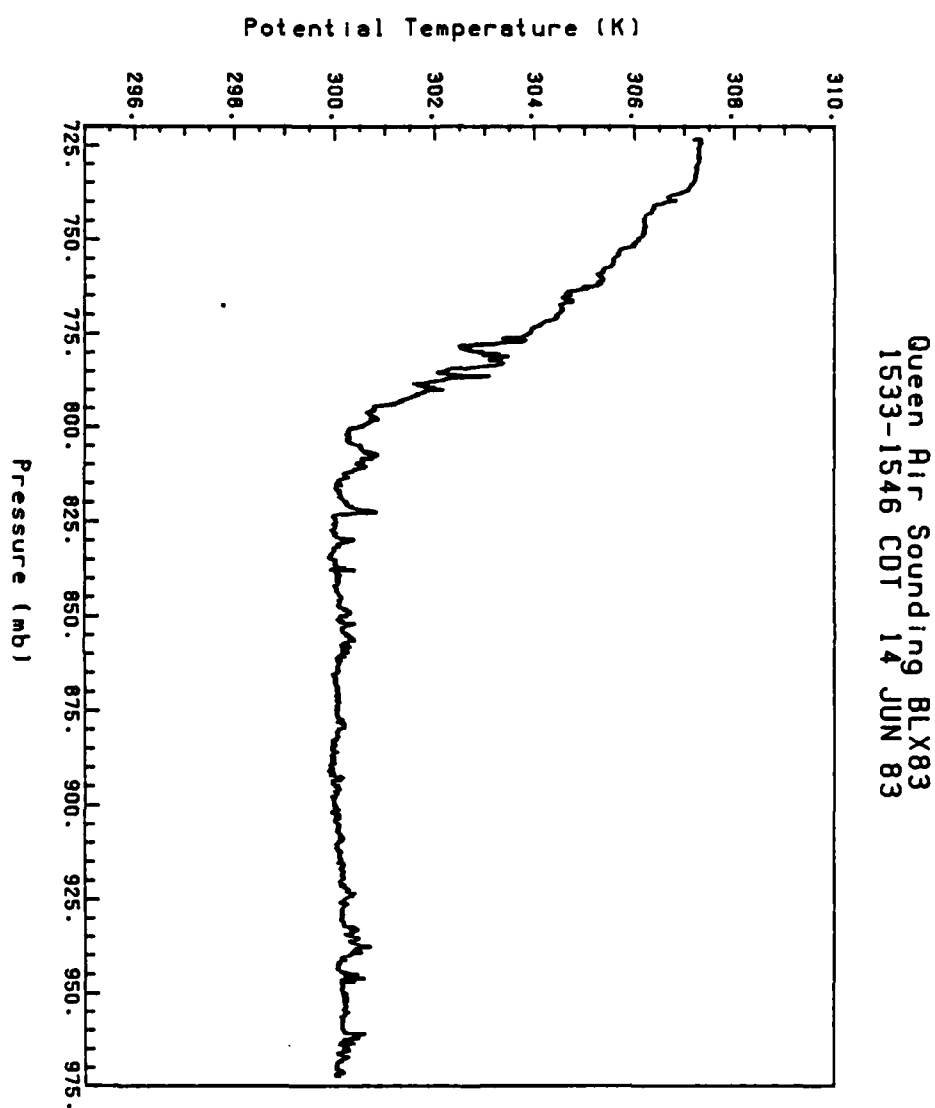


Figure A.23 Plot of potential temperature obtained by the Queen Air 20 Hz sensors during a sounding between 1533-1546 CDT 14 Jun 83, Flight 13.

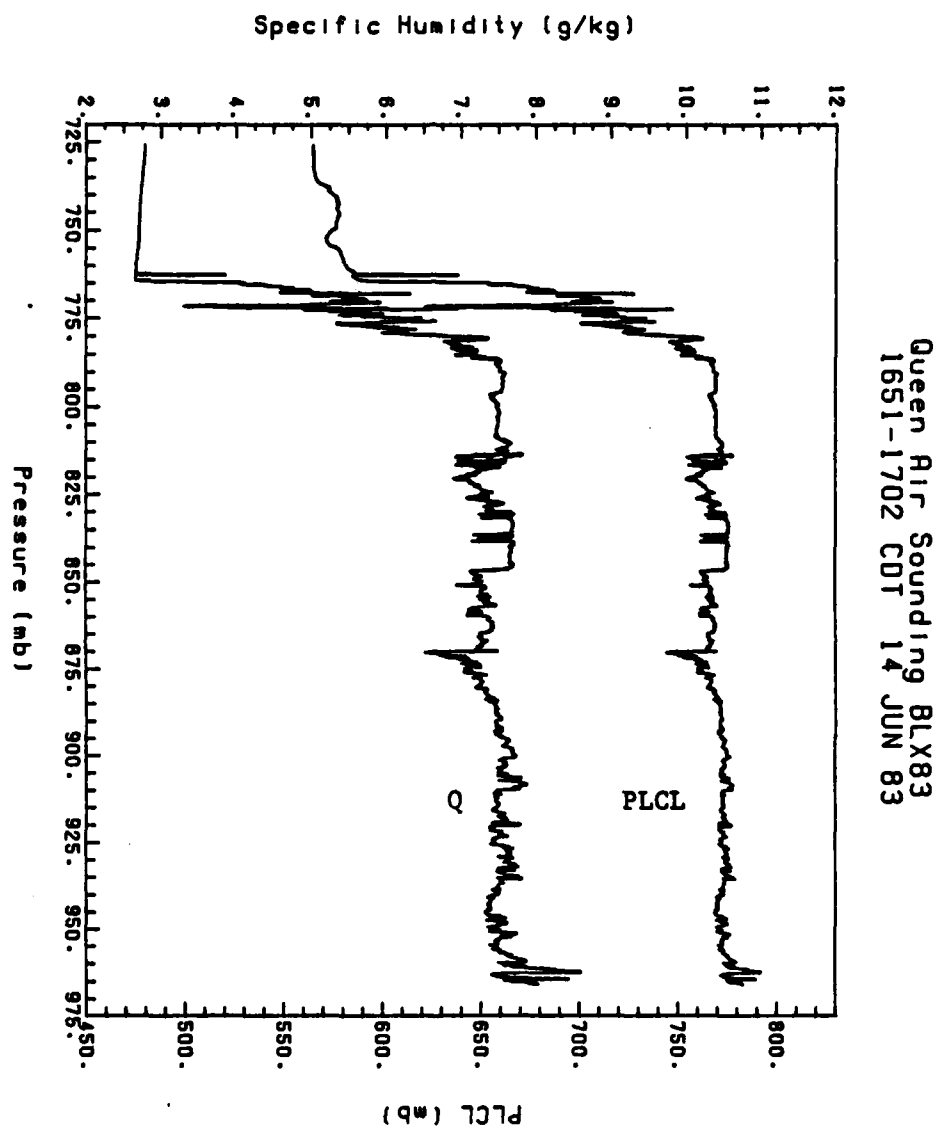


Figure A.24 Plot of specific humidity (Q) and pressure of lifting condensation level (PLCL) obtained by the Queen Air 20 Hz sensors during a sounding between 1651-1702 CDT 14 Jun 83, Flight 13. The constant value of specific humidity above 765 mb is due to saturation of the Lyman alpha logarithmic amplifier.

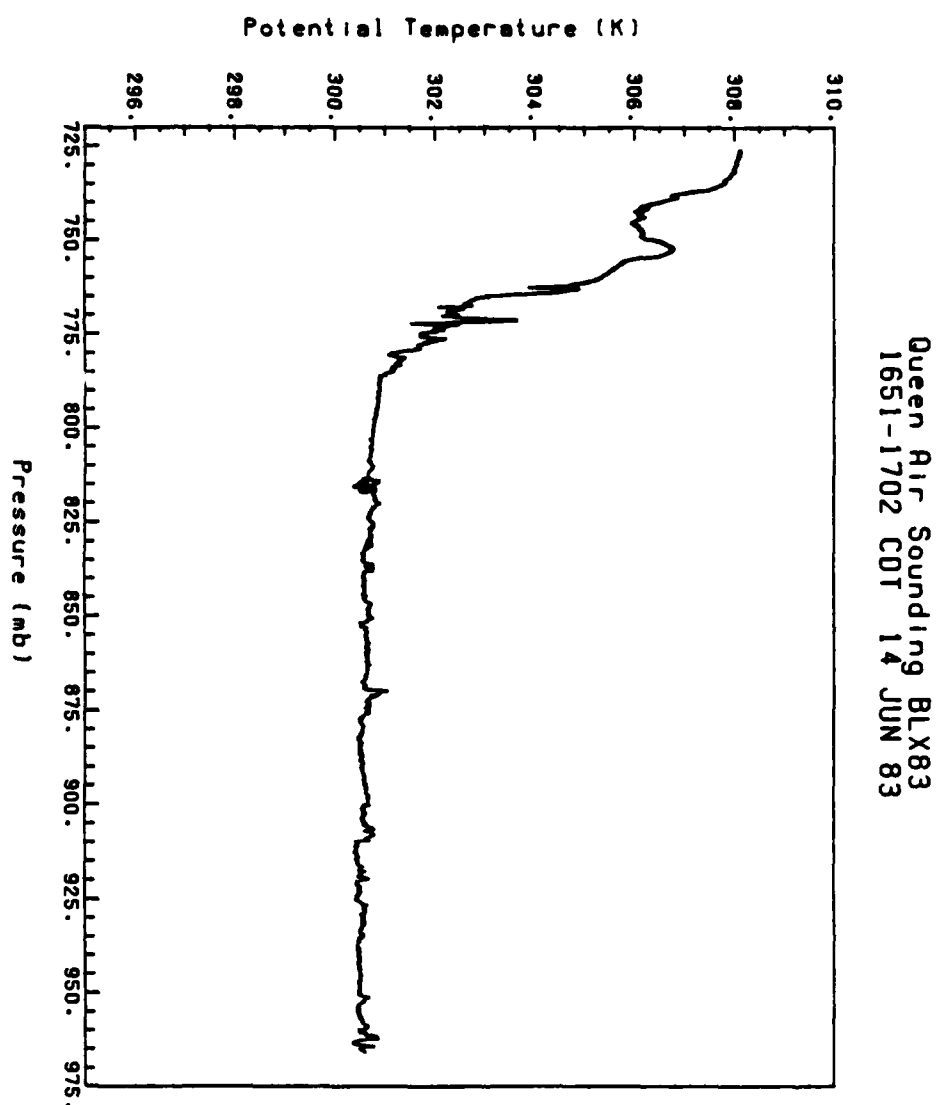


Figure A.25 Plot of potential temperature obtained by the Queen Air 20 Hz sensor during a sounding between 1651-1702 CDT 14 Jun 83, Flight 13.

Lidar Entrainment Zone Heights  
14 JUNE 83

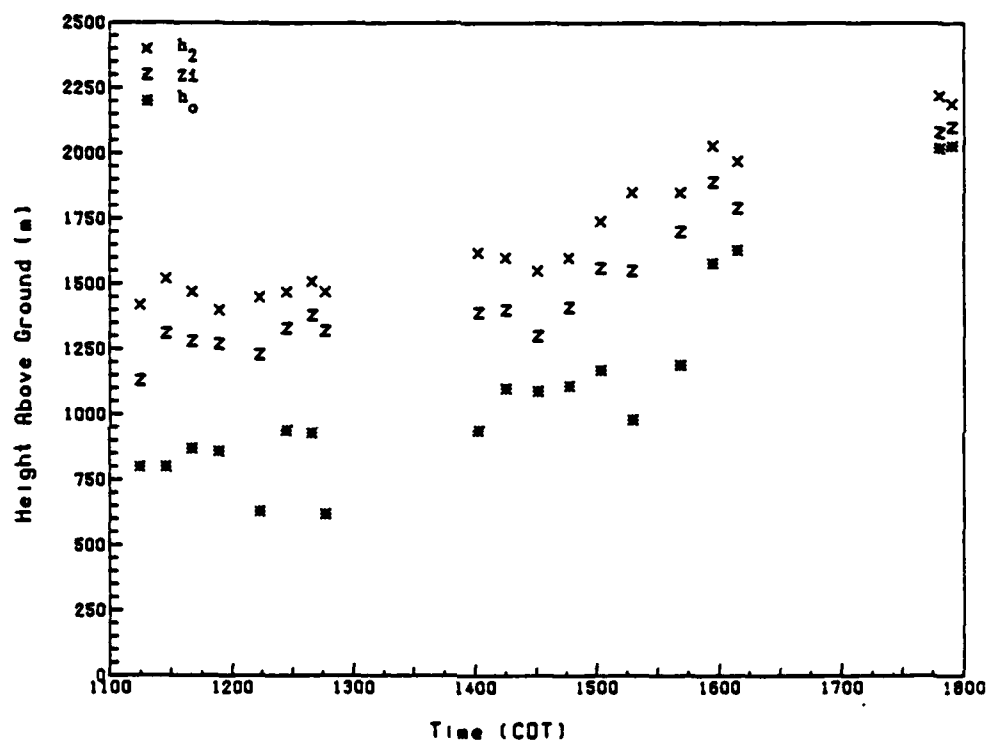


Figure A.26 Time series plot of subjectively-determined estimates, from lidar imagery, of top of CBL ( $h_2$ ), mean depth of CBL ( $Z_1$ ), and bottom of entrainment zone ( $h_0$ ) for times during Flight 13 of the Queen Air, 14 Jun 83.



Figure A.27 GOES imagery at 1100 CDT on 16 Jun 83



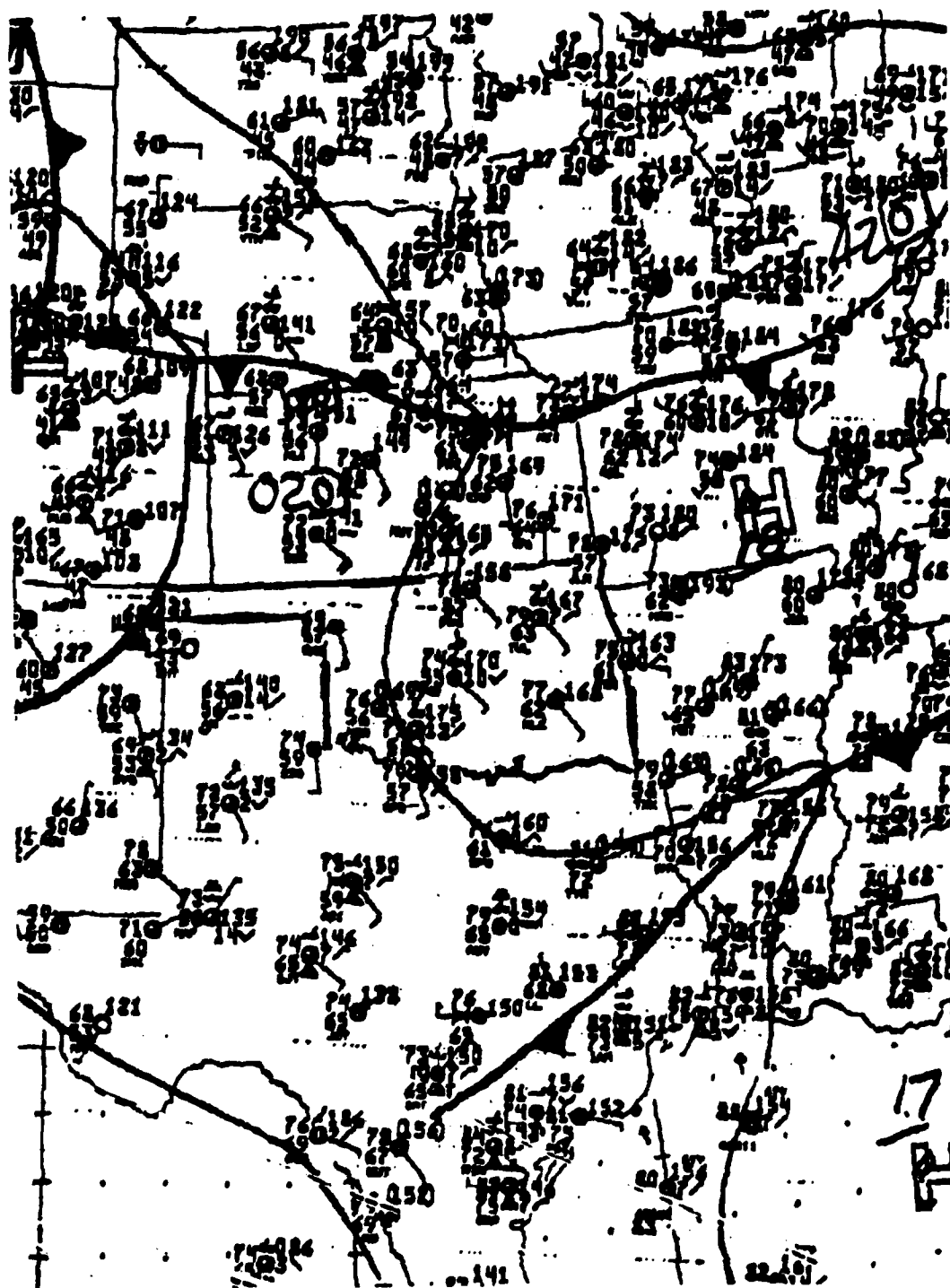


Figure A.28 NWS surface analysis for 1000 CDT on 16 Jun 83

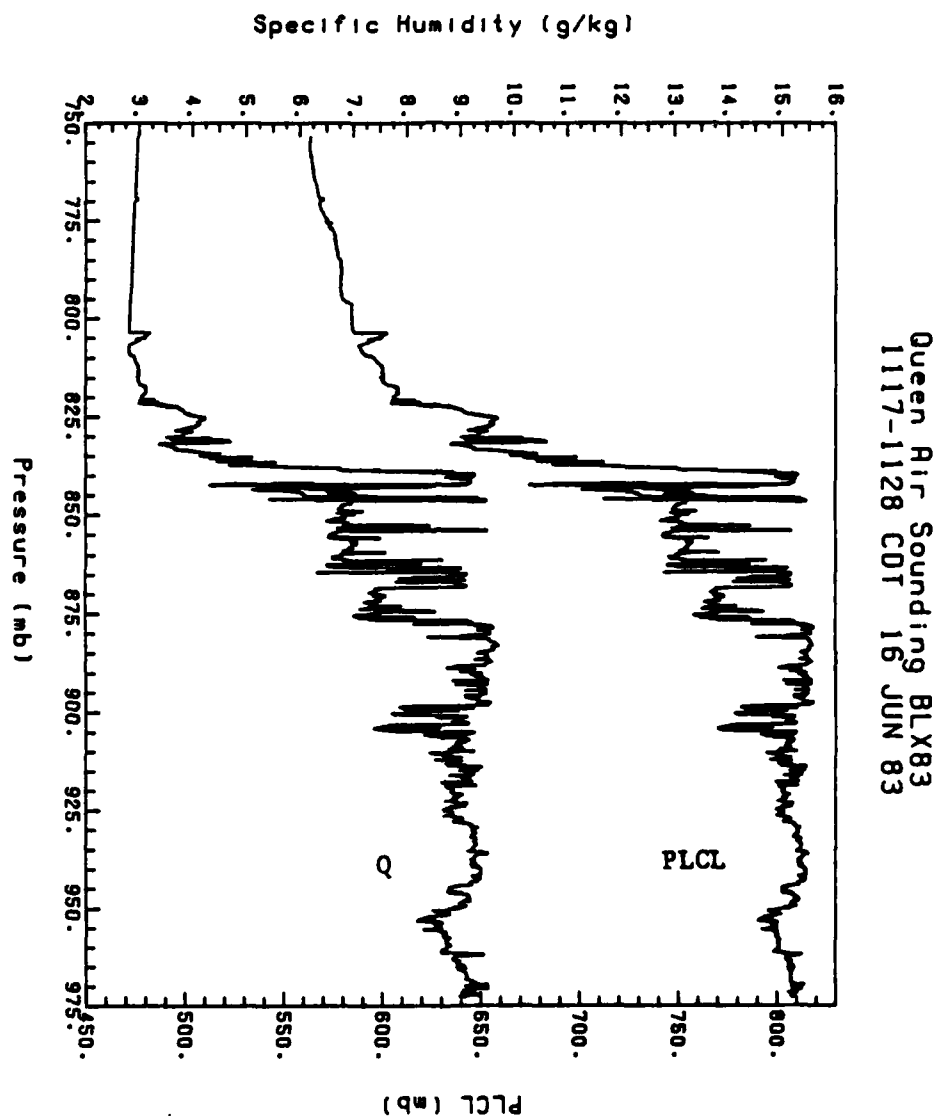


Figure A.29 Plot of specific humidity ( $Q$ ) and pressure of lifting condensation level (PLCL) obtained by the Queen Air 20 Hz sensors during a sounding between 1117-1128 CDT 16 Jun 83, Flight 16. The constant value of specific humidity above 803 mb is due to saturation of the Lyman alpha logarithmic amplifier.

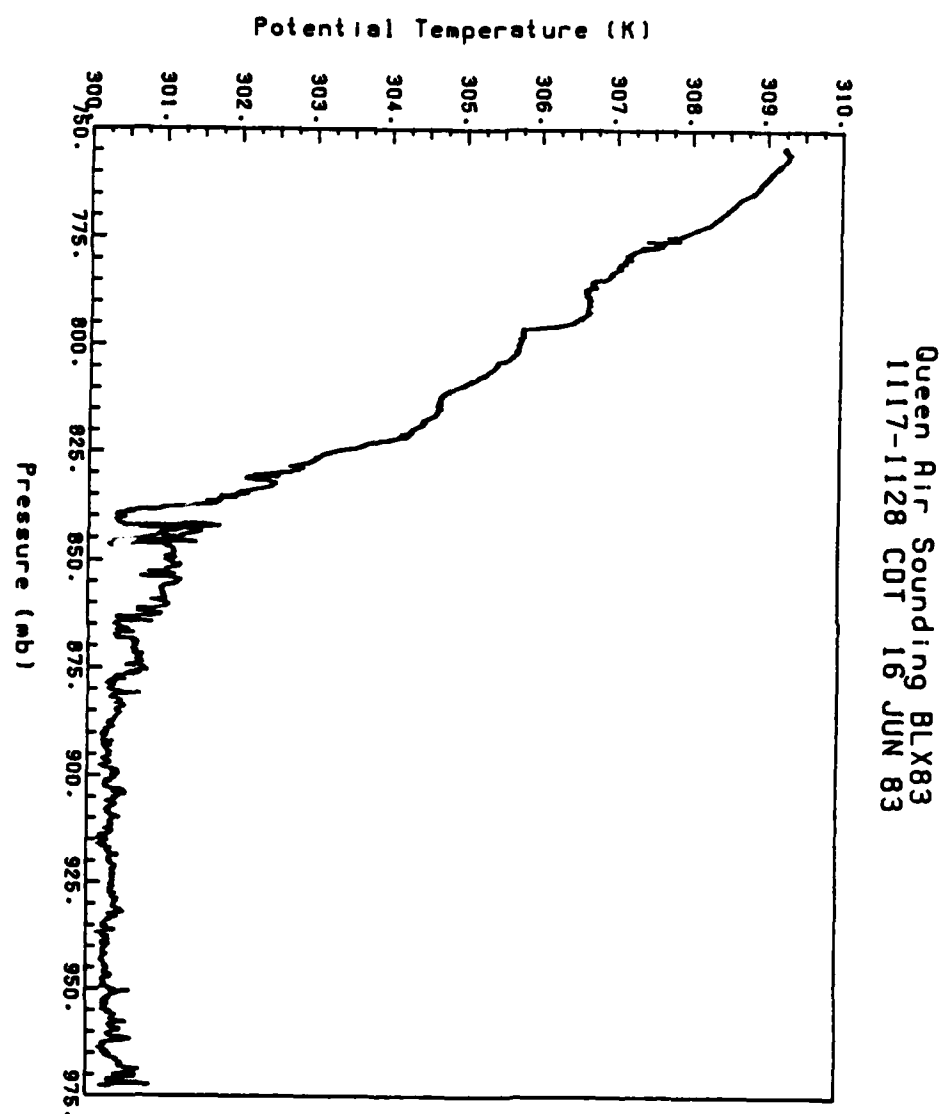


Figure A.30 Plot of potential temperature obtained by the Queen Air 20 Hz sensor during a sounding between 1117-1128 CDT 16 Jun 83, Flight 16.

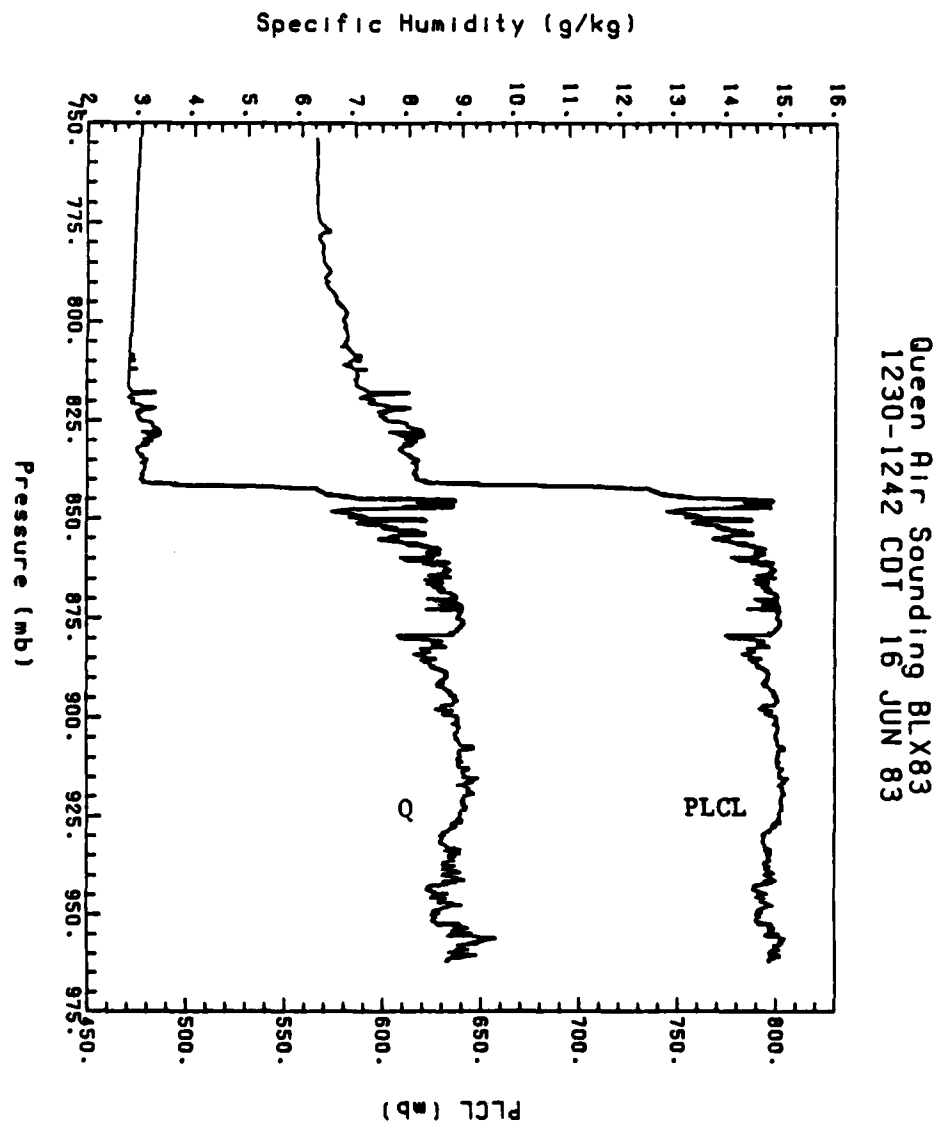


Figure A.31 Plot of specific humidity (Q) and pressure of lifting condensation level (PLCL) obtained by the Queen Air 20 Hz sensors during a sounding between 1230-1242 CDT 16 Jun 83, Flight 16. The constant value of specific humidity above 817 mb is due to saturation of the Lyman alpha logarithmic amplifier.

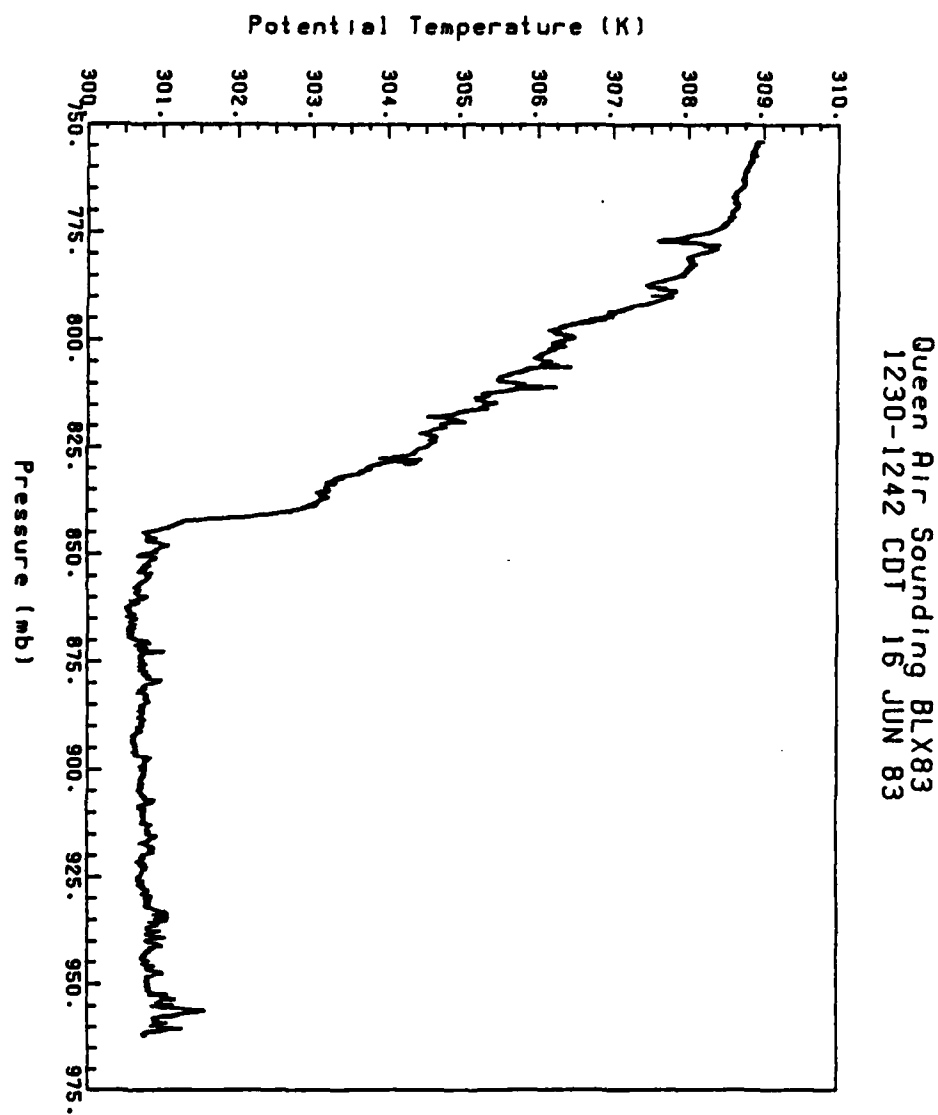


Figure A.32 Plot of potential temperature obtained by the Queen Air 20 Hz sensor during a sounding between 1230-1242 CDT 16 Jun 83, Flight 16.

Lidar Entrainment Zone Heights  
16 JUNE 83

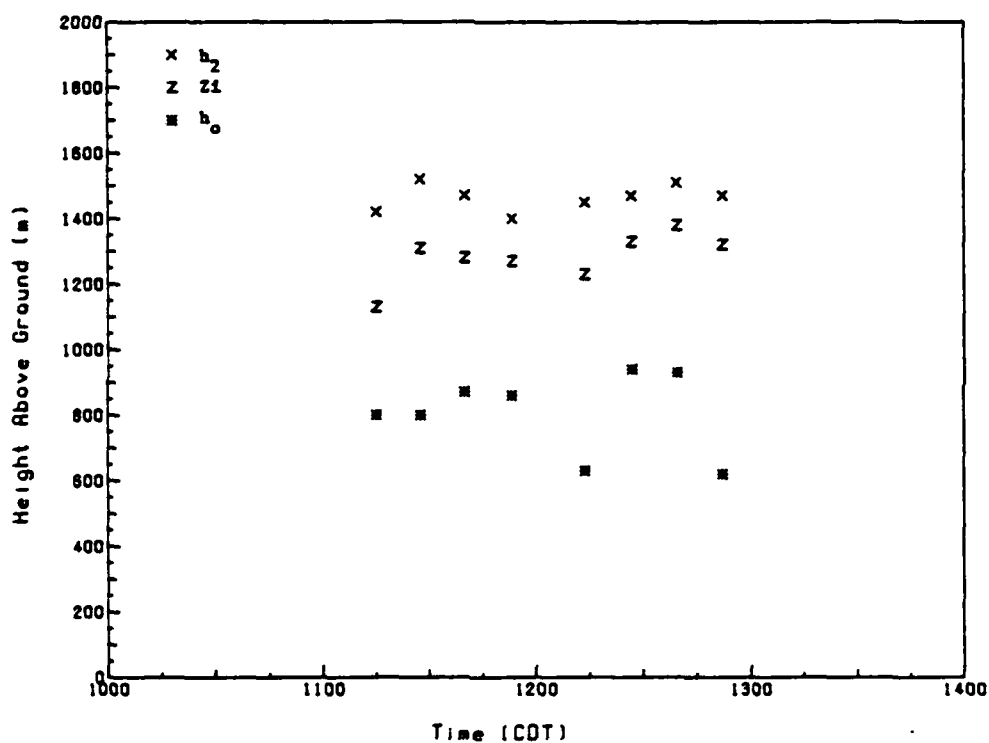


Figure A.33 Time series plot of subjectively-determined estimates, from lidar imagery, of top of CBL ( $h_2$ ), mean depth of CBL ( $Z_i$ ), and bottom of entrainment zone ( $h_0$ ) for times during Flight 16 of the Queen Air, 16 Jun 83.

## Appendix B

### Unsuccessful attempts to calibrate the Lyman alpha

This appendix contains a summary of the approaches attempted in developing the calibration technique for the Lyman alpha. These attempts used the NCAR and manufacturer suggested response time of 1 sec for the chilled-mirror dewpointer. As seen in Chapter 3, this response time is actually on the order of 6 sec and is the one that should have been used in these initial calibration attempts. However, due to the high correlation of the parameters used in the accepted method (section 3.3) and its success in comparison of humidity measurements from independent sensors, the methods described here were not retried with the more appropriate response time for the dewpointer. Some of the following attempts may appear to be fruitless in hindsight, but they highlight the lack of established procedures to perform the calibration.

In the first calibration technique, the system gain ( $V_0$  in eqn 2-5) was computationally adjusted on each leg to minimize the sum of squares (SS) difference between pseudo 20 Hz dewpointer data created by linearly interpolating between 1 Hz dewpointer values (as in Friehe et al., 1985) for each leg

$$SS = \sum_{i=1}^N (q'_{LAi} - q'_{DPi})^2 \quad (B-1)$$

where  $q'_{LAi}$  is the deviation from the leg-average specific humidity of the Lyman alpha for the  $i$ 'th value and  $q'_{DPi}$  is the deviation from the leg-average specific humidity of the dewpointer for the  $i$ 'th value. This adjustment of the system gain parameter was made to determine whether a post facto adjustment for the true system gain was needed. The true system gain could vary due to degregation of the sensor windows or a change in the discharge characteristics of the UH3 discharge lamp. This incorrect approach led to some negative values of specific humidity (unrealistic). Another flaw of this approach is the linear interpolation of dewpointer values to simulate 20 Hz data. The Lyman alpha suggests that the humidities rarely show a linear trend from one ordinal second to another.

In the second calibration attempt, the system gain was adjusted in order to minimize

$$| \bar{q}_{LA} - \bar{q}_{DP} | \quad (B-2)$$

for each leg using the NCAR-derived equations 2-4 through 2-7 to determine  $\bar{q}_{LA}$ . Although there was better agreement of the mean humidities for each leg than with the first approach, some



of the resultant fluxes via this approach yielded values in excess of 2000 watt/m\*\*2--totally unrealistic because this is twice the solar input and the moisture content of the soil was fairly low for the cases studied.

As a third approach, the system gain was varied in order to minimize the sum of squares in equation B-1 after converting the Lyman Alpha to pseudo 1 Hz data. The dewpointer was approximated as a first-order instrument; namely, an instrument having exponential response with time. This led to the general equation for variable S at time T to be

$$S_T = S_{T-1} + \sum_{i=2}^N (S_{T-i} + S_{T-1-i}) \exp \frac{-(i-1)t}{R} \quad (B-3)$$

Hence, this was an effort to mathematically map the Lyman alpha data into that of a slower-response first-order sensor (i.e. the dewpointer). Plots of the "psuedo 1 HZ" Lyman Alpha versus dewpointer where the system gain selected minimized the sum of squares showed much scatter and the best linear fit to the data was not parallel to the "perfect correlation" line. Also, eddy correlation fluxes using w' and Lyman-alpha moisture measured during near-surface flight legs yielded values near the solar input instead of physically realistic values of surface latent heat flux.

Since changing path length in the data reduction equations

does not result in a linear change of computed absolute humidity, a fourth approach was undertaken to try the ideas of Lenschow and Stankov (1981). This approach fixed system gain arbitrarily while varying the path length parameter (between 0.25 and 3 cm) in the calculations to minimize the pseudo 1 HZ sum of squares. Note, however, that the true path length was 0.5 cm. This resulted in apparently better fits of the data (as measured by lower SS values, resultant latent heat fluxes, and the appearance of psuedo  $\rho'_{LA}$  versus  $\rho'_{DP}$  plots).

Encouraged by this improvement, a fifth approach was made minimizing the sum of squares (SS) a two parameter (system gain and path length) problem. This improved the sum of squares, correlation of psuedo versus  $\rho'_{LA}$  and  $\rho'_{DP}$  resulted in even more reasonable latent heat fluxes.

After much discussion it was realized that there is no physical justification to arbitrarily vary system gain, path length, response time and lag offset time computational parameters to maximize the correlation of  $\rho'_{LA}$  and  $\rho'_{DP}$ , given that the respective true values of these parameters were relatively invariant. So this series of experiments was abandoned and the eventual accepted approach was tried.

## Appendix C.

## Lyman alpha Calibration Lines

Figures C.1 through C.13 contain the plots of light leg averages of the two chilled-mirror absolute humidities versus the leg-average Lyman alpha voltages. The Lyman alpha voltages were computed from the raw voltages provided by the log amplifier by making the oxygen absorption correction (eqn 3-4). The resultant least-squares best fit straight line is drawn. This line represents the calibration line used in data processing to transform the Lyman alpha voltages to meteorological units of humidity.

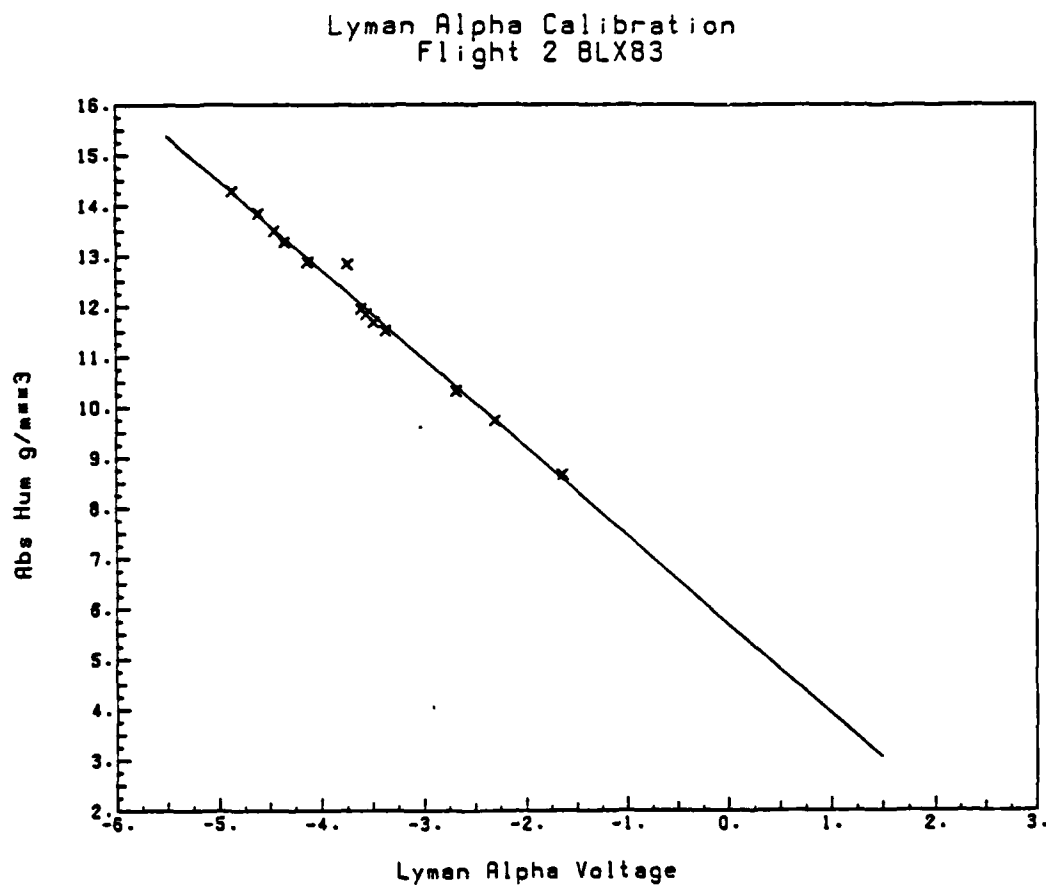


Figure C.1 Plot of leg-average Lyman alpha voltages versus leg-average dewpointer ( $\text{g/m}^3$ ) for Flight 2, 27 May 83. The best-fit straight line is drawn.

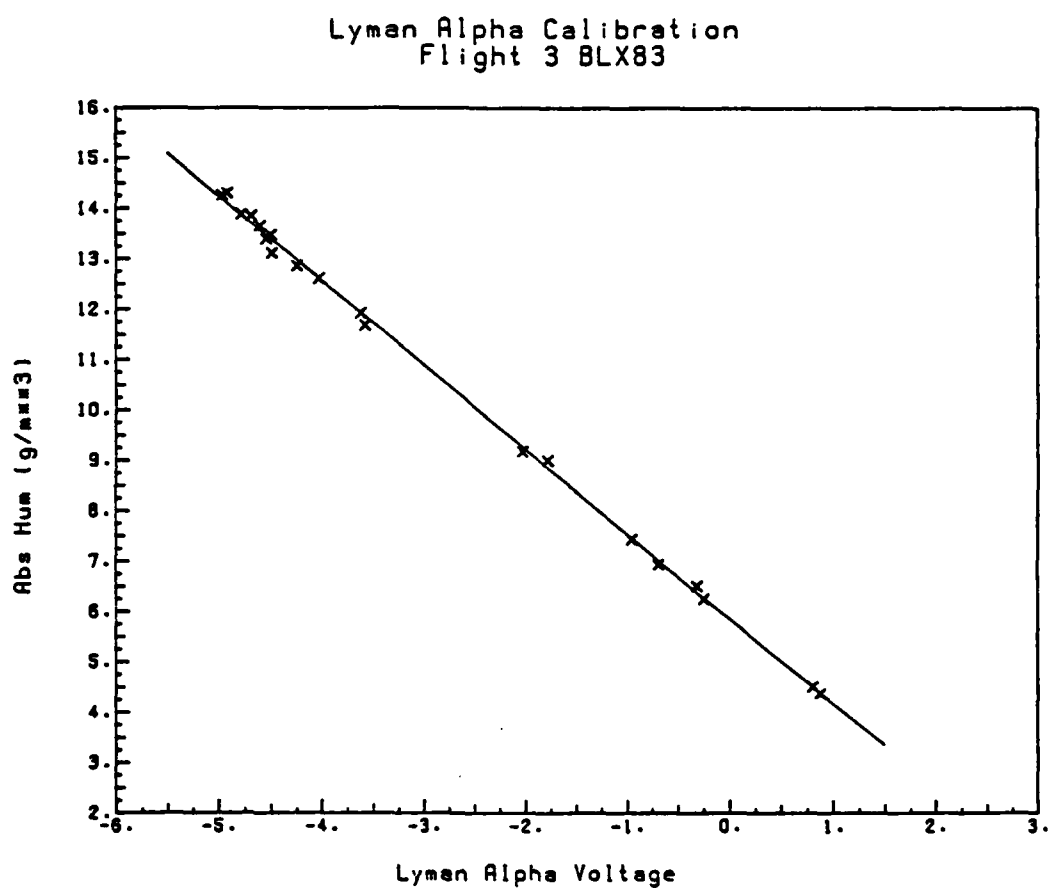


Figure C.2 Same as Figure C.1 except for Flight 3, 28 May 83.

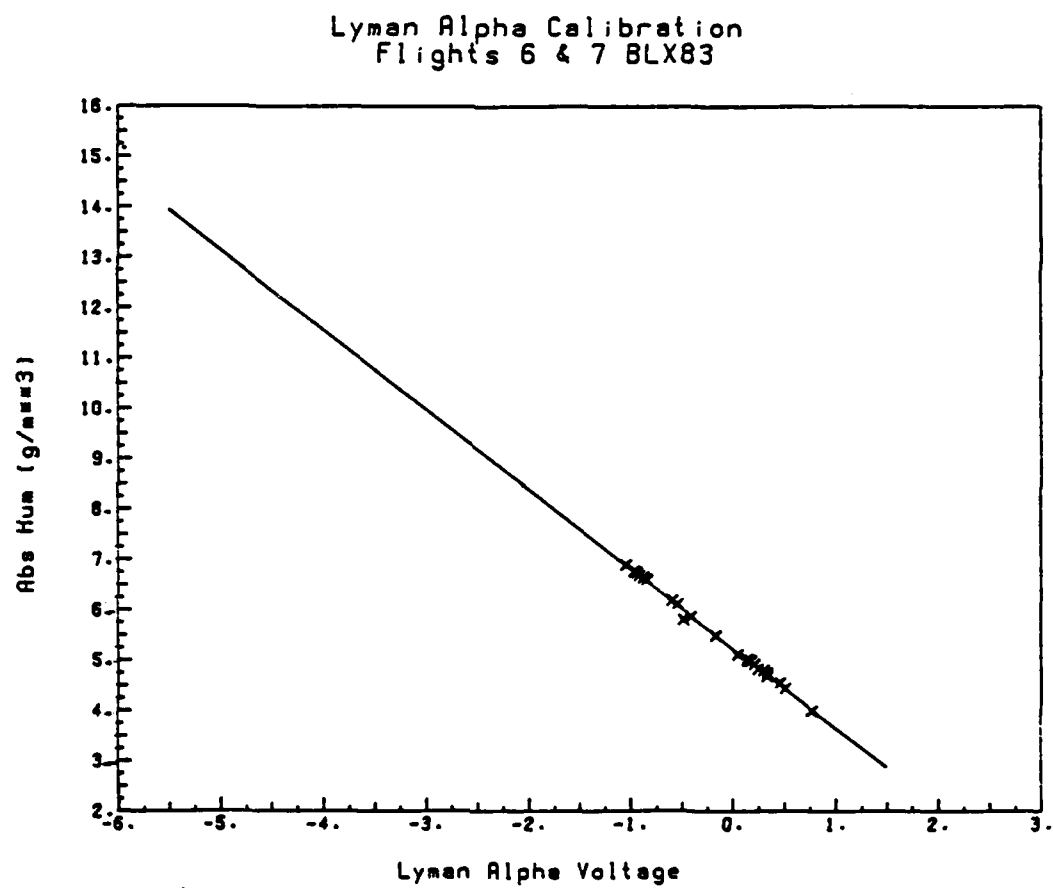


Figure C.3 Same as Figure C.1 except for Flights 6 and 7 Jun 83.

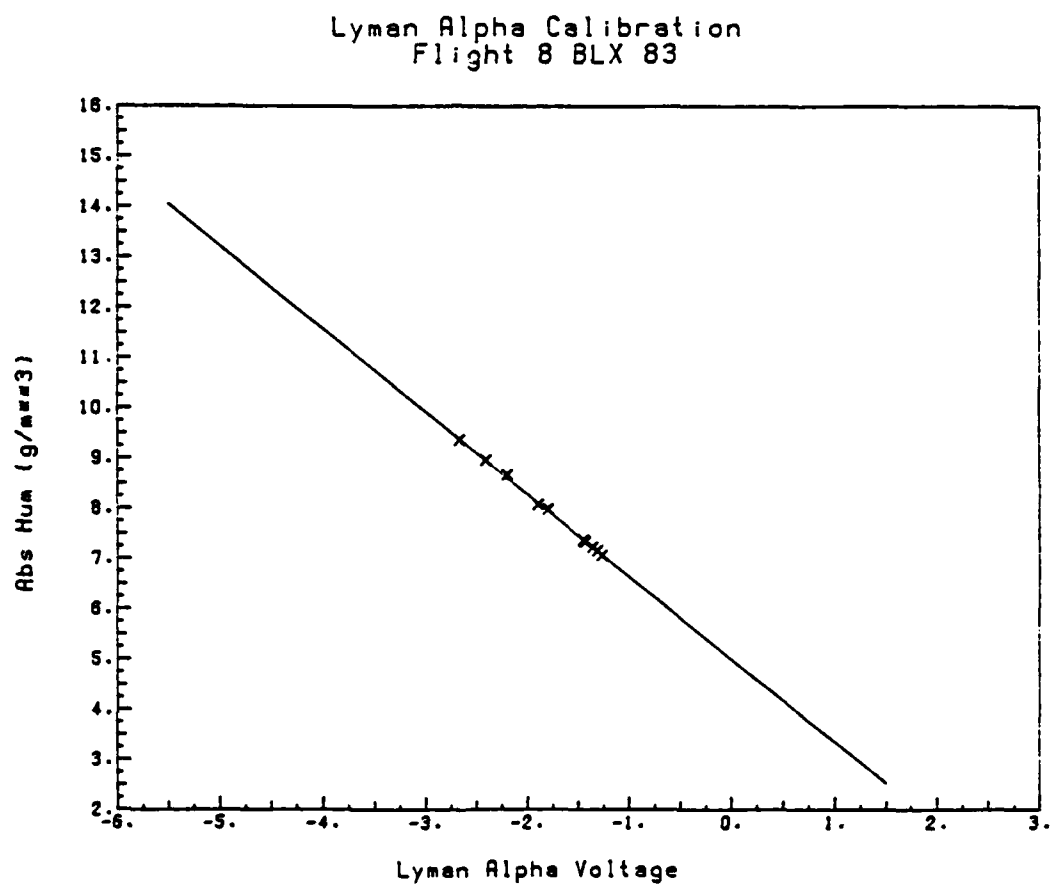


Figure C.4 Same as Figure C.1 except for Flight 8, 8 Jun 83.

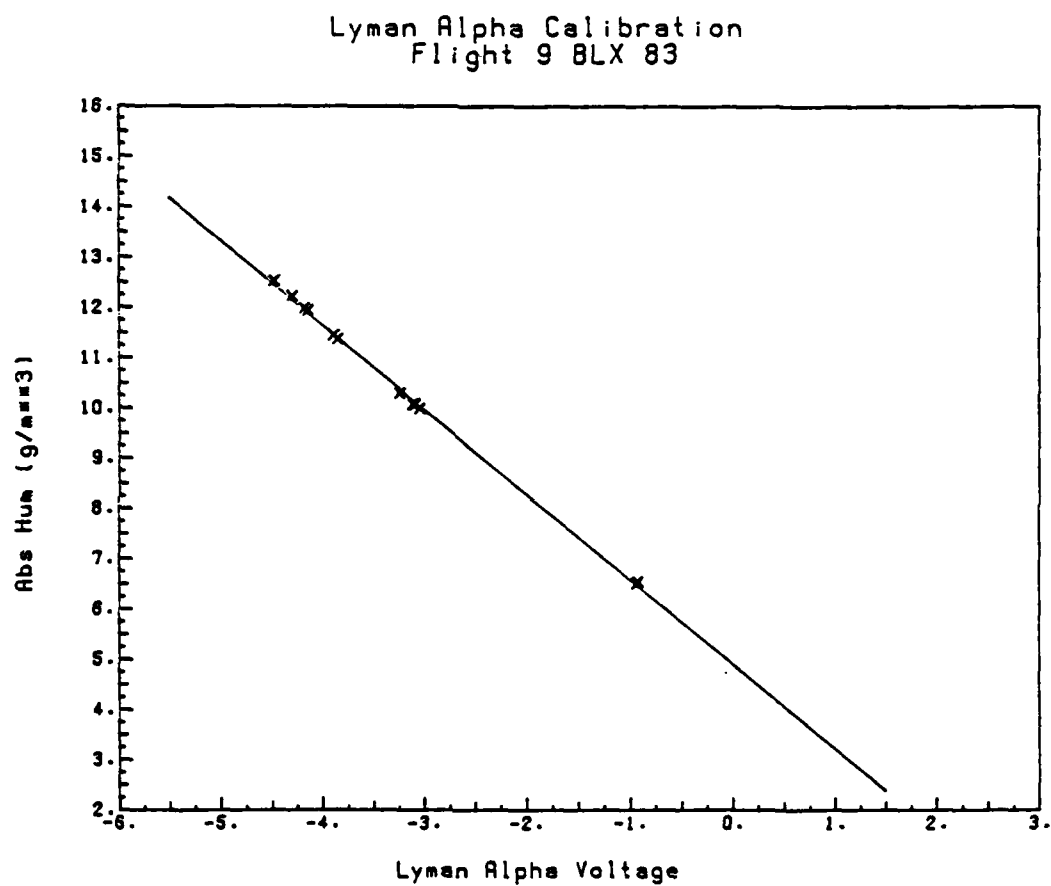


Figure C.5 Same as Figure C.1 except for Flight 9, 9 Jun 83.



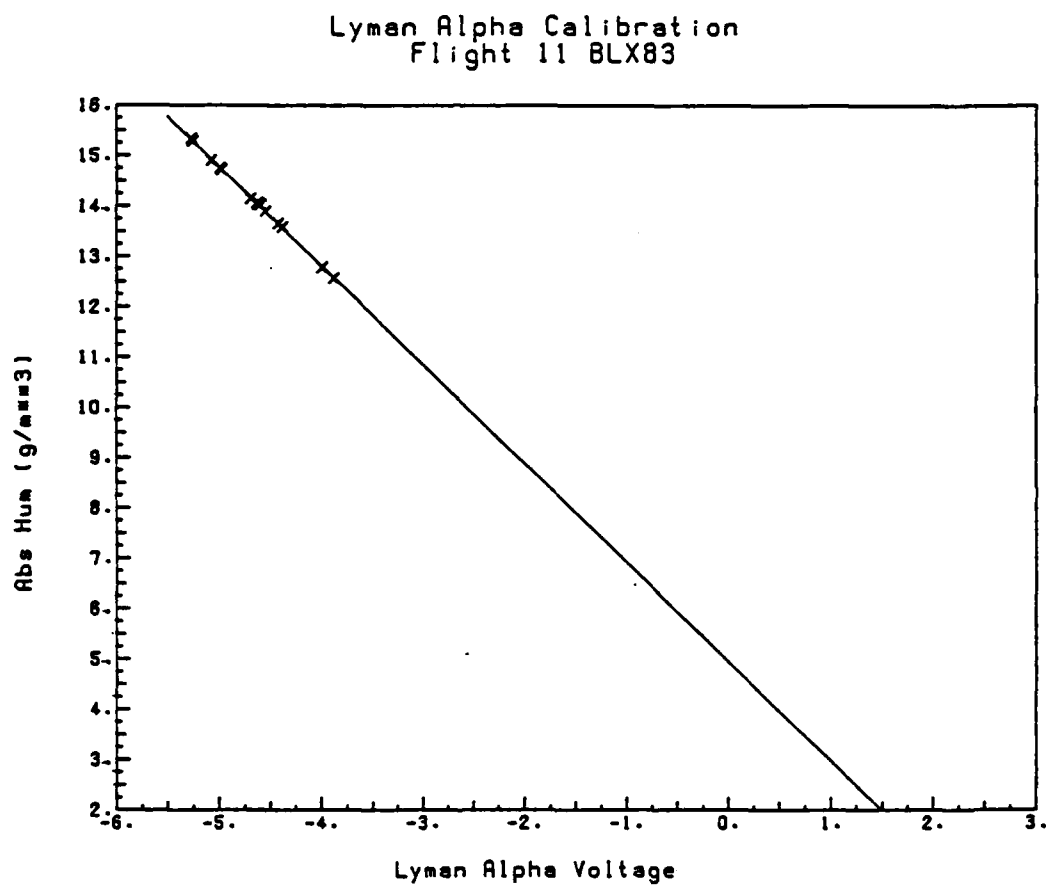


Figure C.6 Same as Figure C.1 except for Flight 11, 12 Jun 83.

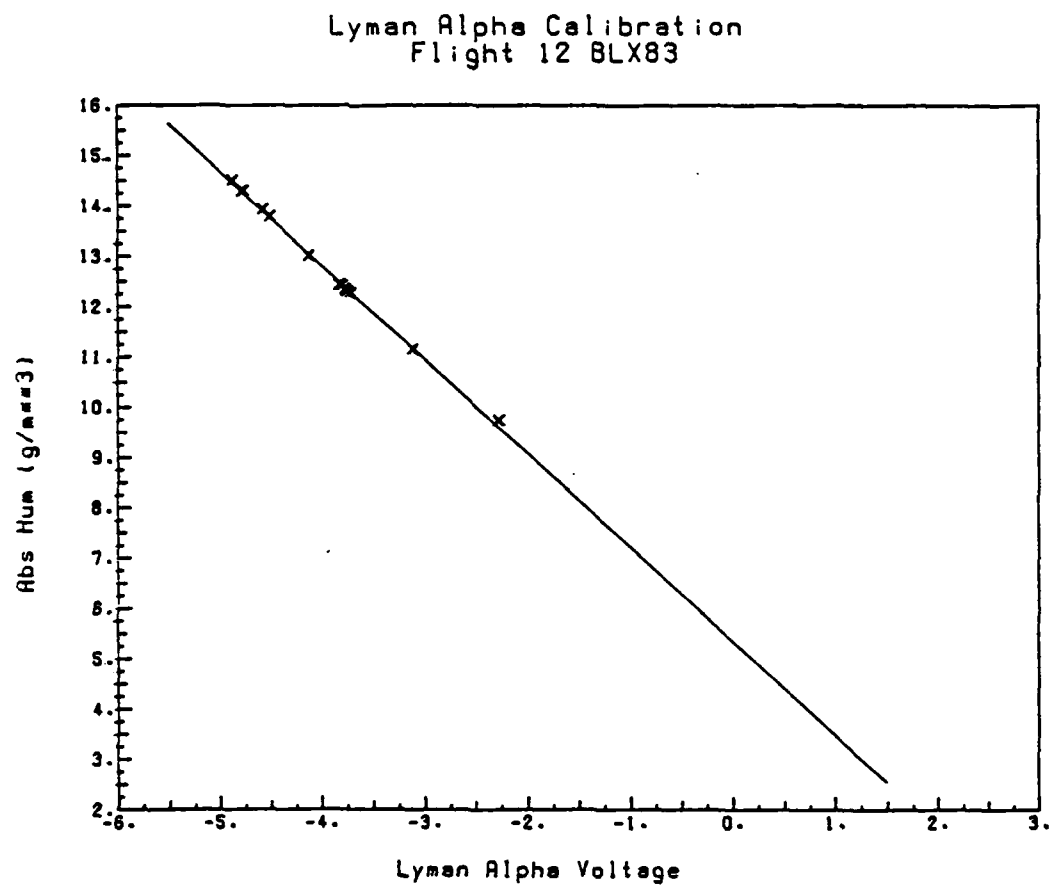


Figure C.7 Same as Figure C.1 except for Flight 12, 12 Jun 83.

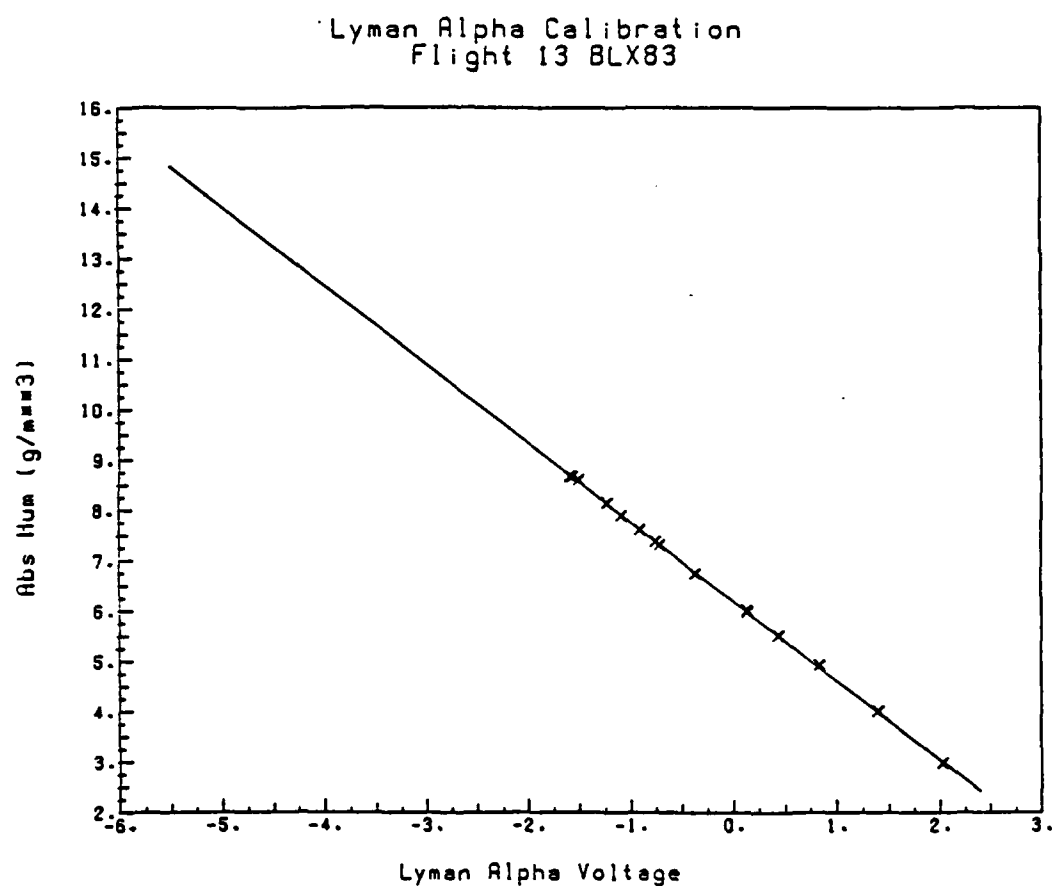


Figure C.8 Same as Figure C.1 except for Flight 13, 14 Jun 83.

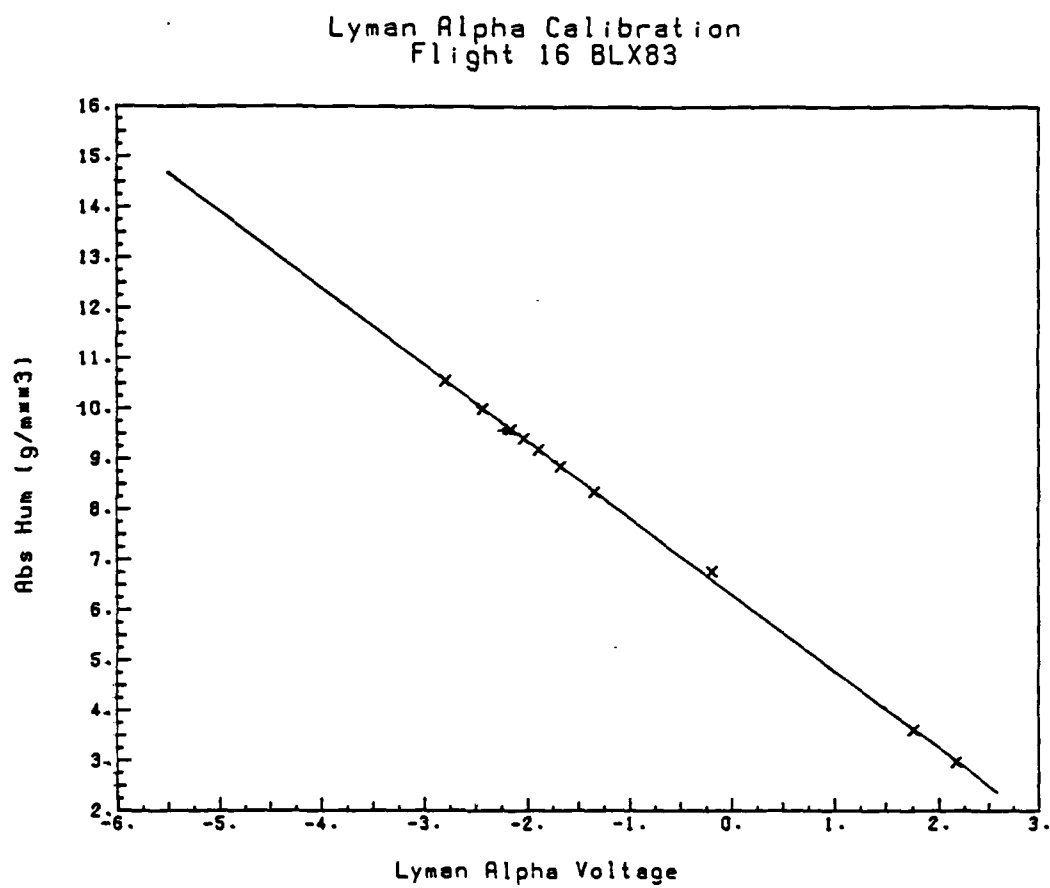


Figure C.9 Same as Figure C.1 except for Flight 16, 16 Jun 83.

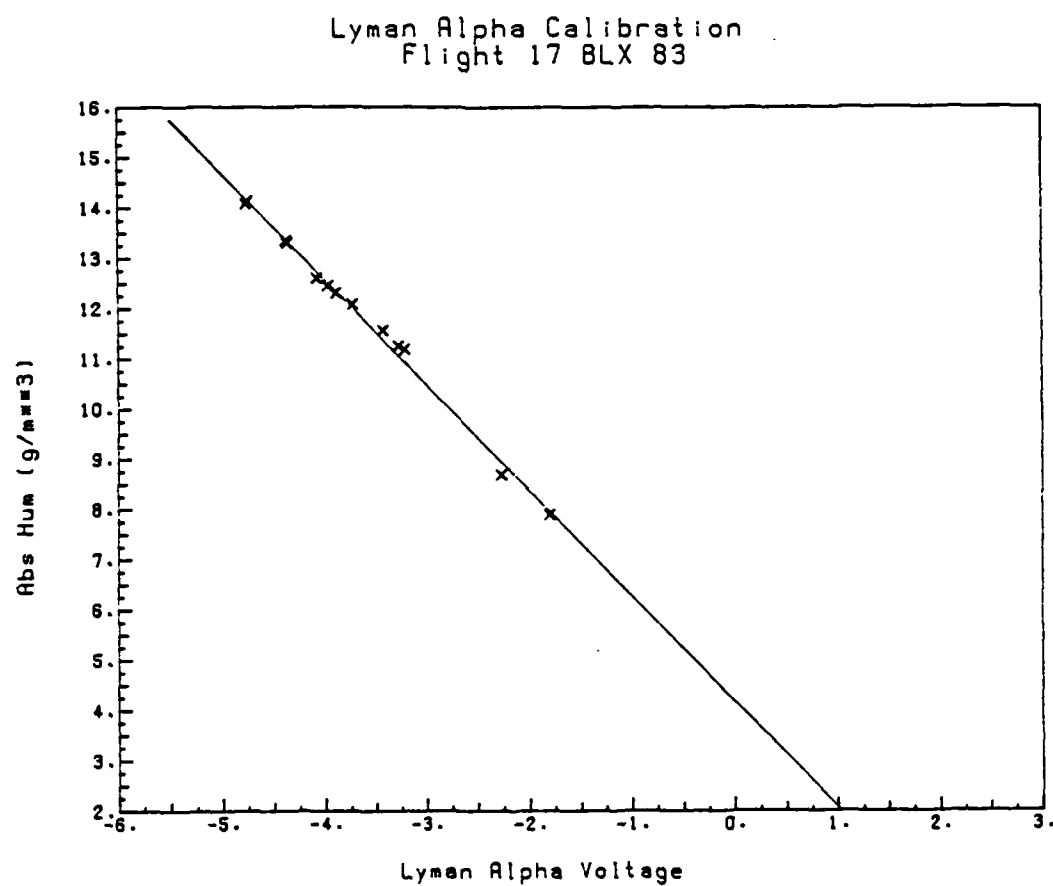


Figure C.10 Same as Figure C.1 except for Flight 17, 17 Jun 83.

251

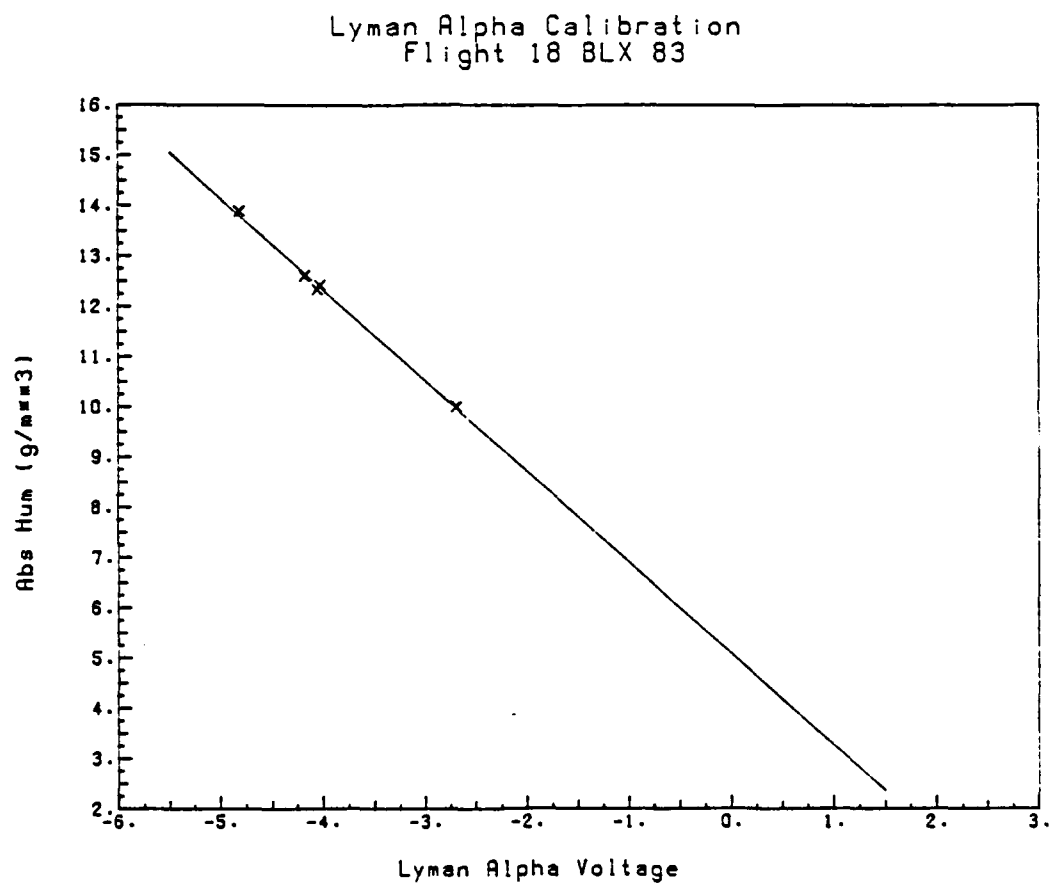


Figure C.11 Same as Figure C.1 except for Flight 18, 17 Jun 83.

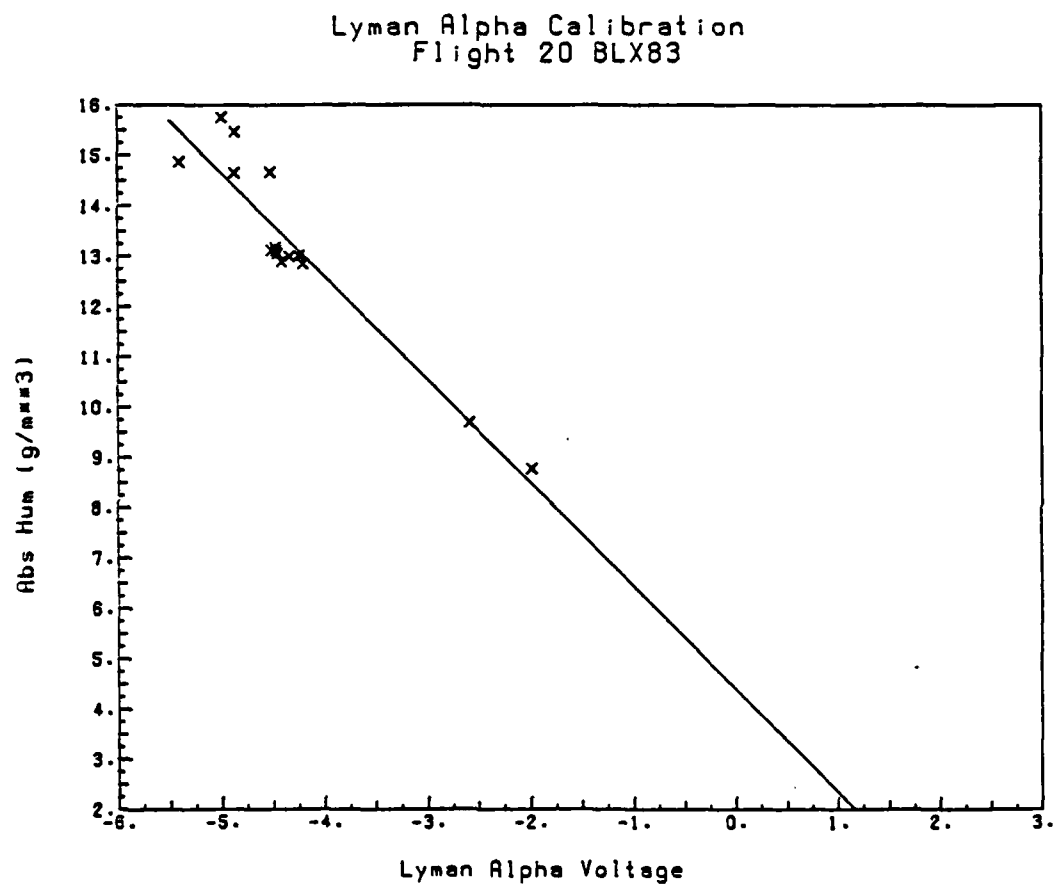


Figure C.12 Same as Figure C.1 except for Flight 20, 18 Jun 83.

## Appendix D.

## Alternate Methods of Flux Determination

Flux gradient relationships for the surface layer are

$$\overline{w'q'} = LE = -K_L \frac{\Delta q}{\Delta Z}, \quad S = \overline{w'T'} = -K_S \frac{\Delta \theta}{\Delta Z} \quad (D-1)$$

Assuming that the sensible heat flux is well known, these two equations can be combined to solve for the moisture flux

$$\overline{w'q'} = \overline{w'\theta'} \frac{K_L}{K_S} \frac{\Delta q}{\Delta \theta} \quad (D-2)$$

Most often, the thermal and moisture eddy diffusivities ( $K_S$  and  $K_L$ ) are considered equal. Hence,

$$\overline{w'q'} = \overline{w'\theta'} \frac{\Delta q}{\Delta \theta} \quad (D-3)$$

Experiments were carried out using this relationship where the surface layer potential temperature gradient was estimated from the difference between the Queen Air sounding's mean potential temperature in the lower CBL and the PAM II potential temperature. The specific humidity gradient was determined in



the same manner. This approach, in most cases, provided a smaller estimate for latent heat flux (yet larger ground flux residual term) than did the eddy correlation method.

Another approach used was to calculate the gradient Bowen ratios

$$B = \frac{C_p \Delta \theta}{\lambda \Delta q} \quad (D-4)$$

and substitute them in equation 3-5, yielding

$$LE = \frac{(Q_* - G)}{1 + B} \quad (D-5)$$

and

$$S = \frac{B(Q_* - G)}{1 + B} \quad (D-6)$$

Since the above expressions for LE and S are merely a partitioning of the known net radiation, this method yields a balance in the energy equation. It yielded larger values for both sensible and latent heat than were observed, but here we must make assumptions on the magnitude of the ground storage term (which we don't know) in order get "accurate" fluxes. So this is merely substituting one unknown for two and was not pursued. The gradients were determined as in the previous method.

A surface heat flux parameterization using a bulk heat transfer coefficient used by Binkowski (1983) in a numerical model of the CBL was also used as a check on the measured sensible heat fluxes. Resulting values were smaller by a factor of four than those measured during BLX83 (larger yet ground flux residual term).

Lastly, a budget box approach similar to that employed by Cattle and Weston (1975) was used. Using representative soundings, the time averaged turbulent flux of sensible and latent heat can be computed by measuring the net increase or decrease in temperature and humidity over the mixed layer depth. Based on conservation equations for heat and moisture, the turbulent flux of sensible heat is

$$S = \rho C_p \int_{Z_{BOT}}^{Z_{TOP}} \left[ \frac{\partial \theta}{\partial t} + \bar{v}_H \cdot \nabla_H \bar{\theta} + \bar{w} \frac{\partial \theta}{\partial Z} - Q \right] dZ \quad (D-7)$$

and for latent heat is

$$LE = \lambda \rho \int_{Z_{BOT}}^{Z_{TOP}} \left[ \frac{d\bar{q}}{dt} + \bar{v}_H \cdot \nabla_H \bar{q} + \bar{w} \frac{d\bar{q}}{dZ} - Q_E \right] dZ \quad (D-8)$$

where  $Z_{TOP}$  is the height that the tallest thermal reaches  $Z_{BOT}$  is the surface, and  $\lambda$  is the latent heat of vaporization.

The first term in D-7 and D-8 is the time rate of change in potential temperature or specific humidity determined from the

soundings. The second term represents the horizontal advection into the area. The advection rates were computed by use of the 13 PAM II stations and examination of synoptic-scale NWS analysis maps. In the cases and time lengths considered, this term is negligible (computed advective changes smaller by a factor of 10 to 20 than the observed changes). The third term represents the vertical advection of heat or moisture across  $Z_{TOP}$  caused by larger scale vertical motion such as subsidence. A linear variation of  $w$  with height, zero at the surface, will be assumed, using subsidence values aloft that are determined from changes in the soundings and divergence values computed by the PAM II stations. The last term is the diabatic source of heat or body source term for moisture. Since the cases presented involved clear sky situations, there were no changes of phase taking place. Also, no moisture source other than the surface was present. Hence, this term can be neglected for humidity. Also, diabatic radiational heating was smaller than the other terms. Thus equations D-7 and D-8 reduce to

$$S = \rho C_P \int_{Z_{BOT}}^{Z_{TOP}} \left[ \frac{\partial \bar{\theta}}{\partial t} + \bar{w} \frac{\partial \bar{\theta}}{\partial Z} \right] dZ \quad (D-9)$$

and

$$LE = \lambda \rho \int_{Z_{BOT}}^{Z_{TOP}} \left[ \frac{d\bar{q}}{dt} + \bar{w} \frac{d\bar{q}}{dZ} \right] dZ \quad (D-10)$$

Budget box flux estimates using equations D-9 and D-10 were applied to Queen Air sounding data collected during entrainment zone flights. These flux estimates are plotted against those obtained by the Queen Air using the eddy correlation technique (Figures D.1 and D.2). These figures show much scatter and a general bias of larger sensible heat fluxes by the budget box method.

As Cattle and Weston (1975) discuss, this approach to estimating surface fluxes is dependent upon obtaining representative soundings. the difference between estimates of  $Z_i$  and  $h$  obtained during a Queen Air sounding and repeated lidar RHI scans frequently differed by 100-300 m.

An estimate of the magnitude of error possible due to this error in height measurement is made. In the simplest example, no subsidence or advection is considered. This reduces equations D-9 and D-10 to

$$S = \rho C_p \int_{Z_{BOT}}^{Z_{TOP}} \frac{\partial \bar{\theta}}{\partial t} dz \quad (D-11)$$

and

$$LE = \lambda \rho \int_{Z_{BOT}}^{Z_{TOP}} \frac{\partial \bar{q}}{\partial t} dz \quad (D-12)$$

# Budget Box and Eddy Correlation Sensible Heat Fluxes

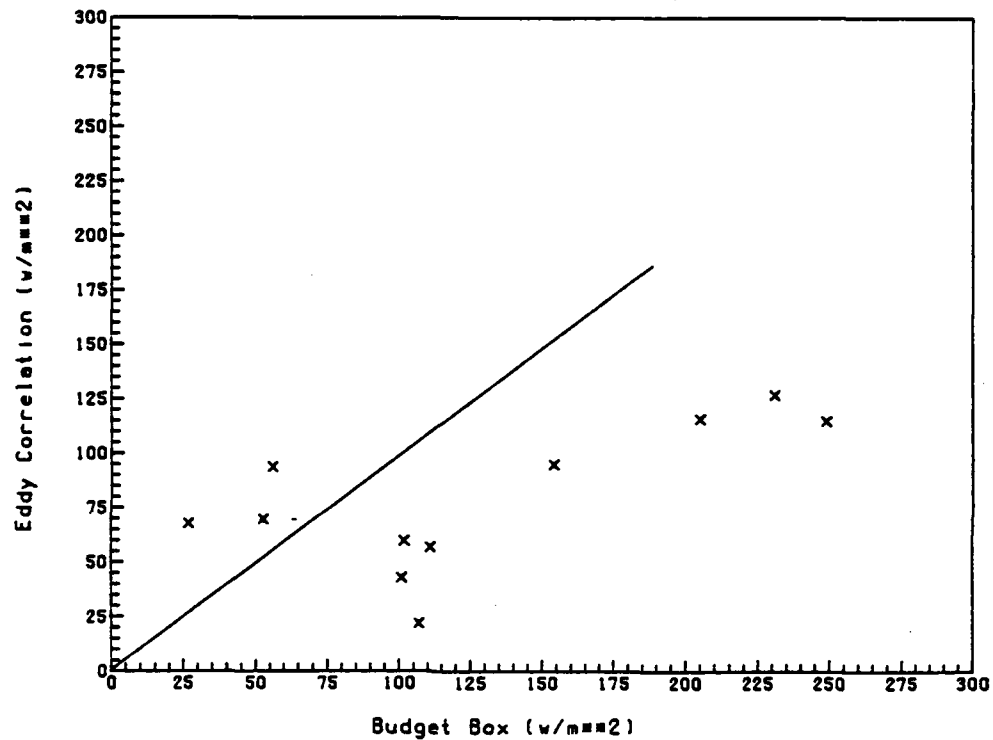


Figure D.1 Plot of sensible heat fluxes calculated by the eddy correlation technique versus fluxes estimated by the budget box approach. The eddy correlation values were calculated from data collected by the Queen Air on near-surface horizontal flight legs flown during entrainment zone flights. The budget box estimates used data obtained by the Queen Air on sounding legs. The perfect correlation line is drawn in.

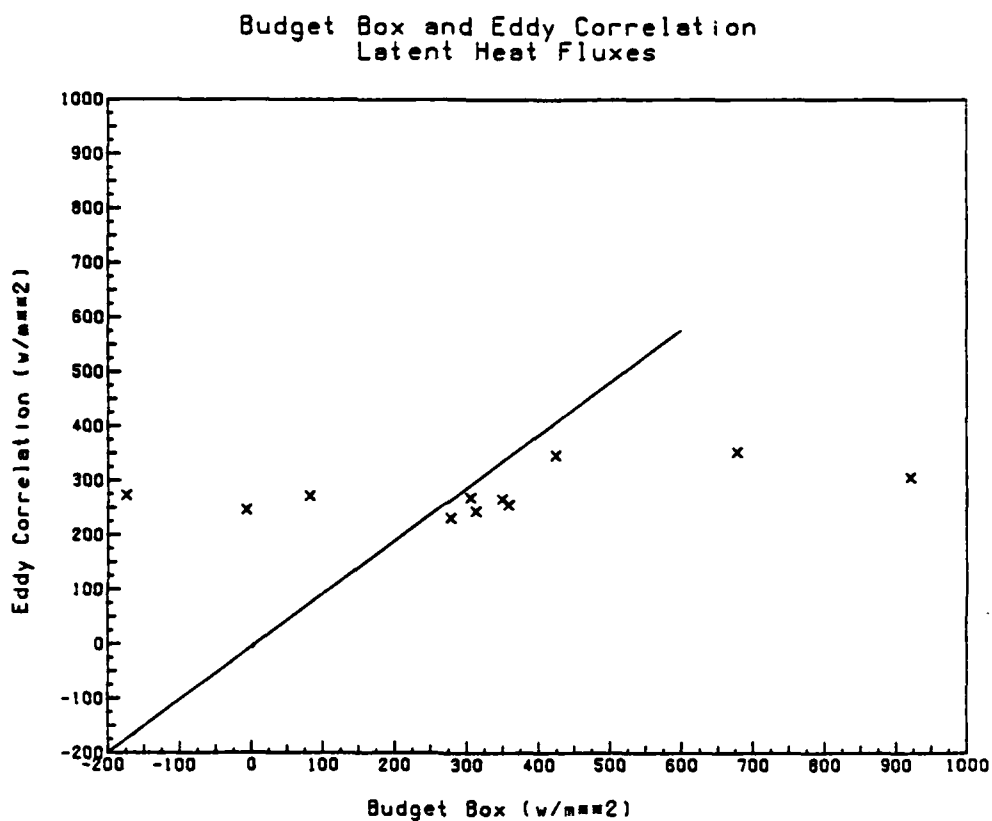


Figure D.2 Same as Figure D.1 except for latent heat flux.  
note the lack of agreement of values between the two methods.

Assume a case of two soundings an hour apart where the only values that changes is  $Z_{TOP}$  due to a measurement "error" of -250 m on one sounding. Using typical values for equations D-11 and D-12

$$\Delta t = 3600 \text{ sec} = 1 \text{ hr}$$

$$\Delta \theta_{\text{Inversion}} = 3.5 \text{ K}$$

$$Z_i = 1500 \text{ m}$$

$$\Delta q_{\text{Inversion}} = 6 \text{ g/kg}$$

a possible error of 25  $\text{w/m}^2$  for sensible heat flux and 1000  $\text{w/m}^2$  for latent heat flux is computed. Adding in the uncertainty for subsidence rates and other sources of error means that the possible errors are larger than the expected latent heat values and compose a large portion of the sensible heat values.

This alternate method of flux determination, like the others in this appendix, did not offer substantial reason to doubt the surface fluxes obtained by the Queen Air on near-surface horizontal flight legs. Since the coincident flux measurements by Argonne National Laboratory were available, this initial budget box effort was not improved upon. This method could be improved by adjusting the soundings such that the soundings' estimate of  $Z_i$  matched that obtained from lidar imagery.

## Appendix E

Selection, Derivation and Illustration of Asymmetrical Double  
Exponential Functions

A range of specific humidity values is observed along a flight path of say 20 km. The range of values observed during near-surface and free atmosphere air horizontal flight legs also varies from flight leg to flight leg. Varying skewnesses to the left and right are observed, but in nearly all cases, the frequency distributions have one mode and tails of finite length.

In order to simplify the task of parameterizing the various distributions, the asymmetrical double exponential probability density function (PDF) was selected to fit the data. This PDF offers the features of simplicity, being unimodal and being able to adapt to the direction and degree of skewness required. Higher-order equations could possibly fit the observed distributions more closely, but they would merely be fitting the random variability of the samples and not improve the general application of this approach.

A modified asymmetrical double exponential with truncated tails (Figure E.1) is used to handle the finite range of observed humidity values. This function is defined by



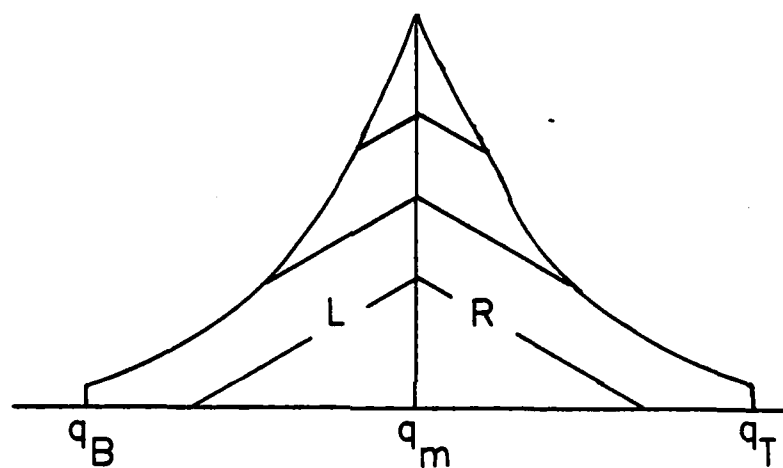


Figure E.1 Schematic of modified asymmetrical double exponential probability density function. The area under the function left of  $q_m$  is  $L$  and the area to the right is  $R$ . The function has truncated tails at  $q_B$  and  $q_T$ .

$$f(q) = \begin{cases} A \exp[-(q-q_m)/\alpha] & q_m \leq q \leq q_T \\ A \exp[(q-q_m)/\beta] & q_B \leq q < q_m \end{cases} \quad (E-1)$$

where  $q_B$  is the smallest specific humidity and  $q_T$  is the largest specific humidity in the sample and  $A$  is the normalization factor which allows  $F(Q=\infty) = 1 = \int_{-\infty}^Q f(Q) dq$ , the area under the integrated PDF, the cumulative distribution function, to be one. For each leg,  $q_T$  and  $q_B$  are known from the observations. The shape parameters are  $\alpha$  and  $\beta$ .

We first solve for  $A$  by integrating (E-1) over its domain and setting it equal to one

$$1 = \int_{q_m}^{q_T} A \exp[-(q-q_m)/\alpha] dq + \int_{q_B}^{q_m} A \exp[(q-q_m)/\beta] dq \quad (E-2)$$

which leads to

$$A = [\alpha(1 - \exp(-(q_T - q_m)/\alpha)) + \beta(1 - \exp((q_B - q_m)/\beta))]^{-1} \quad (E-3)$$

The maximum likelihood approach is used to estimate the parameters  $\alpha$ ,  $\beta$ , and  $q_m$ . The method of maximum likelihood selects as estimates those values of the parameters that maximize

the likelihood (L) of the observed sample. The likelihood is expressed as the product of the probabilities for each observation in the sample.

$$L[\alpha, \beta, q_m] = f_{(\alpha, \beta, q_m)}(q_1, \dots, q_m) = \prod_{i=1}^N f_{(\alpha, \beta, q_m)}(q_i) \quad (E-4)$$

Since the logarithmic function is a monotonically increasing function, the log of L is often maximized instead to simplify the mathematics.

$$\ln(L_{(\alpha, \beta, q_m)}) = \sum_{i=1}^N \ln(f_{(\alpha, \beta, q_m)}(q_i)) \quad (E-5)$$

for N observations and for our case

$$\begin{aligned} \ln(L_{(\alpha, \beta, q_m)}) = n \ln(A) + \frac{1}{\beta} \sum_{i=1}^{n_1} (q_i - q_m) \\ - \frac{1}{\alpha} \sum_{i=n_1+1}^{n_1+n_2} (q_i - q_m) \end{aligned} \quad (E-6)$$

where  $n_2$  is the number of observations with specific humidity greater than or equal to  $q_m$  and  $n_1$  is the number of observations with specific humidities less than  $q_m$ .

Analytically we solve for the three unknowns ( $\alpha$ ,  $\beta$  and  $q_m$ ) by maximizing  $\ln(L)$ ; namely, setting the partial derivative of  $\ln(L)$  with respect to each of the parameters equal to zero.

This results in

$$\frac{\partial(\ln(L))}{\partial \alpha} = 0 = -nA [1 - \exp(-(q_T - q_m)/\alpha) \cdot \left( \frac{q_T - q_m}{\alpha} + 1 \right)] - \frac{n_2}{\alpha^2} q_m + \frac{1}{\alpha^2} \sum_{i=1}^{n_1+n_2} q_i \quad (E-7)$$

$$\frac{\partial(\ln(L))}{\partial \beta} = 0 = -nA [1 + \exp((q_B - q_m)/\beta) \cdot \left( \frac{q_B - q_m}{\beta} - 1 \right)] - \frac{1}{\beta} \sum_{i=1}^{n_1} q_i + \frac{n_1 q_m}{\beta^2} \quad (E-8)$$

$$\frac{\partial(\ln(L))}{\partial q_m} = 0 = -nA [\exp((q_B - q_m)/\beta) - \exp(-(q_T - q_m)/\alpha)] + \frac{n_2}{\alpha} - \frac{n_1}{\beta} \quad (E-9)$$

Simultaneous equations E-7, E-8, and E-9 are then solved for the three unknowns.

Figures E.2 and E.3 show example of the resultant fits using these estimates for  $\alpha$ ,  $\beta$ , and  $q_m$ .

In Chapter 5 a mixture approach was used to describe the distribution of specific humidity values at various heights in the

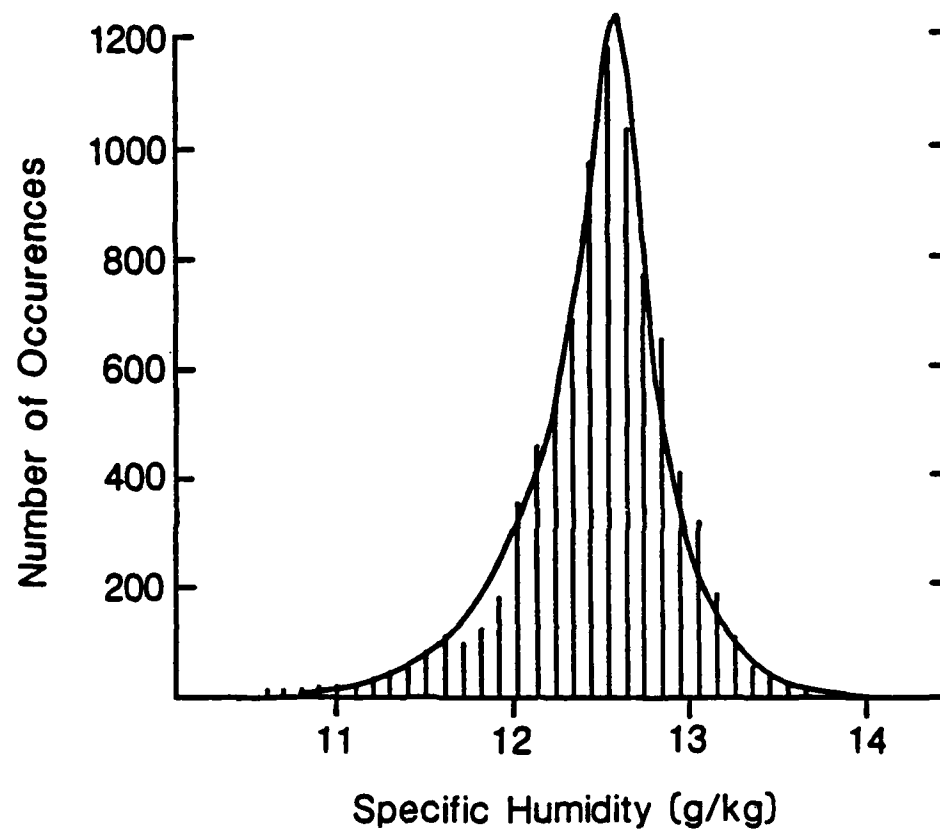


Figure E.2 Example fit of asymmetrical double exponential function to observed histogram of specific humidities observed during a near-surface flight leg. The parameters of the double exponential were estimated from the observations by the method of maximum likelihood.

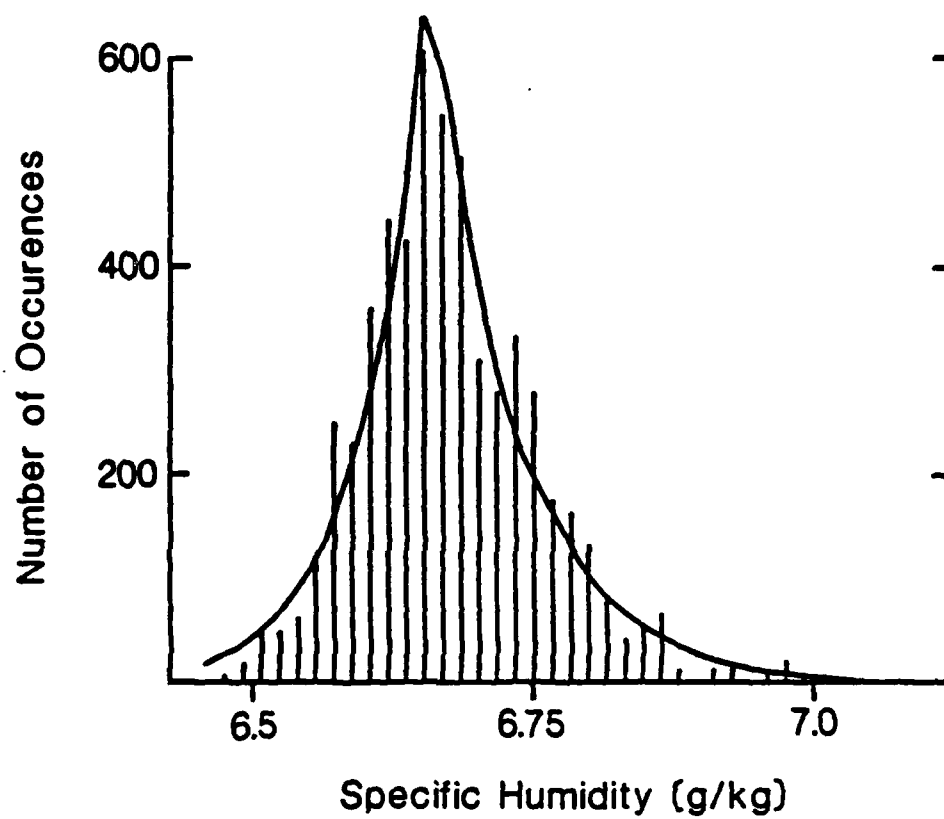


Figure E.3 Same as Figure E.2 except for a free atmosphere flight leg.

entrainment zone. In order to solve for the unknown parameters (assuming that we have correctly identified the number and type of densities present) we again use the method of maximum likelihood. Using asymmetrical double exponential densities for the free atmosphere and surface layer air and Gaussian for the mixed air, equation 5-6 took the form

$$\ln(L) = \sum_{i=1}^N \ln[P_1 f_1(q; q_{m1}) + P_2 f_2(q; \mu, \sigma) + P_3 f_3(q; q_{m3})] \quad (E-10)$$

where

$$f_1(q; q_{m1}) = \begin{cases} A_1 \exp((q - q_{m1})/\beta_1) & q < q_{m1} \\ A_1 \exp(-(q - q_{m1})/\alpha_1) & q \geq q_{m1} \end{cases}$$

and where the parameters with the subscript "1" refer to the free atmosphere values.

The Gaussian distribution is expressed as

$$f_2(q; \mu, \sigma) = \frac{1}{\sigma\sqrt{2\pi}} \exp(-(q - \mu)^2/2\sigma^2)$$

with mean  $\mu$  and standard deviation  $\sigma$ .

The surface layer distribution is described by

$$f_3(q; q_{m3}) = \begin{cases} A_3 \exp((q - q_{m3})/\beta_3) & q < q_{m3} \\ A_3 \exp(-(q - q_{m3})/\alpha_3) & q \geq q_{m3} \end{cases}$$

where the parameters with the subscript "3" refer to surface layer values.

Taking the partial derivatives of E-10 with respect to the unknown parameters ( $P_1$ ,  $P_3$ ,  $q_{m1}$ ,  $q_{m3}$ ,  $\mu$  and  $\sigma$ ) results in a complicated nonlinear set of equations. So E-10 was numerically evaluated directly to find the parameter values which maximized it.



## References

- Arnold, A., J.R. Rowland, T.G. Konrad, J.H. Richter, D.R. Jensen, and V.R. Noonkester, 1975: Simultaneous observations of clear air convection by a pulse radar, an FM-CW radar, an acoustic sounder, and an instrumented aircraft. Preprints, Sixteenth Radar Meteorology Conf., Houston, Amer. Meteor. Soc., 290-295.
- Barnes, S.L., 1964: A technique for maximizing details in numerical weather map analysis. J. Appl. Meteor., 3, 396-409.
- , 1973: Mesoscale objective analysis using weighted time-series observations. NOAA Tech. Memo. ERL NSSL-62, 60 pp. [NTIS COM-73-10781]
- Bean, B.R., R.O. Gilmer, R.F. Hartman, R.E. McGavin, and R.F. Reinking, 1976: Airborne measurement of vertical boundary layer fluxes of water vapor, sensible heat, and momentum during GATE. 83pp., NOAA Technical Memorandum ERL WMPO-36.

- , C.B. Emmanuel, R.O. Gilmer, and R.E. McGavin, 1975: The spatial and temporal variations of the turbulent fluxes of heat, momentum and water vapor over Lake Ontario. J. Phys. Oceanogr., 5, 532-540.
- and E.J. Dutton, 1968: Radio Meteorology, Dover Publications 435pp.
- Betts, A.K., 1982: Saturation point analysis of moist convective overturning. J. Atmos. Sci., 39, 1484-1505.
- Binkowski, F.S., 1983: A simple model for the diurnal variation of the mixing depth and transport flow. Boundary-Layer Meteor., 27, 217-236.
- Boers, R., R.L. Coulter, and E.W. Eloranta, 1984: Lidar observations of mixed layer dynamics: Tests of parameterized entrainment models of mixed layer growth rate. J. Climate Appl. Meteor., 23, 247-266.
- Box, G.E.P. and G.M. Jenkins, 1976: Time Series Analysis Forecasting and Control. Holden-Day, Oakland CA 575pp.

Bradley, E.F., R.A. Antonia, and A.J. Chambers, 1981:

Temperature structure in the atmospheric surface layer.

Boundary-Layer Meteor., 20, 275-292.

Brock, F. and G.H. Saum, 1983: Portable Automated Mesonet II.

Preprints, Fifth Symposium on Meteorological Observations

and Instrumentation, Toronto Ont., Canada Amer. Meteor.

Soc., 314-320.

Browning, K.A., Starr, J.R., and A.J. Whyman, 1973: The

structure of an inversion above a convective boundary layer

as observed using a high-power pulsed Doppler radar.

Boundary-Layer Meteor., 4, 91-111.

Buck, A.L., 1985: Rapid humidity measurements using the

Lyman-alpha absorption technique. Unpublished NCAR

technical note.

-----, 1976: The variable-path Lyman-alpha hygrometer and its

operating characteristics. Bull. Amer. Meteor. Soc., 57,

1113-1118.

----- and L.G. Post, 1980: RSF/RAF Lyman-alpha hygrometer model  
LA-3. Research Systems Facility, National Center for  
Atmospheric Research. 83pp.

Cattle, H. and K.J. Weston, 1975: Budget studies of heat flux  
profiles in the convective boundary layer over land. Quar.  
J. Roy. Meteor. Soc., 101, 353-363.

Caughey, S.J. and S.G. Palmer, 1979: Some aspects of turbulence  
structure through the depths of the convective boundary  
layer. Quar. J. Roy. Meteor. Soc., 105, 811-827.

Coulman, C.E., 1978: Boundary-layer evolution and nocturnal  
inversion dispersal, Part II. Boundary-Layer Meteor., 14,  
493-513.

----- and J. Warner, 1977: Temperature and humidity structure of  
the sub-cloud layer over land. Boundary-Layer Meteor. 11,  
467-484.

Coulter, R.L., 1979: A comparison of three methods for measuring  
mixing layer height. J. Appl. Meteor., 18, 1495-1499.

Crum, T.D., R.B. Stull, and E.W. Eloranta, 1985: Interpretation of aircraft boundary layer observations using coincident lidar images. Submitted to J. Climate Appl. Meteor.

Deardorff, J.W., G.E. Willis, and B.H. Stockton, 1980: Laboratory studies of the entrainment zone of a convectively mixed layer. J. Fluid Mech., 100, 41-64.

-----, -----, and D.K. Lilly, 1969: Laboratory investigation of non-steady penetrative convection. J. Fluid Mech., 35, 7-31.

Desjardins, R.L. and E.R. Lemon, 1974: Limitations of an eddy-correlation technique for the determination of the carbon dioxide and sensible heat fluxes. Boundary-Layer Meteor., 5, 475-488.

Driedonks, A.G.M., 1982: Models and observations of the growth of the atmospheric boundary layer. Boundary-Layer Meteor., 23, 283-306.

Duncan, M.T. and R.C. Brown, 1978: A data acquisition system for airborne meteorological research. Bull. Amer. Meteor. Soc., 59, 1128-1134.

Everitt, B.S. and D.J. Hand, 1981: Finite Mixture Distributions. Chapman and Hall pp143.

Friehe, C.A., R.L. Grossman, and Y. Pann, 1985: Calibration of an airborne Lyman-alpha hygrometer and measurement of water vapor flux using a thermoelectric hygrometer. Submitted to J. Atmos. and Ocean Tech.

Greenhut, G.K., J.K.S. Ching, R. Pearson Jr, and T.P. Repoff, 1984: Transport of ozone by turbulence and clouds in an urban boundary layer. J. Geophys. Res., 89, 4757-4766.

----- and S.J.S. Khalsa, 1982: Updraft and downdraft events in the atmospheric boundary layer over the equatorial Pacific Ocean. J. Atmos. Sci., 39, 1803-1818.

-----, 1982: Stability dependence of fluxes and bulk transfer coefficients in a tropical boundary layer. Boundary-Layer Meteor., 22, 253-264.

----- and B.R. Bean, 1981: Aircraft measurements of boundary-layer turbulence over the central equatorial Pacific Ocean. Boundary-Layer Meteor., 20, 221-241.

Grossman, R.L., 1984: Bivariate conditional sampling of moisture flux over a tropical ocean. J. Atmos. Sci., 41, 3238-3253.

Hall, F.F., J.G. Edinger, and W.D. Neff, 1975: Convective plumes in the planetary boundary layer, investigated with an acoustic sounder, J. Appl. Meteor., 14, 513-523.

Hanson, H.P., 1984: On mixed-layer modeling of the stratocumulus-topped marine boundary layer. Submitted for publication.

Hicks, B.B., and M.L. Wesley, 1980: Heat and momentum transfer characteristics of adjacent fields of soybeans and maize. Boundary-Layer Meteor., 20, 175-185.

Hildebrand, P.H. and B. Ackerman, 1984: Urban effects on the convective boundary layer. J. Atmos. Sci., 41, 76-91.

- Kaimal, J.C., N.L. Abshire, R.B. Chadwick, M.T. Decker, W.H. Hooke, R.A. Kropfli, W.D. Neff, and F. Pasqualucci, and P.H. Hildebrand, 1982: Estimating the depth of the daytime convective boundary layer. J. Atmos. Sci., 21, 1123-1129.
- , J.C. Wyngaard, D.A. Haugen, O.R. Cote, Y. Izumi, S.J. Caughey and C.J. Readings, 1976: Turbulence structure in the convective boundary layer. J. Atmos. Sci., 33, 2152-2169.
- Kalanda, B.D., T.R. Oke and D.L. Spittlehouse, 1980: Suburban Energy balance estimates for Vancouver, B.C., using the Bowen ratio-energy balance approach. J. Appl. Meteor., 19, 791-802.
- Kelley, N.D., 1973: Meteorological uses of inertial navigation. Atmospheric Technology, No.1
- Khalsa, S.J.S and G.K. Greenhut, 1985: Conditional sampling of updrafts and downdrafts in the marine atmospheric boundary layer. Submitted for publication.



-----, and J.A. Businger, 1977: On the structure of convective elements in the air near the surface.

Koch, S.E., M.des Jardins, and P.J. Kocin, 1981: The GEMPAK Barnes objective analysis scheme. NASA Technical Memorandum 83851. 56pp.

Konrad, T.G., 1970: Dynamics of convective process in clear air as seen by radar, J. Atmos. Sci., 27, 1138-1147.

Kunkel, K.E., E.W. Eloranta, and S.T. Shipley, 1977: Lidar observations of the convective boundary layer. J. Appl. Meteor., 16, 1306-1311.

Landsberg, H.E. and T.N. Maisel, 1972: Micro-meteorological observations in an area of urban growth. Boundary-Layer Meteor., 2, 365-370.

Lang, A.R.G., K.G. McNaughton, C. Fazu, E.F. Bradley, and E. Ohtaki, 1983: Inequality of eddy transfer coefficients for vertical transport of sensible and latent heats during advective inversions. Boundary-Layer Meteor., 25, 25-41.

- LeMone, M.A. and E.J. Zipser, 1980: Cumulonimbus vertical velocity events in GATE. Part I: diameter, intensity and mass flux. J. Atmos. Sci., 37, 2444-2457.
- Lenschow, D. and B. Stankov, 1981: Use of Lyman-alpha hygrometer data from STREX. Memo to STREX data users.
- and P.L. Stephens, 1980: The role of thermals in the convective boundary layer. Boundary-Layer Meteor., 19, 509-532.
- , C.A. Cullian, R.B. Friesen and E.N. Brown, 1978: The status of air motion measurements on NCAR aircraft. Preprints, Fourth Symp. Meteorological Observations and Instrumentation, Amer. Meteor. Soc., 433-438.
- Mahrt, L., 1976: Mixed layer moisture structure. Mon. Wea. Rev., 104, 1403-1407.
- Manton, M.J., 1982: A model of fair weather cumulus convection. Boundary-Layer Meteor., 22, 91-107.

-----, 1977: On the structure of convection. Boundary-Layer Meteor., 12, 491-503.

Melfi, S.H., J.D. Spinhirne, and S.H. Chou, 1985: Lidar observations of vertically organized convection in the planetary boundary layer over the ocean. To appear in J.Climate Appl.Meteor.

Milford, J.R., S. Abdulla, and D.A. Mansfield, 1979: Eddy flux measurements using an instrumented powered glider. Quart. J. Roy. Meteor. Soc., 105, 673-693.

Moore, W.H., S.J. Caughey, C.J. Readings, J.R. Milford, D.A. Mansfield, S. Abdulla, T.H. Guymer, and W.B. Johnston, 1979: Measurements of boundary layer structure and development over SE England using aircraft and tethered balloon instrumentation. Quar. J. Roy. Meteor. Soc., 105, 397-421.

NCAR Research Aviation Facility Bulletin No.2, 1981: Queen Air overview and summary of capabilities. 10pp.

----- No.22, 1976: Airborne humidity measurements. 11pp.

Nicholls, S. and M.A. LeMone, 1980: The fair weather boundary layer in GATE: The relationship of subcloud fluxes and structure to the distribution and enhancement of cumulus clouds. J. Atmos. Sci., 37, 2051-2067.

Oke, T.R., 1979: Advectively-assisted evapotranspiration from irrigated urban vegetation. Boundary-Layer Meteor., 17, 167-173.

Palmer, S.G., S.J. Caughey, K.W. Whyte, 1979: An observational study of entraining convection using balloon-borne turbulence probes and high-power doppler radar. Boundary-Layer Meteor., 16, 261-278.

Panofsky, H.A., and G.W. Brier, 1958: Some Applications of Statistics to Meteorology. Pennsylvania State University, University Park, Penn. 224 pp.

Pike, J.M., F.V. Brock and S.R. Semmer, 1983: Integrated Sensors for PAM II. Preprints, Fifth Symposium on Meteorological Observations and Instrumentation, Toronto Ont., Canada Amer. Meteor. Soc., 326-333.

- Rayment, R. and C.J. Readings, 1974: A case study of the structure and energetics of an inversion. Quart. J. Roy. Meteor. Soc., 100, 221-233.
- Readings, C.J., E. Golton, and K.A. Browning, 1973: Fine-scale structure and mixing within an inversion. Boundary-Layer Meteor., 4, 275-287.
- Rowland, J.R., 1973: Intensive probing of a clear air convective field by radar and instrumented drone aircraft. J. Appl. Meteor., 12, 149-155.
- , and A. Arnold, 1975: Vertical velocity structure and geometry of clear air convective elements. Preprints, Sixteenth Radar Meteorology Conf., Houston, Amer. Meteor. Soc., 296-303.
- Russell, P.B. and E.E. Uthe, 1978: Regional patterns of mixing depth and stability: Sodar network measurements for input to air quality models. Bull. Amer. Meteor. Soc., 59, 1275-1287.

Schotanus, P., F.T.M. Nieuwstadt, H.A.R. DeBruin, 1983:

Temperature measurement with a sonic anemometer and its application to heat and moisture fluxes. Boundary-Layer Meteor., 26, 81-93.

Sroga, J.T., E.W. Eloranta, and T. Barber, 1980: Lidar

measurements of wind profiles in the boundary layer. J. Appl. Meteor., 19, 598-605.

Stull, R.B., 1985a: An Introduction to Boundary Layer

Meteorology. Unpublished text.

-----, 1985b: A fair-weather cumulus cloud classification scheme

for mixed-layer studies. J. Climate Appl. Meteor., 24, 49-56.

-----, and E.W. Eloranta, 1984: Boundary Layer Experiment-1983.

Bull. Amer. Meteor. Soc., 65, 450-456.

-----, 1983: Boundary Layer Experiment-1983 BLX83 Scientist's

Flight Log. University of Wisconsin-Madison. 99pp.

Taconet, O. and A. Weill, 1983: Convective plumes in the atmospheric boundary layer as observed with an acoustic doppler sodar. Boundary-Layer Meteor., 25, 143-158.

-----,-----, 1982: Vertical velocity field in the convective boundary layer as observed with an acoustic doppler sodar. Boundary-Layer Meteor., 23, 133-151.

Tennekes, H. and A.G.M. Driedonks, 1981: Basic entrainment equations for the atmospheric boundary layer. Boundary-Layer Meteor., 20, 515-531.

Uthe, E.E., 1972: Lidar observations of the urban aerosol structure. Bull. Amer. Meteor. Soc., 53, 358-360.

Werner, C. and H. Herrmann, 1981: Lidar measurements of the vertical absolute humidity distribution in the boundary layer. J. Appl. Meteor., 20, 476-481.

Wesley, M.L., 1983: Turbulent transport of ozone to surfaces common in the eastern half of the United States. Advan. Sci. Technol., S.E. Schwartz, Ed., Wiley, New York, p345-370.

-----, D.R. Cook, and R.L. Hart, 1983: Fluxes of gases and particles above a deciduous forest in wintertime.

Boundary-Layer Meteor., 27, 237-255.

Wilde, N.P., R.B. Stull and E.W. Eloranta, 1985: The LCL zone and cumulus onset. J. Climate Appl. Meteor., 24, 640-657.

-----, 1984: The lifting condensation level and its relation to convective cloud base. M.S.thesis, University of Wisconsin-Madison, 170pp.

Wilczak, J.M. and J.A. Businger, 1983: Thermally indirect motions in the convective atmospheric boundary layer. J. Atmos. Sci., 40, 343-358.

Wynngaard, J.C., W.T. Pennell, D.H. Lenschow, and M.A. LeMone, 1978: The temperature-humidity covariance budget in the convective boundary layer. J. Atmos. Sci., 35, 47-58.



**END**

**FILMED**

**12-85**

**DTIC**